

Fach Geologie

Mega-glendonites in the Early Eocene Fur Formation

Unraveling paleoenvironmental conditions in the Danish Basin
and their influence on glendonite formation

Inaugural-Dissertation
zur Erlangung des Doktorgrades der Naturwissenschaften
im Fachbereich Geowissenschaften
der Mathematisch-Naturwissenschaftlichen Fakultät
der Westfälischen Wilhelms-Universität Münster

Vorgelegt von
Franziska Nenning
aus Feuchtwangen

- 2017 -

Prodekanin:	Prof. Dr. Gabriele Schrüfer
Erstgutachter:	Prof. Dr. Harald Strauß
Zweitgutachter:	PD Dr. habil. Matthias Zabel
Tag der mündlichen Prüfung:	18.07.2017
Tag der Promotion:	18.07.2017

Abstract

The Early Eocene Fur Formation of Northwestern Denmark comprises one of the largest, world-wide known glendonite, a calcite pseudomorph after the metastable mineral ikaite ($\text{CaCO}_3 \cdot 6\text{H}_2\text{O}$). Several authors used glendonite as an indicator for cold ages in the geologic record, but the Early Eocene is known for its warm climate following the Palaeocene-Eocene Thermal Maximum (PETM). These mega-glendonites of the Fur Formation were investigated for their geochemical composition in order to decipher the paleoenvironmental conditions during ikaite formation in the Early Eocene. Several temperature proxies (Δ_{47} ; $\delta^{18}\text{O}_{\text{carb}}$; $\delta^{18}\text{O}_{\text{diatom}}$) were applied to unravel the thermal history of ikaite formation in the silica-dominated, carbonate-free, and organic rich Danish Basin. The reconstruction of paleotemperatures within the sedimentary column points to cold temperatures for ikaite formation and to a range of +6 to +8 °C for the temperature of the transformation from ikaite to glendonite. Consequently, ikaite formation even occurs in warmer times if the temperatures of the bottom water and in the uppermost sedimentary column are cold enough and if other geochemical factors (high concentrations of phosphate, of magnesium, and of organic matter; high alkalinity) inhibit the formation of calcite and aragonite.

The glendonite of the Fur Formation is often located inside carbonate concretions, but carbonate concretions also occur in horizons without glendonites. Most of the carbonate concretions and the glendonite are bound to certain ash layers embedded within the clayey diatomite of the Fur Formation. Besides temperature proxies, other geochemical parameters were analysed to get further insight into the paleoenvironmental setting during the deposition of the sediments and of the subsequent formation of authigenic minerals. Early diagenetic processes, like organotrophic sulphate reduction and anaerobic oxidation of methane, were identified as key formation processes for ikaite/glendonite and carbonate concretions. In the lowermost part of the Fur Formation, impacts of the PETM were investigated. However, no signs of the PETM were identified within the glendonites and their surrounding carbonate concretions.

Finally, a paleoenvironmental model for the deposition of the Early Eocene Fur Formation was developed in order to reconstruct the conditions for the formation of ikaite and its subsequent transformation to glendonite in the sediments of this warm age.

Table of Contents

Abstract	v
Table of Contents	vi
1 Introduction and scientific objectives of this study	1
1.1. General introduction	1
1.2. Scientific objectives of this study	7
2 State of the art	9
2.1 Ikaite and its subsequent transformation to glendonite	9
2.2 Geological setting	12
2.3 Paleoenvironmental conditions within the Danish Basin	17
3 Materials and methods	21
3.1 Materials	21
3.1.1 Glendonite samples and their surrounding carbonate concretions	21
3.1.2 Carbonate concretions and volcanic ashes of the Fur Formation	22
3.1.3 Diatom samples and glendonite samples for temperature estimates	23
3.2 Methods	26
3.2.1 Sample preparation	26
3.2.2 X-ray diffraction	26
3.2.3 Electron microprobe analyses	26
3.2.4 Carbonate oxygen and carbon isotopes ($\delta^{18}\text{O}_{\text{carb}}$ and $\delta^{13}\text{C}_{\text{carb}}$)	27
3.2.5 Apatite concentration within glendonites (PO_4^{3-})	27
3.2.6 Total carbon (TC), total sulphur (TS), and total inorganic carbon (TIC)	27
3.2.7 Concentration of total organic carbon (TOC) and C/N ratio	28
3.2.8 Organic carbon isotopes ($\delta^{13}\text{C}_{\text{org}}$)	28
3.2.9 Strontium ($^{87}\text{Sr}/^{86}\text{Sr}$) and calcium ($\delta^{44/40}\text{Ca}$) isotopes	29
3.2.10 Sulphur ($\delta^{34}\text{S}_{\text{CAS}}$) and oxygen ($\delta^{18}\text{O}_{\text{CAS}}$) isotopes of CAS and WSS	29
3.2.11 Biomarker analyses	30
3.2.12 Oxygen isotopes of diatom frustules ($\delta^{18}\text{O}_{\text{diatom}}$)	31
3.2.13 Clumped isotopes of replacive calcite (Δ_{47})	34
4 Results	37
4.1 Glendonite of the Fur Formation	37
4.1.1 Macroscopic textures	37
4.1.2 Petrography and mineralogy	38
4.1.3 Geochemistry	41
4.2 Carbonate concretions and volcanic ash layers of the Fur Formation	47
4.2.1 Sediment structures and fossils	47
4.2.2 Volcanic ash layers – Microscopic textures and geochemistry	47
4.2.3 Carbonate concretions – Microscopic investigations	52

4.2.4	Carbonate concretions - Geochemistry	53
4.3	Paleotemperatures	66
4.3.1	Paleotemperatures indicated by the clumped isotope measurements (Δ_{47}) of glendonite	66
4.3.2	Paleotemperatures indicated by $\delta^{18}\text{O}_{\text{carb}}$ of glendonite and carbonate concretions	68
4.3.3	Bottom water temperatures indicated by $\delta^{18}\text{O}_{\text{diatom}}$ values	75
5	Discussion	79
5.1	Glendonite of the Fur Formation	79
5.1.1	The internal structure of glendonite	79
5.1.2	The carbon source for ikaite and the newly built fill cements	82
5.1.3	Oxygen isotopes – temperature estimates vs. pore water composition	84
5.1.4	Apatite as limiting factor for bulk $\delta^{18}\text{O}$ analyses of glendonite samples	86
5.1.5	Did the ash layers enhance the chance for ikaite formation?	87
5.1.6	Paleoenvironmental conditions of ikaite formation and transformation	92
5.2	Carbonate concretions and volcanic ash layers of the Fur Formation	95
5.2.1	Volcanic ash layers – Their possible impact on the formation of carbonate concretions	95
5.2.2	Carbonate concretions – shape and composition	98
5.2.3	Carbon cycling within the Fur Formation – Signals from the PETM?	98
5.2.4	Pore water geochemistry	102
5.2.5	Diagenetic zones within the sedimentary column	105
5.3	Paleotemperatures	111
5.3.1	Previous paleotemperature estimates for the Fur Formation	111
5.3.2	Concept of the multiproxy paleotemperature reconstruction	112
5.3.3	Paleotemperatures derived from clumped isotopes (Δ_{47})	113
5.3.4	Paleotemperatures derived from carbonate oxygen isotopes ($\delta^{18}\text{O}_{\text{carb}}$)	114
5.3.5	Paleotemperatures derived from oxygen isotopes of diatom frustules ($\delta^{18}\text{O}_{\text{diatom}}$)	116
6	Model of the Fur Formation deposition	121
7	Summary and outlook	125
7.1	Summary	125
7.2	Outlook	128
8	References	129
9	Appendices	147
10	Acknowledgements and Curriculum Vitae	161
10.1.	Acknowledgements	161
10.2.	Curriculum vitae	162

1 Introduction and scientific objectives of this study

1.1. General introduction

Glendonite is a calcite pseudomorph after the metastable mineral ikaite (Fig. 1 and Tab. 1). Freiesleben (1827) first described it as “Gerstenkörner”, but other names like thinolite, jarrowite, gennoishi, or pseudogaylussite were used subsequently. The name “glendonite” was recommended by David and Taylor (1905) when reporting these pseudomorphs in the Glendon Valley in New South Wales, Australia, as Dana did during expeditions between 1838 and 1842 (Dana, 1849). After investigating marine, sedimentary ikaite in the Bransfield Strait, Antarctica, Suess et al. (1982) proposed that the mineral ikaite, a calcium carbonate hexahydrate ($\text{CaCO}_3 \cdot 6\text{H}_2\text{O}$), is the precursor of glendonite. Ikaite was initially identified in the laboratory by Pelouze (1831), and in nature in the Ikka fjord, Greenland, by Pauly (1963) (Fig. 1 and Fig. 2). Modern ikaite is often observed in marine, organic-rich, anoxic sediments, growing into the water column, and in the sea ice of polar regions (e.g. Suess et al., 1982; Shearman and Smith, 1985; Jansen et al., 1987; Schubert et al., 1997; Dieckmann et al., 2010; Geptner et al., 2014; Zhou et al., 2015; Tab. 2). Ikaite is metastable with respect to calcite and aragonite and it decomposes under atmospheric conditions (Brooks et al., 1950; Bischoff et al., 1993; Hu et al., 2015). In recent years, ikaite was discovered in terrestrial environments at temperatures up to +10 °C at pH values higher than 11 (Milodowski et al., 2014; Boch et al., 2015; Field et al., 2016), unlike marine ikaite that formed at low temperatures between -1.9 and +3 °C (Zhou et al., 2015). Ikaite was proposed to form at near-freezing temperatures. Thus, glendonite was used as a proxy for identifying cold climatic conditions in the geologic record (Kaplan, 1979; Kemper and Schmitz, 1975, 1981; James et al., 2005; Rogala et al., 2007; Fig. 3). Teichert and Luppold (2013) questioned that ikaite, respectively glendonite, was solely precipitated in cool environments. Instead, they proposed that ikaite was formed at marine methane seep locations via methanotrophic sulphate reduction at temperatures of ca. +10 °C, i.e. temperatures higher than usually reported for ikaite from marine environments.

Several factors like high alkalinity, high contents of organic matter, orthophosphate, or magnesium are thought to increase the stability of ikaite towards higher temperatures (Brooks et al., 1950; Bischoff et al., 1993; Hu et al., 2015). Moreover, two microbial processes are believed to trigger the formation of ikaite at the water sediment interface: the organotrophic and the methanotrophic sulphate reduction (Boggs, 1972; Suess et al., 1982; De Lurio and Frakes, 1999; Geptner et al., 2014; Zhou et al., 2015).

The Early Eocene Fur Formation of Northwestern Denmark was deposited a few 100,000 years after the Palaeocene-Eocene Thermal Maximum (PETM) in a warm, subtropical climate (Bonde, 1966; Pedersen et al., 2011). The PETM is considered to have been a time of extreme climate change, a carbon cycle event where marine bottom waters and high-latitude surface waters warmed in a dramatic way (e.g. Kennett and Stott, 1991; Dickens et al., 1995; Tripathi and

Elderfield, 2005; Pearson et al., 2007; Zachos et al., 2008). A rapid and substantial release of carbon dioxide (CO₂) during the opening of the North Atlantic caused the PETM. In addition, methane (CH₄) was liberated explosively from hydrothermal vent complexes triggered by contact metamorphism of mantle-derived melts in carbon-rich sediments (Svensen et al., 2004; Frieling et al., 2016). Additionally, Mclerney and Wing (2011) and Bowen et al. (2015) proposed two other sources of CO₂ and CH₄, a widespread oxidation of organic carbon and a bolide impact.

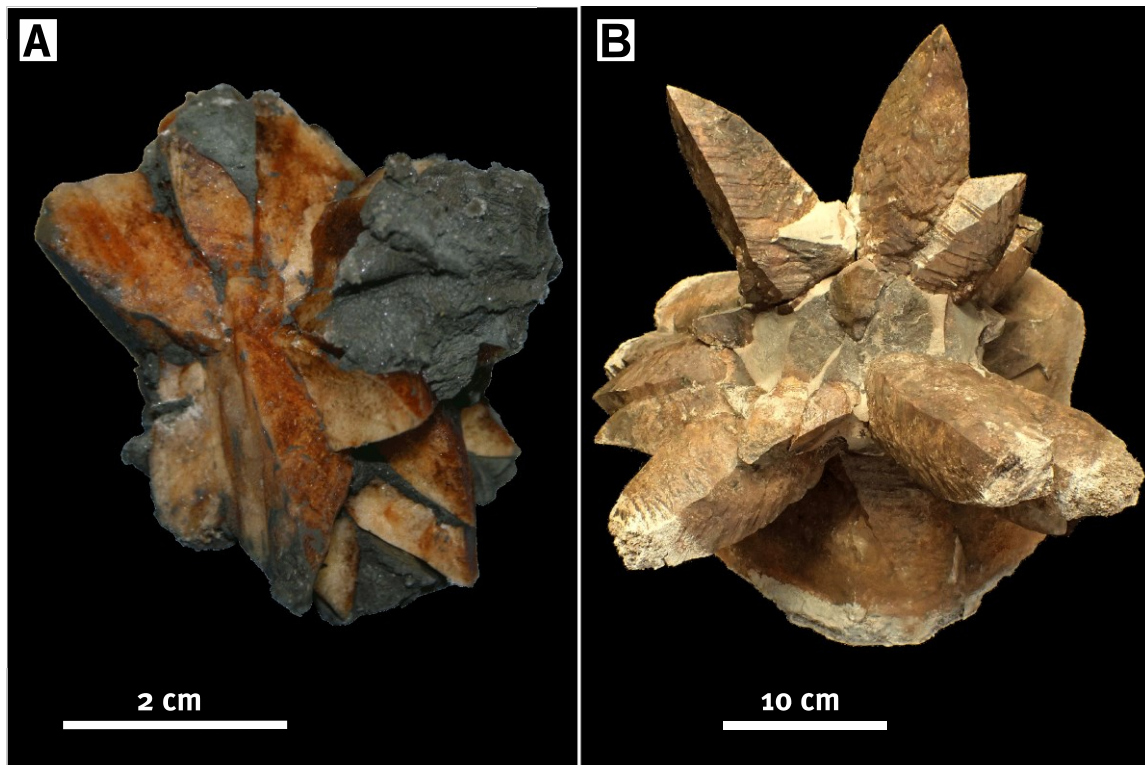


Fig. 1: Photographs of (A) an ikaite, investigated in the Congo fan (Picture: M. Zabel) and (B) gledonite of ash layer +9 of the Fur Formation (Picture: B. Schultz).

The deposition of the Early Eocene Fur sediments occurred in a local upwelling region (Pedersen and Surlyk, 1983; Pedersen et al., 2011) during subtropical conditions pointing to temperatures higher than generally considered for ikaite formation (Collins et al., 2005; Tripathi and Elderfield, 2005; Sluijs et al., 2006; Schoon, 2013). The Fur Formation comprises diatomite alternating with ca. 200 ash layers related to the North Atlantic Igneous Province (NAIP) (Bøggild, 1918; Pedersen et al., 1975; Larsen et al., 2003). In the Fur Formation, solely diatom frustules (Pedersen and Surlyk, 1983; Pedersen and Buchardt, 1996; Pedersen, 2008) can be found, while calcitic micro- and macrofossils are absent. Zechstein salt diapirs migrated upwards into sediments below the Fur Formation (Madirazza, 1976; Larsen and Baumann, 1981; Jørgensen et al., 2005; Pedersen et al., 2011).

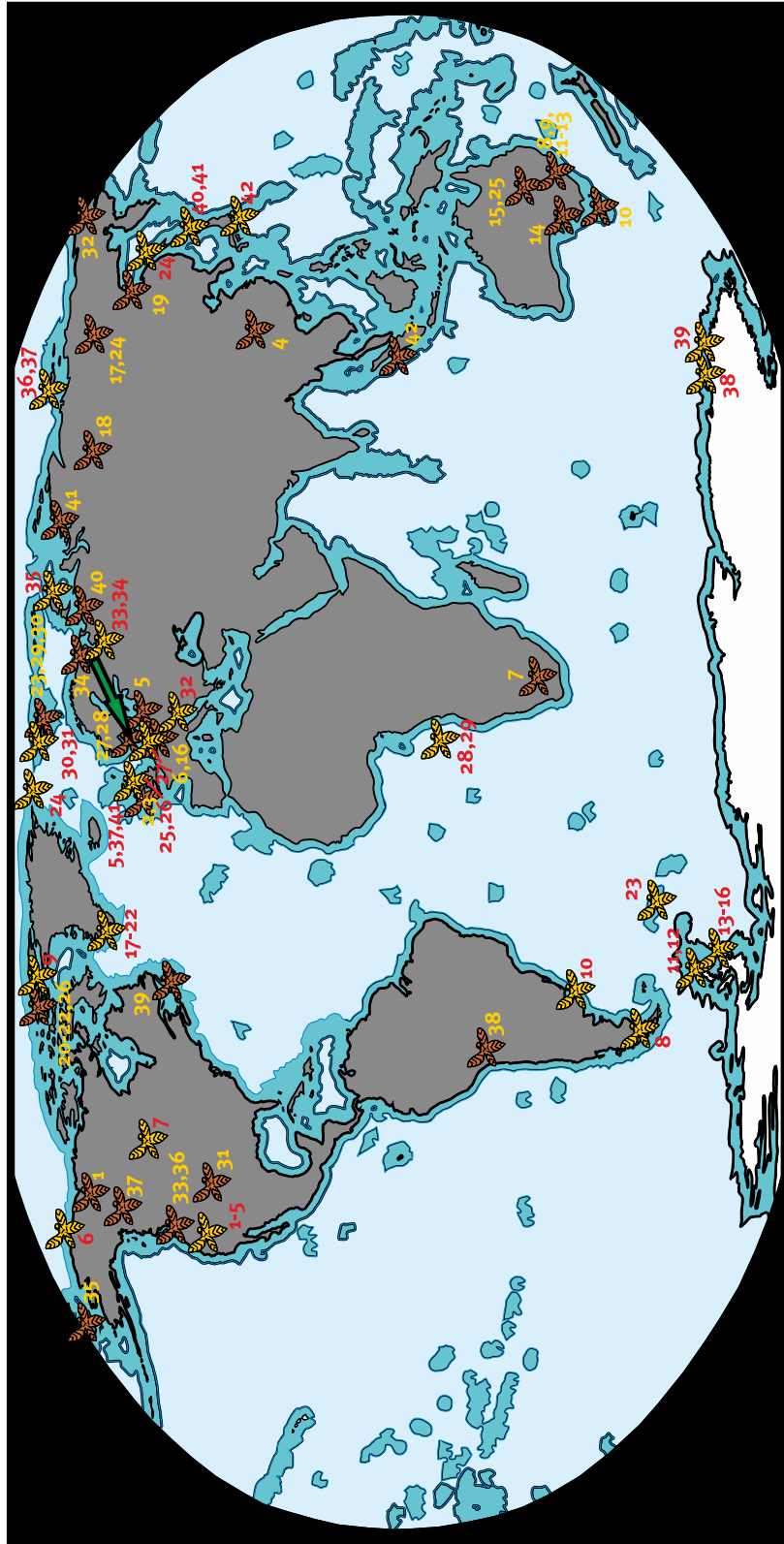


Fig. 2: Main glendonite and ikaite localities on a global map. Recent ikaite/glendonite sites are given in red numbers and yellow signs, fossil findings are labelled with yellow numbers and orange signs. The green arrow points to the location of the Fur Formation. All cited references are given in tables 1 and 2.

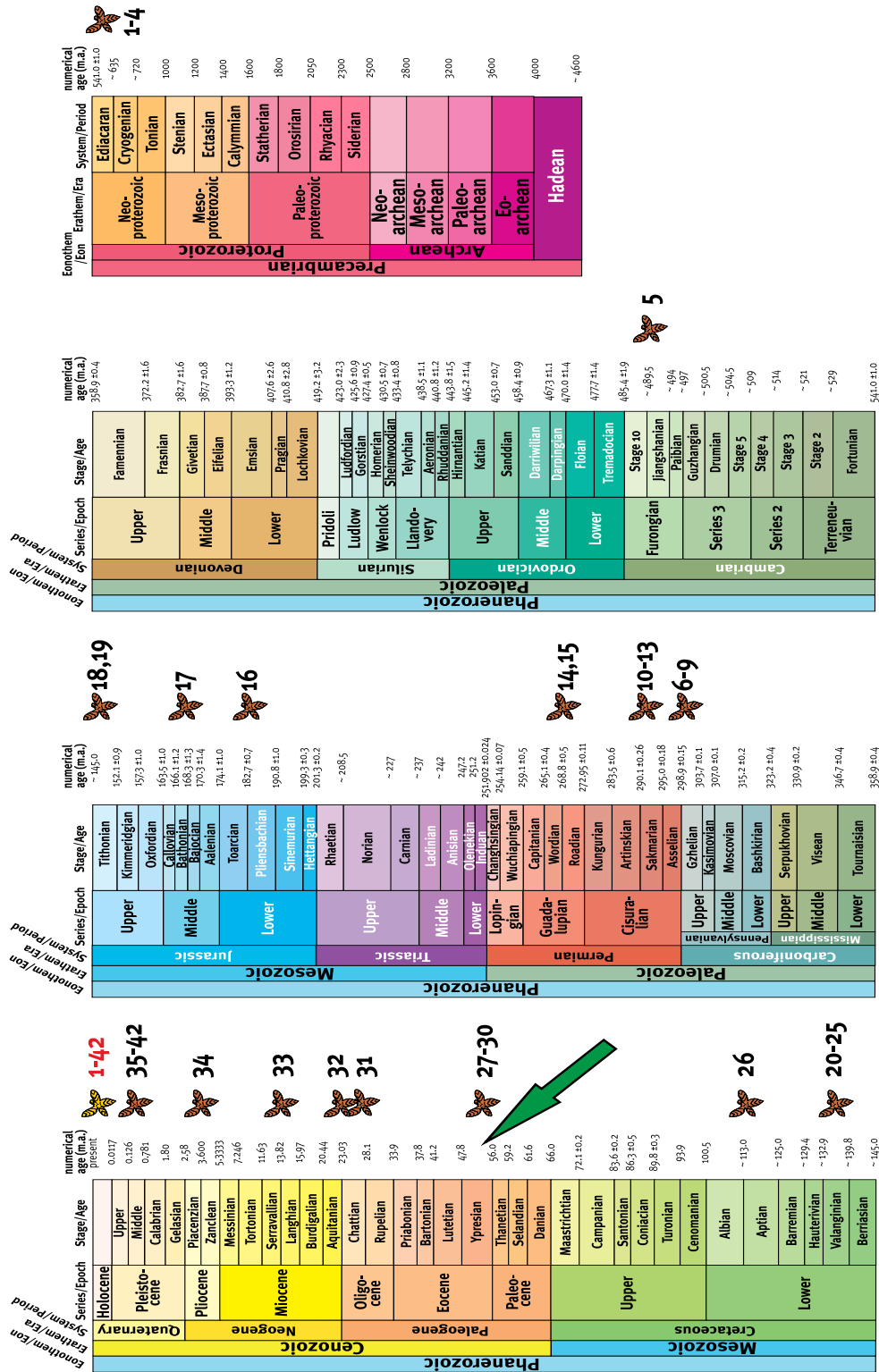


Fig. 3: Main glendonite and ikaite findings in Earth’s history (modified after ICS International Chronostratigraphic Chart 2016). Recent ikaite/glendonite are given in red numbers and yellow signs, fossil findings are labelled with black numbers and orange signs. The green arrow points to the time of the deposition of the Fur Formation. All cited references are given in tables 1 and 2.

Tab. 1: Cited glendonite references shown in figures 2 and 3.

Number	Authors	Year	Site	Country	Age
1	James et al.	2005	Mackenzie Mountains	Canada	Neoproterozoic
2	Johnston	1995	Donegal	Ireland	Neoproterozoic
3	Dempster & Jess	2015	W Scotland	United Kingdom	Neoproterozoic
4	Wang et al.	2016	Zhangcunping, Hubei Province	China	Ediacara
5	Stolley	1909	Bornholm	Denmark	Upper Cambrian
6	Freiesleben	1827	Sangerhausen	Germany	Permo-Carboniferous
7	McLachlan et al.	2001	Great Karoo basin	Southern Africa	Late Carboniferous
8	Dana;David	1849; 1905	Glendon Valley	Australia	Permo-Carboniferous
9	Thomas et al.	2007	New South Wales	Australia	Early Permian
10	Rogala et al.	2007	Tasmania Basin	Australia	Lower Permian
11	Jones et al.	2006	Sydney Basin	Australia	Permian
12	Selleck et al.	2007	Sydney Basin	Australia	Permian
13	Frank et al.	2008	Sydney Basin	Australia	Early Permian
14	Huggett et al.	2005	Black Alley Shale	Australia	Permian
15	Huggett et al.	2005	Carnavon Gorge	Australia	Permian
16	Teichert & Luppold	2013	Cremlingen	Germany	Early Jurassic
17	Morales et al.	2017	N Siberia, Lena river	Russia	Lower/Middle Jurassic
18	Kaplan	1979	NW Siberia	Russia	Jurassic
19	Kaplan	1979	Okhotsk Sea	Russia	Jurassic
20	Kemper & Schmitz	1975	Sverdrup Basin	Canada	Early Cretaceous
21	Föllmi	2012	Sverdrup Basin	Canada	Early Cretaceous
22	Grasby et al.	2017	Sverdrup Basin	Canada	Early Cretaceous
23	Price & Nunn	2010	Svalbard	Norway	Early Cretaceous
24	Rogov & Zakharov	2010	N Siberia, Lena river	Russia	Lower/Middle Jurassic
25	De Lurio & Frakes	1999	Eromanga Basin	Australia	Early Cretaceous
26	Herrle et al.	2015	Axel Heiberg Island	Canada	Mid Cretaceous
27	Huggett et al.	2005	Fur Formation	Denmark	Early Eocene
28	Schultz	2009	Fur Formation	Denmark	Early Eocene
29	Kaplan	1979	Spitsbergen	Norway	Tertiary
30	Spielhagen & Tripati	2009	Spitsbergen	Norway	Paleocene/Eocene
31	Larsen	1994	Colorado	USA	Oligocene
32	Kaplan	1979	Koryak	Russia	Paleogene/Neogene
33	Boggs	1972, 1975	NW Oregon, W Washington	USA	Miocene
34	Selleck et al.	2007	Kola Peninsula	Russia	Late Neogene
35	Kaplan	1979	Chukotka	Russia	Quaternary
36	Bornhold & Firth	1998	Vancouver Island	Canada	Pleistocene
37	James et al.	2005	Twitya-Keele-Fm	Canada	Pleistocene
38	Pueyo et al.	2011	Lake Chungara	Chile	Quaternary
39	Brookes et al.	1982	Newfoundland	Canada	Quaternary
40	Kaplan	1979	Polar Urals	Russia	Quaternary
41	Kaplan	1979	Taimyr	Russia	Quaternary
42	Teichert	2007	Simeulue Seep	Sumatra	Quaternary

Pedersen and Buchardt (1996), Huggett et al. (2005), and Schultz (2009) investigated glendonite in the Danish Fur Formation containing the largest glendonites (so called “mega-glendonites”; Fig. 1) reported so far. Pedersen and Buchardt (1996) were the first to describe the glendonite and analysed carbon and oxygen isotope data for glendonite from the Fur Formation that form a base for respective analyses in this study. Huggett et al. (2005) described glendonite from the Fur Formation, embedded in fine-grained sediments that are rich in organic matter. Glendonite consisting of single crystals or clusters is often partially enclosed in calcareous concretions. Huggett et al. (2005) refer to it as type C glendonite. Brooks (2006) investigated in the calcareous concretions of the Fur Formation large, brown, wedge-shaped crystals of calcite with 10 cm in diameter and up to 30 cm length. The largest glendonite is about 1.5 m long and it was investigated at the Lynghøj pit (N-Mors). Pedersen et al. (2011) reported rosettes of calcite crystals (between ash layers +3 and +62) and concluded that the precursor ikaite could have been

formed within the sediments below the seafloor under cold-water conditions caused by a thermocline between sea surface water and bottom water. Despite all these reports, the formation of ikaite and the subsequent transformation from ikaite to glendonite during the warm Early Eocene remains poorly constrained and will be clarified in this study.

Tab. 2: Cited ikaite references shown in figures 2 and 3.

Number	Authors	Year	Site	Country	Environment	Age
1	Shearman et al.	1989	Lahontan and Mono Lake	USA	terrestrial	recent
2	Bischoff et al.	1991	Mono Lake	USA	terrestrial	recent
3	Bischoff et al.	1993	Mono Lake	USA	terrestrial	recent
4	Council & Bennett	1993	Mono Lake	USA	terrestrial	recent
5	Whititcar & Suess	1998	Mono Lake	USA	terrestrial	recent
6	Kennedy et al.	1987	Esetkoak Lagoon	Alaska, USA	marine	recent
7	Last et al.	2010	N Great Plains	Canada	terrestrial	recent
8	Oehlerich et al.	2013	Laguna Potrok Aike	Argentina	terrestrial	recent
9	Omelson et al.	2001	Axel Heiberg Island	Canada	terrestrial	recent
10	Hensen et al.	2003	W Argentine Basin	Argentina	marine	recent
11	Suess et al.	1982	Bransfield Strait	Antarctica	marine	Permian to recent
12	Whititcar & Suess	1998	Bransfield Strait	Antarctica	marine	Permian to recent
13	Domack et al.	2007	NW Weddell Sea	Antarctica	marine	recent
14	Dieckmann et al.	2008	NW Weddell Sea	Antarctica	marine	recent
15	Lu et al.	2012	NW Weddell Sea	Antarctica	marine	recent
16	Zhou et al.	2015	Firth of Tay	Antarctica	marine	recent
17	Pauly	1963	Ika Fjord	Greenland, Denmark	marine	recent
18	Buchardt et al.	1997	Ika Fjord	Greenland, Denmark	marine	recent
19	Buchardt et al.	2001	Ika Fjord	Greenland, Denmark	marine	recent
20	Stougaard et al.	2002	Ika Fjord	Greenland, Denmark	marine	recent
21	Schmidt et al.	2006	Ika Fjord	Greenland, Denmark	marine	recent
22	Hansen et al.	2011	Ika Fjord	Greenland, Denmark	marine	recent
23	Bell et al.	2016	South Georgia	South Georgia, UK	marine	recent
24	Rysgaard et al.	2012	Arctic Ocean	Arctic Ocean	marine	recent
25	Shearman & Smith	1985	Jarrow Slake	NE England	marine	recent
26	Field et al.	2016	Peak Dale, Derbyshire	United Kingdom	terrestrial	recent
27	Gripp & Tufar	1974	Nordstrand	Germany	marine	recent
28	Jansen et al.	1987	Zaire deep-sea fan	W Africa	marine	recent
29	Zabel & Schultz	2001	Zaire deep-sea fan	W Africa	marine	recent
30	Dieckmann et al.	2010	Kongsfjorden, Svalbard	Norway	marine	recent
31	Nomura et al.	2013	N Svalbard	Norway	marine	recent
32	Boch et al.	2015	Graz/Wien	Austria	terrestrial	recent
33	Kaplan	1979	White Sea	Russia	marine	recent
34	Geptner et al.	2014	White Sea	Russia	marine	Holocene/recent
35	Kodina et al.	2003	Kara Sea	Russia	marine	recent
36	Schubert et al.	1997	Laptev Sea	Russia	marine	recent
37	Haase	1998	Laptev Sea	Russia	marine	recent
38	Fischer et al.	2013	Wilkes Land	Antarctica	marine	recent
39	Fischer	2009	Adelie Land	Antarctica	marine	recent
40	Ito	1996	Shiowakka, Hokkaido	Japan	terrestrial	recent
41	Ito	1998	Shiowakka, Hokkaido	Japan	terrestrial	recent
42	Stein & Smith	1985	Nankai Trough	Japan	marine	recent

1.2. Scientific objectives of this study

Petrographic, geochemical, and isotope data of Early Eocene glendonite from the Fur Formation are presented in the first part of this study (Fig. 4). Analyses at high spatial resolution provide information about the internal structure of glendonite and the transformation processes from ikaite to glendonite. Geochemical and isotope data allow reconstructing environmental conditions for the ikaite precipitation and the stability of glendonite. Finally, the impact of the volcanic ash layers as well as the Zechstein salt diapirs are discussed.

In the second part of this study, geochemical and isotope data for the volcanic ash layers and the carbonate concretions of the Fur Formation are discussed in order to reveal the formation processes of the carbonate concretions. Based on a multi proxy investigation (C_{org} , C/N ratio, $\delta^{34}S_{CAS}$, $\delta^{18}O_{CAS}$, and biomarker), the paleoenvironmental circumstances are reconstructed resolving climate responses for the period after the PETM (riverine organic matter supply, water column stratification). Furthermore, the early diagenetic environment(s) of calcite precipitation are reconstructed for the carbonate concretions.

Finally, prevailing paleotemperatures during the deposition of the sediments are deduced from several geochemical proxies in the third part of this study. For the first time, clumped isotopes (Δ_{47}) representing a direct proxy for the temperature of carbonate precipitation (Eiler, 2007; Huntington et al., 2009; Affek, 2012) have been measured for glendonite samples. Results for clumped isotopes are used to calibrate the $\delta^{18}O$ value for the initial pore water from which the ikaite/glendonite and the carbonate concretions were precipitated. After estimating the $\delta^{18}O$ value of the pore water, two other temperature proxies ($\delta^{18}O_{carb}$ and $\delta^{18}O_{diatom}$) are discussed in respect to the overall paleotemperatures that prevailed in the bottom water and within the uppermost sedimentary column during the Early Eocene.

The ultimate aim of this study is to establish a model for the deposition of the Early Eocene Fur Formation with a special focus on the formation of ikaites and subsequent transformation to glendonites (Fig. 4). A combination of petrographical, geochemical, and isotopic information serves to achieve this research goal.

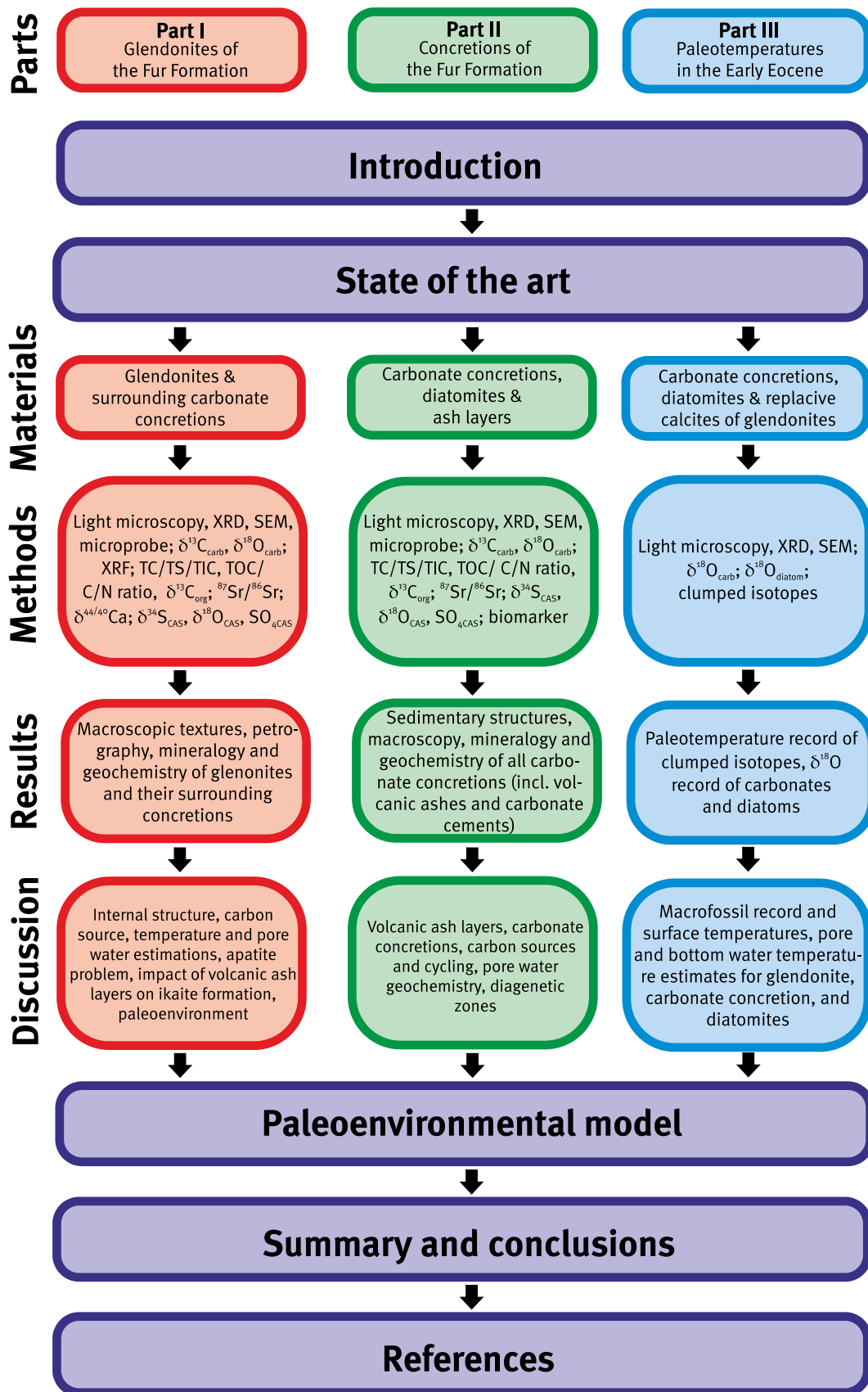


Fig. 4: Flow progress chart of this PhD thesis showing the inner structure and summarizing important keynotes.

2 State of the art

2.1 Ikaite and its subsequent transformation to glendonite

Ikaite

Ikaite is a calcium carbonate hexahydrate ($\text{CaCO}_3 \cdot 6\text{H}_2\text{O}$) and it is metastable as a function of temperature (Marland, 1975; Brecevic and Nielsen, 1993). In addition, several studies discussed the stability of ikaite under various concentrations of phosphate, pH, and other chemical substances (Brooks et al., 1950; House, 1987; Lin and Singer, 2006; Hu et al., 2015). Moreover, laboratory studies examined the thermal expansion behaviour of ikaite (Lennie et al., 2004; Papadimitriou et al., 2014; Zaoui and Sekkal, 2014), Raman, and IR spectra of this monoclinic mineral (Coleyshaw et al., 2003; Sahar et al., 2005; Tang et al., 2009; Rysgaard et al., 2012, Demichelis and Gale, 2014; Boch et al., 2015).

In nature, ikaite is often found in waters with temperature close to the freezing point (e.g. Pauly, 1963; Stein and Smith, 1985; Jansen et al., 1987; Hansen et al., 2011; Oehlerich et al., 2013; Field et al., 2016). Thus, ikaite was thought to decompose at temperatures higher than 4 °C (Hu et al., 2014). In addition, several inhibitors preventing the formation of calcite and aragonite and favoring the formation of ikaite were identified: high Ca concentration, high alkalinity, high $p\text{CO}_2$, high Mg concentration, high organic matter concentration, and a high phosphate concentration as the dominant controlling factor (Bischoff et al., 1993; Gal et al., 1996; Buchardt et al., 1997; Kodina et al., 2002; Zhou et al., 2015). Ikaite often forms in terrestrial and marine environments where two different water masses mix like in the Mono Lake, California, or the Ikka fjord in Greenland (Bischoff et al., 1993; Council and Bennett, 1993; Ito et al., 1996; Buchardt et al., 1997, 2001; Oehlerich et al., 2013; Milodowski et al., 2014; Boch et al., 2015; Field et al., 2016). Recently, ikaite was observed in sea ice (Dieckmann et al., 2008, 2010; Fischer 2009; Rysgaard et al., 2012; Fischer et al., 2013; Hu et al., 2014).

Besides the mixing of different water masses, ikaite also precipitates as a result of early diagenetic processes like organotrophic sulphate reduction via microbial degradation of organic matter in highly reducing environments (e.g. Stein and Smith, 1985; Bischoff et al., 1993; Haase, 1998; Jansen et al., 1987; Kennedy et al., 1987; Schubert et al., 1997; Zabel and Schultz, 2001; Kodina et al., 2002; Zhou et al., 2015; Bell et al., 2016). Stougaard et al. (2002) and Schmidt et al. (2006) investigated sulphate-reducing bacteria ikaite columns at the Ikka fjord in Greenland. The anaerobic oxidation of methane is another source for the bicarbonate ion, which apparently initiates the formation of ikaites (Stein and Smith, 1985; Jansen et al., 1987; Schubert et al., 1997; Zabel and Schultz, 2001; Bell et al., 2016).

Ikaite form in the shallow sedimentary column, where the phosphate and the organic matter concentration in the pore water are high favouring the precipitation of ikaites (Lu et al., 2012; Zhou et al., 2015). Lu et al. (2012) proposed a time interval of several decades for the formation of the ikaite of the Antarctic Peninsula.

Glendonite

Ikaite is metastable, but it has been preserved as glendonite in the geological record since the Ediacaran (Johnston, 1995; James et al., 2005; Dempster and Jess, 2015; Wang et al., 2016; Fig. 3). Suess et al. (1982) established an understanding that the mineral ikaite is the precursor of glendonite. Glendonite was observed as bipyramidal blades, rosettes, and in stellate forms with rhombic prisms in cross sections (e.g. Stolley, 1909; Kaplan, 1979; Kemper and Schmitz, 1981; Suess et al., 1982; Larsen, 1994; Greinert and Derkachev, 2004; Frank et al., 2008; Spielhagen and Tripathi, 2009; Geptner et al., 2014; Teichert and Luppold, 2013; Wang et al., 2015). Glendonite consists of calcite with 98 wt% CaCO_3 (Boggs and Hull, 1975). It exhibits a density of 1.9 g cm^{-3} under friable conditions for loosely deposited calcite after ikaite, named “proto-glendonites” sensu Teichert and Luppold (2013), or a density of 2.65 g cm^{-3} for glendonite that is filled entirely with calcitic cement (Kaplan, 1979).

Glendonite is often reported from laminated sediments where the laminae next to the glendonites were disturbed, or, more precisely, warped around the glendonite pointing to a displacive growth of the ikaite during early diagenesis (Greinert and Derkachev, 2004; McLachlan et al., 2006; Selleck et al., 2007; Frank et al., 2008; Wang et al., 2015). Thus, ikaite is thought to precipitate near the water sediment interface where the nutrients, especially phosphate and organic matter, are very high (Kaplan, 1979; Larsen, 1994; De Lurio and Frakes, 1999; Kodina et al., 2002; Greinert and Derkachev, 2004; Huggett et al., 2005; McLachlan et al., 2006; Zu et al., 2012). Most authors concluded that the precursor ikaite precipitated in marine, dysoxic to anoxic environments where the bicarbonate ion resulted from microbial organotrophic sulphate reduction (Boggs, 1972; Kaplan, 1979; Kemper and Schmitz, 1981; Suess et al., 1982; Larsen, 1994; De Lurio and Frakes, 1999; Kodina et al., 2002; Greinert and Derkachev, 2004; Huggett et al., 2005; Rogala et al., 2007; Selleck et al., 2007; Frank et al., 2008; Spielhagen and Tripathi, 2009; Geptner et al., 2014; Grasby et al., 2017). In addition, anaerobic oxidation of biogenic methane is another source for the bicarbonate ion of the ikaite (Kodina et al., 2002; Greinert and Derkachev, 2004; Teichert and Luppold, 2013). The processes of organotrophic sulphate reduction and anaerobic oxidation of methane were identified using stable carbon isotopes ($\delta^{13}\text{C}_{\text{carb}}$ and $\delta^{13}\text{C}_{\text{org}}$) (e.g. Spielhagen and Tripathi, 2009; Geptner et al., 2014; Teichert and Luppold, 2013; Morales et al., 2015; Grasby et al., 2017).

If the temperatures are higher than $4 \text{ }^\circ\text{C}$ (Hu et al., 2014), ikaite decomposes to a mush of small calcite grains and water (e.g. Zabel and Schultz, 2001; Boch et al., 2015; Field et al., 2016). Under perfect temperature conditions and in environments favouring the stability of the void, ikaite is transformed to glendonite. For this, the primary ikaite crystal is filled with the calcite of the ikaite mineral ($\text{CaCO}_3 \cdot 6\text{H}_2\text{O}$) and, subsequently, with various other calcite cements (Boggs, 1972; Boggs and Hull, 1975; Kaplan, 1979; Larsen, 1994; Greinert and Derkachev, 2004; Huggett et al., 2005; McLachlan et al., 2006; Selleck et al., 2007; Frank et al., 2008; Teichert and Luppold, 2013; Grasby et al., 2017). The first cement phase following the breakdown of ikaite consists of large, loosely packed ovoid calcite crystals and rosettes (Boggs, 1972; Larsen, 1994; De Lurio and Frakes, 1999; Frank et al., 2008; Teichert and Luppold, 2013). This

calcite might have formed very rapidly in a matter of few hours (Huggett et al., 2005) and the released crystal water prevents the collapse of the primary void (Larsen, 1994; Johnston, 1995; Frank et al., 2008). Teichert and Luppold (2013) suggested the transformation to start at the margin preserving the original morphology in a soft, marine sediment. These calcite crystals were often enclosed by a subsequent rim cement (Greinert and Derkachev, 2004; Huggett et al., 2005; Frank et al., 2008; Teichert and Luppold, 2013). Later, the open pore spaces were filled with a sparry calcite (e.g. Kaplan, 1979; Greinert and Derkachev, 2004; Huggett et al., 2005). Additionally, Ito (1998) denoted moisture on the surface of the crystal and magnesium chloride in solution to favour a very slow transformation. This could be an explanation for the preservation of ikaite in marine environments in the geological record. Ikaite was thought to form syndepositionally or during early diagenesis prior to compaction and lithification (Boggs and Hull, 1975; Geptner et al., 2014; Wang et al., 2015).

According to Hu et al. (2014), the transformation of ikaite to glendonite occurs above +4 °C depending on the chemical composition of the pore water. Glendonite was used as a tracer for cold temperatures or, in a larger context, for ice ages, because glendonite has been observed in respective sediments and in the vicinity of dropstones (Kaplan, 1979; Kemper and Schmitz, 1981; Kemper, 1987; Rogala et al., 2007; Spielhagen and Tripathi, 2009). Jones et al. (2006) proposed a direct connection between the formation of ikaite and its subsequent transformation to glendonite for mid to late Permian glendonite within the Bowen-Gunnedah-Sydney Basin System, Eastern Australia, with the upwelling of cold, dense water masses at the continental shelf resulting in decreased surface water temperatures. This glendonite was formed during the warm Permian as indicated by a transgressive and a highstand facies pointing to a temperate climatic condition at the pole. Teichert and Luppold (2013) were the first to question a direct association of glendonite and ice ages analysing the oxygen isotopic composition ($\delta^{18}\text{O}$) of Early Jurassic belemnites and ostracodes and reconstructing a paleotemperature of ca. +10 °C. From the same deposits, glendonite is reported.

In this study, the formation of ikaite within the Early Eocene Fur Formation will be investigated using various geochemical parameters. The Fur Formation mainly bears diatomite and volcanic ash layers, thus, mainly silica-dominated sediments. Pueyo et al. (2011) investigated pseudomorphs after ikaite in Lake Chungará, a silica-dominated lake in an active volcanic setting. They proposed the formation of ikaite during syndepositionary methanogenesis and the leaching of volcanic rocks. The volcanic environment as a contributor for ions is also considered in this study.

2.2 Geological setting

The Fur Formation of Early Eocene age crops out in the Limfjorden region in Northwestern Denmark (Fig. 5) and is accessible at coastal cliff exposures and quarries. The formation consists of 60 m clayey diatomite with ca. 200 volcanic ash layers (Bøggild, 1903; Pedersen and Surlyk, 1983) and was divided into the lower (40 m thick) Knudeklint Member and the upper (20 m thick) Silstrup Member (Pedersen and Surlyk, 1983; Heilmann-Clausen et al., 1985). The name ‘Fur Formation’ was established 1983 by Pedersen and Surlyk. Due to its diatomite content, the Fur Formation was named Mo-clay (‘Moler’) in older publications.

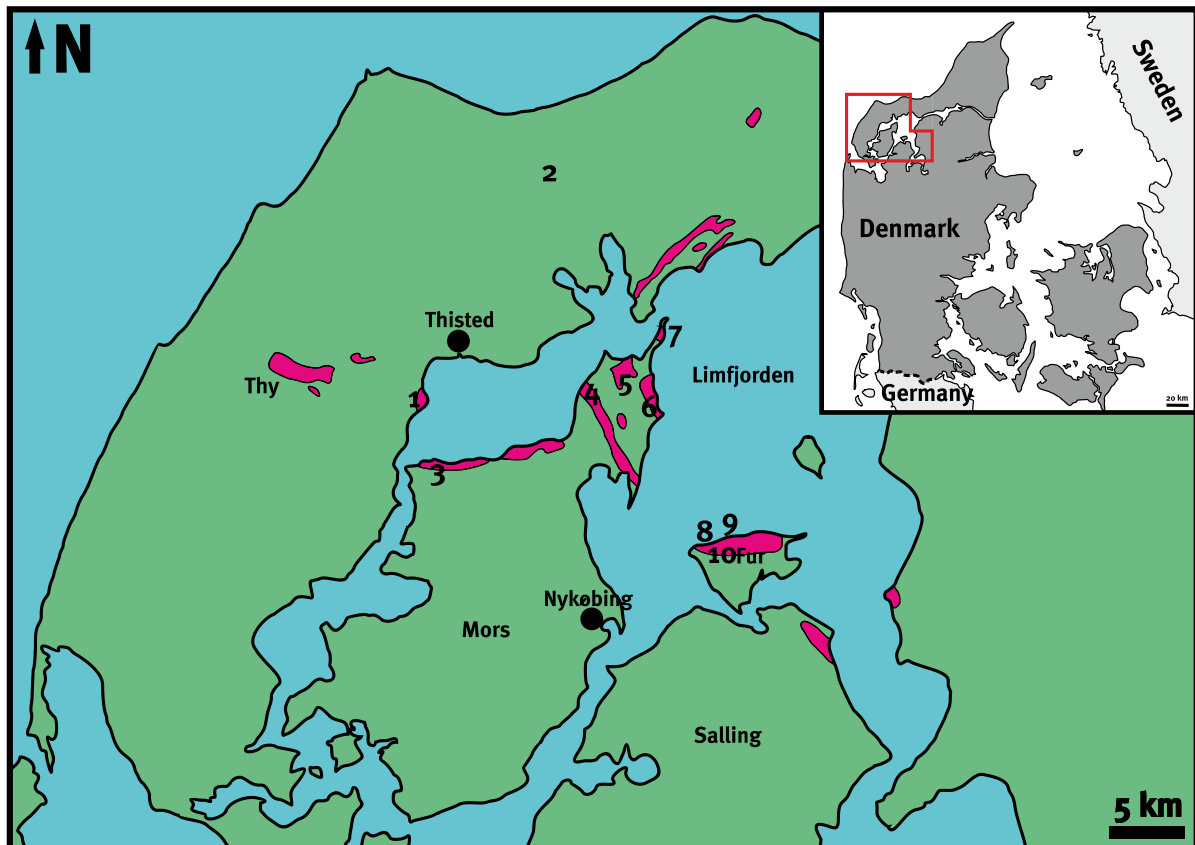


Fig. 5: Map of Northwestern Denmark with studied outcrops: 1) Silstrup coast, 2) Hjardemål pit; 3) Sundby coast, 4) Skarrehage pit, 5) Lynghøj pit, 6) Ejerslev pit, 7) Feggeklit coast, 8) Knudeklint coast (type location), 9) Stolleklint coast and 10) Råkildevej pit. All outcrops of the Fur Formation are displayed in red colour (modified after Willumsen, 2004).

The diatomite is light to dark grey in colour, while weathered surfaces appear white to yellowish. Lamination occurs mainly in the lower Knudeklint Member pointing to anoxic bottom water conditions, while the upper Silstrup Member is characterised by an alternation of bioturbated and laminated diatomite (Pedersen et al., 2011). The diatomite has an average density of 0.8 g cm^{-3} and contains about 65% marine diatoms and clay minerals, mainly montmorillonite (Pedersen, 1978) and smectite (Pedersen et al., 2004). Characteristic of the Fur Formation are the interbedded volcanic ash layers (Fig. 6), which have historically been subdivided into a negative and a positive series (Bøggild, 1918). The negative ash series contains tholeiitic basalt,

crustally contaminated trachyte, rhyolite, alkaline basalt, trachybasalt, Ti-rich nephelinite, and phonolite (Larsen et al., 2003). The positive series is more homogeneous in composition and contains enriched tholeiitic ferrobasalt and two rhyolite layers (ash layers +13 and +19). The ash layers were numbered consecutively from -39 to +140 (Bøggild, 1918). Some thin ash layers discovered later and not included in the original numbered sequence have assigned letters (a, b, c, d). Therefore, the total number of ash layers is about 200 (Larsen et al., 2003). The ash layers are normally graded and vary in thickness from about 1 mm to 19 cm (Larsen et al., 2003). Although petrographic and geochemical analyses suggest different magma sources and four stages of volcanic evolution (Pedersen et al., 1975; Larsen et al., 2003), they, nevertheless, all originate from the North Atlantic Igneous Province (NAIP).

Individual horizons bear concretions of mostly calcitic composition, also called ‘cement-sten’ (Fig. 6 and Fig. 7). The calcite precipitated in the pore space within the diatomite or the ash layers. Most concretions are ellipsoidal in shape, and often reach a horizontal diameter of one metre. Sometimes concretions reach a thickness of half a metre and a lateral extension of several hundred metres. Pedersen und Buchardt (1996) described six stratigraphic levels where calcareous concretions mostly occur: below ash layer -13, between ash layers -11 and +1, below ash layer +19, between ash layers +22 and +35, within ash layers +101 and +102, and below ash layer +135. Some concretions contain stellate glendonite, a calcitic pseudomorph after the mineral ikaite (Pedersen und Buchardt, 1996). Most of the glendonite crystals that were investigated in carbonate concretions stem from the diatomite pits Lynghøj and Ejerslev on Mors. In some horizons, glendonite also occurs without a surrounding concretion (Fig. 7 F). At the Fur Knudeklint coastal outcrop moulds of glendonite were detected (Fig. 8 A) in four different horizons (Tab. 3).

Additionally, several silicified horizons consisting of opal-CT were found between ash layers -33 and -19 in several outcrops of the lowermost Fur Formation (Pedersen et al., 2011; Petersen, 2016). The lower boundary of the Fur Formation is exposed at the Stolleklint coastal outcrop and in the Mo-clay pit at Eskilshøj on Fur where the diatomite overlies the dark-grey, slightly calcareous, silty Stolle Klint Clay (Heilmann-Clausen et al., 1985; Willumsen, 2004). Pedersen and Surlyk (1983) placed the Stolle Klint Clay within the Fur Formation, but Heilmann-Clausen et al. (1985) denoted the sediments between ash layers -39 and -34 as a separate lithological unit. The upper boundary between Fur Formation and Breyning Formation is located at the coastal outcrop Silstrup at ash layer +140.

The base of the Eocene is correlated with a negative carbon isotope excursion (CIE). An abrupt decrease in $\delta^{13}\text{C}_{\text{carb}}$ (Kennett and Stott, 1991) is considered to result from the rapid addition of >1500 gigatons of ^{13}C depleted carbon, either as CO_2 or CH_4 , into the hydrosphere and atmosphere (Dickens et al., 1995). This was the beginning of the PETM. The boundary between Palaeocene and Eocene that marks the beginning of the PETM has been placed at the base of the Stolle Klint Clay (Schoon et al., 2013) and it has been dated at 55.93 m.a. (Westerhold et al., 2012) which, therefore, is also considered to be the age of the base of the Stolle Klint Clay. The most widespread and well recognizable volcanic ash layers -17 and +19 of the Fur Formation, found

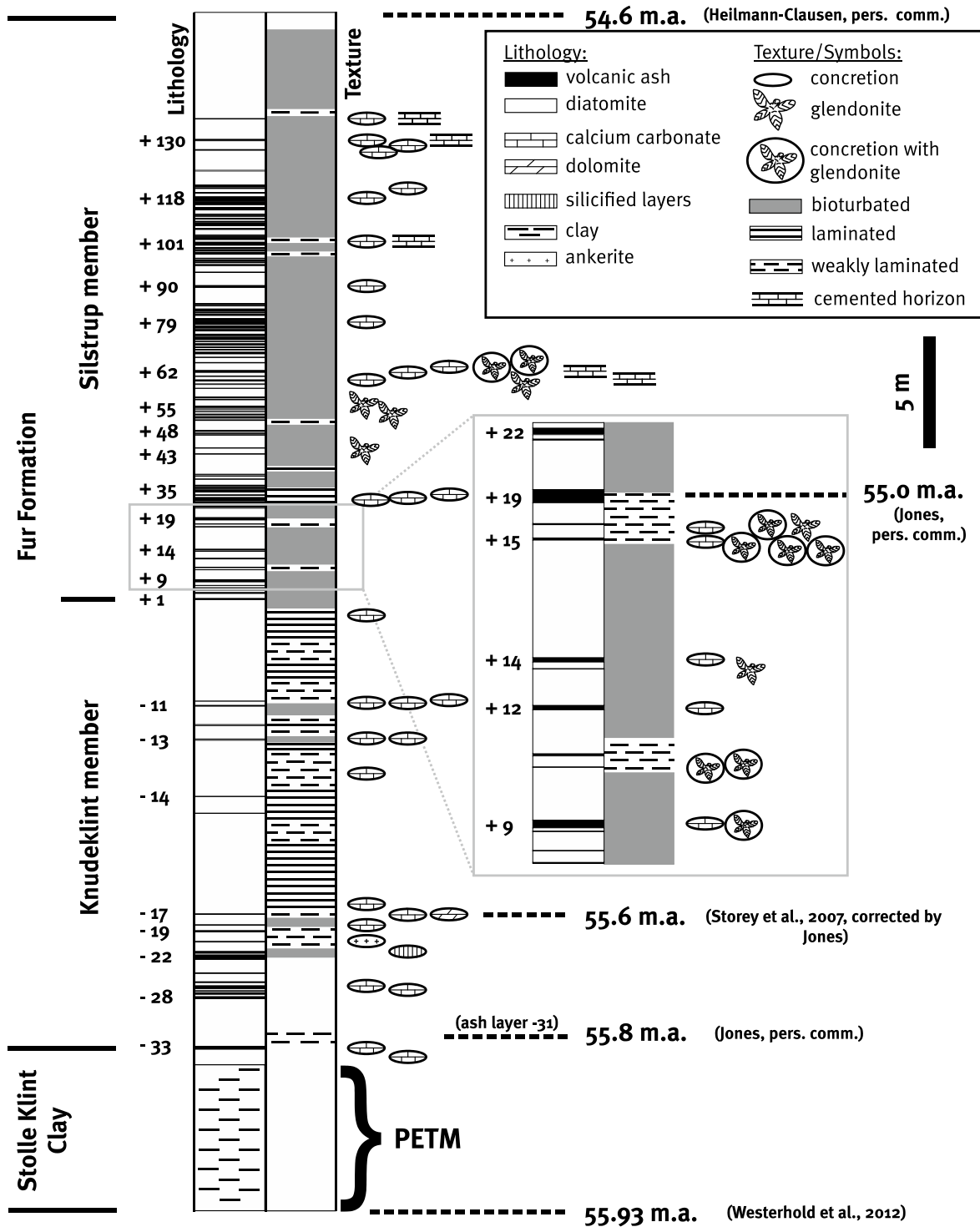


Fig. 6: Lithostratigraphic column showing the different lithologies with ash layer numbering, structures, occurrences of carbonate concretions and glendonite, and age constraints.

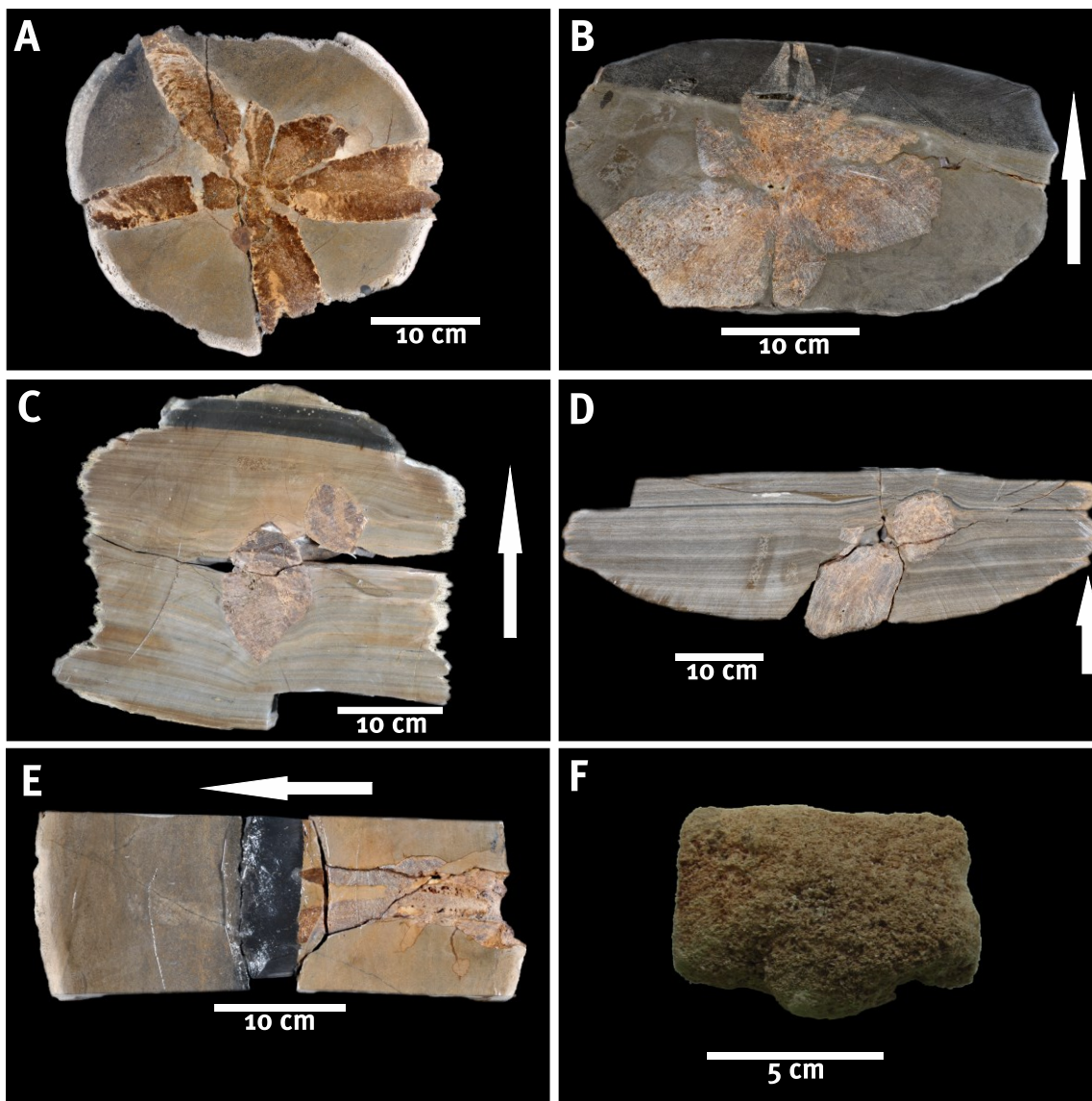


Fig. 7: Photographs of different glendonite crystals situated within carbonate concretions. (A) Stellate glendonite of ash layer +62. (B) Stellate glendonite breaking apparently through ash layer +62. (C) Two bipyramidal glendonite crystals within concretion of ash layer +16a. The lamination at lower edge is disturbed due to crystal growth. (D) Two bipyramidal glendonite crystals at ash layer +15. The lamination at the crystal edges is disturbed due to crystal growth. (E) Twinned glendonite +9b within concretion of ash layer +9. The ikaite stopped growing at the ash layer. (F) Part of bipyramidal proto-glendonite +14b that occurred at ash layer +14. Note that this glendonite has a high porosity because no protecting concretion existed. The white arrow indicates the age pointing to younger sediments.

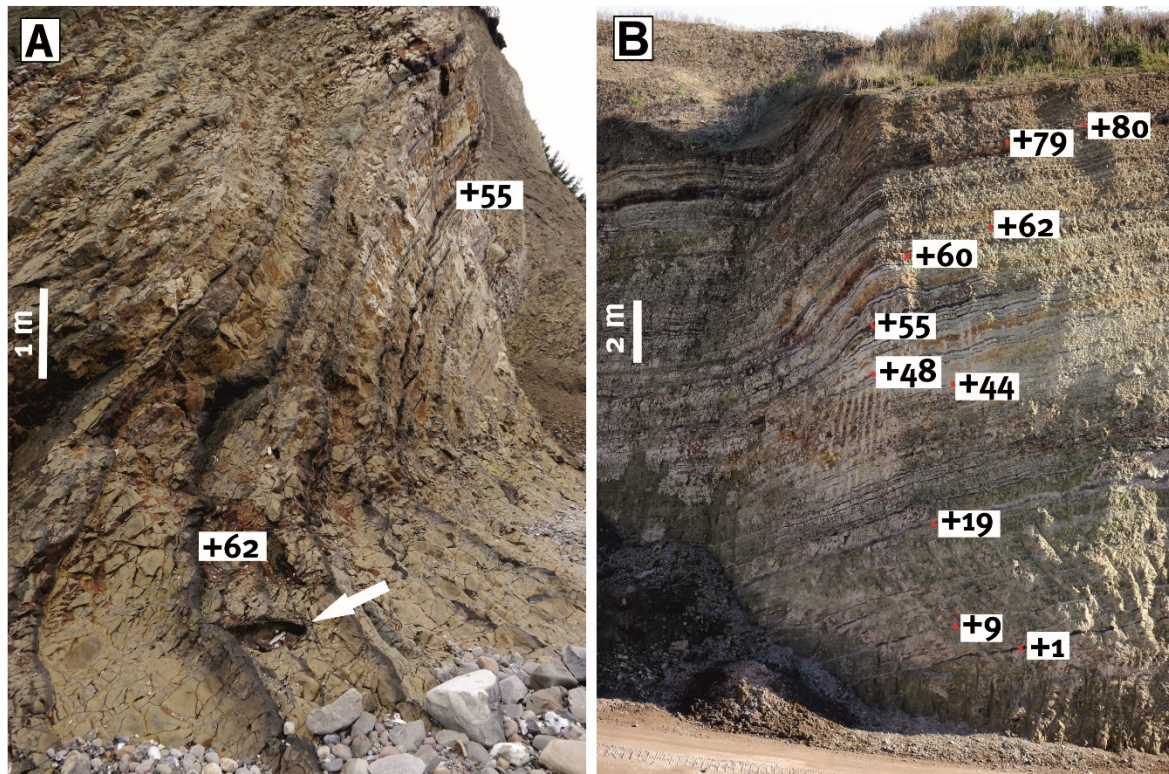


Fig. 8: (A) shows the localization of the glendonite hollow mould of ash layer +62 at Knudeklint outcrop on Fur. (B) (former pit at Råkildevvej on Fur) An example picture of the good correlation potential of volcanic ash layers. The numbers of certain well recognisable ash layers are given within white squares.

all over northern Europe (Berggren, 1995), were subject to many radiometrical and cyclostratigraphical age determinations. Swisher and Knox (1991) and Wing et al. (1991) dated ash layer -17 at 54.5 to 55.0 m.a.. Chambers et al. (2003) used $^{40}\text{Ar}/^{39}\text{Ar}$ dating to calculate the age of ash layer -17 as 54.52 ± 0.05 m.a. and ash layer +19 as 54.05 ± 0.14 m.a.. Storey et al. (2007) estimated an age of 55.12 ± 0.12 m.a. for ash layer -17 via $^{40}\text{Ar}/^{39}\text{Ar}$ dating. Jones (pers. comm.) corrected the age of ash layer -17 to 55.6 ± 0.1 m.a. and the age of ash layer +19 to 55.0 ± 0.2 m.a. based on their U-Pb data. Heilmann-Clausen (pers. comm.) placed the boundary between the Fur Formation and the overlying Breyning Formation at 54.6 m.a..

The Fur Formation contains well-preserved vertebrate, fish and insect fossils (e.g. Bonde, 1966; Bonde et al., 2008; Bannikov and Tyler, 2008; etc.). Diatomite is mined for industrial use as raw material for insulation bricks and absorbing granulates (Pedersen, 2008).

2.3 Paleoenvironmental conditions within the Danish Basin

The sediments of the Danish Basin – diatomite and subordinate clay

Most sediments investigated in the Fur Formation are diatomite, clay, and volcanic ash layers. The diatomite is a white, fine-grained, porous sediment with a low average density of 0.8 g cm^{-3} and a porosity of ca. 70% (Pedersen et al., 2011). The name “diatomite” indicates that this sediment is non-calcareous and composed of diatoms (ca. 65%; Pedersen, 1981; Pedersen, 2008). These are 10 to 200 μm in size and ca. 90 diatom species are distinguished. Other microfossils like radiolarians, silicoflagellates, ebridians, and dinoflagellates can also be identified in the diatomite, whereas calcareous microfossils are absent (Pedersen, 1981). Macrofossils are found, i.e. marine planktonic or nektonic organisms, land-derived fossils, and trace fossils made by invertebrates (Pedersen, 1981). Besides 60 to 70% diatoms, the diatomite contains 30 to 40% clay minerals and fine volcanic ash particles (Pedersen, 1978; Pedersen et al., 2011).

The diatomite appears in two different colours depending on the moisture. When dry and located above the groundwater level, the diatomite shows a white, light yellow-brown to greyish colour with brownish or pinkish shades (Pedersen and Buchardt, 1996; Pedersen, 2008; Pedersen et al., 2011). Thus, jarosite ($\text{KFe}_3^{3+}[(\text{OH})_6(\text{SO}_4)_2]$), a yellowish weathering mineral, is found in cracks, and other iron compounds are deposited in concentric rings (Pedersen et al., 2011). Diatomite located below the groundwater level displays a black colour with a pyrite content of 5 to 8% (Pedersen, 2008; Pedersen et al., 2011). The boundary between weathered and unweathered diatomite is very pronounced and often situated at different height in various moler pits (Pedersen et al., 2011).

Different time spans have been estimated for the deposition of the Fur Formation ranging from 60,000 years (Bonde, 1973; Pedersen et al., 1975; Bonde, 1979) to 3 million years (Sharma, 1969; Pedersen, 1981). More recently, Bonde et al. (2008) proposed a depositional time of 1 to 1.5 m.a. and 600,000 years for the deposition of the positive Silstrup Member, whereas Westerhold et al. (2009) calculated 300,000 years for the deposition of the same stratigraphic unit. The Fur Formation consists of ca. 10% fine-grained ash layers (Bonde, 2008) that are thought to have settled very fast (Pedersen et al., 1975). As a consequence, two different sedimentation rates are discussed: a high rate for the ash layers (within a few days) and a slow deposition of diatom ooze resulting in a high porosity of the sediments and a metastable grain framework (Pedersen and Surlyk, 1977; Pedersen, 1981). The production rate of diatoms in the surface layers was very high, but only 3% of the diatoms were buried (Pedersen et al., 2011). According to Pedersen et al. (2011), the depositional rate was four times higher at the location where the Fur Formation was settled compared to the location of the contemporaneously deposited Ølst Formation. For instance, Beyer et al. (2001) proposed a deposition time of 1.1 million years for the Ølst Formation with an average accumulation rate of 13 mm/1000 years. In contrast, Heilmann-Clausen (pers. comm.) estimated rates ranging from 16 to 50 mm/1000 years for the Fur Formation. The Stolle Klint clay was deposited more slowly during 0.6 m.a., if compared to the depositional rates of the Fur Formation (Beyer et al., 2001; Heilmann-Clausen, pers. comm.).

Upwelling of nutrients and nutrients derived from volcanic events

The high rate of diatom production was forced by widespread upwelling of nutrients in the Danish Basin during the Early Eocene due to offshore, southerly winds, which resulted in a rich planktonic life (Bonde, 1973; Larsson, 1975; Bonde, 1979; Pedersen et al., 2011). The upwelling area was parallel to the Scandinavian coast in a length of ca. 100 to 300 km (Bonde, 1979, 1997; Pedersen et al., 2011). The production of diatoms was highest in the upwelling zone caused by a constant supply of nutrients from the cold, nutrient rich bottom waters of the Norwegian Trench (Pedersen and Surlyk, 1983; Bonde, 1997). The diatom blooms were restricted to the upper water column, not deeper than 200 m water depth, where light was available for photosynthesis (Bonde, 1979; Pedersen et al., 2011). Additionally, Petersen (2016) suggested differences in solar insolation paced by Milankovitch cycles forcing different developments of upwelling. Hence, a high solar insolation could strengthen offshore winds resulting in an increased upwelling of cold, nutrient rich bottom waters (Yao et al., 2015).

A volcanic nutrient source was not considered previously for the Fur Formation in relation to diatom blooming causing the deposition of the diatomite. Due to the fast dissolution of ions from the volcanic glass particles into the seawater, most of the ions were bound into the upper water column and solely few ions leached from ash layers after the deposition on the seafloor. Jones and Gislason (2008) found out that basaltic ashes lower the pH value by 3.5 during the first contact with water. Ions are expected to be released within 1.25 hours when the basaltic ash comes in contact with seawater at 25 °C. During their laboratory studies, the basaltic ash released 63.4 mol g⁻¹ SO₄²⁻, 22.1 μmol g⁻¹ Ca²⁺, 16.1 μmol g⁻¹ Al, and 13.8 μmol g⁻¹ Si when mixed with recent Atlantic seawater. Due to the release of ions within the upper water column, the biological activity is enhanced, but ecological stress could be favoured if the toxicity levels are breached (Smith and White, 1985; Kockum et al., 2006). Because of the increased biological activity, primary productivity and rain of organic carbon were favoured in areas where volcanic ash falls occurred. Consequently, fertilization by aeolian ash import is expected to be another important factor causing the blooming of algae (diatoms, radiolarian, ebridians, etc.).

Characteristics of the Danish Basin

Due to the fact that most of the diatomite was deposited in fine horizontal laminae without bigger disruptions, the water depth had to be below storm wave base with minimal bottom current activity (Andersen, 1948; Knox and Harland, 1979; Pedersen, 1981; Pedersen and Surlyk, 1983; Heilmann-Clausen et al., 1985; Pedersen et al., 2011). Only few slump structures have been observed between ash layers -17 and -14 and Pedersen and Surlyk (1983) denoted that these small-scale structures were caused by weak bottom currents a short time after deposition. Because of the absence of larger slump structures, Pedersen (1981) proposed the bottom topography of the basin to have been smooth.

Various authors suggested a moderate depth for the Danish Basin of 200 to 500 m based on the fish fauna (Bonde, 1966; Pedersen et al., 1975; Pedersen, 1981; Bonde, 1997; Heilmann-

Clausen, 2006; Heilmann-Clausen and Rasmussen, 2010; Pedersen et al., 2011; Herold et al., 2014; Bourdon et al., 2016). In contrast, Schmitz et al. (1996) proposed a depth of 600 to 1000 m for the basin that would agree with deep-water deposition (Collins et al., 2005) and a deep shelf depositional environment (Heilmann-Clausen et al., 1985).

Andersen (1948) was the first to propose that the Danish Basin was a part of the North Sea Basin. Knox and Harland (1979) pronounced a restricted sea based on the fossil assemblage of diatoms, dinoflagellates, silicoflagellates, and fishes. The Danish subbasin was part of an extensive shelf flanking the Central Graben of the North Sea (Ziegler, 1975). Unlike Pedersen (1981) who concluded that the Fur Formation was deposited relatively close to the land area, many other authors proposed that the Fur Formation was deposited in a distance between 100 to 200 km to the nearest coast in northern direction (Bonde, 1966; Bonde, 1979; Fenner, 1994; Bonde, 2008; Knox et al., 2010; Pedersen et al., 2011; Bourdon et al., 2016). Early Eocene coastlines for the Danish Basin are known from England, Holland, and Northern Germany (Bonde, 1979; Pedersen et al., 2011), but the nearest coast was located in the SW of Scandinavia. The location of this coast was difficult to determine due to the fact that sediments were eroded there during subsequent uplifting (Pedersen et al., 2011).

Pedersen and Buchardt (1996) declared the Danish Basin and the North Sea to be restricted marine basins with deep-water masses, but without any connection to the Atlantic Ocean. In contrast, Schmitz et al. (1996) proposed a water exchange with the open ocean based on oxygen isotope data. Thus, they regarded the North Sea as a semi-enclosed basin with restricted contact to the open ocean in the NW.

The semi-enclosed basin received fossil and sediment material by riverine input (Andersen, 1948), mostly from the SW coast of Scandinavia (Larsson, 1975). A minor contribution was caused by river inflow from other terrains surrounding the Danish and the North Sea Basin (Pedersen et al., 2004). Clay minerals from weathered volcanic ashes and wood fragments from mangrove swamps that were located not far away from the coast were transported into both basins (Collins et al., 2005; Pedersen et al., 2011). Additionally, ash particles and winged insects were brought into the Danish Basin by northern winds (Larsson, 1975; Bonde, 1979; Archibald and Makarkin, 2006; Bonde et al., 2008) and they were deposited within the sediments of the Fur Formation. In the North Sea region, the landscape of the Early Eocene was rich in stagnant and slowly flowing waters with meadows, low moving streams, and the low vegetation of a steppe (Larsson, 1975). Based on floral and faunal components observed in the sediments of the Fur Formation, Vedding-Kristoffersen (1999) concluded that large parts of the surrounding land was covered by forests.

Marine fish and silicoflagellate species point to an overall marine environment (Heilmann-Clausen et al., 1985). According to Schoon et al. (2015), the Stolle Klint clay was deposited below storm wave base, probably in outer neritic water depths between 100 and 200 m. While the North Sea Basin shrank during this time, the coasts moved forward (Petersen, 2016). Beyer

et al. (2001) described the formation of the Stolle Klint clay in a marine environment with restricted circulation. Bonde (1997) denoted that the lowest sea level below ash layer -33 was a trigger for a restricted water circulation in the bottom water and a lowered salinity in the surface waters. Due to the finding of marine fish, Pedersen et al. (2011) concluded a water deepening during the deposition of the lower part of the Knudeklint Member (between ash layers -33 and -19b), where the *Apectodinium* decreased in frequency and the diatom blooms increased rapidly. This sea level rise resulted in better links with the North Atlantic Ocean during the formation of the Fur Formation, and many marine, pelagic fish groups entered the Danish and the North Sea Basin (Bonde, 1997; Pedersen et al., 2011).

3 Materials and methods

3.1 Materials

3.1.1 Glendonite samples and their surrounding carbonate concretions

Samples used in this study were collected over the years by the Moler Museet Mors and the Fur Museum, as well as during fieldwork in 2014. In total, 12 glendonite and 7 concretions containing glendonite were investigated. 2 glendonites studied were found without surrounding concretions and 10 within carbonate concretions. All of the analysed glendonite samples stem from the diatomite pits Lynghøj and Ejerslev on Mors.

These two glendonite without surrounding carbonate concretions are so called “proto-glendonites” after Teichert and Luppold (2013) due to their mineralogical properties. In 2014, four additional glendonite moulds were discovered at the Knudeklint outcrop at ash layers +44, +50, +55, and +62 on the Fur island (Tab. 3). As only moulds were found, no sample material could be obtained. In total, six glendonites without protecting carbonate concretions were investigated.

For bulk analyses 11 glendonite and 7 carbonate concretions surrounding glendonite were pulverised, while 189 samples from glendonite and 60 samples from concretions were microdrilled with a handheld drilling device (see chapter 3.2.1). The glendonite of the concretion above ash layer +62 (named “+62a”) was not pulverised. Consequently, only microdrilled sub-samples of this sample were investigated.

Tab. 3: Overview of glendonite samples and their localization within the Fur Formation.

Ash layer	Sample ID	Position	Locality	Host rock/sediment	Structure	Concretion	Note
+62	+62a	above	Ejerslev	diatomite/ash layer	bioturbated	yes	sampled
+62	+62b	within	Ejerslev	diatomite/ash layer	bioturbated	yes	sampled
+62	+62c	below	Ejerslev	diatomite	bioturbated	yes	sampled
+62	-	below	Knudeklint	diatomite	bioturbated	no	not sampled
+56	-	below	Knudeklint	diatomite	bioturbated	no	not sampled
+50	-	above	Knudeklint	diatomite	bioturbated	no	not sampled
+44	-	below	Knudeklint	diatomite/ash layer	bioturbated	no	not sampled
+16	+16a	within	Ejerslev	diatomite/ash layer	laminated	yes	sampled
+16	+16b	below	Ejerslev	diatomite	laminated	no	sampled
+15	+15a	within	Ejerslev	diatomite/ash layer	laminated	yes	sampled
+15	+15b	within	Ejerslev	diatomite/ash layer	laminated	yes	sampled
+15	+15c	within	Ejerslev	diatomite/ash layer	laminated	yes	sampled
+14	+14b	within	Ejerslev	diatomite	laminated	no	sampled
+10	+10a	above	Lynghøj	diatomite	bioturbated	yes	sampled
+10	+10b	above	Ejerslev	diatomite	bioturbated	yes	sampled
+9	+9b	within	Ejerslev	diatomite/ash layer	bioturbated	yes	sampled

3.1.2 Carbonate concretions and volcanic ashes of the Fur Formation

46 carbonate concretion samples recovered from 36 individual carbonate cemented horizons were analysed for their petrography and geochemical parameters (Tab. 4).

Tab. 4: Overview of analysed concretions and their localization within the Fur Formation.

Ash layer	Sample ID	Position	Locality	Host rock/sediment	Glendonite?	Structure	Number bulk samples	Number drilled samples
+135	+135	within	Silstrup	diatomite/ash layer	no	laminated	2	12
+130	+130	above	Feggeklit	diatomite	no	laminated	1	7
+130	+130 Sil	within	Silstrup	diatomite/ash layer	no	laminated	1	0
+130	+129/+130	below	?	ash layer	no	ash	1	6
+102	+101/+102	within	Hjardemal	diatomite/ash layer	no	laminated	2	5
+90	+90	within	Ejerslev	diatomite/ash layer	no	bioturbated	1	5
+62	+62	above	Ejerslev	diatomite/ash layer	yes	bioturbated	1	9
+62	+62b	within	Ejerslev	diatomite/ash layer	yes	bioturbated	2	4
+62	+62c	below	Ejerslev	diatomite/ash layer	yes	bioturbated	3	5
+31	+31	within	Ejerslev	diatomite/ash layer	no	laminated	2	11
+30	+30	within	Ejerslev	diatomite/ash layer	no	laminated	2	8
+28	+28	within	Ejerslev	diatomite/ash layer	no	laminated	1	3
+26	+26	within	Ejerslev	diatomite/ash layer	no	laminated	1	4
+25	+25+29	within	Sundby	diatomite/ash layer	no	laminated	1	6
+19	+15+19	within	Ejerslev	diatomite/ash layer	no	laminated	1	7
+16	+16a	within	Ejerslev	diatomite/ash layer	yes	laminated	2	14
+16	+15/+16	within	Ejerslev	diatomite/ash layer	no	laminated	1	2
+15b,c	+15a	within	Ejerslev	diatomite/ash layer	yes	laminated	1	4
+15b-d	+15d	within	?	diatomite/ash layer	no	laminated	1	9
+14	+14a	within	Ejerslev	diatomite	no	bioturbated	1	4
+10	+10b	above	Ejerslev	diatomite/ash layer	yes	bioturbated	1	10
+9	+9a	within	Ejerslev	diatomite/ash layer	no	bioturbated	1	13
+9	+9b	within	Ejerslev	diatomite/ash layer	yes	bioturbated	1	7
+4	+3+4	within	Ejerslev	diatomite/ash layer	no	bioturbated	1	13
-11	-11a	above	Ejerslev	diatomite	no	laminated	2	15
-11	-11b	within	Rakilde	diatomite	no	structureless	2	8
-13	-13	below	Skarrebage	diatomite	no	structurel./lam.	2	9
-17	-17a	above	Skarrebage	diatomite	no	weakly laminated	1	5
-17	-17b	around	Sundby	diatomite	no	weakly laminated	1	5
-20	-20	below	Sundby	diatomite	no	structureless	1	6
-21	-21	within	Skarrebage	shist	no	structureless	1	0
-24	-24-28	within	Stolleklint	diatomite/ash layer	no	laminated	1	24
-26	-20-30	between	?	diatomite	no	structureless	1	4
-26	-20-30	between	Skarrebage	shist	no	structureless	1	0
-33	-33	within	Knudeklint	diatomite/ash layer	no	structureless	1	0
-34	-34	above	Stolleklint	clay/diatomite	no	structureless	1	3

Due to the fact that the cemented horizons are not equally distributed over the entire profile, several diatomite samples were investigated for their total carbon (TC), total sulphur (TS), carbonate concentration (CaCO_3), organic carbon concentration (C_{org}), organic carbon isotopic composition ($\delta^{13}\text{C}_{\text{org}}$), and carbon-nitrogen ratio (C/N).

Tab. 5: Overview of diatom samples measured for the geochemical profiles and their localization within the Fur Formation.

Ash layer	Sample ID	Position	Profile height (m)	Locality
+135	Si+135_6	2.7 m above +135	45.31	Silstrup
+135	Si+135_1	0.2 m above +135	45.29	Silstrup
+123	Si+123_1	0.1 m above +123	42.77	Silstrup
+118	Kn2+118_1	directly above +118	41.38	E Knudeklint
+114	Kn2+114_1	between +114 and +115	40.89	E Knudeklint
+110	Kn2+110_1	between +109 and +110	40.44	E Knudeklint
+95	Kn+95_1	between +95 and +96	38.54	W Knudeklint
+87	Kn+87_2	directly below +90	36.34	W Knudeklint
+83	Kn+83_1	between +82 and +83	36.02	W Knudeklint
+79	Kn+79_1	between +80 and +81	35.35	W Knudeklint
+75	Kn+75_1	between +74 and +75	35.03	W Knudeklint
+66	Kn+66_1	between +66 and +67	33.98	W Knudeklint
+55	Kn+55_1	directly below +56	31.31	W Knudeklint
+52	Kn+52_1	between +52 and +53	30.97	W Knudeklint
+46	Kn+46_1	between +46 and +47	29.99	W Knudeklint
+42	Kn+42_1	0.4 m above +42	28.08	W Knudeklint
+35	Kn+35_1	between +35 and +36	27.41	W Knudeklint
+5	Kn+5_1	between +5 and +6	22.60	W Knudeklint
-10	Kn-10_7	1.3 m below +1	22.03	W Knudeklint
-10	Kn-10_4	2.8 m below +1	17.11	W Knudeklint
-15	St-15_1	between -15 and -14	11.69	Stolleklint
-18	St 1 m u.-17	1 m below +17	6.80	Stolleklint
-33	St 0.5m o. -33	0.5 m above -33	0.77	Stolleklint
-34	St zw. -33-34	between -34 and -33	0.02	Stolleklint
-35	St 0.2 m u.-34	0.2 m below -34	0.00	Stolleklint

In addition, four uncemented ash layers were analysed for their $^{87}\text{Sr}/^{86}\text{Sr}$ signal. The ashes were taken from the ash layers -12, +19, +55, and +79. All ash samples stem from the island of Fur.

3.1.3 Diatom samples and glendonite samples for temperature estimates

During the field expedition in 2014, 98 diatomite samples were collected in order to measure the oxygen isotope composition of diatom frustules ($\delta^{18}\text{O}_{\text{diatom}}$). From these, 41 samples were prepared. Finally, 15 pure diatom samples were subjected to oxygen isotope measurements (Tab. 6), because the other 26 samples were not clean enough for $\delta^{18}\text{O}_{\text{diatom}}$ measurements.

For clumped isotope analyses (Δ_{47}), 10 samples of the glendonites of the Fur Formation were prepared. From these, replacive calcite, i.e. the first cement generation after the ikaite breakdown, was drilled with a 0.8 mm micro twist drill. Two of the 10 drilled samples were weathered, eight were pure replacive calcite samples (Tab. 7).

For comparison, clumped isotope data were also determined for the glendonites of the Simeulue Seep in the forarc off Sumatra (Fig. 9). The glendonites stem from two layers of bore-hole 131 SL in 322 and 342 centimetres below seafloor (cmbsf). 4 samples of the Sumatra glendonite were prepared for the measurement of clumped isotopes (Tab. 7).

Tab. 6: Overview of the diatom samples prepared for $\delta^{18}\text{O}_{\text{diatom}}$ analyses of diatom frustules and their localization within the Fur Formation.

Ash layer	Sample ID	Position	Locality	$\delta^{18}\text{O}$ analysis?
+135	Si +135_6	2.7 m above +135	Silstrup	no
+135	Si +135_3	1.2 m above +135	Silstrup	no
+130	Si +130_2	0.7 m above +130	Silstrup	yes
+123	Si +123_2	0.7 m above +123	Silstrup	yes
+118	Kn2 +118_1	between +118 and +119	E Knudeklint	no
+114	Kn2 +114_1	between +114 and +115	E Knudeklint	no
+104	Kn2 +104_1	between +104 and +105	E Knudeklint	no
+90	Kn +90_1	between +90 and +91	W Knudeklint	no
+87	Kn+87_2	directly below +90	W Knudeklint	yes
+83	Kn+83_1	between +82 and +83	W Knudeklint	no
+79	Ej +79_1	between +80 and +81	Ejerslev	no
+79	Kn +79_1	between +80 and +81	W Knudeklint	no
+66	Ej +66_1	between +66 and +67	Ejerslev	no
+61	Kn +61_1	between +61 and +62	W Knudeklint	no
+59	Kn +59_1	between +59 and +60	W Knudeklint	no
+52	Kn +52_1	between +52 and +53	W Knudeklint	yes
+44	Kn +44_1	0.2 m above +44	W Knudeklint	no
+42	Kn +42_1	0.4 m above +42	W Knudeklint	yes
+21	Ej +21_1	between +21 and +22	Ejerslev	no
+21	Kn +21_1	between +21 and +22	W Knudeklint	no
+14	Ej +14_2	directly below +16	Ejerslev	yes
+14	Ra u. +16	directly below +16	Råkilde	yes
+14	Kn +14_2	directly below +16	W Knudeklint	yes
+11	Kn +11_1	between +11 and +12	W Knudeklint	no
+1	Kn +1_1	between +1 and +3	W Knudeklint	yes
-10	Kn -10_7	1.3 m below +1	W Knudeklint	yes
-10	Kn -10_4	2.8 m below +1	W Knudeklint	no
-11	Kn -11_1	between -11 and -10	W Knudeklint	no
-12	Ra -12_1	directly above -12	Råkilde	yes
-12	Kn -12_1	directly above -12	W Knudeklint	no
-14	St 0.5m u. -13	0.5 m below -13	Stolleklint	no
-14	Kn -14_2	0.8 m above -14	W Knudeklint	yes
-17	St -17_8	directly below -15	Stolleklint	no
-17	St -17_6	1.1 m below -15	Stolleklint	yes
-17	St -17_5	1.6 m below -15	Stolleklint	no
-17	St -17_2	3.1 m below -15	Stolleklint	yes
-18	St 0.5m u. -17	0.5 m below -17	Stolleklint	no
-18	St 1m u. -17	1 m below -17	Stolleklint	no
-33	St o. -33	0.5 m above -33	Stolleklint	yes
-34	St zw. -33 & -34	between -34 and -33	Stolleklint	no
-35	St 0.2 m u. -34	0.2 m below -34	Stolleklint	no

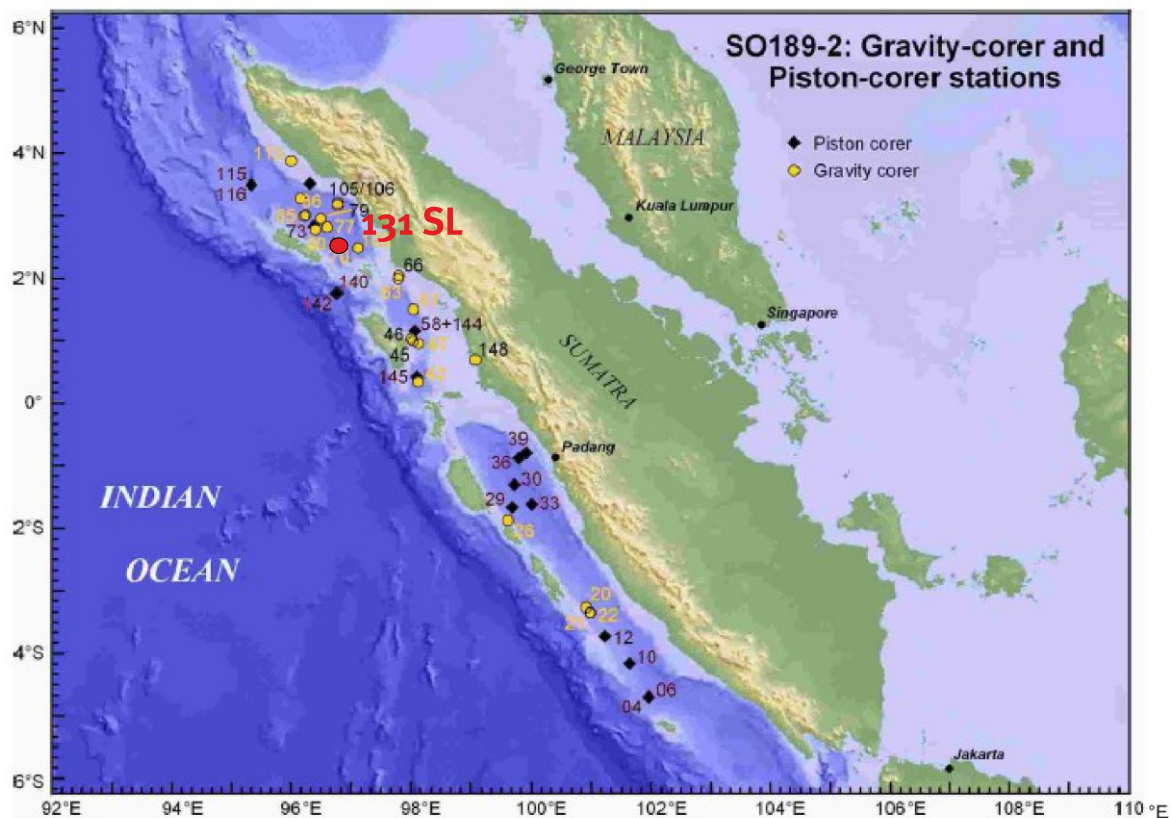


Fig. 9: The location of the bore hole 131 SL of the R/V Sonne cruise SO139 Leg 2 that was executed in autumn 2006 (latitude: 2°33,780 N; longitude: 96°45,429 E; water depth: 1134 m; core length: 367 cm) (after Wiedicke-Hombach et al. (2006)).

Tab. 7: Overview of samples prepared for clumped isotope measurements and their locations.

Ash layer	Sample ID	Location	Working name	Preservation	Weight (mg)
+62	+62b rCc	Fur Formation	+62b	pure	22.49
+62	+62c rCc	Fur Formation	+62c	pure	21.28
+16	+16a rCc	Fur Formation	+16	pure	21.30
+15	+15a rCc	Fur Formation	+15a	pure	29.91
+15	+15b rCc	Fur Formation	+15b_1	weathered	130.94
+15	+15b rCc	Fur Formation	+15b_2	pure	22.03
+15	+15c rCc	Fur Formation	+15c_1	weathered	69.03
+15	+15c rCc	Fur Formation	+15c_2	pure	21.17
+10	+10b rCc	Fur Formation	+10	pure	26.87
+9	+9b rCc	Fur Formation	+9	pure	23.65
-	SO189 13156 342 cm Aggregate	Simeulue Seep/Sumatra	A_1	cleaned	241.84
-	SO189 13156 342 cm rCc weiß	Simeulue Seep/Sumatra	A_2a	cleaned	46.12
-	SO189 13156 342 cm rCc gelb	Simeulue Seep/Sumatra	A_2b	cleaned	30.23
-	SO189 13156 322 cm Aggregate	Simeulue Seep/Sumatra	B_1	cleaned	36.70

3.2 Methods

3.2.1 Sample preparation

For bulk analyses, 50 to 150 g of glendonite, concretion, volcanic ash, and diatomite was pulverised using a ring and puck mill. In addition, samples from glendonite and from concretions were microdrilled using a handheld drilling device (Proxxon MicroMot 50/E) equipped with a 2.3 mm carbide drill. Profiles were drilled across the glendonite and concretions. Three of four different cement phases within the glendonite were separated using a 0.8 mm micro twist drill driven by a Proxxon MicroMot 50/E under the microscope. From 8 glendonite samples, it was possible to obtain separate cement samples. One cement phase (secondary rim cement) was not sampled using the micro drill, because the secondary rim cement is very thin, and it was not possible to extract a pure sample with 100% material of this phase.

Thin sections of glendonite, carbonate concretions, and diatomite were prepared for petrographic investigations using light microscopy, a scanning electron microscope (SEM), and electron microprobe.

3.2.2 X-ray diffraction

Bulk powder samples from glendonite, carbonate concretions, diatomite, and a clay sample were analysed via X-ray diffraction (XRD) using randomly oriented samples fixed on the rotary table of a Phillips X^ˆPert powder diffractometer (Institut für Mineralogie, Münster). CuK α radiation was used with runs from 20° to 60° 2 θ , a scan speed of 813.015 s per step with a step size of 0.0144326 °2 θ at 45 kV, and 40 mA within a position-sensitive detector setup for glendonite and carbonate concretions (n=57). Mineral phases < 5 wt% cannot be identified with this method. A quartz standard was added to the samples to measure the shift of the d(104) calcite peak and to calculate the Mg content of the carbonates after Lumsden (1979).

For 3 diatomite samples, one silicified sample, and one clay sample, XRD runs were obtained from 0° to 90° with no quartz standard added. In this way, it was possible to obtain the mineralogical composition of these samples.

3.2.3 Electron microprobe analyses

Petrographic studies of glendonite samples and concretions were carried out on polished thin sections. The thin sections of glendonite (carbon coated) were further used for electron microprobe analyses to quantify major and trace elements (Ca, Mg, Ba, Mn, Fe, and Sr) as well as to study the different cement generations in detail. A JEOL 8900 and a JEOL JXA 8350F electron microprobe (acceleration voltage: 15 kV; current: 20 nA; spot size: 5 nm) were used at the Institut für Mineralogie, Münster. Back-scatter electron pictures were taken with a JEOL JSM-6610 SEM.

Additionally, volcanic ash layers containing the glendonites of +9b and +62b were analysed with a JEOL 8900 microprobe (acceleration voltage: 15 kV; current: 5 nA; spot size: 10 nm). The following major and trace elements were measured during this analysis: Na, Al, K, Cr, Mg, Si, Ca, Mn, Ti, and Fe.

3.2.4 Carbonate oxygen and carbon isotopes ($\delta^{18}\text{O}_{\text{carb}}$ and $\delta^{13}\text{C}_{\text{carb}}$)

Carbonate oxygen and carbon isotopes ($\delta^{18}\text{O}_{\text{carb}}$ and $\delta^{13}\text{C}_{\text{carb}}$) of glendonite and carbonate concretions were measured using a Gasbench II coupled to a ThermoFinnigan Delta Plus XL mass spectrometer (Institut für Geologie und Paläontologie, Münster). 200 to 300 μg of powder were reacted with 105% phosphoric acid (H_3PO_4) (cf. Wachter and Hayes, 1985) at a temperature of 70 °C. Analytical performance was monitored with three standards (NBS19, IAEA CO-1, and IAEA CO-8) and their reproducibility was better than $\pm 0.15\text{‰}$ for $\delta^{18}\text{O}$ and $\pm 0.13\text{‰}$ for $\delta^{13}\text{C}$. All values are given in the standard δ -notation in per mil (‰) relative to the Vienna-Peedee Belemnite Standard (V-PDB). Whenever possible, all samples and standards were measured as duplicates. The analytical precision was better than $\pm 0.37\text{‰}$ for $\delta^{13}\text{C}$ and $\pm 0.20\text{‰}$ for $\delta^{18}\text{O}$ for glendonite. The precision was better than $\pm 0.13\text{‰}$ for $\delta^{13}\text{C}$ and $\pm 0.20\text{‰}$ for $\delta^{18}\text{O}$ for carbonate concretions. The reason for larger errors between samples and standards is the better homogeneity of the standard material compared to the samples analysed.

3.2.5 Apatite concentration within glendonites (PO_4^{3-})

Apatite concentrations (PO_4^{3-}) in glendonite were determined via X-ray fluorescence (XRF) at the Institut für Mineralogie, Münster. The samples were prepared as melt pellets: 4 g of lithium tetraborate and 0.5 g sample were placed inside a melting pot and were prepared in an Eagon 2 Oven. A PANalytical Epsilon3-XL EDXRF was used with the international standards for basalt (BCR-2, BE-N, BHVO-2), andesite (AGV-2, JA-1), limestone (JLS-1, KH, VB-K2), and granite (G A, SARM-1). The precision of the samples did not exceed 0.01 wt%. For the analyses of the P_2O_5 content, detector 3, sequence 5, $\text{K}\alpha$ line, and 50 kV voltage were used for 600 s. For the analyses of XRF, the loss of ignition (LOI) was determined after heating the sample at 1050 °C for 3 h.

3.2.6 Total carbon (TC), total sulphur (TS), and total inorganic carbon (TIC)

The total carbon (TC), total sulphur (TS), and total inorganic carbon (TIC) of all bulk samples (glendonite, carbonate concretions and several diatomite samples) were measured with a Ströhlein Instrument CS-MAT 5500 Elemental Analyzer either via combustion in an oxygen stream (TC, TS) or via reaction with hydrochloric acid (HCl) at 70 °C (TIC). Pure CaCO_3 (MERCK) and NIST 2692b Bituminous coal were used as standard materials yielding a reproducibility of $\pm 0.14\%$ (TC), $\pm 0.30\%$ (TIC), and $\pm 0.13\%$ (TS), respectively. The precision of samples analysed

as duplicates was better than ± 0.18 , ± 0.20 , and $\pm 0.55\%$ for TC, TS, and TIC, respectively. The TIC values were converted into carbonate content (CaCO_3).

3.2.7 Concentration of total organic carbon (TOC) and C/N ratio

Total organic carbon (TOC) and total nitrogen (TN) were analysed for decarbonated samples using an Eurovector/Hekatech EA 3000 elemental analyzer at the Institut für Landschaftsökologie, Münster. For this, two glendonite samples (+62b and +9b), all carbonate concretion samples, and several diatomite samples (Tab. 4 and Tab. 5) were decarbonated using 1 g of sample material. After placing 1 g sample in a 60 mL Falcon tube, all samples were reacted with 10% HCl in a 40 °C warm water bath for approximately 12 h. After complete decarbonation, each sample was washed 5 times with deionised water. After drying for ca. 2 days at 40 °C, the carbonate content was determined by weight difference.

15 to 30 mg of decarbonated sample material was placed into tin capsules and measured with the elemental analyzer. Every fifth sample was measured as duplicate to verify the measured data. The reproducibility of the Acetanilide standard ($\text{C}_8\text{H}_9\text{NO}$; CE Instruments P/N 338 44012) was 1.01 for TOC and 0.18 for TN. The standard deviation within samples was better than ± 0.07 for TOC and ± 0.01 for TN. TOC and TN were normalised using their molar masses and the C/N ratio was calculated. The reproducibility was better than ± 0.15 for the acetanilide standard ($n=33$) and better than ± 0.26 for the samples, respectively.

3.2.8 Organic carbon isotopes ($\delta^{13}\text{C}_{\text{org}}$)

39 carbonate concretions and 10 diatomite samples were measured for their organic carbon isotopic composition ($\delta^{13}\text{C}_{\text{org}}$) via sealed tube combustion (cf. Strauss et al., 1992). For this, 15 to a maximum of 500 mg of decarbonated sample material was weighed into a 9 mm diameter quartz tube. The samples were sealed into the glass tube under vacuum with 1 g of copper oxide (CuO). After mixing the sample powder and CuO, the glass tube was placed into a muffle furnace at 500 °C for 2 h and at 850 °C for 5 h. At a vacuum line, the liberated CO_2 was purified by cryogenic distillation and its CO_2 concentration was volumetrically measured before it was trapped into a 6 mm diameter pyrex tube, from which it was later released into the mass spectrometer.

The carbon isotopic composition was analysed using a ThermoFinnigan MAT Delta Plus mass spectrometer. The international standard USGS 24 and the internal lab standard MSLSK-1 were measured for quality control and the reproducibility was better than ± 0.04 ($n=13$). The reproducibility of all samples was better than ± 0.09 , when measured as duplicates or triplicates.

3.2.9 Strontium ($^{87}\text{Sr}/^{86}\text{Sr}$) and calcium ($\delta^{44/40}\text{Ca}$) isotopes

Strontium ($^{87}\text{Sr}/^{86}\text{Sr}$) and calcium ($\delta^{44/40}\text{Ca}$) isotopes were measured from drilled carbonate samples (glendonite and carbonate concretions) and from bulk samples of distinct volcanic ash layers via thermal ionisation mass spectrometry (TIMS) using a Thermo-Finnigan TRITON TI at the Institut für Mineralogie, Münster. Powdered carbonate samples were dissolved in 1 N acetic acid, evaporated and redissolved in 3 N nitric acid (HNO_3). As described in Teichert et al. (2005), strontium separation was carried out using a 100 μl column chemistry with Sr Resin (EICHROM). Sr isotopes are normalised to the NBS 987 standard with a $^{87}\text{Sr}/^{86}\text{Sr}$ ratio of 0.71025. A mean value of 0.71023 (2σ mean of 0.000012, $n=29$) for repeated measurements of NBS 987 was obtained over the course of this study. All isotope ratios were normalised to a $^{86}\text{Sr}/^{88}\text{Sr}$ ratio of 0.1194.

For Ca isotope analyses, drilled glendonite cements were dissolved in 1 N acetic acid. Samples were mixed with a ^{42}Ca - ^{43}Ca doublespike (Gussone et al., 2011) to correct for isotope fractionation during ion chromatography and data acquisition in the mass spectrometer. The Ca of the samples was isolated using a 100 μl column and HCl-chemistry with MCI Gel CK08P, 75-100 μm (modified after Teichert et al., 2009). About 300 ng Ca were loaded on outgassed rhenium-single filaments with a tantalum activator in sandwich technique. Fractionation correction was carried out using the exponential law as described by Heuser et al. (2002). Data reduction is based on the iterative approach of Compston and Oversby (1969). Blanks were usually below 1% of total Ca used for Ca-chemistry and never exceeded 3%. The Ca isotope values are expressed as $\delta^{44/40}\text{Ca}$ values ($\delta^{44/40}\text{Ca}$ [‰SRM915a] = $((^{44}\text{Ca}/^{40}\text{Ca})_{\text{sample}} / (^{44}\text{Ca}/^{40}\text{Ca})_{\text{standard}} - 1) \times 1000$) relative to SRM915a from the National Institute of Standards and Technology. The 2σ standard deviation was 0.08‰ for replicate measurements.

3.2.10 Sulphur ($\delta^{34}\text{S}_{\text{CAS}}$) and oxygen ($\delta^{18}\text{O}_{\text{CAS}}$) isotopes of CAS and WSS

Carbonate-associated sulphate (CAS) was extracted from glendonite and carbonate concretions and measured for its sulphur ($\delta^{34}\text{S}$) and oxygen ($\delta^{18}\text{O}$) isotopes (cf. Wotte et al., 2012). About 30 g of powdered sample material was washed repeatedly with a 10% sodium chloride (NaCl) solution under constant stirring for 24 h until no more water soluble sulphate (WSS) was released. Each time, 10% barium-chloride solution (BaCl_2 ; 10% of the solution volume) was added to precipitate the dissolved sulphate. Barium sulphate (BaSO_4) precipitates were filtered off and dried at 40 °C overnight. Subsequently, carbonate was dissolved with 3 M HCl and the CAS was precipitated as BaSO_4 , too. The concentration of the CAS was calculated using the weight of the BaSO_4 precipitate and the initial weight of the sample material.

Around 200 μg of each BaSO_4 precipitate was placed into tin capsules for $\delta^{34}\text{S}$ measurements (together with 300 – 600 μg vanadium pentoxide; V_2O_5) and into silver capsules for $\delta^{18}\text{O}$ measurements. $\delta^{34}\text{S}$ isotopic composition was measured with an Elemental Analyzer con-

nected to a ThermoFinnigan Delta Plus mass spectrometer and results are reported in the δ -notation as per mil difference from the Vienna-Canyon Diablo Troilite (V-CDT) standard. For quality control, international standards IAEA-S-1, IAEA-S-2, IAEA-S-3, and internal lab standards (Ag_2S and CdS) were analysed. Based on duplicate measurements, the standard deviation was usually better than $\pm 0.30\text{‰}$ for standards and $\pm 0.35\text{‰}$ for samples. $\delta^{18}\text{O}$ values were determined using a high temperature reduction furnace (TC-EA) coupled to a ThermoFinnigan Delta Plus XL mass spectrometer and results are reported in the δ -notation as per mil difference from the Vienna-Standard Mean Ocean Water (V-SMOW) standard. A BaSO_4 lab standard as well as international reference materials NBS-127, IAEA SO-5, and IAEA SO-6 were measured for their $\delta^{18}\text{O}$ isotopic composition. The standard deviation for $\delta^{18}\text{O}$ was better than $\pm 0.65\text{‰}$ V-SMOW for almost all measurements.

3.2.11 Biomarker analyses

Biomarker analyses were performed in the Department for Geodynamics and Sedimentology, University of Vienna. 150 to 300 g of sample yielded sufficient biomarkers for two glendonite samples and three carbonate concretions in the residue after dissolution of ca. 80% of the carbonate matrix with 10% HCl (cf. Birgel et al., 2006). Two diatomite samples (30 – 40 g) were powdered within an agate mortar to measure their biomarker composition as well.

Following Birgel et al. (2014), biomarkers were extracted 3 x with a CEM Discover microwave extraction system at 80 °C and maximum 250 W for 15 min with dichloromethane (DCM):methanol (MeOH) (3:1). These extracts were acidified with 10% HCl to pH 1 to remove the free fatty acids (FAs) to the organic solvent phase. The extract was cleaned previously by separation into n-hexane soluble and DCM soluble fractions prior to the gas chromatography (GC) analysis. Following Birgel et al. (2008), the n-hexane soluble fraction was separated via column chromatography into four fractions of increasing polarity: hydrocarbons (4 mL n-hexane), ketones/esters (6 mL n-hexane:DCM (3:1, v/v)), alcohols (7 mL DCM:acetone (9:1, v/v)), and carboxylic acids (8 mL 2% formic acid in DCM). Alcohols were bound by adding 100 μL pyridine and 100 μL N,O-bis(trimethylsilyl)trifluoroacetamide (BSTFA) to the alcohol fraction at 70 °C for 30 min. The derivatised alcohol fraction was nitrogen dried and dissolved in n-hexane before it was injected. Carboxylic acids were separated via 1 mL 14% boron trifluoride (BF_3) in MeOH at 70 °C for 1 h to form FA methyl esters. After cooling, the mixture was extracted 4 x with 2 mL n-hexane.

The separated fractions of alcohols, fatty acids, and hydrocarbons were measured via GC-mass spectrometry with an Agilent 7890 A GC system coupled to an Agilent 5975C inert MSD mass spectrometer. The concentration of the individual compounds was determined via GC-flame ionization detection (GC-FID) with an Agilent 7820 A GC system. A Rxi-5 ms fused silica column (30 m x 0.25 mm, 0.25 μm film thickness) was mount for the GC systems (Hoffmann-Sell et al., 2011). The GC was flushed with He as carrier gas and the used GC temperature programme for all fractions was 60 °C for 1 min to 150 °C at a velocity of 10 °C/min. When 150 °C were

reached, the temperature was increased by 4 °C/min until 320 °C were reached. This temperature was maintained for 27 min for hydrocarbons and 37.5 min for alcohols. Compounds were identified comparing the measured GC retention times and mass spectra with published data and reference compounds. For the measurements of hydrocarbons, the standard 5- α -cholestone was added, for fatty acids 2-methyl-octadecane acid and for alcohols 1-nonadecanol. Compound-specific carbon isotope analyses were performed in duplets of a sample via Thermo Fisher Trace GC Ultra connected to a Thermo Fisher Delta V Advantage mass spectrometer via Thermo Fisher GC Isolink interface. The same gas chromatography was used as for those of compound identification (Kiel et al., 2013). A mixture of n-alkanes (C_{14} to C_{38}) with a known isotopic composition was used to monitor the instrument precision.

3.2.12 Oxygen isotopes of diatom frustules ($\delta^{18}O_{\text{diatom}}$)

41 diatomite samples were prepared for the $\delta^{18}O_{\text{diatom}}$ analyses performed at the Institute of Earth Surface Dynamics (IDYST), University of Lausanne. Initially, 5 to 10 g of sample was powdered in an agate mortar. Subsequently, the powder was reacted with 10% HCl and 10% hydrogen peroxide (H_2O_2) to dissolve carbonates and organic compounds. For 12 h, the samples and reactants were placed in a 40 °C warm ultrasonic bath for a better reaction. A 5% tetra-sodium diphosphate decahydrate solution ($Na_4O_7P_2 \cdot 10H_2O$) was added to disaggregate the sediment (Hatte et al., 2008) and the sample was heated with 100 °C for ca. 30 min. After cooling and settling, the samples were sieved with 80, 40, and 10 μm mesh size sieves and the fraction between 10 and 40 μm was kept. The settling method after Morley et al. (2004) was performed to separate diatoms from other heavier particles via centrifugation. Heavy liquid separation was applied using 3 to 5 mL sodium polytungstate ($3Na_2WO_4 \cdot 9WO_3 \cdot H_2O$). Subsequently, both fractions were washed several times with deionised water and the weight of the purified sample was determined. Residues were categorised into different purities based on the colour of their powder after preparation. After an additionally executed point counting, only clean white samples (Fig. 10 E and F) were processed.

Light microscopy and secondary electron imaging (JEOL JSM 6610; Institut für Mineralogie, Münster; see chapter 3.2.3) were applied to evaluate the purity of the diatom samples and to quantify the different diatom species. For this, a point counter was connected to a Leica DMRX light microscope. Finally, 15 diatom samples were clean enough for subsequent oxygen isotope analyses.

For these 15 samples, the concentration of all SiO_2 fossils range between 94.3 and 100.0% with the lowest value for sample “Kn+87_2” (ash layer +87) and the highest value for samples “Kn+42_1” (ash layer +42), “Ra u. +16” and “Ej+14_2” (both stem from the diatomite horizon between ash layers +14 and +16; Tab. 8). “Ra-12_1” at ash layer -12 bears the highest diatom concentration with 95.3%, whereas sample “St o. -33” which is located a few cm above ash layer -33 contains the smallest amount of diatoms with 58.3%. Consequently, sample “St

o. -33” contains the biggest percentage of other SiO₂ fossils (ebridians, radiolarian, silicoflagellates, etc.) with a proportion of 39.3% in order to obtain a high SiO₂-fossil concentration of > 95%.

Tab. 8: Overview of the composition of the diatom samples after point counting.

Ash layer	Sample ID	Profile height (m)	Sample weight (mg)	Diatoms (%)	Other SiO ₂ fossils (%)	All SiO ₂ fossils (%)	Minerals (%)	Total (%)
+130	Si +130_2	44.34	125	92.98	6.33	99.31	0.66	99.97
+123	Si+123_2	43.27	223	72.65	27.33	99.98	0.00	99.98
+87	Kn+87_2	36.40	127	86.31	8.00	94.31	5.66	99.97
+52	Kn +52_1	30.97	269	85.00	12.33	97.33	2.66	99.99
+42	Kn+42_1	28.08	193	94.65	5.33	99.98	0.00	99.98
+16	Kn+14_2	24.80	503	92.31	7.66	99.97	0.00	99.97
+16	Ra u.+16	24.80	248	88.98	11.00	99.98	0.00	99.98
+16	Ej+14_2	24.80	340	86.98	13.00	99.98	0.00	99.98
+1	Kn +1_1	21.90	297	87.31	7.66	94.97	5.00	99.97
~-3	Kn-10_7	18.73	98	90.32	7.33	97.65	2.33	99.98
-12	Ra-12_1	14.23	324	95.31	3.33	98.64	1.33	99.97
-14	Kn-14_2	12.51	368	86.64	13.00	99.64	0.33	99.97
~-16	St-17_6	10.20	118	86.99	10.00	96.99	3.00	99.99
-17	St-17_2	8.20	507	93.98	4.33	98.31	1.66	99.97
-33	St o. -33	0.77	38	58.32	39.33	97.65	2.33	99.98

The concentration of minerals is an average of 1.7%, whereas the highest abundance was estimated for sample “Kn+87_2” with 5.7%.

Tab. 9: Summary of different diatom species found within the diatom samples.

Ash layer	Sample ID	Profile height (m)	Coscino-discus (%)	Trinacria (%)	Hemiaulus (%)	Rhizosolenia (%)	Pterotheca (%)	Omphalotheca (%)	Pseudostictodiscus (%)
+130	Si +130_2	44.34	23.33	7.33	37.33	0.00	0.00	0.33	24.66
+123	Si+123_2	43.27	21.33	10.66	34.66	0.00	0.00	0.00	6.00
+87	Kn+87_2	36.40	15.00	15.66	44.33	0.00	0.00	0.66	10.66
+52	Kn +52_1	30.97	19.00	0.00	59.00	0.00	0.00	0.00	7.00
+42	Kn+42_1	28.08	20.33	13.00	43.33	0.00	1.66	0.00	16.33
+16	Kn+14_2	24.80	23.00	3.66	17.66	0.00	0.66	0.00	42.00
+16	Ra u.+16	24.80	34.33	9.00	35.66	0.00	0.33	0.00	9.66
+16	Ej+14_2	24.80	18.66	11.66	24.66	2.33	0.00	0.00	35.00
+1	Kn +1_1	21.90	24.66	13.66	41.33	2.33	0.00	0.00	5.33
~-3	Kn-10_7	18.73	9.66	9.00	47.33	3.33	1.00	0.00	20.00
-12	Ra-12_1	14.23	14.66	5.00	52.33	0.00	1.66	0.00	21.66
-14	Kn-14_2	12.51	22.66	4.33	30.33	7.66	3.33	0.00	18.33
~-16	St-17_6	10.20	21.00	10.00	34.00	2.66	3.00	0.00	16.33
-17	St-17_2	8.20	38.00	14.66	25.00	2.66	0.00	0.33	13.33
-33	St o. -33	0.77	17.00	2.00	29.00	0.00	5.66	0.00	4.66

Point counting analyses revealed different distributions of diatom species within each diatom sample. The main diatom species found within the diatom samples are *Coscinodiscus*, *Hemiaulus*, and *Pseudostictodiscus* with minor contribution of *Trinacria*, *Rhizosolenia*, *Pterotheca*, and *Omphalotheca*. There are no trends visible across the profile according to the distribution of diatom species. Even in samples of the same height (“Kn+14_2”, “Ra u. +16”, and “Ej+14_2”) between ash layers +14 and +16, the diatom species assemblage differs. These three samples were collected at three different sites on the islands of Mors (Ej = Ejerslev pit) and Fur

(Ra = Råkilde pit; Kn = Knudeklint coast). Each diatom species exhibits a certain vital effect affecting the oxygen isotopic composition of its frustule, i.e. living environment, light intensity, nutrients and the growth during different seasons (Shemesh et al., 1995; Swann and Leng, 2009). Hence, the distribution of species was taken into account.

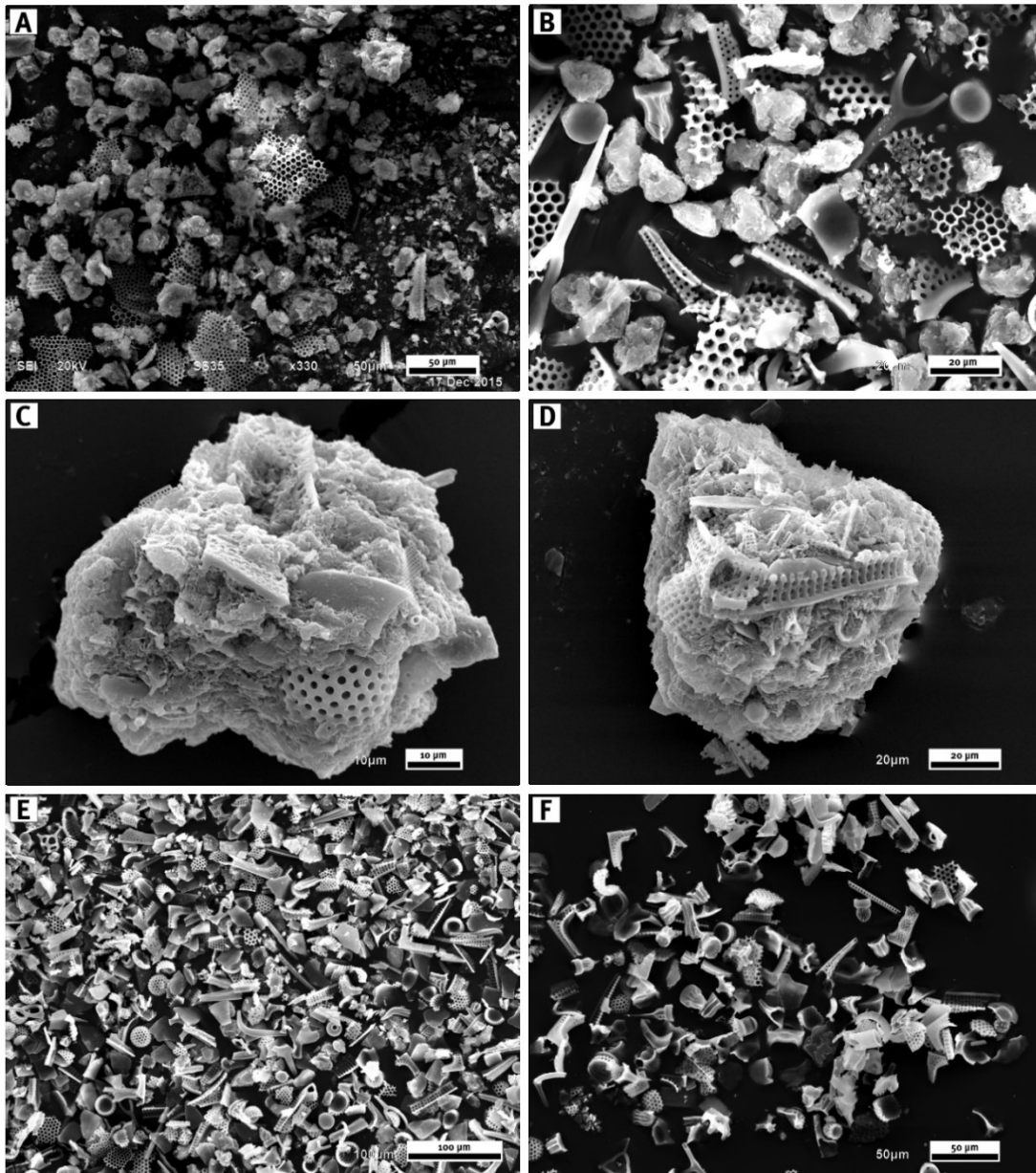


Fig. 10: SEM images of diatom samples in different preparation stages. (A) Overview of sample Kn2+104_1 after the settling step after Morley et al. (2004). (B) Same sample like in (A), but more in detail and after the 4th step of the preparation (SPT separation). There are still some clay minerals left lying on the diatoms or occurring within the diatoms. (C) An agglomerate of sample Ra u. +16 containing clay minerals, diatoms, and other SiO₂-frustules. (D) An agglomerate of sample Si+123_2 exhibiting the same properties as the agglomerate in picture (C). These agglomerates were broken using of a sodium diphosphate decahydrate solution. (E) Overview of the cleaned sample Ej+14_2. Diatoms and other SiO₂ fossils (silicoflagellates, ebridians, and sponge spiculae) can be seen on this image. (F) Overview of the clean sample St-17_6 with diatoms, silicoflagellates, and ebridians.

The oxygen isotopic composition (^{16}O , ^{18}O) in 15 samples was measured according to Vennemann et al. (2001). Between 0.5 to 2 mg of biogenic silica was mixed with pure optical grade BaF_2 , loaded onto a small Pt-sample holder and pumped out to a vacuum of about 10^{-6} mbar. After prefluorination of the sample chamber overnight, the samples were heated with a CO_2 -laser in 50 mbars of pure F_2 . Excess F_2 was separated from the O_2 produced by conversion to Cl_2 using potassium chloride (KCl) held at 150 °C. The extracted O_2 is collected on a molecular sieve (5A) and subsequently expanded into the inlet of a Finnigan MAT 253 isotope ratio mass spectrometer. Oxygen isotopic compositions are given in the standard δ -notation, expressed relative to Vienna-Standard Mean Ocean Water (V-SMOW) in permil (‰). Replicate oxygen isotope analyses of the standard used (LS-1 quartz; $n=6$) had an average precision of $\pm 0.15\text{‰}$. The accuracy of $\delta^{18}\text{O}$ values was better than 0.2‰ compared to accepted $\delta^{18}\text{O}$ values for NBS-28 of $+9.64\text{‰}$.

3.2.13 Clumped isotopes of replacive calcite (Δ_{47})

The microdrilled glendonite samples of the Fur Formation were pure and homogenised enough for the measurement of Δ_{47} (Fig. 11). The Sumatra glendonites were hosted within a clayey sediment and cleaned using deionised water to which ammonia water (NH_4OH) was added to reach a pH value of 7 to prevent the calcite from dissolution. Water was squeezed onto the glendonite bearing samples for cleaning. After ca. 2 min in ultrasonic bath, the water was removed from the sample with pipettes after 30 s of sample settling. This was repeated until the sample was clean enough (cf. Barker et al., 2003). Additionally, ethanol was tried for further clay removal.

Two replacive calcite samples were picked for the glendonite of the Simeulue Seep off Sumatra: yellow and white replacive calcite. Microprobe investigations revealed two different rim cements for the edges of the replacive calcite. The rim cement of the yellowish replacive calcite (A) appears thicker than the rim cement of the whitish replacive calcite (B) (Fig. 11). In addition to the size of the rim cement, the rim cement of the yellowish replacive calcite shows 3.2 mol% MgCO_3 , while the MgCO_3 concentration within the rim cement of the whitish replacive calcite is merely 1.7 mol%. Consequently, the sample of the whitish replacive calcite was chosen for Δ_{47} analyses, because it appears more homogenous.

The whitish replacive calcite of Sumatra (working name: A_2a) and the replacive calcite of the glendonites of ash layer +16 (working name: +16) and of ash layer +62 (working name: +62c) (see Tab. 7) were selected for clumped isotope analyses. The glendonite of ash layer +16 was chosen, because three diatomite samples of nearly the same horizon were processed for $\delta^{18}\text{O}$ measurements. The glendonite of ash layer +62 represents the uppermost glendonite-bearing horizon observed within the Fur Formation and an additional analysis of a glendonite should clarify the predominant sedimentary column temperature of the Early Eocene.

Preparation for clumped isotope measurements followed the method described by Wacker et al. (2013). Briefly, 4 to 8 mg of carbonate powder was filled into silver capsulus and dropped in a common acid bath with 105 to 106 wt% H_3PO_4 (cf. Wachter and Hayes, 1985) at 90 °C for 30 min. The evolved CO_2 was frozen in liquid nitrogen (LN_2) for 20 to 30 min. After a cryogenic cleaning step, the CO_2 concentration was determined manometrically. The CO_2 was passed through a GC column to remove traces of hydrocarbons and it was frozen for 30 min in LN_2 .

The CO_2 was measured against an Oztech reference gas using a dual inlet system on a Thermo Scientific MAT 253 mass spectrometer at the Institut für Geowissenschaften, Frankfurt/Main. All clumped isotope data (Δ_{47}) were corrected with a fractionation factor Δ_{47}^{*25-90} of +0.069‰ (Guo et al., 2009). The raw data were corrected using equilibrated gases and the background correction was exceeded scaling the m/z 47 background to the intensity of the m/z 49 signal (Fiebig et al., 2016). The analytical performance was monitored with two standards: international NBS-19 (Carrara limestone) and the well-homogenised shell material of an aragonitic cold-water bivalve (*Arctica islandica*) as internal standard (Wacker et al., 2014).

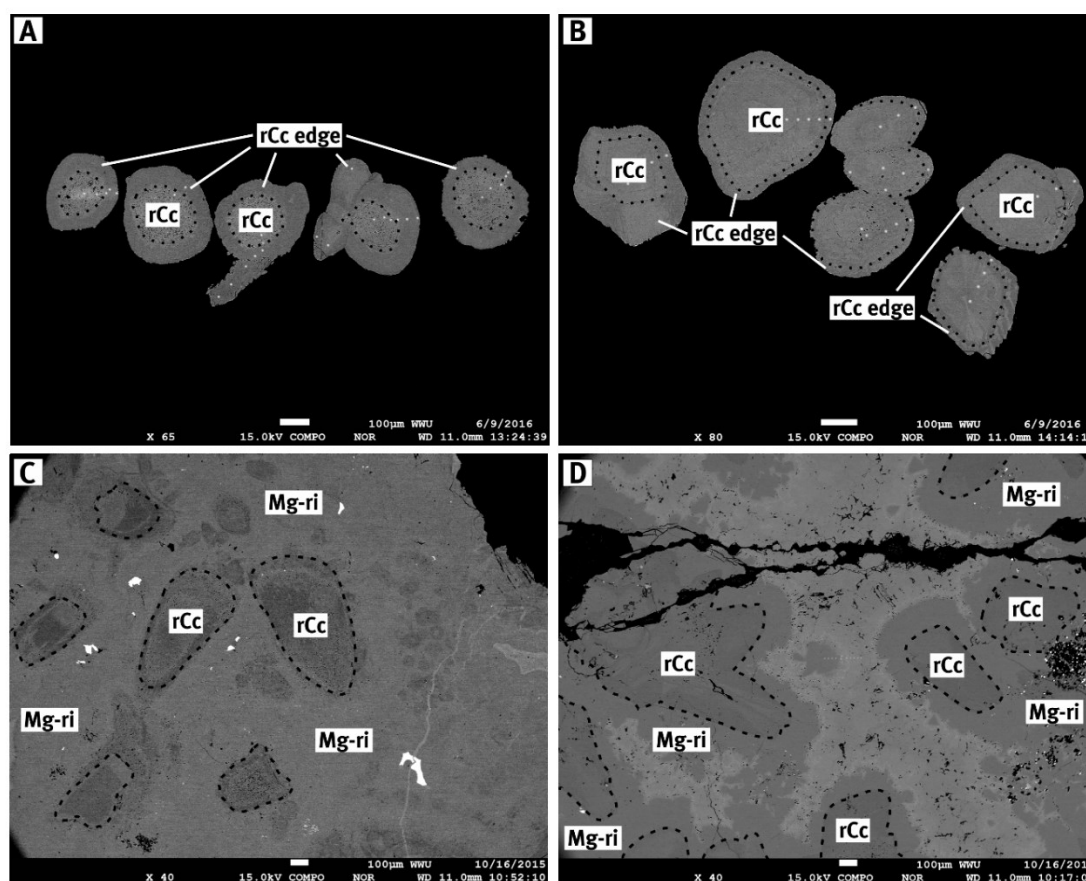


Fig. 11: Back-scatter electron images of the samples for the clumped isotope analyses. (A) Yellowish replacive calcite of the Simeulue Seep glendonite. (B) Whitish replacive calcite of the Simeulue Seep glendonite. (C) Replacive calcite of glendonite +9b from ash layer +9. (D) Replacive calcite of glendonite +62b from ash layer +62. The dotted line envelopes the crystal of the replacive calcite.

4 Results

4.1 Glendonite of the Fur Formation

4.1.1 Macroscopic textures

Glendonite

Glendonites appear as bipyramids (blades), twinned, and stellate pseudomorphs within carbonate concretions. Cross sections show rhombic prisms with bipyramidal terminations. The bipyramidal terminations occur in every glendonite, even in twinned and stellate specimens. The crystal surfaces are smooth, but bear ridges and grooves in irregular intervals. The contact of the monoclinic precursor mineral ikaite with the surrounding sedimentary matrix is sharp. The colour is beige to light brownish if the glendonites are surrounded by carbonate concretions. Glendonite without a protecting carbonate concretion appears reddish to brownish with loose calcite crystals. These loose calcite crystals appear tabular and are also found in glendonite that is surrounded by a carbonate concretion. The glendonite crystals studied here are between 10 and 25 cm high and ca. 50 cm in diameter. The glendonite specimens without surrounding concretions are bipyramidal and only 10 cm in length. Two observations are made: (i) the precursor ikaite stopped growing upward when reaching a specific ash layer (Fig. 7 E) and (ii) the ikaite was able to grow into the ash layer (Fig. 7 B). Moreover, ikaite often grew displacively into the sediment forming small-scale perturbations within the horizontally settled and often laminated diatomite (Fig. 7 C and D).

Concretions surrounding glendonite

The carbonate concretions are usually between 15 and 80 cm thick with a diameter up to 1 m, but distinct horizons are almost completely cemented. Only one glendonite bearing concretion stems from one of these cemented horizons (ash layer +62). Usually, the concretions appear bright grey, brownish to dark grey and the shape is ellipsoidal. The ash layers are dark grey to black traced horizontally into the carbonate concretions. Most of the concretions investigated containing glendonite were derived from ash layer +62 (n=3), others were found at ash layers +9, +10, +15, and +16.

Glendonite is generally located in carbonate concretions below the particular ash layer. The glendonite containing concretions exhibit a diameter between 30 and 35 cm and a thickness of 19 cm (+15a and +62b) and 35 cm (+9b, +10b, and +16a). The concretions of ash layers +9, +10, and +62 are structureless, while the concretions of ash layers +15 and +16 show a laminated diatomite (Fig. 7 C and D).

4.1.2 Petrography and mineralogy

Bulk sample XRD reveals that the glendonite consists of pure calcite, with a maximum Mg content of 2.7 wt%. In one of the glendonite samples (+15c), pyrite was detected. Additionally, the occurrence of pyrite in several glendonites was proven using light microscopy, whereas it was not possible to determine pyrite in other glendonite via XRD.

Microprobe analyses reveal different carbonate phases and the subsequent precipitation of cements as well as of accessory minerals. Differences in the cement distribution are determined at the centre and the rim parts of the glendonite. Depending on preservation of the glendonite, various cement phases are distinguished representing defined generations.

The first generation of calcium carbonate is the replacive calcite (rCc) with tabular to ovoid crystals and rosette clusters (up to 1.5 mm in length, see figures 12 and 13). Organic matter is often included within these crystals as small rings that are thicker towards the crystal's edge. The MgCO_3 content in the centre is lower than at the edge of the replacive calcite. On average, the MgCO_3 content lies at 1.7 mol%, but a MgCO_3 content up to 3.6 mol% was observed at the margin of the rCc.

The second carbonate phase is a radiaxial fibrous to spherulitic isopachous Mg-bearing calcite as rim cement (Mg-ri; ca. 3 mol% MgCO_3) overgrowing the rCc crystals. The Mg-ri is yellow to light brown under the microscope and contains small grains of pyrite and apatite (Fig. 13 B and D). The apatite crystals of the Mg-ri are on average 20 μm long with a maximum length of 100 μm . Brown organic matter particles are often incorporated into this phase causing the yellowish to brownish colour.

The glendonite (+9b) of ash layer +9 reveals a secondary, translucent rim cement that is located at the edge of the brownish Mg-ri cement with the highest content in MgCO_3 (average 7.5 mol%, maximum 10.1 mol%), MnCO_3 (average 1.5 mol%, maximum 2.7 mol%) and FeCO_3 (average 1.1 mol%, maximum 5.7 mol%). Therefore, this cement phase is named Iron-Manganese-Magnesium-rich calcite rim cement (Fe-Mn-Mg-ri). The glendonite (+62b) of ash layer +62 shows this secondary rim cement solely in the central parts, but its abundance is just as high as in the glendonite of ash layer +9. This cement phase is only present in glendonite that is surrounded by a calcareous concretion and in the glendonite (+14b) of ash layer +14. In the glendonite (+16b) of ash layer +16, no Fe-Mn-Mg-ri has been detected. Usually, the secondary rim cement (Fe-Mn-Mg-ri) is found in the central parts of the glendonite. The rCc and the two rim cements comprise circa 80% of the glendonite. The rim cement partially leached off the glendonite when the glendonite was not surrounded by a carbonate concretion (Fig. 12 F, Fig. 13 E, and F).

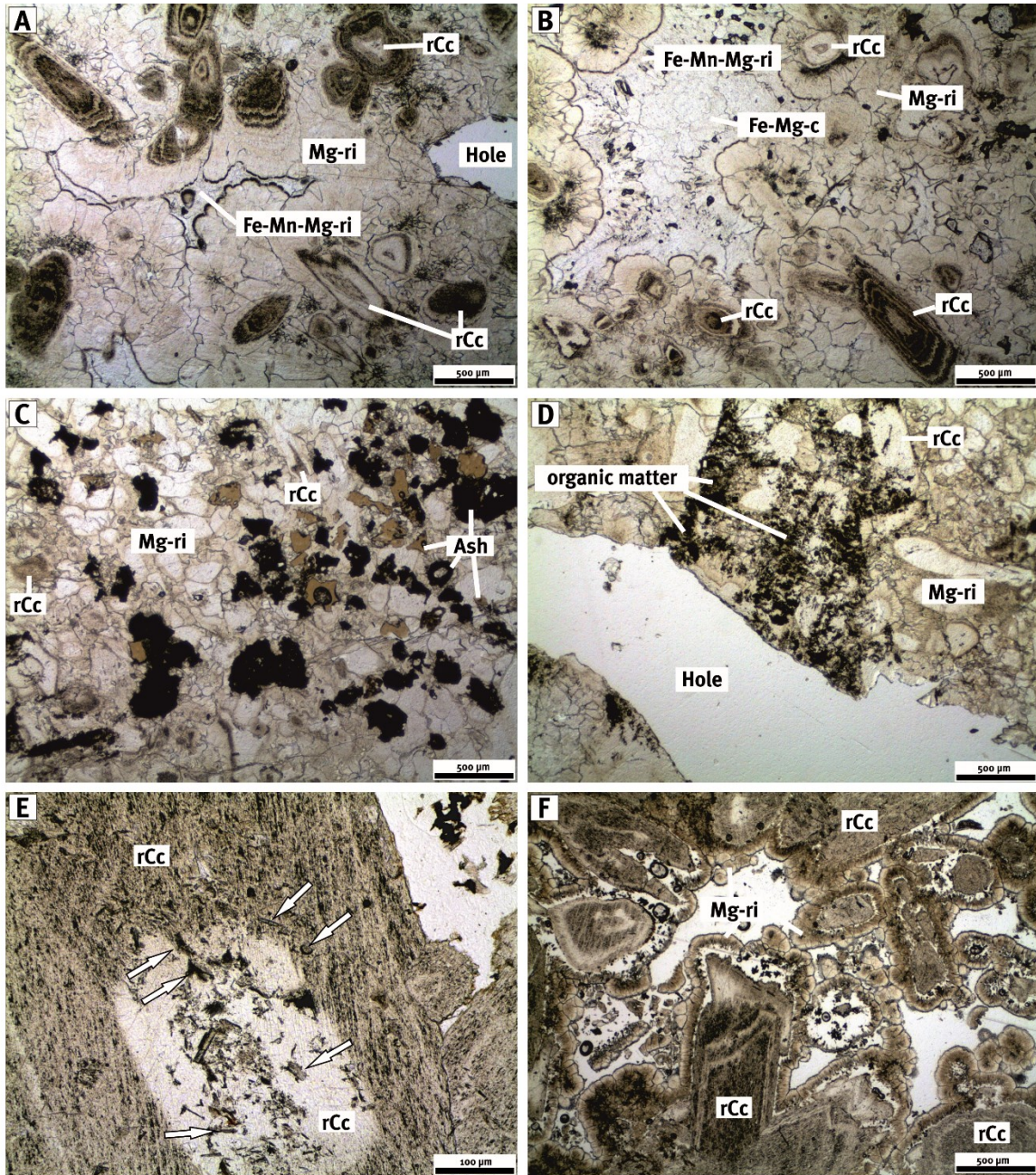


Fig. 12: Photomicrographs in plain-polarised light. (A) Central part of the glendonite of ash layer +9 with rCc: replacive calcite, Mg-ri: Magnesium-bearing rim cement, and Fe-Mn-Mg-ri: Iron-Manganese-Magnesium-rich rim cement. (B) Margin part of the glendonite +9b with rCc, Mg-ri, Fe-Mn-Mg-ri cement, and Fe-Mg-c: Iron-Magnesium-bearing fill cement. (C) Central part of the glendonite below ash layer +62 (+62b), where the glendonite expanded inside the ash layer. Ash particles appear as brownish, black minerals. (D) Central part of the glendonite of picture (C). Brownish organic matter and diatoms are embedded within the glendonite in this area. (E) Central part of the glendonite +16b. (F) Margin part of the glendonite of picture (E). Dissolution fringes of the Mg-ri and the open pore space, where the Fe-Mg-c leached off, can be seen. The location of diatoms within the phases of rCc and Mg-ri is marked with white arrows.

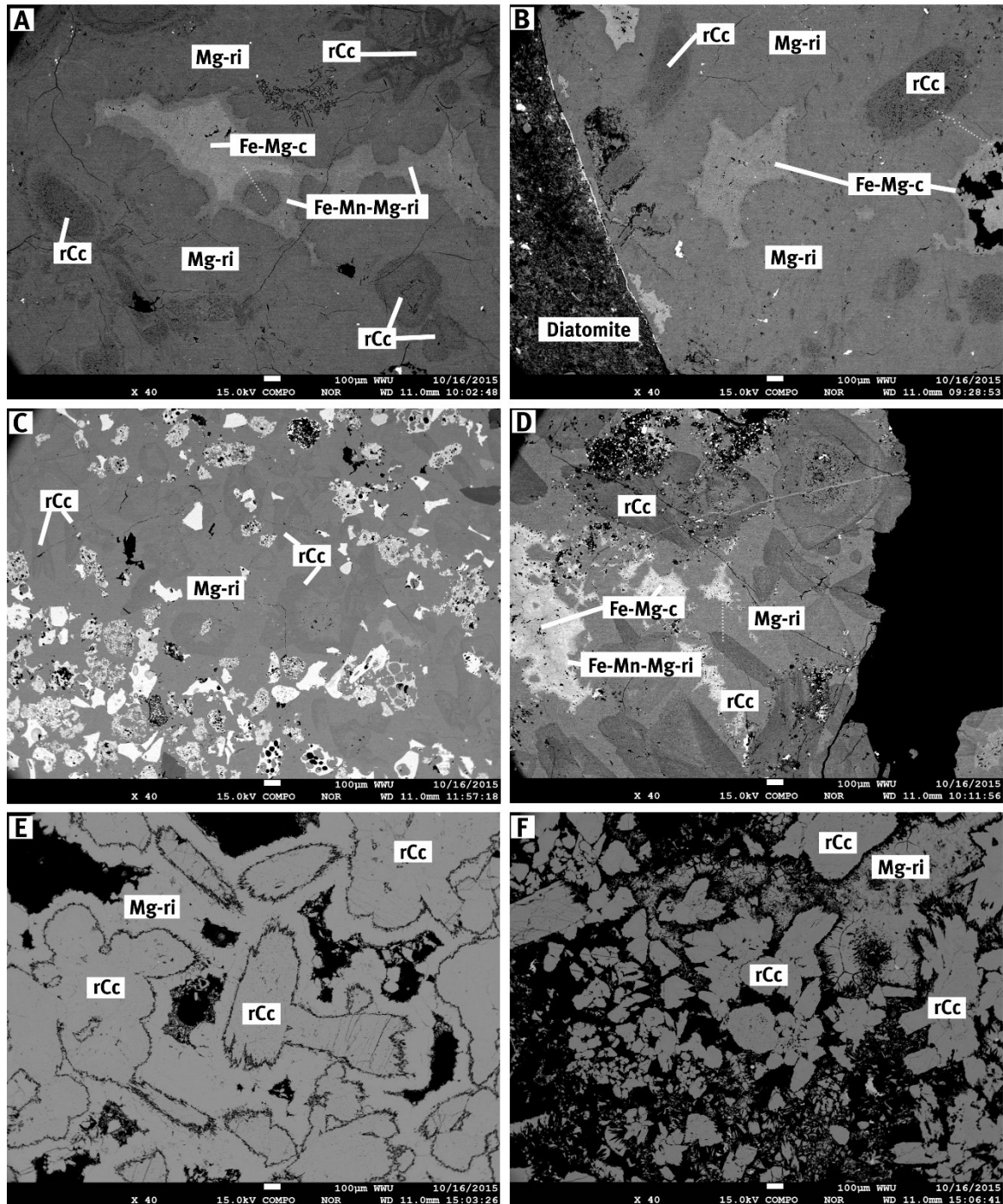


Fig. 13: Back-scatter electron images of the same glendonite crystals like in figure 12. (A) Central part of the glendonite +9b of ash layer +9 with rCc: replacive calcite; Mg-ri: Magnesium-bearing rim cement, and Fe-Mn-Mg-ri: Iron-Manganese-Magnesium-rich rim cement. (B) Margin part of the +9b glendonite. The secondary rim cement phase (Fe-Mn-Mg-ri) could not be seen in the margin area. (C) Central part of the glendonite of ash layer +62b, where the glendonite expanded inside the ash layer. (D) Central part of the glendonite of picture (C). (E) Central part of the +16b. The Fe-Mg-c leached off. (F) Margin part of the glendonite of picture (C). Dissolution fringes of the Mg-ri and the open pore space, where the Fe-Mg-c leached off, are displayed.

The youngest carbonate phase within the glendonite is a sparry, bright calcite filling the open pore space during burial. The magnesium content is low with an average of 2.5 mol% MgCO_3 , while the MnCO_3 (average 0.1 mol% in glendonite of ash layer +9) and the FeCO_3 (average 0.6 mol%) concentrations are slightly enriched. This phase is named Iron-Magnesium-bearing fill cement (Fe-Mg-c). It often leached off when the glendonite was not protected by a surrounding carbonate concretion. Thus, this is the most soluble cement phase of the glendonite. The Fe-Mg-c is completely absent in glendonite samples +14b and +16b.

Few diatoms are embedded within the rCc and the Mg-ri (less than 1% of the glendonite; Fig. 12 E). Inclusions of host sediment within the glendonites are rare and occur only at the marginal part of the glendonites (Fig. 12 D). Organic matter is found as 2.5 to 10 μm particles in the rCc and in the Mg-ri.

4.1.3 Geochemistry

TC, TS, CaCO_3 , and C_{org} concentration

The carbonate content in the glendonite ranges between 92.3 and 97.8 wt% CaCO_3 pointing to pure calcite. The glendonite sample containing the lowest concentration for CaCO_3 is the glendonite +15c of ash layer +15. The total sulphur (TS) content of the glendonite ranges between 0.01 and 0.14 wt% (Tab. 10). Only glendonite +15c of ash layer +15 bears a minor, but via XRD detectable content of pyrite. The organic carbon content (C_{org}) is very high (10.2 and 19.8 wt%) for both glendonite samples of ash layer +62, if compared to the surrounding concretions.

The carbonate concretions consist of diatomite and sometimes of ash layers that are cemented by carbonate cements (mostly calcite). The total carbonate content ranges between 76.3 and 88.6 wt% CaCO_3 . XRD reveals that the main mineral is calcite with up to 4 mol% MgCO_3 . The concretions contain a slightly higher concentration of total sulphur (TS) compared to the glendonite with up to 0.20 wt% sulphur in the concretion +62a of ash layer +62 where the mineral pyrite was detected via XRD. For ash layers observed in some carbonate concretions, volcanic minerals like (titano-)magnetite, anorthite, and albite are identified. The TOC concentration is much lower than in glendonite with values between 0.1 and 4.4 wt%.

Tab. 10: Results for concretions and glendonite bulk samples.

Ash layer	Sample ID	Profile height (m)	Type	$\delta^{13}\text{C}_{\text{carb}}$ (‰V-PDB)	$\delta^{18}\text{O}_{\text{carb}}$ (‰V-PDB)	MgCO ₃ (Mol-%)	TS (wt.%)	CaCO ₃ (wt.%)	TOC (wt.%)	C/N	$\delta^{13}\text{C}_{\text{org}}$ (‰V-PDB)	$\delta^{34}\text{S}_{\text{CAS}}$ (‰V-CDT)	$\delta^{18}\text{O}_{\text{CAS}}$ (‰V-SMOW)	CAS (ppm)
+62	+62a	33.12	glendonite	-23.79	-2.64	n.a.	n.a.	n.a.	n.a.	n.a.	n.a.	n.a.	n.a.	n.a.
+62	+62b	33.02	"	-22.23	-2.43	2.7	0.03	97.82	10.23	n.a.	n.a.	65.00	24.25	1141
+62	+62c	33.02	"	-24.71	-2.47	2.0	0.01	96.35	n.a.	n.a.	n.a.	56.30	24.03	2437
+62	+62c dup1	33.02	"	-23.35	-2.49	1.9	0.05	97.29	19.79	14.53	n.a.	61.00	24.61	1876
+62	+62c dup2	33.02	"	-23.57	-2.72	n.a.	n.a.	n.a.	n.a.	n.a.	n.a.	60.60	24.75	1592
+16	+16a	25.54	"	-23.60	-2.72	1.7	0.02	93.87	n.a.	n.a.	n.a.	59.40	25.10	1031
+16	+16b	25.00	"	-20.80	-2.88	2.2	0.03	96.74	n.a.	n.a.	n.a.	37.96	n.a.	164
+15b,c	+15a	24.47	"	-23.05	-2.84	1.9	0.14	96.04	n.a.	n.a.	n.a.	54.00	24.22	495
+15	+15c	24.47	"	-23.30	-2.80	1.7	0.01	92.30	n.a.	n.a.	n.a.	17.49	13.30	547
+14	+14b	23.88	"	-22.88	-2.92	n.a.	n.a.	n.a.	n.a.	n.a.	n.a.	n.a.	n.a.	n.a.
+10	+10a_1	23.475	"	-22.09	-2.44	2.0	0.01	96.35	n.a.	n.a.	n.a.	52.36	23.34	404
+10	+10a_2	23.475	"	-23.01	-2.60	2.9	0.05	95.48	n.a.	n.a.	n.a.	65.16	24.02	583
+10	+10b_1	23.47	"	-22.15	-2.30	1.9	0.04	97.15	n.a.	n.a.	n.a.	58.91	24.11	673
+10	+10b_2	23.47	"	-23.98	-2.75	2.2	0.02	96.21	n.a.	n.a.	n.a.	68.23	24.49	563
+9	+9b	22.92	"	-25.10	-2.42	2.4	0.03	95.34	n.a.	n.a.	n.a.	33.20	16.82	96
+62	+62a	33.12	concretion	-22.51	-2.07	3.9	0.20	76.34	1.04	11.49	-26.17	17.60	11.89	244
+62	+62b	33.02	"	-21.62	-2.26	3.7	0.14	79.54	0.06	n.a.	-25.85	n.a.	n.a.	n.a.
+62	+62c	33.02	"	-24.02	-2.59	3.2	0.08	77.13	0.90	15.41	-25.97	n.a.	n.a.	n.a.
+62	+62c dup1	33.02	"	-24.02	-2.54	n.a.	n.a.	n.a.	n.a.	n.a.	n.a.	27.00	12.06	3
+16	+16a	25.54	"	-18.63	-2.03	3.6	0.07	88.59	4.43	26.11	-26.92	23.26	21.39	460
+15b,c	+15a	24.47	"	-18.17	-2.11	3.0	0.07	87.85	3.60	19.81	-27.16	17.10	17.66	379
+10	+10b	23.47	"	-23.55	-2.18	3.0	0.03	82.93	1.42	18.21	-26.23	32.86	19.04	752
+9	+9b	22.92	"	-18.16	-2.16	3.3	0.01	79.98	0.81	20.19	-26.59	29.50	n.a.	400

Carbon and oxygen isotopes ($\delta^{13}\text{C}_{\text{carb}}$ and $\delta^{18}\text{O}_{\text{carb}}$) of carbonates

$\delta^{13}\text{C}_{\text{carb}}$ values in the drilled samples of carbonate concretions range between -24.7 and -17.2‰ V-PDB, while the drilled glendonite samples display slightly lighter $\delta^{13}\text{C}$ values between -25.8 and -18.5‰. $\delta^{18}\text{O}_{\text{carb}}$ values of the carbonate concretions vary between -2.8 and -1.8‰, and for the glendonite between -3.6 and -1.7‰ (Tab. 10). Bulk rock $\delta^{13}\text{C}$ isotopic composition ranges from -25.1 to -20.8‰ and from -24.0 to -18.2‰ for glendonite and carbonate concretion samples, respectively. The mean $\delta^{13}\text{C}$ value of bulk glendonite samples is $-23.2 \pm 1.1\text{‰}$, while the average $\delta^{13}\text{C}$ value of bulk samples of carbonate concretions is more enriched in ^{13}C with a value of $-21.3 \pm 2.6\text{‰}$. $\delta^{18}\text{O}$ values of bulk glendonite samples range between -2.9‰ and -2.3‰ and for bulk concretions between -2.6‰ and -2.0‰. The mean $\delta^{18}\text{O}$ values are $-2.6 \pm 0.2\text{‰}$ and $-2.2 \pm 0.2\text{‰}$ for glendonite and concretions, respectively.

The carbon and oxygen data of different cement generations reveal a more detailed picture (Tab. 11, Fig. 14 and Fig. 15). The $\delta^{13}\text{C}$ isotopic composition of the replacive calcite shows the lowest values of all three cement generations with an average value of $-24.7 \pm 0.9\text{‰}$ V-PDB. The rim cement samples (average value: $-22.7 \pm 1.4\text{‰}$) are up to 2‰ higher in their $\delta^{13}\text{C}$ compared to the rCc and the youngest cement generation (c; average $\delta^{13}\text{C}$ value: $-18.9 \pm 3.6\text{‰}$) is up to 8‰ higher than the rim cement. The bulk data are always more ^{13}C enriched than the rCc (up to 2‰). Sometimes they fall between the rim cement and the fill cement. In most samples, the $\delta^{18}\text{O}$ values shift to ^{18}O enriched values from the replacive calcite across the rim cement to the fill cement. Solely for glendonite +16a of ash layer +16, this sequence is completely reversed with the lightest value analysed for the fill cement (-2.6‰) and the heaviest value for the replacive calcite (-2.0‰). In general, the rCc depicts $\delta^{18}\text{O}$ values between -2.7 and -2.0‰, the rim cements values between -2.4 and -1.7‰, and the fill cement values between -2.6 and -0.6‰. Bulk $\delta^{18}\text{O}$ values of the glendonites exhibit more ^{18}O depleted values than all corresponding cement phases of the particular sample. The bulk samples are about 0.2‰ lighter than the lightest cement phase (often rCc).

Strontium and calcium isotope geochemistry ($^{87}\text{Sr}/^{86}\text{Sr}$ and $\delta^{44}/^{40}\text{Ca}$)

The $^{87}\text{Sr}/^{86}\text{Sr}$ values of the carbonate concretions (~ 0.70774) are slightly enriched in ^{87}Sr with respect to the glendonite (~ 0.70773) (Tab. 11). The rCc and Mg-ri (average of 0.70774) show $^{87}\text{Sr}/^{86}\text{Sr}$ values that are normally heavier than for the glendonite bulk samples. Excluding the glendonite +62b of ash layer +62, the fill cement is generally more enriched in ^{87}Sr with an average value of 0.70781 than the other two cement phases.

The calcium isotopic composition of the three different glendonite cements (rCc, Mg-ri, and c) is very homogeneous with a mean value of $0.70 \pm 0.06\text{‰}$ SRM915a. Within each of the four samples, the $\delta^{44}/^{40}\text{Ca}$ values of the three cements are identical within analytical error. In every sample, the rCc exhibits a mean value of 0.71‰, which is very similar to the mean value

of the fill cement generation (0.73‰). Solely the rim cement displays a slightly lower value of 0.67‰.

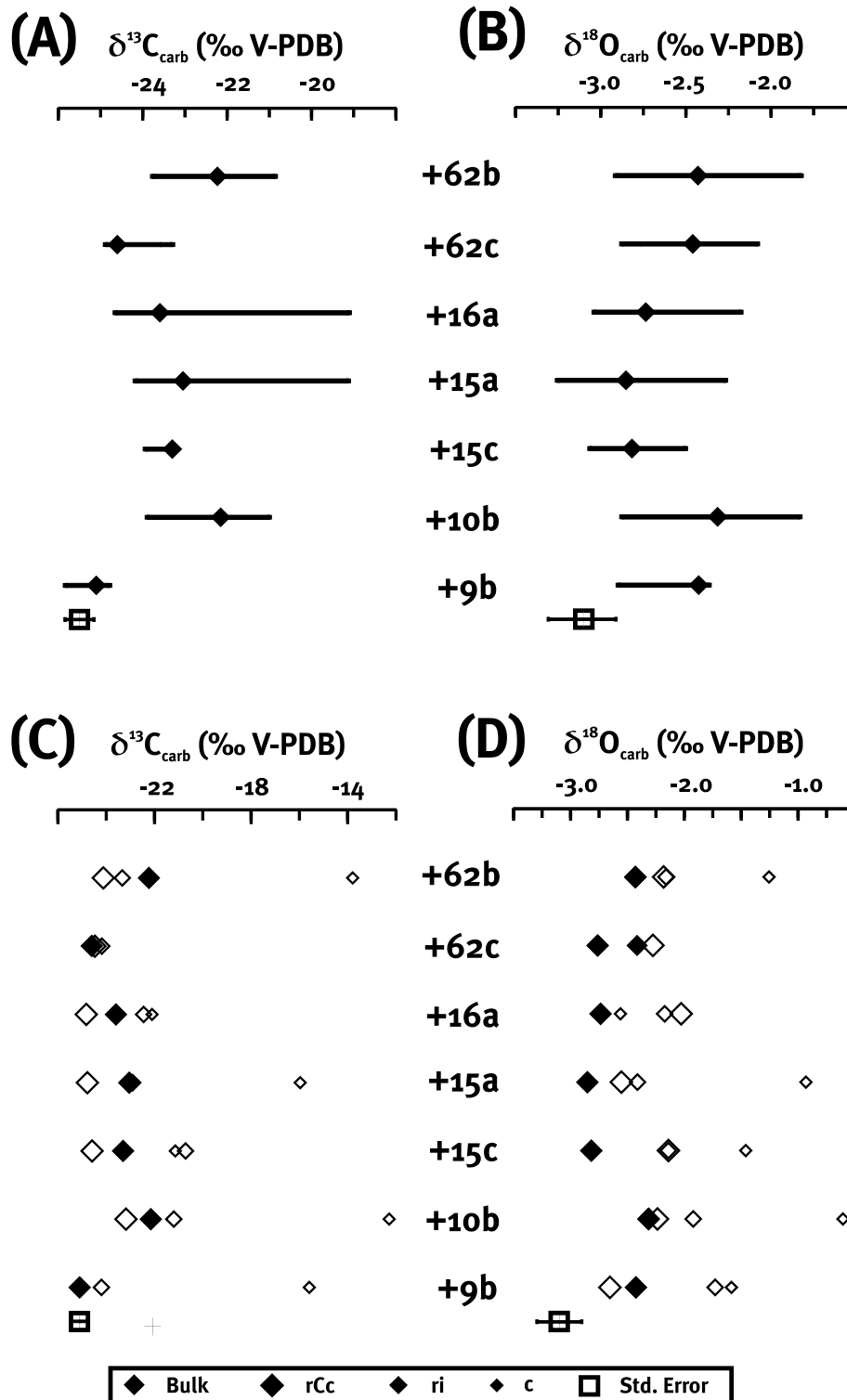


Fig. 14: (A) $\delta^{13}\text{C}_{\text{carb}}$ values of the drilled samples of glendonite in comparison to the bulk glendonite values. (B) $\delta^{18}\text{O}_{\text{carb}}$ values in the same arrangement as in (A). (C) $\delta^{13}\text{C}_{\text{carb}}$ values of the different cement phases and the bulk glendonite values. (D) $\delta^{18}\text{O}_{\text{carb}}$ values of the cement phases as in diagram (C).

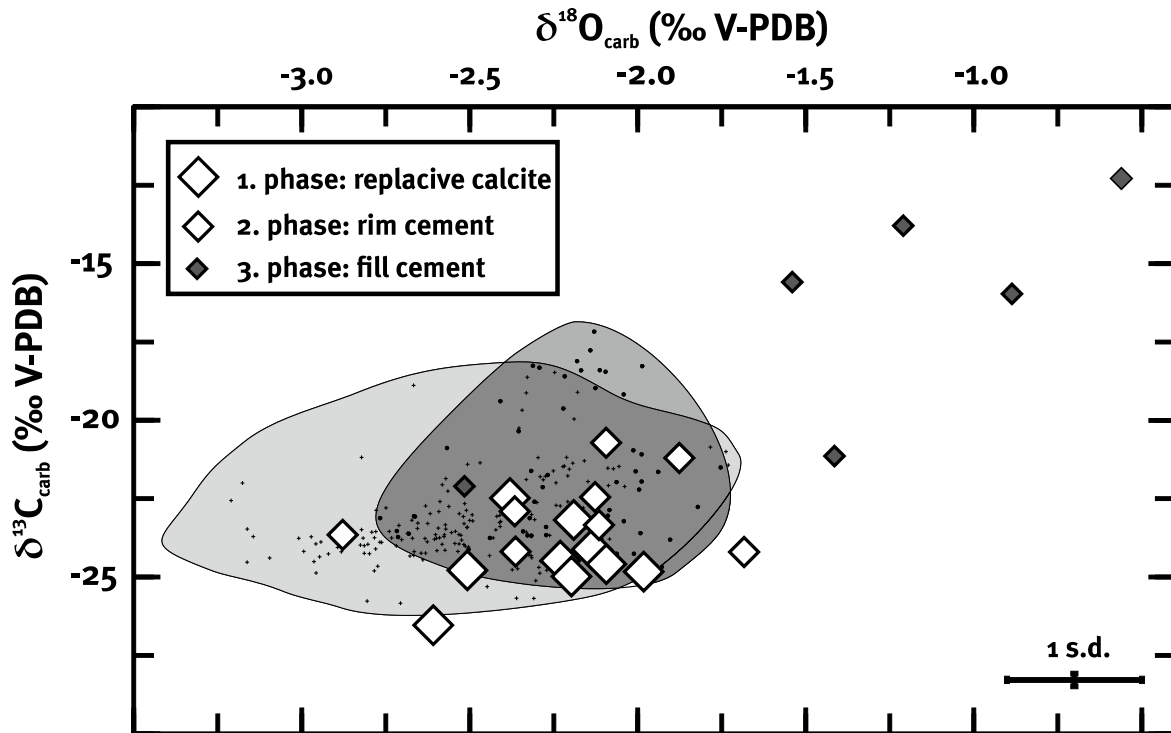


Fig. 15: Plot of $\delta^{13}\text{C}_{\text{carb}}$ values versus $\delta^{18}\text{O}_{\text{carb}}$ values of glendonite and surrounding concretions. The bulk $\delta^{13}\text{C}$ and $\delta^{18}\text{O}$ values are displayed as shaded data areas (light grey: glendonite; dark grey: carbonate concretions), and the values of the cement measurements are given as diamonds.

Tab. 11: $\delta^{13}\text{C}_{\text{carb}}$, $\delta^{18}\text{O}_{\text{carb}}$, $^{87}\text{Sr}/^{86}\text{Sr}$, and $\delta^{44}/^{40}\text{Ca}$ values of glendonite cement samples. The abbreviation “rCc” stands for replacive calcite, “ri” for the first rim cement and “c”, for fill cement.

Ash layer	Sample ID	Profile height (m)	Cement phase	$\delta^{13}\text{C}_{\text{carb}}$ (‰V-PDB)	$\delta^{18}\text{O}_{\text{carb}}$ (‰V-PDB)	$^{87}\text{Sr}/^{86}\text{Sr}$	$\delta^{44}/^{40}\text{Ca}$ (‰ SRM915a)
+62	+62b	33.02	rCc	-24.13	-2.18	0.70773	0.73
+62	+62b	"	ri	-23.34	-2.16	0.70773	0.75
+62	+62b	"	c	-13.79	-1.26	0.70773	0.80
+62	+62c	33.02	rCc	-24.48	-2.28	n.a.	n.a.
+62	+62c	"	ri	-24.19	-2.41	n.a.	n.a.
+16	+16a	25.54	rCc	-24.83	-2.03	n.a.	n.a.
+16	+16a	"	ri	-22.45	-2.17	n.a.	n.a.
+16	+16a	"	c	-22.11	-2.56	n.a.	n.a.
+16	+16b	25.00	rCc	-24.98	-2.24	n.a.	n.a.
+16	+16b	"	c	-17.30	-1.44	n.a.	n.a.
+15b,c	+15a	24.47	rCc	-24.78	-2.55	0.70774	0.69
+15b,c	+15a	"	ri	-22.91	-2.41	0.70774	0.66
+15b,c	+15a	"	c	-15.97	-0.93	0.70776	0.78
+15	+15c	24.47	rCc	-24.59	-2.14	n.a.	n.a.
+15	+15c	"	ri	-20.72	-2.14	n.a.	n.a.
+15	+15c	"	c	-21.14	-1.46	n.a.	n.a.
+10	+10b	23.47	rCc	-23.18	-2.24	0.70774	0.74
+10	+10b	"	ri	-21.20	-1.92	0.70775	0.68
+10	+10b	"	c	-12.29	-0.61	0.70782	0.72
+9	+9b	22.92	rCc	-26.54	-2.65	0.70774	0.67
+9	+9b	"	ri	-24.20	-1.73	0.70773	0.57
+9	+9b	"	c	-15.59	-1.59	0.70781	0.63

Sulphur and oxygen isotopes of carbonate-associated sulphate ($\delta^{34}\text{S}_{\text{CAS}}$ and $\delta^{18}\text{O}_{\text{CAS}}$)

Concentrations of CAS in glendonite range between 96 and 2437 ppm (Tab. 10). The highest CAS concentrations were found in the glendonite samples of ash layer +16 (glendonite +16a) and +62 (glendonite +62c) that are both surrounded by a carbonate concretion. The proto-glendonite +16b of ash layer +16 depicts a CAS concentration of 164 ppm. The lowest CAS concentration (96 ppm) was recorded for glendonite +9b of ash layer +9.

Most of the glendonite crystals display $\delta^{34}\text{S}_{\text{CAS}}$ values between +50 and +75‰ V-CDT and $\delta^{18}\text{O}_{\text{CAS}}$ values between +22 and +25‰ V-SMOW (Tab. 10). Solely the glendonite +16b of ash layer +16 displays a lighter value of +38‰ for $\delta^{34}\text{S}$ ($\delta^{18}\text{O}$ was not measured due to insufficient BaSO_4 material). Even lighter values were measured for the glendonite +15c of ash layer +15 ($\delta^{34}\text{S}$ of +17‰ and $\delta^{18}\text{O}$ of +14‰) and for the glendonite +9b of ash layer +9 ($\delta^{34}\text{S}$ value of +33‰ and $\delta^{18}\text{O}$ value of +17‰). Both glendonite samples contain substantial amounts of pyrite as identified via XRD. For glendonite +9b and +15c, chromium-reducible sulphur (CRS, i.e. pyrite sulphur) yielded $\delta^{34}\text{S}_{\text{CRS}}$ values of -27 and -35‰, respectively.

CAS concentrations of the carbonate concretions between 379 and 752 ppm are lower than the respective concentrations of the glendonite. Moreover, the carbonate concretions analysed exhibit lower isotope values than the glendonite with values between +17 and +35‰ for $\delta^{34}\text{S}$ and between +12 and +22‰ for $\delta^{18}\text{O}$.

4.2 Carbonate concretions and volcanic ash layers of the Fur Formation

4.2.1 Sediment structures and fossils

Remeasured thicknesses of diatomite and ash layers are summed up in appendix 1 and a summarizing profile for all investigations of 2014 field work was drawn (Fig. 16). Beside glendonite moulds (Tab. 3), several other structures were found. One metre above ash layer -11, ghost rocks, looking like large, reddish concretions, were observed in several outcrops (Fig. 17 A; Knudeklint coastal outcrop, Råkilde pit on Fur, and Ejerslev pit on Mors). Slumping structures (Fig. 17 B) were observed between ash layers -17 and -14 at the coast of Fur Knudeklint. A mould of ca. 5 cm in diameter and 2 cm height was found between ash layers -10 and +1 (Fig. 17 C). This could be a mould of a chert nodule. Macrofossils like bivalves, bones, and cochleae were found in horizons of ash layers between -28 and -24, +31, and +130. Several ash layers of the Silstrup Member exhibit abundant burrows made by animals (Fig. 17 D).

The macroscopic picture of the carbonate concretions is very variable (Fig. 18). Several horizons are cemented by carbonate for several hundred metres in diameter (ash layers -11, +62, +101/+102, +130, +135). The carbonate horizons studied here are between 5 and 70 cm thick with an average of ca. 25 cm. The ellipsoidal concretions are between 15 and 80 cm in diameter with an average of 34 cm. The diameter of several concretions was not measured, because either the concretion was not complete or the concretions stem from a cemented horizon. The most remarkable concretions are those that contain glendonite and the one between ash layers -28 and -24 which contains numerous bones, bivalves, and several ash layers (Fig. 18 F).

Additionally, several sedimentary structures were found in the concretion between ash layers -28 and -24: areas incised, slumping, and erosional structures (Fig. 18 F).

4.2.2 Volcanic ash layers – Microscopic textures and geochemistry

Microscopic textures

Volcanic ash layers bear brown sideromelane and black, opaque tachylite glass particles. Some of the sideromelane particles appear brownish-yellow with sharp edges (Fig. 19 A and C). Others contain abundant voids (Fig. 19 C and D). Point counting revealed a proportion of 95% for the glass particles of the whole ash layer. The remaining 5% pyroclasts are rock particles with microlitic textures and crystal fragments with mostly calcite-rich plagioclase. Sometimes diatoms, radiolarians, and silicoflagellates are embedded within the volcanic ash layers (Fig. 19 B). The grains at the lower boundary are coarser with a diameter of ca. 500 µm and a fining up to a particle size of ca 100 µm in average can be seen in every ash layer. No sedimentary structures are discernible by light microscopy within the ash layers. Some of the positive ash layers have been relocated by burrowing animals like *Teichichnus* and *Planolites*

(Pedersen and Surlyk, 1983) and, thus, are arranged as burrows within the underlying diatomite.

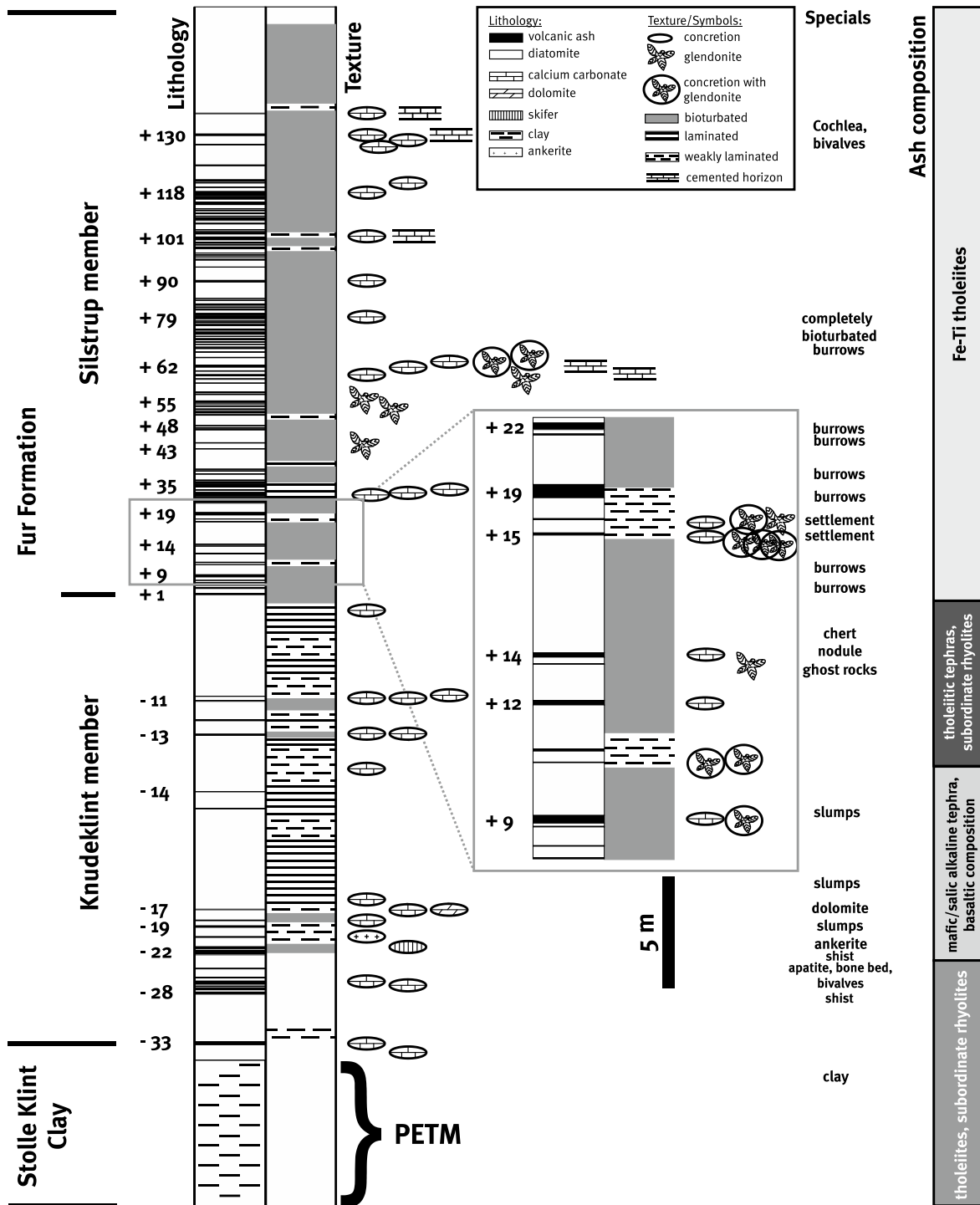


Fig. 16: Lithostratigraphic column of the Fur Formation showing the different lithologies with ash layer numbering, structures, occurrences of carbonate concretions and glendonite, ash layer chemistry, and fossils. The ash composition was added using data of Larsen et al. (2003).

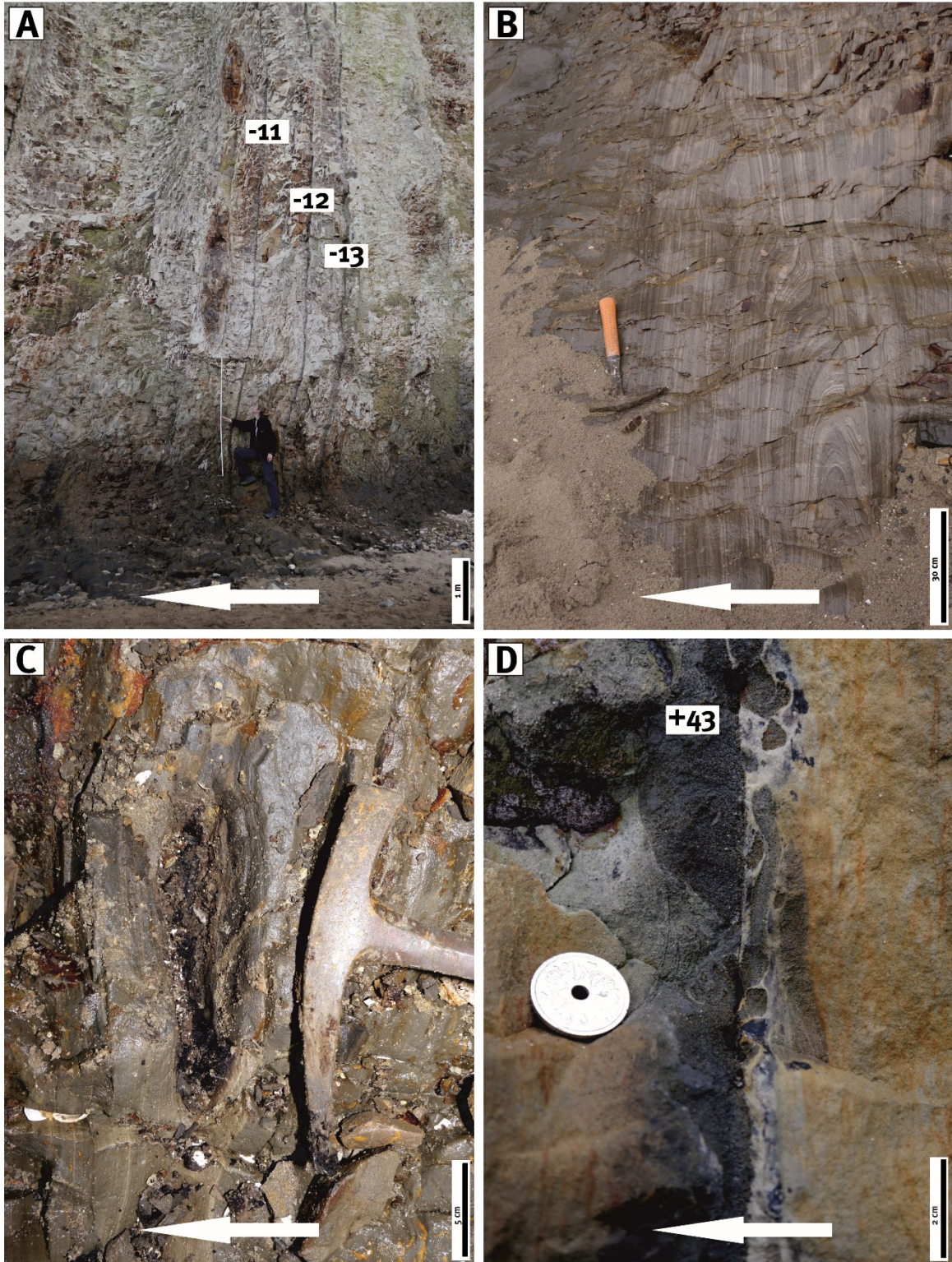


Fig. 17: Photographs of different structures found during the field investigations in 2014 at Knudeklint coastal outcrop on Fur. (A) Ghost rocks, which are concretions in pretence, slightly above ash layer -11. (B) Slumping structures between ash layers -17 and -14. (C) Hole of a chert nodule ca. 3 m above ash layer -10. (D) Bioturbation below ash layer +43. The number of the individual ash layers are given within the white squares. The white arrow indicates the age pointing to younger sediments.

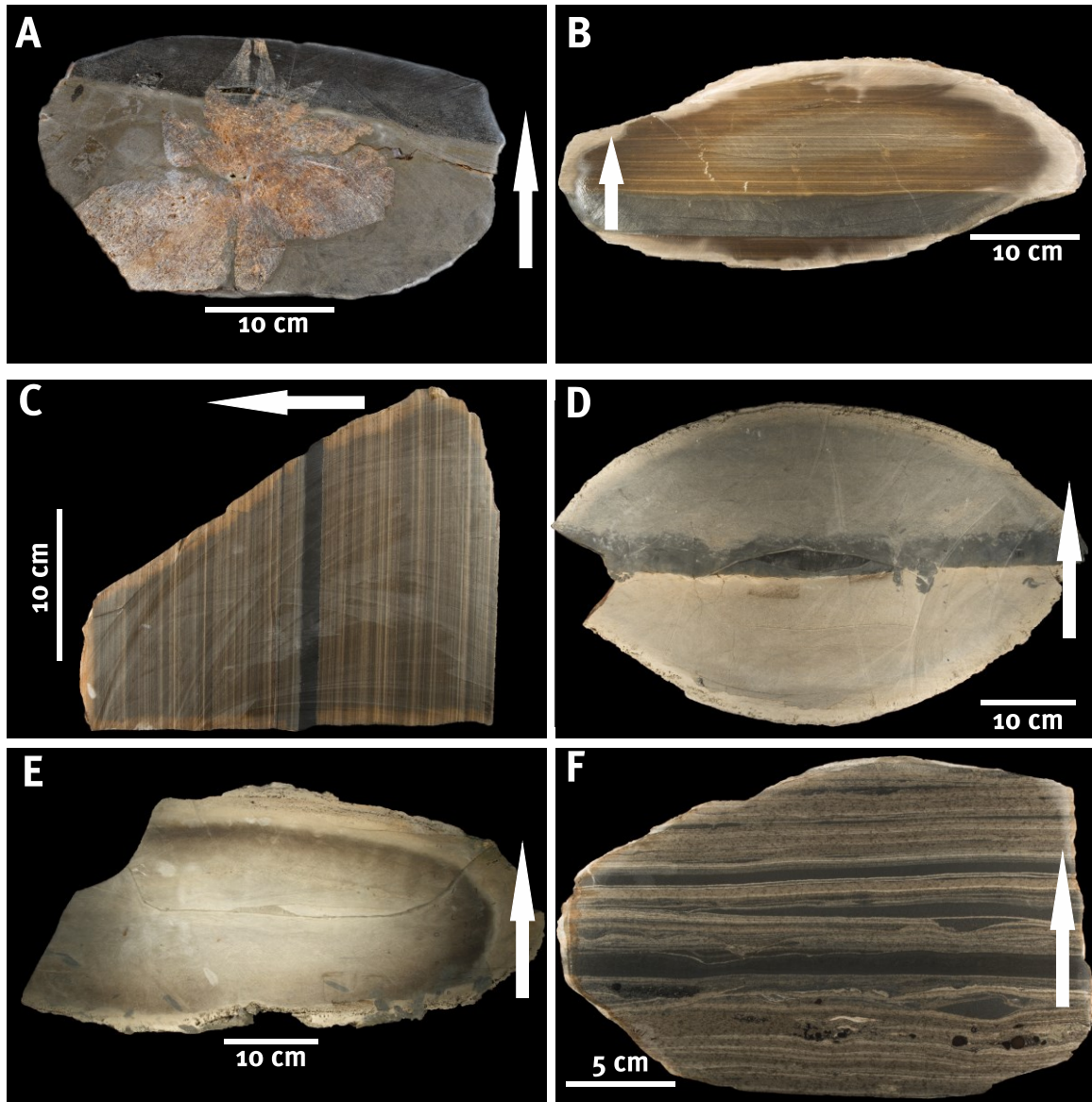


Fig. 18: Photographs of some concretions. (A) Concretion holding ash layer +62 and a stellate glendonite, which grew inside the ash layer. (B) Concretion of ash layer +31. (C) Concretion of ash layer +26 with a flat, horizontal lamination. (D) Concretion +9a bearing ash layer +9. At the lower boundary, the ash layer is bioturbated and ash particles occur in burrows. (E) Concretion between ash layers +3 and +4 that is bioturbated. Thus, no lamination can be seen. (F) The so-called “sribet” cementsten (Andersen and Andersen, 1996; Pedersen et al., 2011) between ash layers -28 and -24 that holds ash layers, bone beds, bivalves, and sedimentary structures. The white arrow indicates the age pointing to younger sediments.

Geochemistry

Two thin sections (bearing ash layers +9 and +62) were prepared for electron microprobe analyses. Both ash layers belong to the group of Fe-Ti tholeiites. The ashes vary in degree and grading in crystallinity from clear isotropic yellow and dark brown glasses to fine-grained crystalline basalt particles.

The volcanic ash layers of horizon +9 and +62 are very similar in their chemical composition (Tab. 12) with concentrations of Si 52.83, Ca 13.13, Fe 12.50, Al 8.62, Mg 8.41, Na 3.07, and Ti 2.64 (all values given in norm%). Minor concentrations of K, Cr, and Mn were measured. Some particles exhibit higher Al concentrations with 18.36 norm%. The volcanic ash layers are cemented with a homogenous calcite cement exhibiting average Ca (61.64 norm%) and Mg (1.81 norm%) concentrations. The diatomite within carbonate concretions display calcitic cementation with a higher concentration of Si (11.84 norm%; Tab. 12).

Four samples of uncemented ash layers (-12, +19, +55, and +79) were analysed for their $^{87}\text{Sr}/^{86}\text{Sr}$ ratio and yield values between 0.70407 and 0.70693 with an average of 0.70508 when corrected by age (Tab. 13).

Tab. 12: Electron microprobe analyses of volcanic ash particles, diatomite, calcite cement, and other compounds found inside the thin sections of +62b and +9b. Average values are listed.

Ash layer	Sample ID	Description	Na (norm%)	Al (norm%)	K (norm%)	Cr (norm%)	Mg (norm%)
+62	+62b	volcanic ash: volcanic ash particles	2.97	8.73	0.34	0.01	8.45
+62	+62b	volcanic ash: calcite cement	0.06	0.04	0.01	0.01	2.20
+62	+62b	volcanic ash: calcite, edge to volcanic ash	0.36	1.21	0.04	0.03	2.58
+9	+9b	volcanic ash: volcanic ash particles	3.18	8.51	0.38	0.01	8.36
+9	+9b	volcanic ash: calcite cement	0.09	0.01	0.01	0.01	1.43
+9	+9b	volcanic ash: volcanic ash particle, Al rich	4.42	18.36	0.16	0.01	0.40
+9	+9b	volcanic ash: pyrite	0.00	0.03	0.02	0.00	2.05
+9	+9b	diatomite: calcite cement	0.06	0.29	0.05	0.01	2.31
+9	+9b	diatomite: diatoms	0.03	1.08	0.01	0.01	0.03
+9	+9b	diatomite: organic matter	0.22	1.97	0.38	0.00	2.37

Ash layer	Sample ID	Description	Si (norm%)	Ca (norm%)	Mn (norm%)	Ti (norm%)	Fe (norm%)
+62	+62b	volcanic ash: volcanic ash particles	52.03	13.88	0.20	2.50	12.07
+62	+62b	volcanic ash: calcite cement	0.27	61.82	0.13	0.05	0.22
+62	+62b	volcanic ash: calcite, edge to volcanic ash	6.00	55.35	0.20	0.27	2.46
+9	+9b	volcanic ash: volcanic ash particles	53.63	12.38	0.19	2.77	12.92
+9	+9b	volcanic ash: calcite cement	0.09	61.46	0.24	0.01	0.51
+9	+9b	volcanic ash: volcanic ash particle, Al rich	58.14	14.78	0.03	0.20	1.12
+9	+9b	volcanic ash: pyrite	0.42	16.52	2.21	0.03	35.49
+9	+9b	diatomite: calcite cement	11.84	49.16	0.55	0.06	1.36
+9	+9b	diatomite: diatoms	19.79	0.27	0.69	0.00	1.60
+9	+9b	diatomite: organic matter	38.57	26.07	0.30	0.53	1.01

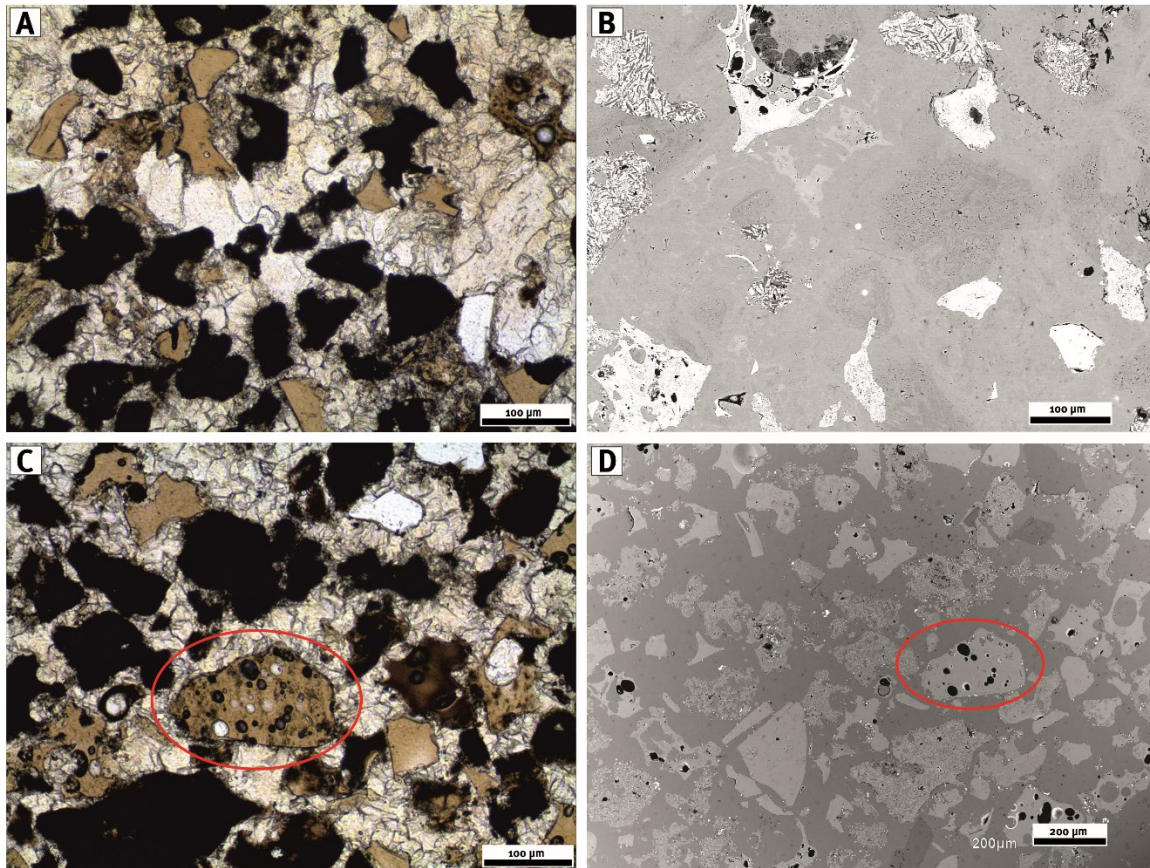


Fig. 19: Photomicrographs in plain-polarised light and back-scatter electron images of volcanic ash particles. (A) Photomicrograph of ash layer +9 where a glendonite grew inside the ash layer. (B) Back-scatter electron image of the same ash layer with few, bright particles. The matrix is glendonite cement with three different cement generations. In the upper left corner, a radiolarian was investigated. (C) Photomicrograph of ash particles within concretion +62b of ash layer +62. The ash particles are embedded in a calcitic matrix. (D) Same excerpt of concretion +62b as a back-scatter electron image. Some of the ash particles exhibit abundant voids. One particle with many voids is marked in red.

4.2.3 Carbonate concretions – Microscopic investigations

The carbonate concretions are cemented with a calcite cement. Other compounds are ash particles, diatoms, clay minerals, bivalves, bones, and the glendonite minerals described above (chapter 4.2.1). The diatoms are well preserved and are present in every thin section. Diatoms occur within glendonite cements and in between ash layers. Several diatom species were identified: *Coscinodiscus*, *Hemiaulus*, *Trinacria*, and *Pseudostictodiscus*. Radiolarian, ebridian, silicoflagellates, and sponge spiculae are also abundant (see chapter 3.2.12).

Besides diatoms (Fig. 20 A), other fossils are visible within the thin sections, most prominently within a “bone” bed layer of the carbonate concretion between ash layers -28 and -24 (Fig. 20 C - F). This layer features fish and arthropod remains (bones, flakes, hair, skin, and teeth), in addition to coprolites produced by fishes with plant remains and insect pieces (Markus Bertling, pers. comm.).

Tab. 13: $^{87}\text{Sr}/^{86}\text{Sr}$ of bulk volcanic ashes of this study and additional published $^{87}\text{Sr}/^{86}\text{Sr}$ values of ashes of the Fur Formation (Morton and Evans, 1988; Larsen et al., 2003).

Ash layer	Publication	Profile height (m)	Locality	measured $^{87}\text{Sr}/^{86}\text{Sr}$	initial $^{87}\text{Sr}/^{86}\text{Sr}$
+79	This study	35.35	Knudeklint	0.70458	0.70447
+55	This study	29.90	Knudeklint	0.70417	0.70407
+19	This study	25.80	Østklint	0.70763	0.70693
-12	This study	14.05	Knudeklint	0.70484	0.70484
+114	Morton & Evans (1988)	40.89	Knudeklint	0.70451	0.70438
+60	Morton & Evans (1988)	32.20	Knudeklint	0.70436	0.70425
+51	Morton & Evans (1988)	30.70	Knudeklint	0.70473	0.70462
+35	Morton & Evans (1988)	27.41	Knudeklint	0.70413	0.70404
+1	Morton & Evans (1988)	22.00	Knudeklint	0.70406	0.70396
+92	Larsen et al. (2003)	36.50	Knudeklint	0.70426	0.70416
+55	Larsen et al. (2003)	29.90	Knudeklint	0.70412	0.70402
+28	Larsen et al. (2003)	26.90	Thy	0.70376	0.70365
+19	Larsen et al. (2003)	25.80	Knudeklint	0.70790	0.70684
+18	Larsen et al. (2003)	25.56	Knudeklint	0.70378	0.70370
-12	Larsen et al. (2003)	14.05	Knudeklint	0.70489	0.70480
-13	Larsen et al. (2003)	13.30	Knudeklint	0.70476	0.70467
-19b	Larsen et al. (2003)	6.90	Knudeklint	0.70525	0.70461
-21a	Larsen et al. (2003)	6.00	Knudeklint	0.70348	0.70335
-22	Larsen et al. (2003)	5.70	Skarrehage	0.70431	0.70417
-33	Larsen et al. (2003)	0.77	Knudeklint	0.71991	0.70613

4.2.4 Carbonate concretions - Geochemistry

X-ray diffraction analyses

The carbonate concretions consist mainly of calcite with a varying concentration of Mg. The Mg content is 7.1 wt% in average with a minimum of 2.0 wt% and a maximum of 16.7 wt% for the calcite carbonate concretions. The dolomite concretion -17b of ash layer -17 and the ankerite concretion of ash layer -20 display a Mg concentration of 47.0 wt% in average (Tab. 14).

The calcite-cemented concretions consist of diatomite and occasionally of ash layers. Bulk sample XRD analyses reveal magmatic minerals like albite, anorthite, and (titano-)magnetite for those concretions that bear volcanic ashes (Tab. 15). Pyrite or marcasite concentrations above 5 wt% were identified in the following concretions: -17a, -13b, -11b_2, -11a_2, +3/4, +25+29, +30b, +31, +62a, +129/+130, and +130b. In the lowermost 6 m of the Knudeklint Member, the concretions exhibit a high abundance of phosphate with hydroxylapatite as the main mineral for the concretion between ash layers -30 and -20 and as nodules in the concretion between ash layers -28 and -24. A sample of a silicified layer between ash layers -30 and -20 consists of quartz, pyrite, magnetite, montmorillonite, and anorthite. Two diatomite samples (Ra u. +16 and Ej+21_1) are composed of quartz (SiO_2) and clay minerals. The SiO_2 is mainly Opal-A, which stems from diatoms.

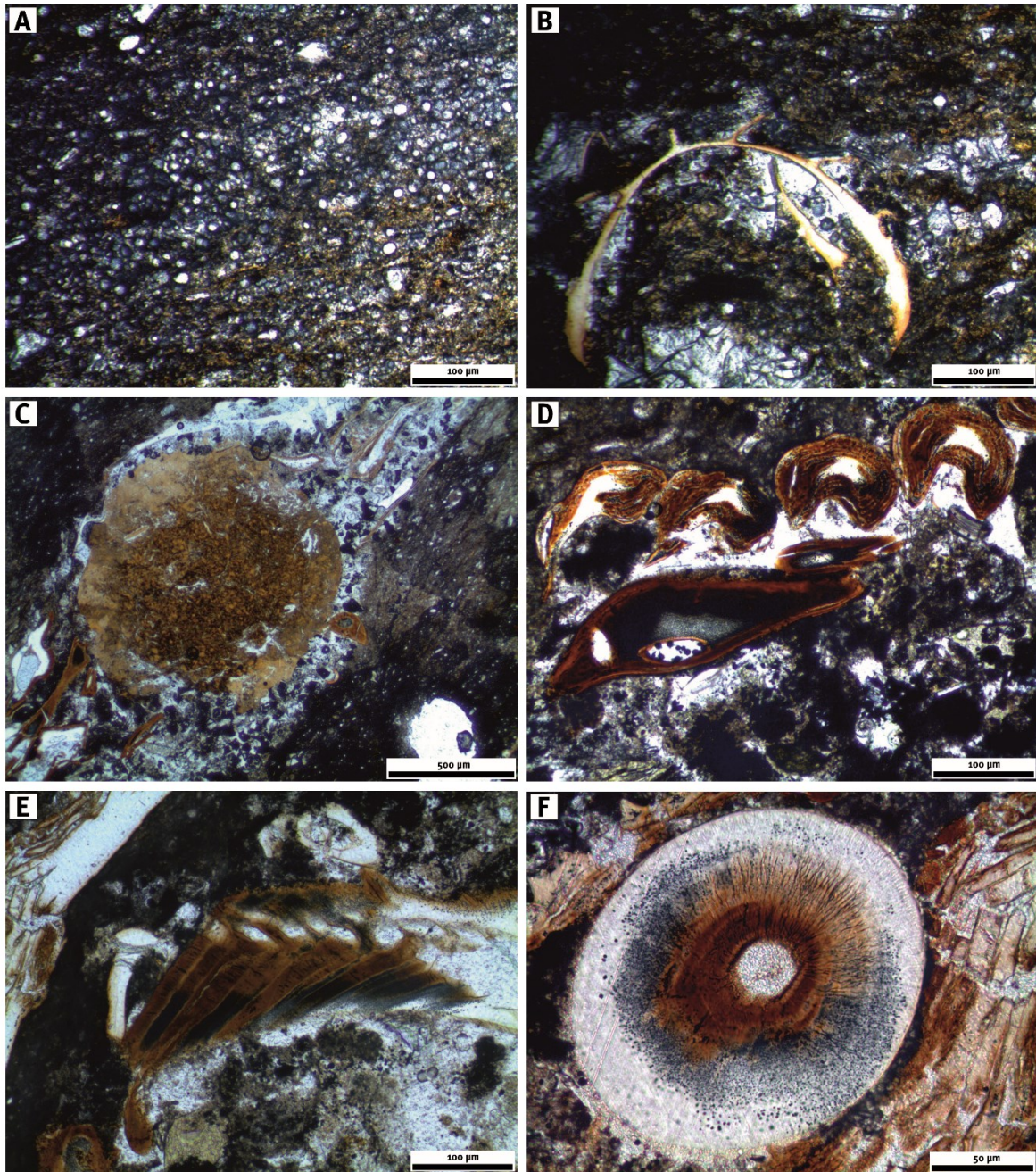


Fig. 20: Photomicrographs in plain-polarised light. (A) Laminated diatomite of ash layer +31. In the middle part, a bright lamina with many diatoms (mainly *Coscinodiscus*) can be seen. In the upper and lower part of the picture, brownish appearing laminae with organic matter and clay minerals are shown. (B) Arthropod fragment in the thin section of concretion +31. (C) Coprolite (phosphate nodule). (D) Arthropod fragments are visible in the upper half of the picture. A fish flake is located in the lower left part. (E) Another arthropod fragment. (F) Unidentified round fossil component. Pictures (C) to (F) are taken from a thin section of the carbonate concretion between ash layers -28 and -24.

Tab. 14: Results of bulk carbonate concretion samples.

Ash layer	Sample ID	Profile height (m)	Type	Cement type	$\delta^{13}\text{C}_{\text{carb}}$ (‰V-PDB)	$\delta^{18}\text{O}_{\text{carb}}$ (‰V-PDB)	MgCO ₃ (Mol-%)	TS (wt-%)	CaCO ₃ (wt-%)	TOC (wt-%)	C/N	$\delta^{13}\text{C}_{\text{org}}$ (‰V-PDB)	$\delta^{15}\text{N}_{\text{org}}$ (‰V-CDD)	$\delta^{18}\text{O}_{\text{carb}}$ (‰V-SMOW)	CAS (ppm)
+135	+135a	45.29	diatomite	calcite	-22.08	-1.80	7.2	0.00	91.30	3.41	20.52	-27.68	n.a.	n.a.	n.a.
+135	+135b	45.29	diatomite	calcite	-23.88	-0.47	11.0	0.19	89.20	2.42	20.05	-27.85	n.a.	n.a.	n.a.
+130	+130a	44.24	diatomite	calcite	-20.59	-1.13	6.2	0.16	85.23	3.41	21.64	-27.54	26.80	22.43	1159
+130	+130b	44.24	diatomite/ash layer	calcite	-22.17	-1.86	3.6	2.00	32.56	0.48	29.40	-26.05	n.a.	n.a.	n.a.
+129	+129/130	44.03	diatomite/ash layer	calcite	-22.10	-1.96	3.8	0.27	36.96	0.34	28.70	-26.22	n.a.	n.a.	n.a.
+102	+102a	39.46	diatomite	calcite	-22.50	-2.15	8.3	0.01	88.95	2.81	22.02	-26.53	n.a.	n.a.	n.a.
+102	+102b	39.46	diatomite/ash layer	calcite	-11.51	-0.17	10.3	0.61	44.65	0.04	n.a.	n.a.	n.a.	n.a.	n.a.
+90	+90	37.14	diatomite	calcite	-24.09	-2.18	4.1	0.10	82.48	1.19	15.74	-26.08	n.a.	n.a.	n.a.
+62	+62a	33.12	diatomite	calcite	-22.51	-2.07	3.9	0.20	76.34	1.04	11.49	-26.17	17.60	11.89	244
+62	+62b_1	33.02	diatomite	calcite	-21.62	-2.26	3.7	0.14	79.54	0.06	n.a.	n.a.	n.a.	n.a.	n.a.
+62	+62c_2	33.02	diatomite/ash layer	calcite	-22.70	-2.19	3.9	0.45	45.99	0.09	n.a.	-25.85	n.a.	n.a.	n.a.
+62	+62c_1	33.02	diatomite	calcite	-23.36	-2.09	6.9	0.06	76.05	1.26	19.13	-26.16	n.a.	n.a.	n.a.
+62	+62c_2	33.02	diatomite	calcite	-23.89	-2.21	6.3	0.24	59.96	0.55	12.60	n.a.	n.a.	n.a.	n.a.
+62	+62c_3	33.02	diatomite	calcite	-24.02	-2.59	3.2	0.08	77.13	0.90	15.41	-25.97	27.00	12.06	3
+31	+31a	27.23	diatomite	calcite	-21.45	-2.80	10.8	0.10	86.03	5.48	25.38	-27.02	n.a.	n.a.	n.a.
+31	+31b	27.23	diatomite/ash layer	calcite	-21.22	-1.09	13.9	0.94	48.89	0.02	n.a.	n.a.	n.a.	n.a.	n.a.
+30	+30a	27.07	diatomite	calcite	-21.34	-0.82	14.6	0.67	78.05	3.24	23.94	-26.99	n.a.	n.a.	n.a.
+30	+30b	27.07	diatomite/ash layer	calcite	-21.10	-0.93	13.4	0.72	47.16	0.04	n.a.	-28.19	n.a.	n.a.	n.a.
+28	+28	26.91	diatomite	calcite	-20.75	-1.03	11.3	0.30	82.62	3.36	23.14	-27.06	n.a.	n.a.	n.a.
+26	+26	26.83	diatomite	calcite	-14.95	-2.23	14.1	0.16	85.82	4.35	26.58	-26.88	n.a.	n.a.	n.a.
+25	+25-29	26.81	diatomite	calcite	-17.49	-1.25	2.7	0.12	78.07	2.76	24.91	-26.70	n.a.	n.a.	n.a.
+18	+15-19	25.56	diatomite	calcite	-17.00	-2.34	3.0	0.07	91.72	4.45	25.59	-27.02	26.30	17.28	250
+16	+16a_1	25.54	diatomite	calcite	-18.63	-2.03	3.6	0.08	88.59	4.43	26.11	-26.92	23.26	21.39	460
+16	+16a_2	25.54	diatomite/ash layer	calcite	-19.04	-2.31	2.9	0.56	39.25	0.13	5.70	n.a.	n.a.	n.a.	n.a.
+16	+15/16	25.00	diatomite	calcite	-19.62	-2.56	2.0	0.23	84.20	2.05	20.39	-27.05	n.a.	n.a.	n.a.
+15	+15a	24.47	diatomite	calcite	-18.17	-2.11	3.0	0.07	87.85	3.60	19.81	-27.16	17.10	17.66	379
+15	+15d	24.47	diatomite	calcite	-19.04	-2.46	12.4	0.04	85.93	2.46	25.89	-27.10	n.a.	n.a.	n.a.
+14	+14a	24.41	diatomite/ash layer	calcite	-16.82	-2.22	3.5	0.22	59.03	0.36	15.51	-25.91	n.a.	n.a.	n.a.
+10	+10b	23.47	diatomite	calcite	-23.55	-2.18	3.0	0.03	82.93	1.42	18.21	-26.23	32.86	19.04	752
+9	+9a	22.92	diatomite	calcite	-21.90	-1.75	3.8	0.01	80.20	0.56	14.84	-26.43	n.a.	n.a.	n.a.
+9	+9b_1	22.92	diatomite	calcite	-18.16	-1.92	3.3	0.01	79.98	0.81	20.19	n.a.	29.50	n.a.	400
+9	+9b_2	22.92	diatomite/ash layer	calcite	-22.51	-2.14	3.0	0.65	48.93	0.15	6.11	-26.59	n.a.	n.a.	n.a.
+3	+3/4	22.33	diatomite	calcite	-18.85	-1.86	3.2	0.02	85.09	1.27	15.58	-26.29	23.83	12.95	238
-11	-11a_1	16.87	diatomite	calcite	-16.77	-2.49	11.3	0.53	86.23	2.36	18.09	-26.77	n.a.	n.a.	n.a.
-11	-11a_2	16.87	diatomite	calcite	-16.60	-2.50	11.8	0.15	85.99	2.28	19.10	-26.94	n.a.	n.a.	n.a.
-11	-11b_1	15.98	diatomite	calcite	-17.14	-2.30	8.4	0.26	85.52	2.26	19.85	-26.71	n.a.	n.a.	n.a.
-11	-11b_2	15.98	diatomite	calcite	-14.81	-3.11	11.0	0.19	88.03	3.49	18.49	-26.55	n.a.	n.a.	n.a.
-13	-13a	15.23	diatomite	calcite	-8.95	-0.73	2.8	0.97	76.17	2.51	20.58	-26.82	n.a.	n.a.	n.a.
-13	-13b	12.51	diatomite	calcite	-9.15	-0.88	16.7	1.22	72.48	2.57	21.29	-26.99	n.a.	n.a.	n.a.
-17	-17a	7.20	diatomite	calcite	-5.69	-2.29	13.8	0.21	72.44	1.77	26.05	-26.58	12.50	8.08	434
-17	-17b	6.80	diatomite	dolomite	6.95	1.09	47.7	0.23	89.58	3.12	40.82	-27.41	n.a.	n.a.	23
-20	-20	5.96	diatomite	ankerite	5.89	-0.39	46.3	0.13	80.08	1.02	107.61	-26.96	n.a.	n.a.	n.a.
-24	-24-28	4.00	diatomite / ash layer	calcite	-16.93	-2.30	15.0	1.09	73.88	2.10	23.20	-30.01	-5.60	2.88	297
-26	-20-30	3.58	diatomite	apatite	n.a.	n.a.	n.a.	0.74	5.52	0.90	24.41	-26.41	n.a.	n.a.	n.a.
-33	-33	0.77	diatomite	calcite	-18.54	-2.45	15.3	0.22	47.37	0.04	0.40	n.a.	n.a.	n.a.	239
-34	-34	0.00	clay	clay	n.a.	n.a.	n.a.	2.72	0.00	2.18	25.14	-30.97	n.a.	n.a.	n.a.

Tab. 15: Mineralogical composition of carbonate concretions.

Ash layer	Sample ID	Profile height (m)	Type	Cement type	Mineral 1	Mineral 2	Mineral 3	Mineral 4
+135	+135a	45.29	diatomite	calcite	Calcite, magnesian	-	-	-
+135	+135b	45.29	diatomite	calcite	Calcite, magnesian	-	-	-
+130	+130a	44.24	diatomite	calcite	Calcite, magnesian	Calcite, magnesian	-	-
+130	+130b	44.24	diatomite/ash layer	calcite	Calcite	Anorthite	Marcasite	-
+129	+129/130	44.03	diatomite/ash layer	calcite	Calcite	Albite	Pyrite	Magnetite
+102	+102a	39.46	diatomite	calcite	Magnesium calcite	-	-	-
+102	+102b	39.46	diatomite/ash layer	calcite	Magnesium calcite	Albite	-	-
+90	+90	37.44	diatomite	calcite	Magnesium calcite	-	-	-
+62	+62a	33.12	diatomite	calcite	Magnesium calcite	-	-	-
+62	+62b_1	33.02	diatomite	calcite	Magnesium calcite	Pyrite	-	-
+62	+62b_2	33.02	diatomite	calcite	Magnesium calcite	Albite	-	-
+62	+62c_1	33.02	diatomite/ash layer	calcite	Magnesium calcite	Magnetite	Anorthite sodian	-
+62	+62c_2	33.02	diatomite	calcite	Magnesium calcite	-	-	-
+62	+62c_3	33.02	diatomite	calcite	Magnesium calcite	Albite	-	-
+31	+31a	27.23	diatomite	calcite	Calcite	-	-	-
+31	+31b	27.23	diatomite/ash layer	calcite	Magnesium calcite	Pyrite	-	-
+30	+30a	27.07	diatomite	calcite	Calcite magnesian	Anorthite	-	-
+30	+30b	27.07	diatomite/ash layer	calcite	Calcite, magnesian	Pyrite	-	-
+28	+28	26.91	diatomite	calcite	Magnesium calcite	Albite	-	-
+26	+26	26.83	diatomite	calcite	Calcite, magnesian	Magnesium calcite	-	-
+25	+25+29	26.81	diatomite	calcite	Calcite	Pyrite	-	-
+18	+15+19	25.56	diatomite	calcite	Calcite	-	-	-
+16	+16a_1	25.54	diatomite	calcite	Magnesium calcite	-	-	-
+16	+16a_2	25.54	diatomite/ash layer	calcite	Magnesium calcite	Titanomagnetite	Anorthite	-
+16	+15/16	25.00	diatomite	calcite	Calcite, magnesian	Calcium carbonate	-	-
+15	+15a	24.47	diatomite	calcite	Calcite	-	-	-
+15	+15d	24.47	diatomite	calcite	Calcite, magnesian	-	-	-
+14	+14a	24.41	diatomite/ash layer	calcite	Calcite	Albite	-	-
+10	+10b	23.47	diatomite	calcite	Calcite	-	-	-
+9	+9a	22.92	diatomite	calcite	Calcite	-	-	-
+9	+9b_1	22.92	diatomite	calcite	Calcite	-	-	-
+9	+9b_2	22.92	diatomite	calcite	Magnesium calcite	-	-	-
+3	+3/4	22.33	diatomite/ash layer	calcite	Calcite	Albite	Magnetite	-
-11	-11a_1	16.87	diatomite	calcite	Calcite	Pyrite	-	-
-11	-11a_2	16.87	diatomite	calcite	Calcite, magnesian	-	-	-
-11	-11b_1	15.98	diatomite	calcite	Calcite, magnesian	Pyrite	-	-
-11	-11b_2	15.98	diatomite	calcite	Magnesium calcite	-	-	-
-13	-13a	15.23	diatomite	calcite	Calcite, magnesian	Pyrite	-	-
-13	-13b	12.51	diatomite	calcite	Magnesium calcite	Calcite, magnesian	-	-
-17	-17a	7.20	diatomite	calcite	Calcite, magnesian	Pyrite	Anorthite	-
-17	-17b	6.80	diatomite	dolomite	Magnesium calcite	Pyrite	Magnetite	-
-20	-20	5.96	diatomite	ankerite	Dolomite	-	-	-
-24	-24+28	4.00	diatomite/ash layer	calcite	Ankerite	Pyrite	Natrophosphate	-
-26	-20-30	3.58	diatomite	apatite	Calcite, magnesian	-	-	-
-33	-33	0.77	diatomite	calcite	Hydroxylapatite	-	-	-
-34	-34	0.00	clay	clay	Calcite, magnesian	Pyrite, Illite	Montmorillonite	Spinel group

Carbonate content (CaCO₃) and total sulphur (TS)

The carbonate content of the carbonate concretions ranges between 47.4 and 91.7 wt% (average 81.0 wt%), while the bulk samples containing volcanic ash layers depict much smaller values of 32.6 to 59.0 wt% and a mean value of 44.8 wt%. The ankerite and the dolomite concretions exhibit a carbonate content (CaCO₃) similar to other carbonate concretions with values of 89.6 and 80.1 wt%, respectively. The hydroxylapatite concretion between ash layers -30 and -20 depicts a CaCO₃ concretion of 5.5 wt% and the clayey concretion of ash layer -34 the lowest CaCO₃ concentration, namely 0 wt% (Tab. 14). The diatomite samples display an average CaCO₃ concentration of 0.9 wt% with a maximum of 1.6 wt% (Tab. 16).

The carbonate concretions display an average total sulphur (TS) content of 0.2 wt% with a maximum of 1.2 wt%, while the TS is higher in the bulk samples of the carbonate concretions exhibiting volcanic ash layers with an average of 0.7 wt% and a maximum of 2.0 wt%. The dolomite, ankerite, and hydrophosphate samples depict TS values between 0.1 and 0.7 wt%. In contrast, the bulk powder sample of ash layer -34, a clayey concretion, displays the highest TS concentration (2.7 wt%) of all concretions. The diatomite samples show highly variable TS values between 0.0 and 9.0 wt% with a mean of 1.1 wt% and, thus, bear more sulphur than the carbonate concretions.

Tab. 16: TS, CaCO₃, C_{org}, δ¹³C_{org}, and C/N values of diatomite samples.

Ash layer	Sample ID	Profile height (m)	TS (wt.%)	CaCO ₃ (wt.%)	C _{org} (wt.%)	C/N	δ ¹³ C _{org} (‰V-PDB)
+135	Si+135_6	45.31	0.02	1.29	n.a.	n.a.	n.a.
+135	Si+135_1	45.29	0.15	0.03	1.18	17.48	n.a.
+123	Si+123_1	42.77	0.19	0.76	0.90	15.14	-26.70
+118	Kn2+118_1	41.38	0.01	0.34	0.56	12.37	n.a.
+114	Kn2+114_1	40.89	0.03	0.01	0.52	14.76	n.a.
+110	Kn2+110_1	40.44	8.95	0.03	5.28	21.99	-27.78
+95	Kn+95_1	38.54	2.15	1.32	0.79	17.15	n.a.
+87	Kn+87_2	36.34	1.65	0.03	0.86	16.40	n.a.
+83	Kn+83_1	36.02	2.03	1.53	1.32	18.34	-26.19
+79	Kn+79_1	35.35	1.10	1.32	0.77	15.45	n.a.
+75	Kn+75_1	35.03	2.31	1.56	0.78	12.93	-26.30
+66	Kn+66_1	33.98	2.45	0.04	1.09	17.97	n.a.
+55	Kn+55_1	31.31	0.03	1.24	0.58	11.01	n.a.
+52	Kn+52_1	30.97	0.19	1.39	1.05	15.10	n.a.
+46	Kn+46_1	29.99	0.07	1.48	0.55	11.67	-26.20
+42	Kn+42_1	28.08	0.02	1.32	0.24	6.85	n.a.
+35	Kn+35_1	27.41	0.10	1.32	0.57	13.95	-26.74
+5	Kn+5_1	22.60	0.09	1.25	0.96	15.83	n.a.
-10	Kn-10_7	22.03	0.16	1.28	0.86	13.36	-26.43
-10	Kn-10_4	17.11	0.09	0.03	0.69	11.51	n.a.
-15	St-15_1	11.69	0.04	0.01	0.88	14.07	n.a.
-18	St 1 m u.-17	6.80	0.28	0.95	1.66	20.82	n.a.
-33	St 0.5m o. -33	0.77	0.24	0.50	2.23	22.37	-31.02
-34	St zw. -33-34	0.02	1.32	1.44	4.00	27.88	-31.11
-35	St 0.2 m u.-34	0.00	2.55	1.39	3.39	26.16	-31.13

Carbon and oxygen isotopes (δ¹³C_{carb} and δ¹⁸O_{carb})

The δ¹³C_{carb} values of the bulk calcitic carbonate concretions range between -24.1 and -5.7‰ V-PDB and have an average value of -18.9‰. Calcitic cemented volcanic ash layers within the concretions depict a mean of -19.9‰. The calcite cements of the volcanic ash layers lie in an array of -22.7 to -11.5‰. The carbonate concretions of the lower Knudeklint Member below ash layer -11 exhibit more ¹³C enriched values between -17.1 to -5.7‰. The dolomite sample (-17b) of ash layer -17 displays the heaviest δ¹³C value of +7.0‰ and the ankerite sample of ash layer -20 has a δ¹³C_{carb} value of +5.9‰ (Tab. 14). The oxygen isotope values (δ¹⁸O_{carb}) of the carbonate concretions lie between -3.1 and -0.5‰ with an average of -2.0‰. The δ¹⁸O values of the volcanic ash bearing carbonate concretion samples are slightly enriched in ¹⁸O with δ¹⁸O values ranging from -2.3 to -0.2‰ V-PDB around a mean

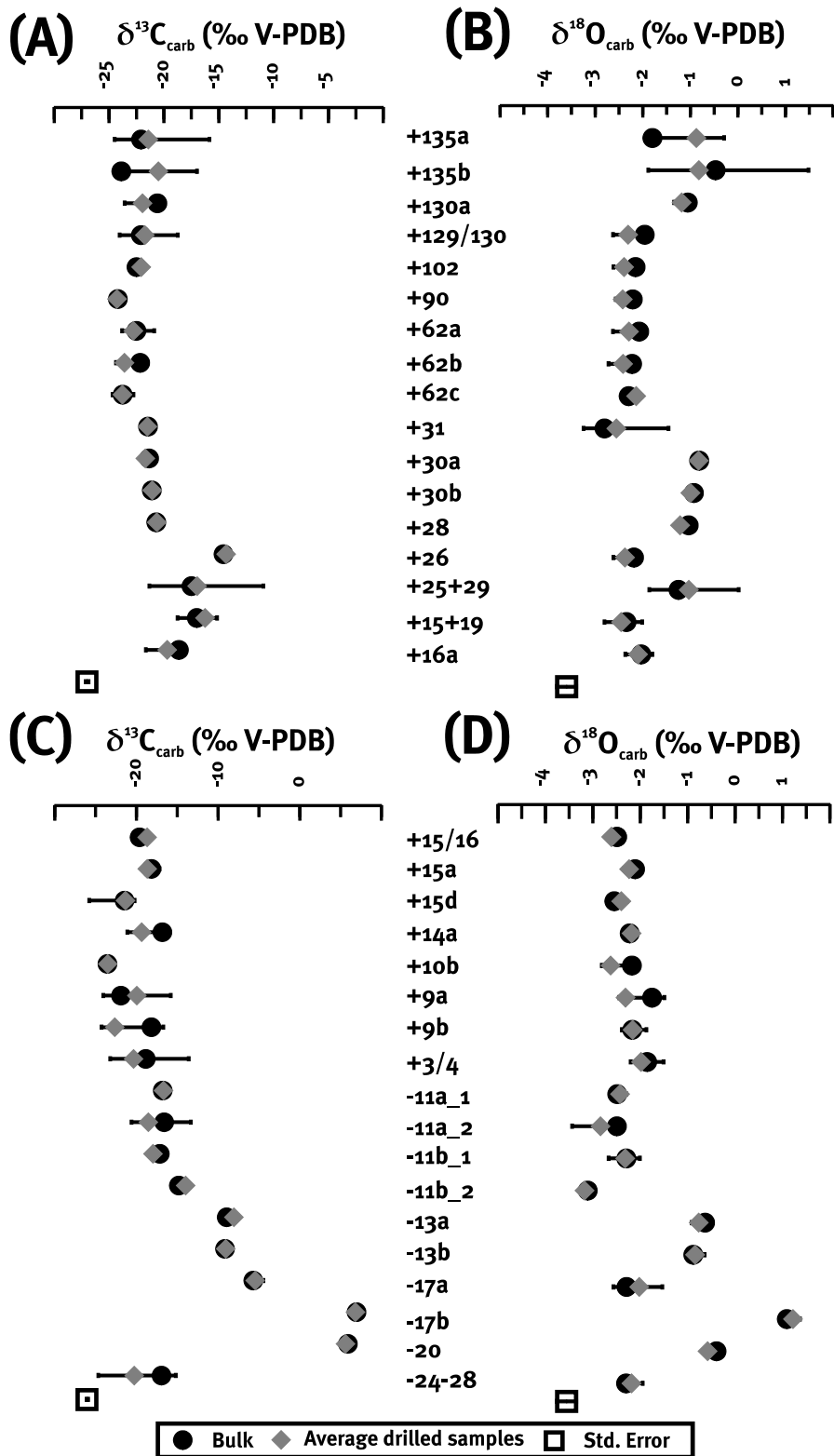


Fig. 21: (A) $\delta^{13}\text{C}_{\text{carb}}$ values of the drilled samples of carbonate concretions in comparison to the bulk values. (B) $\delta^{18}\text{O}_{\text{carb}}$ values in the same arrangement as in (A). (C) $\delta^{13}\text{C}_{\text{carb}}$ values of the drilled samples of carbonate concretions in comparison to the bulk values (continuation of (A)). (D) $\delta^{18}\text{O}_{\text{carb}}$ values in the same arrangement as in (C) (continuation of (B)).

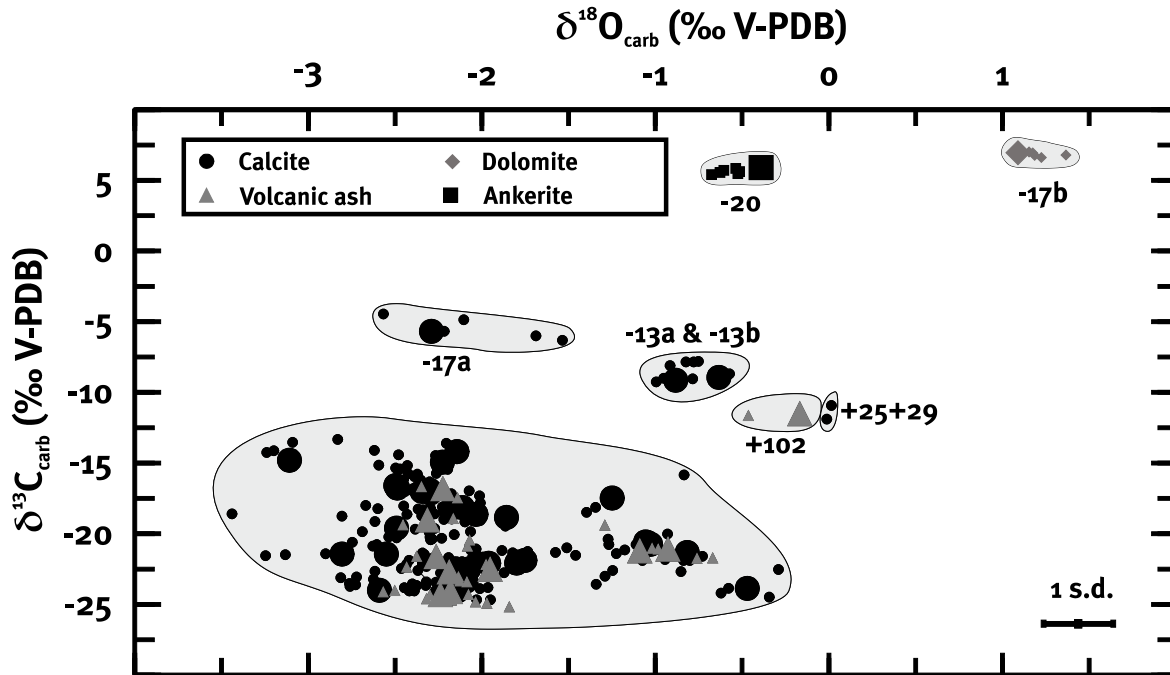


Fig. 22: Plot of $\delta^{13}\text{C}_{\text{carb}}$ values versus $\delta^{18}\text{O}_{\text{carb}}$ values of all carbonate concretions. The bulk $\delta^{13}\text{C}$ and $\delta^{18}\text{O}$ values of most of the carbonate concretions are displayed in the shaded area in the lower left corner. Solely the $\delta^{13}\text{C}$ and $\delta^{18}\text{O}$ values of concretions -20, -17b, -17a, -13b, -13a, +25+29, and +102 are not this area. Big symbols represent bulk analyses, while small symbols depict the values of drilled samples.

value of -1.7‰ . No stratigraphic trend is discernible across the profile in the oxygen isotope data when compared with the carbon isotope data. The ankerite concretion depicts a $\delta^{18}\text{O}$ value of -0.4‰ , whereas the heaviest oxygen isotopic composition was measured for the dolomite concretion of ash layer -17 at $+1.1\text{‰}$.

Based on microdrilled samples, some concretions exhibit a wide range of individual carbon and oxygen values, in particular, the concretions of ash layers -28-24, -17a, -11a, +3/4, +9b, +9a, +15d, +25+29, +31, +130, and +135 with variations of up to 10‰ and 3.5‰ V-PDB for $\delta^{13}\text{C}$ and $\delta^{18}\text{O}$, respectively (Fig. 21). Yet, most concretions display carbon and oxygen values that are rather homogenous. Moreover, in most samples the bulk powder values agree well with the average values of the individual samples drilled.

Most drilled samples of the carbonate concretions show $\delta^{18}\text{O}_{\text{carb}}$ values between -3.5 and -0.5‰ and $\delta^{13}\text{C}_{\text{carb}}$ values between -27 to -12‰ (Fig. 22). The concretion of ash layer +102 displays ^{13}C and ^{18}O enriched material. The concretion -17a of ash layer -17 bears higher $\delta^{13}\text{C}$ values than the other concretions. Both concretions of ash layer -13 have $\delta^{13}\text{C}$ values of -10 to -5‰ and lie between concretion -17a and the other concretions. The most remarkable difference in $\delta^{13}\text{C}$ and $\delta^{18}\text{O}$ isotopic composition is recorded for the dolomite and ankerite concretions.

Total organic carbon, carbon/nitrogen ratio, and organic carbon isotopic composition (TOC, C/N ratio, and $\delta^{13}\text{C}_{\text{org}}$)

The carbonate concretions show total organic carbon concentrations (TOC) ranging from 0.0 to 5.5 wt% with an average of 2.3 wt%, while the volcanic ash samples within the carbonate concretions yield lower TOC values between 0 and 0.5 wt% (average of 0.2 wt%). Other concretions, namely dolomite (sample -17b) and ankerite (sample -20) cement, fall into the same range of the TOC concentration (Tab. 14). The diatomite samples display TOC values of 0.2 to 5.3 wt% around an average of 1.3 wt% and, thus, plot in the same range as the carbonate concretions.

The C/N ratios of all calcitic bound carbonate concretions, including the bulk sample powders with volcanic ash particles, range between 0.4 and 29.4 (Fig. 23). The concretions of ash layer -34 and the one between ash layers -28 and -24 hold C/N values of ca. 25, while the dolomite (sample -17b) and the ankerite (sample -20) concretions have strongly N depleted C/N ratios with 40.8 and 107.6, respectively. The diatomite samples illustrate C/N ratios between 6.9 and 27.9 with a mean value of 16.3 (Tab. 16).

All organic carbon isotope data ($\delta^{13}\text{C}_{\text{org}}$) fall into a range between -31.0 and -25.9‰ V-PDB (Fig. 23). The average value of $\delta^{13}\text{C}_{\text{org}}$ is -26.9‰. The lightest ^{13}C depleted value was found in the lowermost sample within the clayey concretion of ash layer -34 with -31.0‰. The diatomite samples display $\delta^{13}\text{C}_{\text{org}}$ isotopic compositions with a maximum of -26.2 and a minimum of -31.1‰ (average: -28.0‰). The lightest outstanding data are measured in the lowermost part of the profile for diatomite samples and the clayey concretion of ash layer -34.

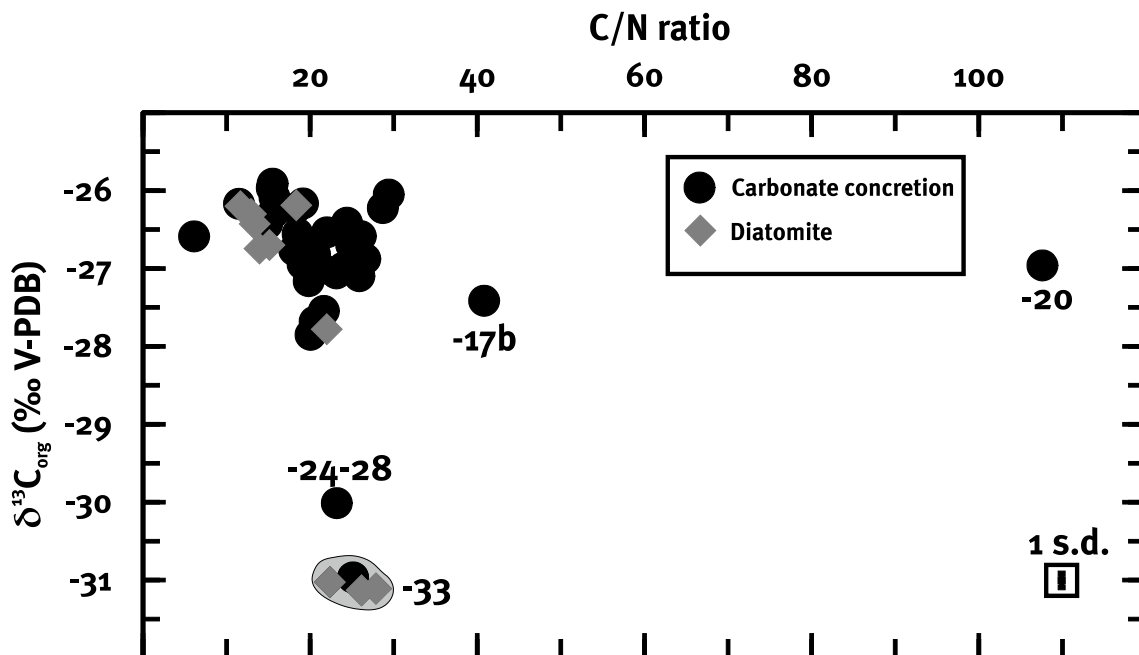


Fig. 23: Plot of $\delta^{13}\text{C}_{\text{org}}$ value versus C/N ratio of the carbonate concretions and the diatomite. All distant data points are labelled.

Sulphur and oxygen isotopes of carbonate-associated sulphate ($\delta^{34}\text{S}_{\text{CAS}}$ and $\delta^{18}\text{O}_{\text{CAS}}$)

CAS in 13 carbonate concretions exhibits a concentration between 3 and 1159 ppm with an average of 441 ppm (Tab. 14). The highest CAS concentration occurs in the concretion of ash layer +130. The dolomite concretion -17b of ash layer -17 bears a low CAS concentration of 23 ppm (Tab. 14). The lowest CAS concentration was identified for the calcite concretion of +62c of ash layer +62 with 3 ppm. This value is very low and is treated like an offset value.

The values of the stable sulphur isotopic composition ($\delta^{34}\text{S}_{\text{CAS}}$) fall into an array between -5.6 and +32.9‰ V-CDT with a mean value of +21.0‰ (Fig. 24). Nearly all $\delta^{34}\text{S}_{\text{CAS}}$ values are in a range between +17 and +33‰. The carbonate concretion found between ash layers -28 and -24 shows the lightest $\delta^{34}\text{S}_{\text{CAS}}$ value of -5.6‰.

The $\delta^{18}\text{O}_{\text{CAS}}$ values range between +2.9 and +22.4‰ V-SMOW with an average of +14.6‰ (Fig. 24). The lightest value was measured for the carbonate concretion between ash layers -28 and -24 and another comparably low value of +8.1‰ was measured for another sample of the Knudeklint Member (-17a). Thus, a trend to heavier $\delta^{18}\text{O}_{\text{CAS}}$ values towards the higher horizons of the Fur Formation is apparent. The Silstrup Member exhibits a mean $\delta^{18}\text{O}_{\text{CAS}}$ value of +16.8‰.

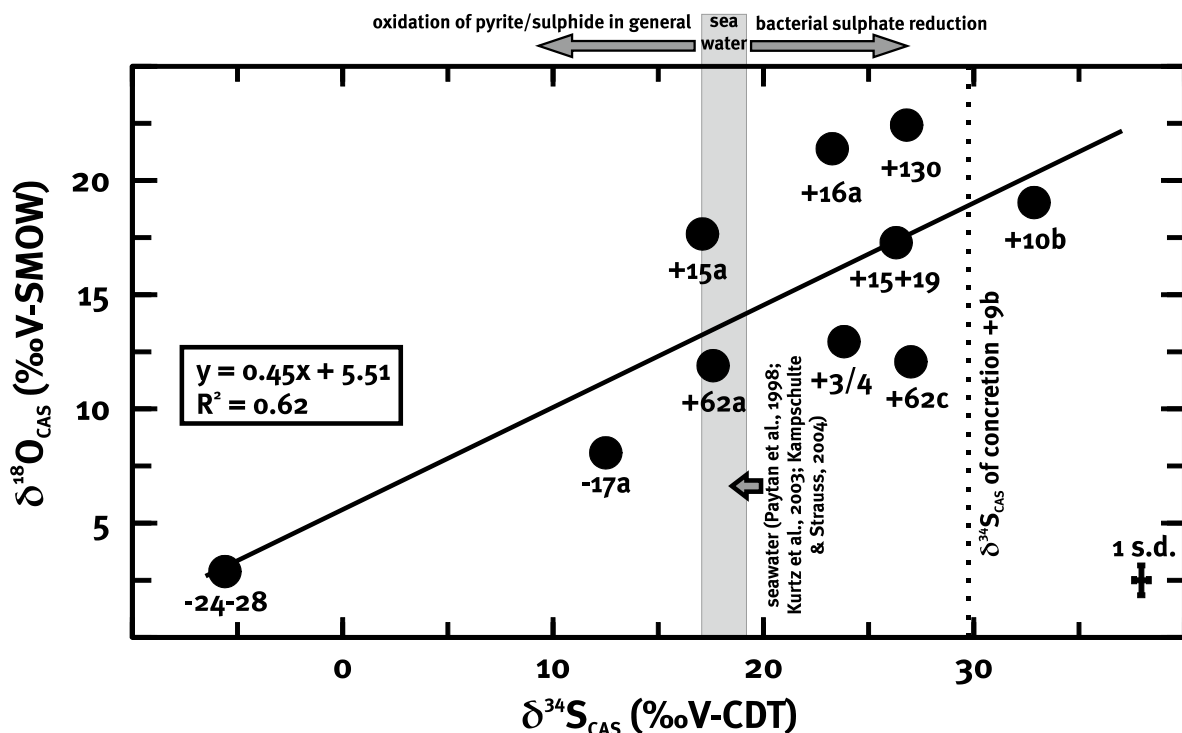


Fig. 24: Plot of $\delta^{18}\text{O}_{\text{CAS}}$ versus $\delta^{34}\text{S}_{\text{CAS}}$ isotopic composition of the carbonate concretions. The Early Eocene seawater $\delta^{34}\text{S}_{\text{CAS}}$ composition of several authors is given as a shaded array.

Strontium geochemistry ($^{87}\text{Sr}/^{86}\text{Sr}$)

The $^{87}\text{Sr}/^{86}\text{Sr}$ values of calcitic carbonate concretions yield values between 0.70772 and 0.70784 with a mean of 0.70775 (Tab. 17). A decrease in $^{87}\text{Sr}/^{86}\text{Sr}$ can be identified towards the top of the Fur Formation. The highest values are found within the Knudeklint Member, while the $^{87}\text{Sr}/^{86}\text{Sr}$ values keep decreasing over the whole Silstrup Member. With 0.70839, the highest $^{87}\text{Sr}/^{86}\text{Sr}$ value was determined for the dolomite concretion -17b of ash layer -17.

Tab. 17: $^{87}\text{Sr}/^{86}\text{Sr}$ ratios of selected carbonate concretions.

Ash layer	Sample ID	Profile height (m)	Type	$^{87}\text{Sr}/^{86}\text{Sr}$
+135	+135a	45.29	diatomite	0.70773
+130	+130b	44.24	diatomite/ash layer	0.70772
+62	+62a	33.12	diatomite	0.70772
+62	+62b	33.02	diatomite	0.70772
+62	+62c	33.02	diatomite	0.70776
+26	+26	26.83	diatomite	0.70775
+18	+15+19	25.56	diatomite	0.70773
+16	+16a	25.54	diatomite	0.70774
+15	+15a	24.47	diatomite	0.70774
+10	+10b	23.47	diatomite	0.70774
+9	+9b	22.92	diatomite	0.70775
+3	+3/4	22.33	diatomite	0.70775
-17	-17a	7.20	diatomite	0.70784
-17	-17b	6.80	diatomite	0.70839
-24	-24-28	4.00	diatomite/ash layer	0.70780
-33	-33	0.77	diatomite	0.70778

Biomarker analyses and compound specific $\delta^{13}\text{C}$ values

Biomarker results of glendonite (n=2), carbonate concretions (n=3), and diatomite (n=2) are described below. The results for glendonite are added in this chapter, because the content of biomarker determined within glendonite was very poor.

Hydrocarbons:

Whereas both glendonites (named “+15aG” and “+10bG” in figure 25) contain only minor amounts of n-alkanes, the concretions contain a lot of them with long-chains more prominent, especially in concretion -17b of ash layer -17 and in +135a of ash layer +135.

In concretion +135a, two hopanes, namely hop-17(21)-ene are identified. Except for n-alkanes, no other compounds of hydrocarbons are preserved.

The diatomite of ash layer +135 depicts the same signature as the corresponding carbonate concretion. Solely the hopanes and hopenes are missing. In the diatomite sample of Ra-11 at ash layer -11 (Fig. 25), the signals are very low and an unresolved complex mixture (UCM) is detected at the beginning of the diagram. This is also documented for concretion -17b.

Fatty acids:

In both glendonite samples, short-chain fatty acids are the most abundant compounds (Fig. 25). Furthermore, hexadecanoic acid and octadecanoic acid are accompanied by unsaturated fatty acids. The glendonite also contains some iso- and anteiso-fatty acids. However, the contents within the glendonite are very low.

All concretions contain short-chain fatty acids with the highest concentrations of all, but all of them also contain mid-chain to long-chain fatty acids. Especially, the concretions -17b of ash layer -17 and +135a of ash layer +135 show high contents of fatty acids with 24 to 30 carbon atoms. Iso- and anteiso-fatty acids are found, but only in trace amounts. Furthermore, all concretions contain some contents of hopanoic acids with 31, 32, and 33 carbon atoms. Concretion -17b also depicts biphytanic diacid, an isoprenoid with 40 carbon atoms, in reasonable amounts.

The concentrations of fatty acids within the diatomite are less than in the carbonate concretion. The compounds are the same as in the glendonite and in the concretions. The even numbered C-chains within the concretions are higher than the uneven chains, which cannot be seen within the diatomite pointing to a higher level of biological degradation within the diatomite.

Alcohols:

The compounds of the alcohol fraction in both glendonite samples are very low (Fig. 25). The only compounds identified are unspecific n-alcohols and some dialcohols. Moreover, cholesterol is present. In glendonite +15a of ash layer +15, unsaturated alcohols and some branched alcohols (iso) are found, but they are most likely from secondary sources (Daniel Birgel, pers. comm.).

As for the other fractions, the concretions show many more compounds and their concentrations are much higher. All concretions contain n-alcohols maximizing with longer chains. Furthermore, sterols, especially brassicasterol and dinosterol, are detected within the concretions. Biphytanediols (black triangles, Fig. 25) are likewise found in the concretions as well as biphytanes, archaeal diethers, and monoethers. Smaller amounts of archaeol (isoprenoidal diether) are given in the concretions -17b and +135a. The monoethers are only present in concretion -17b. Hopanoids are only found in concretions -17b and +135a. AnhydroBHT, a degradation product of BHT, an unspecific hopanoid, is only present in concretion -17b. Apart from hopanoids, until today not further assigned macrocyclic diether lipids (see Blumenberg et al., 2007; Baudrand et al., 2010) are also present, as well as dialkyl glycerol diethers (DAGEs; only in concretion +135a).

The alcohol fractions of diatomite are variable. The compounds of the +135 diatomite are similar to those of the concretion +135a, but the concentrations are much lower in the

diatomite than in the concretion. There are also sterols, di-alcohols, and biphytane diols in the diatomite.

Compound specific carbon isotopes ($\delta^{13}\text{C}$)

The compound of hexadecanoic acid depicts $\delta^{13}\text{C}$ values between -30 and -26‰ V-PDB for glendonite and carbonate concretion samples, while the octadecanoic acid data are slightly ^{13}C enriched in each sample (-29 to -25‰) (Tab. 18). Hexacosanoic acid and bishomohopanoic acid in the concretions +135a of ash layer +135 and -17b of ash layer -17 show $\delta^{13}\text{C}$ values of ca. -30.5‰. In the same concretions, archaeol is found and yields -34 and -33‰ for the $\delta^{13}\text{C}$ composition of +135a and -17b, respectively. Monoether compounds of concretion -17b demonstrate a $\delta^{13}\text{C}$ value of -33‰. Biphytanedliols are identified in all concretions and their corresponding $\delta^{13}\text{C}$ values fall into a range between -23 and -21‰. The compound of monocyclic biphytanedliols of concretion +135a is ^{13}C depleted with a value of -28‰. Tricyclic biphytanedliols yield $\delta^{13}\text{C}$ values between -23 and -21‰ for all carbonate concretions.

Tab. 18: Biomarker compounds and their corresponding $\delta^{13}\text{C}$ values. The abbreviation “tr” stands for traces that were identified, but not quantified.

Compound	Correction	+135a	+15aC	+15aG	+10bG	-17b
Hexadecanoic acid (‰)	MeOH-corrected	-30.11	-26.18	-27.56	-27.88	-28.78
Octadecanoic acid (‰)	MeOH-corrected	-29.16	-26.94	-24.72	-28.73	-29.37
Hexacosanoic acid (‰)	MeOH-corrected	-31.04	tr	tr	tr	-30.52
Bishomohopanoic acid (‰)	MeOH-corrected	-30.41	tr	n.a.	n.a.	-29.64
Bishomohopanol (‰)	TMS-corrected	tr	n.a.	n.a.	n.a.	-32.87
Archaeol (‰)	TMS-corrected	-34.22	n.a.	n.a.	n.a.	-32.81
sn2-ph-monoether (‰)	TMS-corrected	n.a.	n.a.	n.a.	n.a.	-33.04
sn3-ph-monoether (‰)	TMS-corrected	n.a.	n.a.	n.a.	n.a.	-33.36
Acyclic biphytanedliol (‰)	TMS-corrected	-21.89	-22.29	n.a.	n.a.	-21.43
Monocyclic biphytanedliol (‰)	TMS-corrected	-28.34	tr	n.a.	n.a.	tr
Bicyclic biphytanedliol (‰)	TMS-corrected	-23.16	tr	n.a.	n.a.	-21.78
Tricyclic biphytanedliol (‰)	TMS-corrected	-20.90	-22.28	n.a.	n.a.	-23.05
C ₃₀ -DAGE (‰)	TMS-corrected	-39.16	n.a.	n.a.	n.a.	n.a.
MDGD (‰)	TMS-corrected	n.a.	n.a.	n.a.	n.a.	-33.33

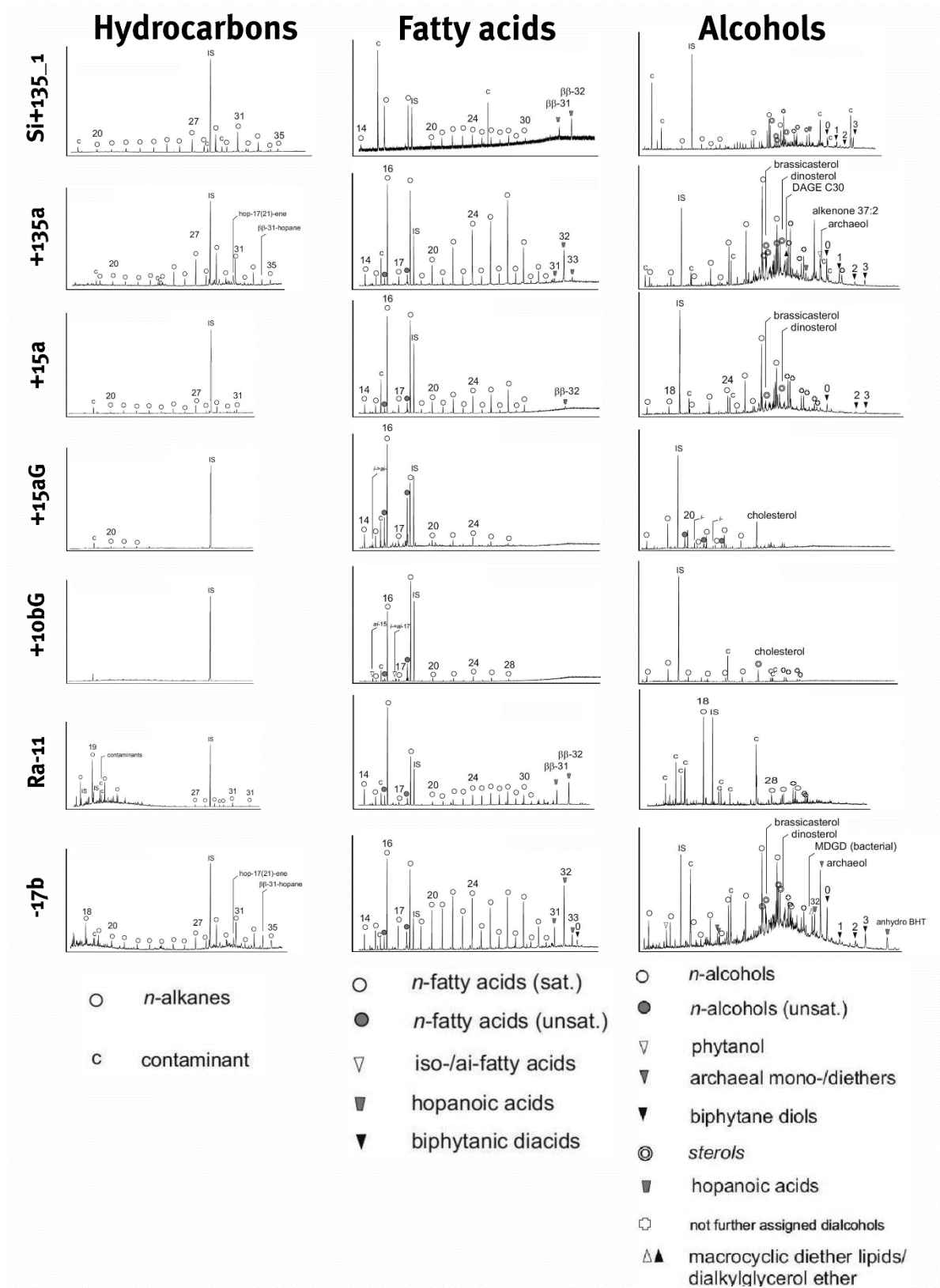


Fig. 25: Biomarker data of carbonate concretions (-17b, +15a, and +135a), glendonite (+10bG, +15aG), and diatomite (Ra-11, Si+135_1) are displayed this diagram. The individual fractions are listed in columns.

4.3 Paleotemperatures

Three different paleotemperature proxies were measured to assess the prevailing temperatures in the bottom water and in the sedimentary column during the deposition and the early diagenesis of the sediments of the Early Eocene Fur Formation. Initially, the clumped isotopes (Δ_{47}) of replacive calcite from glendonite samples were analysed to determine the temperature of the ikaite to glendonite transformation.

Resulting temperature values were applied to calculate the Eocene $\delta^{18}\text{O}$ bottom/pore water ($\delta^{18}\text{O}_{\text{H}_2\text{O}}$) after Kim and O'Neil (1997). This $\delta^{18}\text{O}_{\text{H}_2\text{O}}$ value of -4.5‰ calculated for the Early Eocene bottom and pore water was used for the calculation of the paleotemperatures of all carbonates based $\delta^{18}\text{O}_{\text{carb}}$ data. Furthermore, the paleotemperatures for all carbonate samples were calculated by applying a $\delta^{18}\text{O}_{\text{H}_2\text{O}}$ value of -1‰ V-SMOW for the ice-free Early Eocene.

These paleotemperature values were compared with paleotemperatures obtained by oxygen isotope measurements on the SiO_2 of pure diatom samples ($\delta^{18}\text{O}_{\text{diatom}}$). Again, the calculated $\delta^{18}\text{O}_{\text{H}_2\text{O}}$ value of -4.5‰ V-SMOW was inserted into an equation for the paleotemperature reconstruction.

4.3.1 Paleotemperatures indicated by the clumped isotope measurements (Δ_{47}) of glendonite

Three samples were analysed for their clumped isotope values in this study: the whitish replacive calcite (rCc) of the Simeulue Seep off Sumatra and of the rCc of ash layer +16 and of ash layer +62 of the Fur Formation.

Based on Wacker et al. (2014) (equation 1) and Δ_{47} data from this study (Tab. 19), paleotemperatures were calculated according to:

$$\Delta_{47} = 0.0327 (\pm 0.026) * 10^6 * T^{-2} + 0.3030 (\pm 0.0308) \quad (1)$$

Respective paleotemperatures range between -3 and +17 °C (n=4) around an average of +6 °C for the rCc of ash layer +16 and between 0 and +9 °C with an average of +5 °C (n=4) for the rCc of ash layer +62. In contrast, the Sumatra rCc yields temperature values between +2 and +26 °C with an average of +13 °C (n=6; Fig. 26). When looking at the $\delta^{13}\text{C}_{\text{carb}}$ and $\delta^{18}\text{O}_{\text{carb}}$ values of the Sumatra replacive calcite (Tab. 19), they are significantly different compared to the replacive calcite of the glendonite of the Fur Formation.

Tab. 19: Clumped isotope values (Δ_{47}) of the rCcs and the calculated paleotemperatures after Wacker et al. (2014).

Ash layer	Sample ID	Location	Date	$\delta^{13}\text{C}$ (V-PDB)	$\delta^{18}\text{O}$ (V-PDB)	Δ_{47}	T (°C)
+16	+16a rCc	Fur Formation	21.10.2016	-23.63	-2.59	0.732	3
+16	+16a rCc	Fur Formation	24.10.2016	-23.62	-2.55	0.752	-3
+16	+16a rCc	Fur Formation	24.11.2016	-23.56	-2.47	0.715	9
+16	+16a rCc	Fur Formation	03.12.2016	-23.39	-2.53	0.691	17
	Average:			-23.55	-2.54	0.722	6
	Std. dev.:			0.11	0.05	0.026	4
	StError:			0.05	0.03	0.013	
+62	+62b rCc	Fur Formation	20.01.2017	-23.89	-2.55	0.732	3
+62	+62b rCc	Fur Formation	27.01.2017	-23.64	-2.54	0.742	0
+62	+62b rCc	Fur Formation	22.02.2017	-24.01	-2.43	0.715	9
+62	+62b rCc	Fur Formation	26.02.2017	-23.89	-2.38	0.717	8
	Average:			-23.86	-2.48	0.727	5
	Std. dev.:			0.16	0.08	0.013	2
	StError:			0.08	0.04	0.006	
-	S0189 13156 342 cm rCc weiß	Simeulue Seep/Sumatra	21.10.2016	-49.64	2.72	0.694	16
-	S0189 13156 342 cm rCc weiß	Simeulue Seep/Sumatra	25.10.2016	-49.38	2.73	0.706	12
-	S0189 13156 342 cm rCc weiß	Simeulue Seep/Sumatra	03.12.2016	-49.54	2.68	0.668	26
-	S0189 13156 342 cm rCc weiß	Simeulue Seep/Sumatra	20.01.2017	-49.30	2.70	0.704	12
-	S0189 13156 342 cm rCc weiß	Simeulue Seep/Sumatra	27.01.2017	-49.53	2.65	0.711	10
-	S0189 13156 342 cm rCc weiß	Simeulue Seep/Sumatra	21.02.2017	-49.46	2.50	0.734	2
	Average:			-49.48	2.66	0.703	13
	Std. dev.:			0.12	0.08	0.022	3
	StError:			0.05	0.03	0.009	

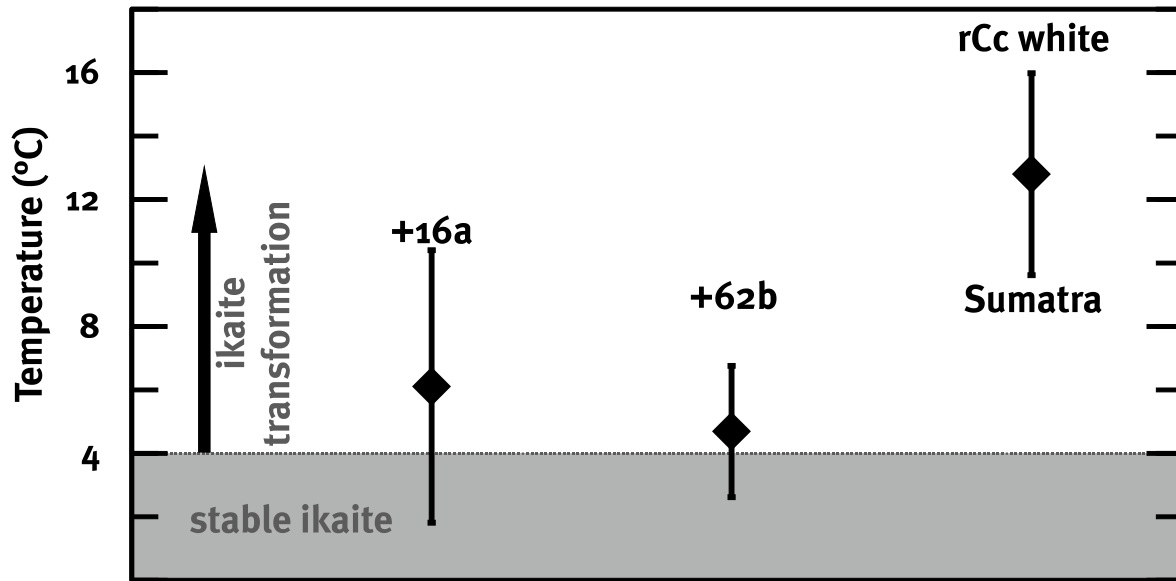


Fig. 26: Clumped isotope temperatures of glendonite rCc. The grey area marks the ikaite stability field after Hu et al. (2014). The black arrow points to the temperatures of ikaite transformation.

4.3.2 Paleotemperatures indicated by $\delta^{18}\text{O}_{\text{carb}}$ of glendonite and carbonate concretions

Several equations have been published for various fractionation factors between calcite and water for selected temperature ranges (Tab. 20). Solving these equations for temperature and estimating the ambient $\delta^{18}\text{O}$ value of the surrounding water allow calculating the paleotemperatures.

Tab. 20: Summary of published equations for calculating paleotemperatures based on $\delta^{18}\text{O}_{\text{carb}}$ analyses.

Author	Year	Material	Equation	Unit	Number
Epstein et al.	1953	Carbonate	$T (^{\circ}\text{C}) = 16.5 - 4.3 * (\delta^{18}\text{O}_{\text{c}} - \delta^{18}\text{O}_{\text{H}_2\text{O}}) + 0.14 * (\delta^{18}\text{O}_{\text{c}} - \delta^{18}\text{O}_{\text{H}_2\text{O}})^2$	$^{\circ}\text{C}$	1
Craig	1965	Carbonate	$T (^{\circ}\text{C}) = 16.9 - 4.2 * (\delta^{18}\text{O}_{\text{c}} - \delta^{18}\text{O}_{\text{H}_2\text{O}}) + 0.13 * (\delta^{18}\text{O}_{\text{c}} - \delta^{18}\text{O}_{\text{H}_2\text{O}})^2$	$^{\circ}\text{C}$	2
O'Neil et al.	1969	Calcite	$1000 \ln \alpha_{\text{calcite-water}} = 2.78 * 10^6 * T^{-2} - 2.89$	K	3
Shackleton & Kennett	1975	Calcite	$T (^{\circ}\text{C}) = 16.9 - 4.28 * (\delta^{18}\text{O}_{\text{c}} - \delta^{18}\text{O}_{\text{H}_2\text{O}}) + 0.10 * (\delta^{18}\text{O}_{\text{c}} - \delta^{18}\text{O}_{\text{H}_2\text{O}})^2$	$^{\circ}\text{C}$	4
Anderson	1983	Carbonate	$T (^{\circ}\text{C}) = 16.0 - 4.14 * (\delta^{18}\text{O}_{\text{c}} - \delta^{18}\text{O}_{\text{H}_2\text{O}}) + 0.13 * (\delta^{18}\text{O}_{\text{c}} - \delta^{18}\text{O}_{\text{H}_2\text{O}})^2$	$^{\circ}\text{C}$	5
Kim & O'Neil	1997	Calcite	$1000 \ln \alpha_{\text{calcite-water}} = 18.03 * 10^3 * T^{-1} - 32.42$	K	6
Leng & Marshall	2004	Carbonate	$T (^{\circ}\text{C}) = 13.8 - 4.58 * (\delta^{18}\text{O}_{\text{c}} - \delta^{18}\text{O}_{\text{H}_2\text{O}}) + 0.08 * (\delta^{18}\text{O}_{\text{c}} - \delta^{18}\text{O}_{\text{H}_2\text{O}})^2$	$^{\circ}\text{C}$	7

In this study, equation 6 (Kim and O'Neil, 1997) was used, as it is most often utilised in recent paleotemperature calculations. First, a $\delta^{18}\text{O}_{\text{H}_2\text{O}}$ value of -1‰ V-SMOW was considered for the ice-free Early Eocene (Tab. 21 and Tab. 22).

The temperature equation of Vasconcelos et al. (2005; equation 2) for the fractionation of dolomite was applied for the dolomite concretion -17b of ash layer -17.

$$1000 \ln \alpha_{\text{dolomite-water}} = (2.73 \times 10^6) T^{-2} + 0.26 \quad (2)$$

Tab. 21: Calculated paleotemperatures of glendonites computed with a $\delta^{18}\text{O}_{\text{H}_2\text{O}}$ value of -1‰ V-SMOW.

Ash layer	Sample ID	Profile height (m)	Type	$\delta^{18}\text{O}_{\text{carb}}$ (‰V-PDB)	T (°C)
+62	+62a	33.12	glendonite bulk	-2.64	21.4
+62	+62b	33.02	glendonite bulk	-2.43	20.4
+62	+62b	33.02	glendonite rCc	-2.18	19.2
+62	+62b	33.02	glendonite ri	-2.16	19.1
+62	+62b	33.02	glendonite c	-1.26	14.9
+62	+62c	33.02	glendonite bulk	-2.47	20.6
+62	+62c dup1	33.02	glendonite bulk	-2.49	20.7
+62	+62c dup2	33.02	glendonite bulk	-2.72	21.7
+62	+62c	33.02	glendonite rCc	-2.28	19.6
+62	+62c	33.02	glendonite ri	-2.41	20.3
+16	+16a	25.54	glendonite bulk	-2.72	21.7
+16	+16a	25.54	glendonite rCc	-2.03	18.5
+16	+16a	25.54	glendonite ri	-2.17	19.1
+16	+16a	25.54	glendonite c	-2.56	21.0
+16	+16b	25.00	glendonite bulk	-2.88	22.5
+16	+16b	25.00	glendonite rCc	-2.24	19.5
+16	+16b	25.00	glendonite c	-1.44	15.7
+15b,c	+15a	24.47	glendonite bulk	-2.84	22.3
+15b,c	+15a	24.47	glendonite rCc	-2.55	21.0
+15b,c	+15a	24.47	glendonite ri	-2.41	20.3
+15b,c	+15a	24.47	glendonite c	-0.93	13.4
+15	+15c	24.47	glendonite bulk	-2.80	22.1
+15	+15c	24.47	glendonite rCc	-2.14	19.0
+15	+15c	24.47	glendonite ri	-2.14	19.0
+15	+15c	24.47	glendonite c	-1.46	15.8
+14	+14b	23.88	glendonite bulk	-2.92	22.8
+10	+10a_1	23.48	glendonite bulk	-2.44	20.4
+10	+10a_2	23.48	glendonite bulk	-2.60	21.2
+10	+10b_1	23.47	glendonite bulk	-2.30	19.7
+10	+10b_2	23.47	glendonite bulk	-2.75	21.9
+10	+10b	23.47	glendonite rCc	-2.24	19.4
+10	+10b	23.47	glendonite ri	-1.92	18.0
+10	+10b	23.47	glendonite c	-0.61	11.9
+9	+9b	22.92	glendonite bulk	-2.42	20.3
+9	+9b	22.92	glendonite rCc	-2.65	21.5
+9	+9b	22.92	glendonite ri	-1.73	17.1
+9	+9b	22.92	glendonite c	-1.59	16.4

The average temperature value of all glendonite measurements (bulk, rCc, ri, and c) (Tab. 21) is +19.4 °C. The bulk glendonite displays an average temperature value of +21.3 °C, the replacive calcite one of +19.7 °C, the rim cement one of +19.0 °C, and the fill cement one of +16.5 °C.

The carbonate concretions cementing solely diatomite display an average paleotemperature value of +18 °C, whereas an average value of +17 °C was calculated for carbonate concretions containing some volcanic ash particles (Tab. 12). Thus, the heavier $\delta^{18}\text{O}$ values of carbonate concretions containing volcanic ash particles yield slightly lower temperatures than pure diatomite carbonate concretions. It should be noted that, for several bulk samples (Fig. 18), ash layers could not be separated from diatomite prior to pulverization.

Tab. 22: Calculated paleotemperatures of carbonate concretions with a $\delta^{18}\text{O}_{\text{H}_2\text{O}}$ of -1‰ V-SMOW. Concretions around glendonites are marked in bold.

Ash layer	Sample ID	Profile height (m)	Type	$\delta^{18}\text{O}_{\text{carb}}$ (‰V-PDB)	T (°C)
+135	+135a	45.29	diatomite	-1.80	17.4
+135	+135b	45.29	diatomite	-0.47	11.3
+130	+130a	44.24	diatomite	-1.13	14.3
+130	+130b	44.24	diatomite/ash layer	-1.86	17.7
+129	+129/130	44.03	diatomite/ash layer	-1.96	18.1
+102	+102a	39.46	diatomite	-2.15	19.1
+102	+102b	39.46	diatomite/ash layer	-0.17	9.9
+90	+90	37.14	diatomite	-2.18	19.2
+62	+62a	33.12	diatomite	-2.07	18.7
+62	+62b_1	33.02	diatomite	-2.26	19.6
+62	+62b_2	33.02	diatomite/ash layer	-2.19	19.2
+62	+62c_1	33.02	diatomite	-2.09	18.8
+62	+62c_2	33.02	diatomite	-2.21	19.3
+62	+62c_3	33.02	diatomite	-2.59	21.1
+31	+31a	27.23	diatomite	-2.80	22.2
+31	+31b	27.23	diatomite/ash layer	-1.09	14.1
+30	+30a	27.07	diatomite	-0.82	12.8
+30	+30b	27.07	diatomite/ash layer	-0.93	13.4
+28	+28	26.91	diatomite	-1.03	13.8
+26	+26	26.83	diatomite	-2.23	19.4
+25	+25-29	26.81	diatomite	-1.25	14.8
+18	+15-19	25.56	diatomite	-2.34	20.0
+16	+16a_1	25.54	diatomite	-2.03	18.5
+16	+16a_2	25.54	diatomite/ash layer	-2.31	19.8
+16	+15/16	25.00	diatomite	-2.56	21.0
+15	+15a	24.47	diatomite	-2.11	18.9
+15	+15d	24.47	diatomite	-2.46	20.5
+14	+14a	24.41	diatomite/ash layer	-2.22	19.4
+10	+10b	23.47	diatomite	-2.18	19.2
+9	+9a	22.92	diatomite	-1.75	17.2
+9	+9b_1	22.92	diatomite	-1.92	17.9
+9	+9b_2	22.92	diatomite/ash layer	-2.14	19.0
+3	+3/4	22.33	diatomite	-1.86	17.7
-11	-11a_1	16.87	diatomite	-2.49	20.6
-11	-11a_2	16.87	diatomite	-2.50	20.7
-11	-11b_1	15.98	diatomite	-2.30	19.7
-11	-11b_2	15.98	diatomite	-3.11	23.7
-13	-13a	15.23	diatomite	-0.73	12.5
-13	-13b	12.51	diatomite	-0.88	13.1
-17	-17a	7.20	diatomite	-2.29	19.7
-17	-17b	6.80	diatomite	1.09	15.4
-20	-20	5.96	diatomite	-0.39	10.9
-24	-24-28	4.00	diatomite / ash layer	-2.30	19.8
-26	-20-30	3.58	diatomite	n.a.	n.a.
-33	-33	0.77	diatomite	-2.45	20.5
-34	-34	0.00	clay	n.a.	n.a.

The highest temperature value of +23.7 °C was calculated for a carbonate concretion from ash layer -11. Samples with lower temperatures are from ash layers -13, +30, +102, +130 and +135 with values between +10 and +14 °C. The glendonite bearing carbonate concretions show an average temperature value of ca. +18 °C (Tab. 12).

Considering the paleotemperatures derived from clumped isotope measurements for the rCcs, the $\delta^{18}\text{O}$ value of the ambient pore water was recalculated. A $\delta^{18}\text{O}_{\text{H}_2\text{O}}$ value of -4.5‰ for the ambient water was considered for the subsequent calculations (Tab. 23 and Tab. 24).

Tab. 23: Calculated paleotemperatures of glendonites assuming a $\delta^{18}\text{O}_{\text{H}_2\text{O}}$ value of -4.5‰ V-SMOW.

Ash layer	Sample ID	Profile height (m)	Type	$\delta^{18}\text{O}_{\text{carb}}$ (‰V-PDB)	T (°C)
+62	+62a	33.12	glendonite bulk	-2.64	5.4
+62	+62b	33.02	glendonite bulk	-2.43	4.5
+62	+62b	33.02	glendonite rCc	-2.18	3.5
+62	+62b	33.02	glendonite ri	-2.16	3.4
+62	+62b	33.02	glendonite c	-1.26	-0.4
+62	+62c	33.02	glendonite bulk	-2.47	4.7
+62	+62c dup1	33.02	glendonite bulk	-2.49	4.8
+62	+62c dup2	33.02	glendonite bulk	-2.72	5.7
+62	+62c	33.02	glendonite rCc	-2.28	3.9
+62	+62c	33.02	glendonite ri	-2.41	4.4
+16	+16a	25.54	glendonite bulk	-2.72	5.7
+16	+16a	25.54	glendonite rCc	-2.03	2.8
+16	+16a	25.54	glendonite ri	-2.17	3.4
+16	+16a	25.54	glendonite c	-2.56	5.1
+16	+16b	25.00	glendonite bulk	-2.88	6.4
+16	+16b	25.00	glendonite rCc	-2.24	3.7
+16	+16b	25.00	glendonite c	-1.44	0.3
+15b,c	+15a	24.47	glendonite bulk	-2.84	6.3
+15b,c	+15a	24.47	glendonite rCc	-2.55	5.0
+15b,c	+15a	24.47	glendonite ri	-2.41	4.4
+15b,c	+15a	24.47	glendonite c	-0.93	-1.8
+15	+15c	24.47	glendonite bulk	-2.80	6.1
+15	+15c	24.47	glendonite rCc	-2.14	3.3
+15	+15c	24.47	glendonite ri	-2.14	3.3
+15	+15c	24.47	glendonite c	-1.46	0.4
+14	+14b	23.88	glendonite bulk	-2.92	6.6
+10	+10a_1	23.48	glendonite bulk	-2.44	4.5
+10	+10a_2	23.48	glendonite bulk	-2.60	5.2
+10	+10b_1	23.47	glendonite bulk	-2.30	3.9
+10	+10b_2	23.47	glendonite bulk	-2.75	5.9
+10	+10b	23.47	glendonite rCc	-2.24	3.7
+10	+10b	23.47	glendonite ri	-1.92	2.3
+10	+10b	23.47	glendonite c	-0.61	-3.1
+9	+9b	22.92	glendonite bulk	-2.42	4.5
+9	+9b	22.92	glendonite rCc	-2.65	5.5
+9	+9b	22.92	glendonite ri	-1.73	1.5
+9	+9b	22.92	glendonite c	-1.59	0.9

Bulk glendonite samples display an average paleotemperature of +5.4 °C. The individual calcite cements reveal a more detailed picture of the paleotemperatures: on average, the rCc yields a value of +3.9 °C, the rim cement of +3.3 °C, and the fill cement of +1.0 °C. With

ca. +6 °C, the highest temperatures were calculated for the bulk glendonite samples of ash layers +15 and +16 (Fig. 27). The lowest temperatures were computed for the fill cement. All bulk samples of the glendonite plot above the stability field of ikaite, while most of the drilled cement phases, especially the fill cement, fall into the ikaite stability field.

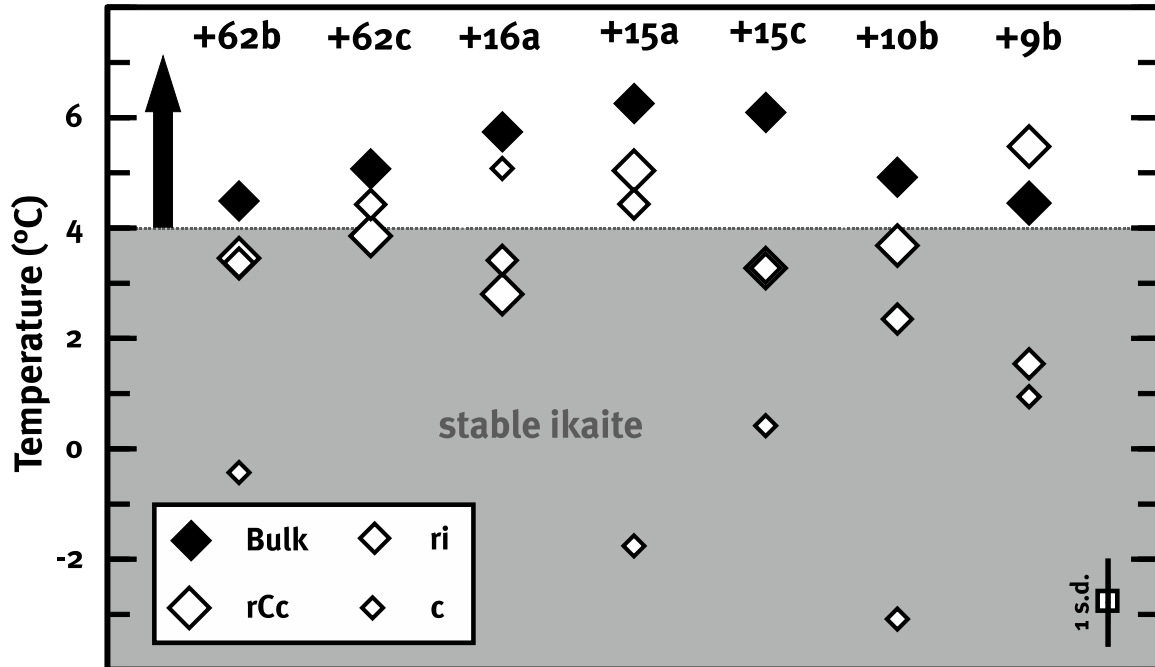


Fig. 27: Paleotemperatures of bulk cements and separated cement phases (rCc: replacive calcite; ri: rim cement; c: fill cement) of the glendonite. The grey area marks ikaite stability after Hu et al. (2014) and the black arrow points to the temperatures of ikaite transformation.

An average value of +2.4 °C for all carbonate cemented diatomite concretions was calculated. The carbonate concretions with volcanic ash particles in their bulk samples exhibit an average value of +1.5 °C. Temperature values below the freezing point of water were computed for the concretions of ash layers -20, -13, between ash layers +20 and +30, and of ash layer +135. The highest value was obtained for the carbonate concretion of ash layer -11 with +7.4 °C. Glendonite bearing concretions show an average paleotemperature value of +3.7 °C.

All temperature values of bulk samples of the carbonate concretions coincide well with the average temperature value derived from drilled samples across the whole profile of each concretion (Fig. 28). Solely the values computed for carbonate concretion +135a of ash layer +135 do not match resulting in a difference of ± 5 °C. This carbonate concretion is one of the concretions displaying a wide range of temperatures values. Other concretions with a sizeable temperature range are concretions -17a, -11a_2, +25/+29, +31, and +135b. No trends are discernible regarding the size of the data range and the quantity of the drilled samples (Fig. 28). There are samples with more than 10 different drilled samples pointing to a low temperature distribution of approximately ± 3 °C.

Tab. 24: Calculated paleotemperatures of the carbonate concretions using a $\delta^{18}\text{O}_{\text{H}_2\text{O}}$ of -4.5‰ V-SMOW. Concretions around glendonite are marked in bold.

Ash layer	Sample ID	Profile height (m)	Type	$\delta^{18}\text{O}_{\text{carb}}$ (‰V-PDB)	T (°C)
+135	+135a	45.29	diatomite	-1.80	1.8
+135	+135b	45.29	diatomite	-0.47	-3.6
+130	+130a	44.24	diatomite	-1.13	-1.0
+130	+130b	44.24	diatomite/ash layer	-1.86	2.1
+129	+129/130	44.03	diatomite/ash layer	-1.96	2.5
+102	+102a	39.46	diatomite	-2.15	3.3
+102	+102b	39.46	diatomite/ash layer	-0.17	-4.9
+90	+90	37.14	diatomite	-2.18	3.4
+62	+62a	33.12	diatomite	-2.07	3.0
+62	+62b_1	33.02	diatomite	-2.26	3.8
+62	+62b_2	33.02	diatomite/ash layer	-2.19	3.5
+62	+62c_1	33.02	diatomite	-2.09	3.1
+62	+62c_2	33.02	diatomite	-2.21	3.6
+62	+62c_3	33.02	diatomite	-2.59	5.2
+31	+31a	27.23	diatomite	-2.80	6.1
+31	+31b	27.23	diatomite/ash layer	-1.09	-1.1
+30	+30a	27.07	diatomite	-0.82	-2.2
+30	+30b	27.07	diatomite/ash layer	-0.93	-1.8
+28	+28	26.91	diatomite	-1.03	-1.4
+26	+26	26.83	diatomite	-2.23	3.6
+25	+25-29	26.81	diatomite	-1.25	-0.5
+18	+15-19	25.56	diatomite	-2.34	4.1
+16	+16a_1	25.54	diatomite	-2.03	2.8
+16	+16a_2	25.54	diatomite/ash layer	-2.31	4.0
+16	+15/16	25.00	diatomite	-2.56	5.1
+15	+15a	24.47	diatomite	-2.11	3.1
+15	+15d	24.47	diatomite	-2.46	4.6
+14	+14a	24.41	diatomite/ash layer	-2.22	3.6
+10	+10b	23.47	diatomite	-2.18	3.4
+9	+9a	22.92	diatomite	-1.75	1.6
+9	+9b_1	22.92	diatomite	-1.92	2.3
+9	+9b_2	22.92	diatomite/ash layer	-2.14	3.3
+3	+3/4	22.33	diatomite	-1.86	2.1
-11	-11a_1	16.87	diatomite	-2.49	4.7
-11	-11a_2	16.87	diatomite	-2.50	4.8
-11	-11b_1	15.98	diatomite	-2.30	3.9
-11	-11b_2	15.98	diatomite	-3.11	7.4
-13	-13a	15.23	diatomite	-0.73	-2.6
-13	-13b	12.51	diatomite	-0.88	-2.0
-17	-17a	7.20	diatomite	-2.29	3.9
-17	-17b	6.80	diatomite	1.09	1.1
-20	-20	5.96	diatomite	-0.39	-4.0
-24	-24-28	4.00	diatomite / ash layer	-2.30	4.0
-26	-20-30	3.58	diatomite	n.a.	n.a.
-33	-33	0.77	diatomite	-2.45	4.6
-34	-34	0.00	clay	n.a.	n.a.

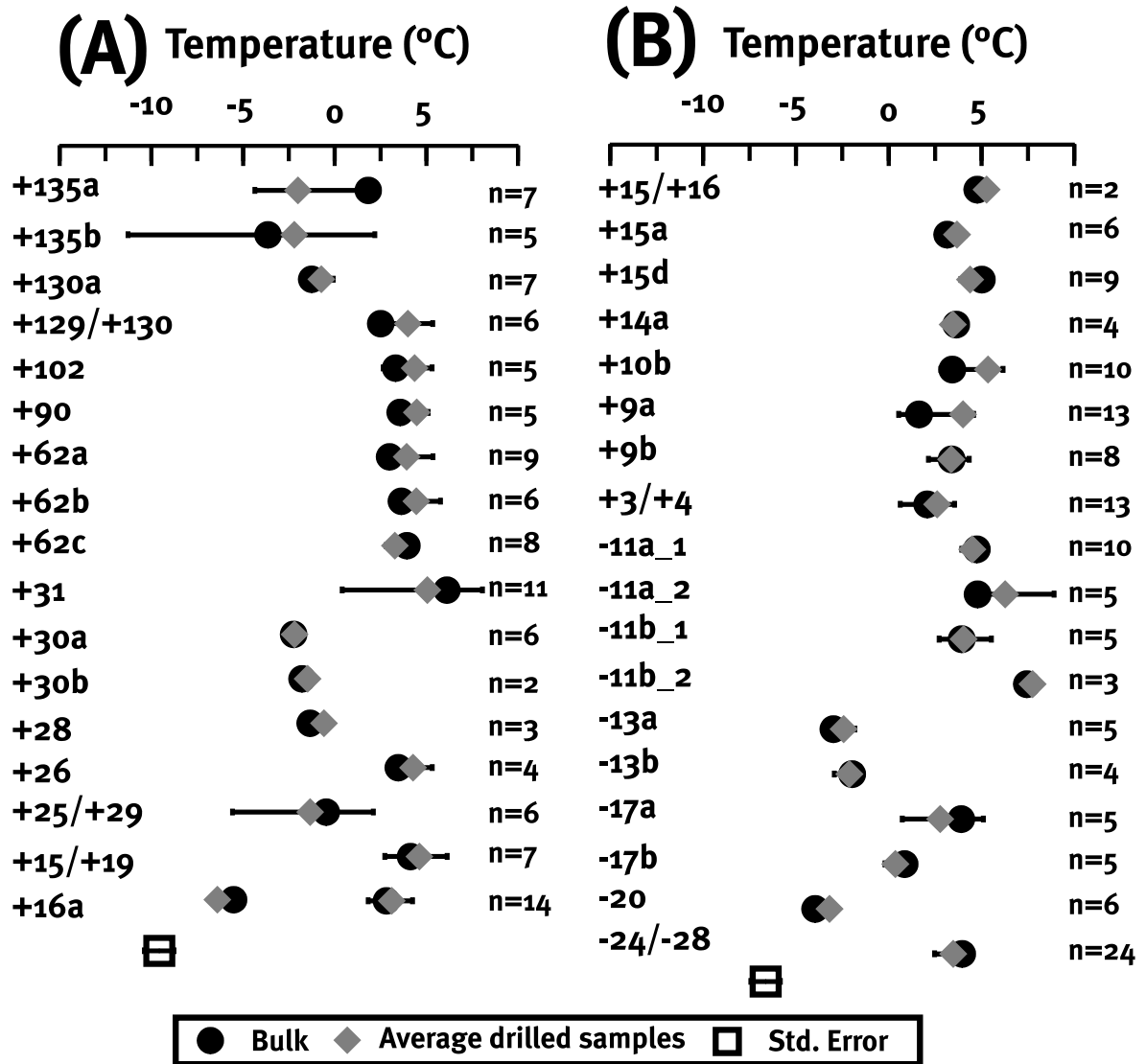


Fig. 28: Reconstructed paleotemperatures of the carbonate concretions (A) between ash layers +16 and +135, and (B) between ash layers -28-24 and +15/16. The black lines indicate the temperature distribution of drilled samples.

4.3.3 Bottom water temperatures indicated by $\delta^{18}\text{O}_{\text{diatom}}$ values

Oxygen isotope measurements ($\delta^{18}\text{O}_{\text{diatom}}$) were conducted on 15 pure, white diatom samples. Equations of various fractionation factors between quartz, chert, diatoms, silica in general, and water are displayed in table 25.

Tab. 25: Comparison of equations for calculating paleotemperatures based on $\delta^{18}\text{O}_{\text{diatom}}$.

Author	Year	Material	Equation	Unit	Number
Clayton et al.	1972	Quartz	$1000 \ln \alpha_{\text{quartz-calcite}} = 3.38 * 10^6 * T^2 - 3.4$	K	1
Shiro & Sakai	1972	Quartz	$1000 \ln \alpha_{\text{quartz-calcite}} = 3.09 * 10^6 * T^2 - 3.29$	K	2
Labeyrie	1974	Diatoms	$T (^{\circ}\text{C}) = 5 - 4.1 * (\delta^{18}\text{O}_{\text{SiO}_2} - \delta^{18}\text{O}_{\text{H}_2\text{O}} - 40)$	$^{\circ}\text{C}$	3
Kita et al.	1985	Quartz	$1000 \ln \alpha_{\text{quartz-water}} = 3.52 * 10^6 * T^2 - 4.35$	K	4
Juillet-Leclerc & Labeyrie	1987	Silica	$T (^{\circ}\text{C}) = 17.2 - 2.4 * (\delta^{18}\text{O}_{\text{SiO}_2} - \delta^{18}\text{O}_{\text{H}_2\text{O}} - 40) - 0.2 * (\delta^{18}\text{O}_{\text{SiO}_2} - \delta^{18}\text{O}_{\text{H}_2\text{O}} - 40)^2$	$^{\circ}\text{C}$	5
Juillet-Leclerc & Labeyrie	1987	Silica	$1000 \ln \alpha_{\text{silica-water}} = 3.26 * 10^6 * T^2 + 0.45$	K	6
Shemesh et al.	1992	Silica	$T (^{\circ}\text{C}) = 11.03 - 2.03 * (\delta^{18}\text{O}_{\text{SiO}_2} - \delta^{18}\text{O}_{\text{H}_2\text{O}} - 40)$	$^{\circ}\text{C}$	7
Brandriss et al.	1998	Diatoms	$1000 \ln \alpha_{\text{silica-water}} = 15.56 * 10^3 * T^1 - 20.92$	K	8
Moschen et al.	2005	Silica	$T (^{\circ}\text{C}) = 190.07 - 5.05 * (\delta^{18}\text{O}_{\text{SiO}_2} - \delta^{18}\text{O}_{\text{H}_2\text{O}})$	$^{\circ}\text{C}$	9
Dodd & Sharp	2010	Silica	$1000 \ln \alpha_{\text{silica-water}} = 2.39 * 10^6 * T^2 + 4.23$	K	10

Samples containing the highest concentrations of minerals and other fossils composed of SiO_2 display lower $\delta^{18}\text{O}$ values than pure diatom samples. Consequently, a correction for a mixed $\delta^{18}\text{O}_{\text{meas}}$ value (diatoms, other SiO_2 fossils, silt, clay, etc.) was used according to Leng and Barker (2006, equation 3):

$$\delta^{18}\text{O}_{\text{meas}} = \delta^{18}\text{O}_{\text{silt}} * A + \delta^{18}\text{O}_{\text{diatom corr}} * B \quad (3)$$

A and B are the abundances of silt and diatoms, respectively, resulting from point-counting.

Calculated temperatures consider a $\delta^{18}\text{O}_{\text{silt}}$ value of +11.7‰ for the mineral fraction (clay and silt; Brewer et al., 2008) and -4.5‰ V-SMOW for the ambient water. Following Dodd and Sharp (2010), the paleotemperature data for the $\delta^{18}\text{O}_{\text{diatom}}$ results were calculated (equation 10 in table 25).

The $\delta^{18}\text{O}_{\text{diatom}}$ values yield paleotemperatures between -3.6 $^{\circ}\text{C}$ and +32.3 $^{\circ}\text{C}$ (Tab. 26). The lowest temperature value of -3.6 $^{\circ}\text{C}$ was calculated for sample “Ra u. +16” between ash layer +14 and +16 and the highest value of +32.3 $^{\circ}\text{C}$ for sample “Kn+1_1”, which stems from ash layer +1. All but one paleotemperature value fall into a range between -4 $^{\circ}\text{C}$ and +18 $^{\circ}\text{C}$ (Fig. 29).

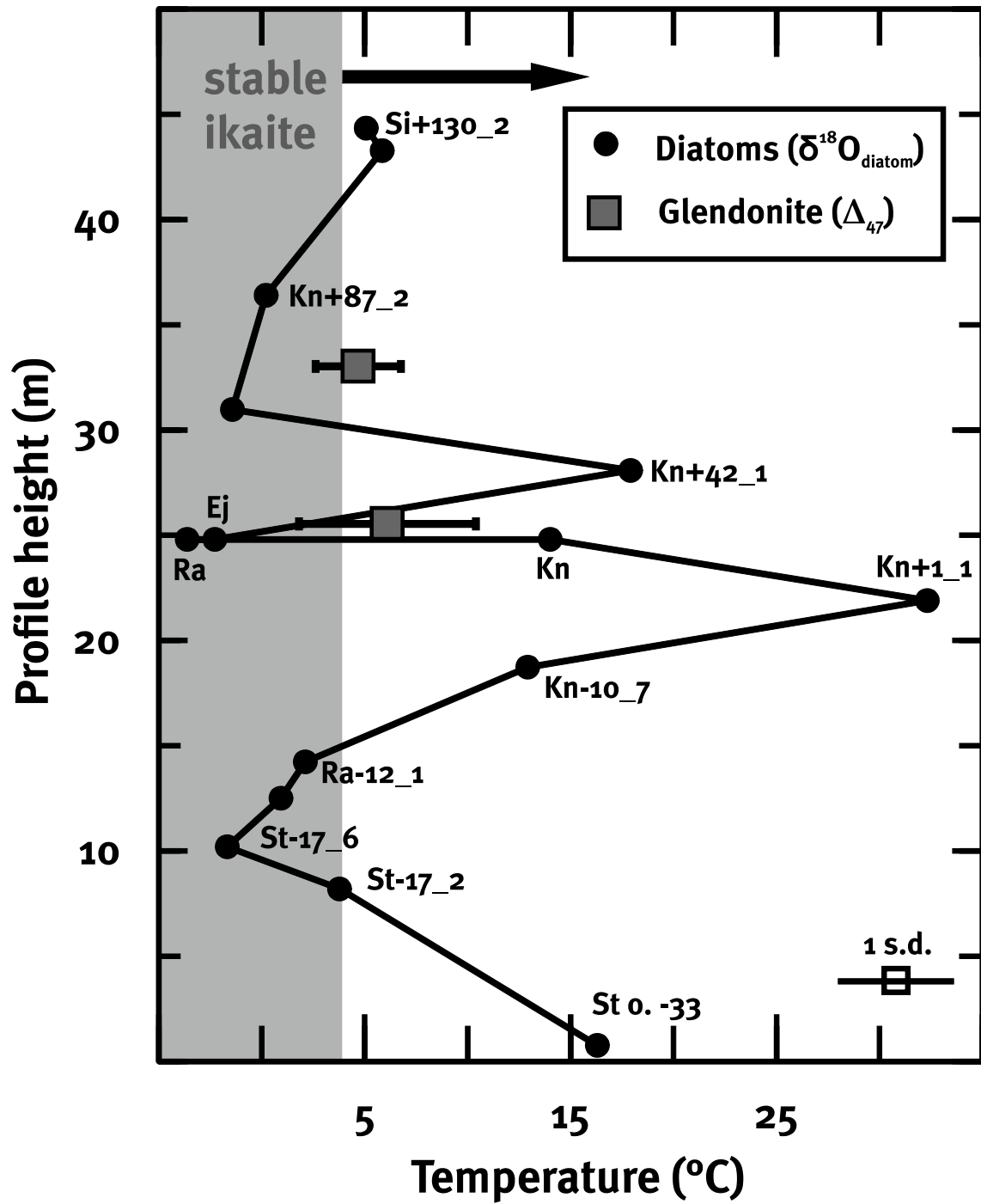


Fig. 29: Paleotemperatures indicated by $\delta^{18}\text{O}_{\text{diatom}}$ values plotted against profile height. The grey area marks the temperature range of ikaite stability (Hu et al., 2014). The black arrow points to temperatures of ikaite transformation.

Tab. 26: Calculated paleotemperatures from a $\delta^{18}\text{O}_{\text{H}_2\text{O}}$ value of -4.5‰ V-SMOW. According to equation 3 for the contamination with clay and silt minerals, all $\delta^{18}\text{O}_{\text{meas}}$ were corrected.

Ash layer	Sample ID	Profile height (m)	$\delta^{18}\text{O}_{\text{meas}}$ (‰V-SMOW)	$\delta^{18}\text{O}_{\text{diatom corr}}$ (‰V-SMOW)	T (°C)
+130	Si +130_2	44.34	30.93	31.07	5.1
+123	Si+123_2	43.27	30.89	30.89	5.8
+87	Kn+87_2	36.40	31.04	32.21	0.2
+52	Kn +52_1	30.97	32.05	32.61	-1.4
+42	Kn+42_1	28.08	28.32	28.33	17.9
+16	Ej+14_2	24.80	32.82	32.82	-2.3
+16	Ra u.+16	24.80	33.15	33.16	-3.6
+16	Kn+14_2	24.80	29.11	29.12	14.0
+1	Kn +1_1	21.90	24.95	25.66	32.3
~-3	Kn-10_7	18.73	28.93	29.35	12.9
-12	Ra-12_1	14.23	31.48	31.76	2.1
-14	Kn-14_2	12.51	31.96	32.04	0.9
~-16	St-17_6	10.20	32.04	32.67	-1.7
-17	St-17_2	8.20	31.03	31.37	3.8
-33	St o. -33	0.77	28.25	28.65	16.3

5 Discussion

5.1 Glendonite of the Fur Formation

5.1.1 The internal structure of glendonite

The glendonites of the Fur Formation are very large and occur in the shape of rosettes and blades. In contrast, these glendonites (maximum length of 1.5 m) are bigger than usually reported for other localities. The observed crystal forms were previously reported by Selleck et al. (2007), Frank et al. (2008), Spielhagen and Tripathi (2009), and Teichert and Luppold (2013). The glendonite depicts fir-tree zoning after Raven and Dickson (1989) at their crystal edges. This growth form is established when the growth ratio between two crystal sectors is periodically reversed. As a consequence, crystal boundaries are formed in zigzag shape.

Only six proto-glendonite crystals sensu Teichert and Luppold (2013) consisting mostly of replacive calcite (rCc) have been found: below ash layers +14, +16, +44, +50, +56, and +62. The proto-glendonite was not protected against weathering by a surrounding carbonate concretion.

Four distinct calcite cement generations were investigated within the glendonite in this study. Other petrographic studies revealed that marine glendonite exhibits three cement generations with different geochemical compositions (David and Taylor, 1905; Boggs and Hull, 1975; Kaplan, 1979; Larsen, 1994; De Lurio and Frakes, 1999; Huggett et al., 2005; McLachlan et al., 2006; Selleck et al., 2007; Frank et al., 2008; Grasby et al., 2017). In contrast, Greinert and Derkachev (2004) reported only two distinct cements of different origin, while Boggs (1972) and Teichert and Luppold (2013) were able to distinguish four cement generations.

Following Teichert and Luppold (2013), the first cement generation was named “replacive calcite” (rCc), whereas Huggett et al., who in 2005 published some data of the glendonite of the Fur Formation, named this phase “type 1” (Tab. 27). The rCc usually occurs as 3.0 mm big, tabular to ovoid crystals and clusters with abundant organic matter. The organic matter is arranged in rings in the outer parts of the rCc, just like seen by Huggett et al. (2005) in back scatter electron microscope analyses. Boggs (1972) documented the arrangement of organic matter resulting from concentric inclusions of brownish organic matter. The rCc is the most MgCO₃ depleted phase within the glendonite (Tab. 27) with an increasing MgCO₃ concentration towards the edge of the granular, imperfectly formed calcites. The increasing concentration of MgCO₃ towards the rim was previously documented by Huggett et al. (2005) and Teichert and Luppold (2013).

The second cement phase within the glendonite is a yellowish spherulitic cement overgrowing the first calcite cement generation like a rim cement. Fine, brown organic dust (Fig. 12 B and D) and apatite (Fig. 13 A, B, and D) were often incorporated into the second cement phase. Pyrite was also found under reflected light microscopy in the glendonite of ash layers +10 and

+15. Due to its higher MgCO_3 content (3.17 mol%), this phase was named Mg-ri in this study. Teichert and Luppold (2013) used the same name, but Huggett et al. (2005) called it “type 2” (Tab. 27). The high organic matter content leading to the yellowish colour was also proposed by Boggs and Hull (1975) and Huggett et al. (2005).

Tab. 27: Energy dispersive X-ray analyses of various cement generations within the glendonite of this study and of Huggett et al. (2005).

Publication	Cement phase	Mg (mol%)	Fe (mol%)	Mn (mol%)	Sr (mol%)	Ba (mol%)
This study	rCc	1.70	0.06	0.05	0.13	0.02
This study	Mg-ri	3.17	0.12	0.20	0.16	0.03
This study	Fe-Mn-Mg-ri	7.53	1.10	1.49	0.14	0.08
This study	Fe-Mg-c	2.48	0.60	0.14	0.13	0.06
Huggett et al., 2005	type 1	0.61	0.00	0.01	0.11	n.d.
Huggett et al., 2005	type 2	3.01	0.08	0.23	0.13	n.d.
Huggett et al., 2005	type 3	2.99	1.69	1.98	0.07	n.d.

Unlike Huggett et al. (2005) who could not identify a secondary rim cement, the secondary rim cement (Fe-Mn-Mg-ri) observed here exhibits the highest concentrations of MgCO_3 , MnCO_3 , FeCO_3 , and BaCO_3 (Tab. 27), when compared to other cement phases. Yet, the Fe and Mg contents of the secondary rim cement of the Fur Formation glendonite are not as high as reported by Teichert and Luppold (2013) for the glendonite of Early Jurassic age.

The youngest cement generation is a calcite spar that filled the remaining pore space. Where present in a glendonite, it is less stable and extensively leached. This cement exhibits slightly higher Fe and Mg concentrations (Fe-Mg-c) than the rCc. Huggett et al. (2005) reported a CaCO_3 of 93.27 mol%, a MgCO_3 of 2.99 mol%, a FeCO_3 of 1.69 mol%, and a MnCO_3 of 1.98 mol% for the glendonite of the Fur Formation. In this study, the concentrations of Fe, Mn, and Mg are less than reported by Huggett et al. (2005) (Tab. 27).

Ikaite formation and its transformation to glendonite were studied before (Larsen, 1994; Greinert and Derkachev, 2004; Tang et al., 2009; Zaoui and Sekkal, 2014). Larsen (1994) reported that the replacive calcite (rCc) represents about 31.4% of the newly formed glendonite. The rCc is thought to precipitate during the initial phase of ikaite breakdown when the end of the stability field of ikaite is reached. The centre of the rCc depicts a very low content of magnesium in many crystals. Jansen et al. (1987), Schubert et al. (1997), and Buchardt et al. (2001) previously described the low magnesium concentration found within rCc. Stein and Smith (1985) supposed that mixing processes of ikaite crystal water and surrounding interstitial water result in the zonation of the rCc with low a MgCO_3 in the centre and a higher MgCO_3 at the edges of the rCc at the ikaite breakdown.

Both rim cements, i.e. Mg-ri and Fe-Mn-Mg-ri, precipitated from a mixture of the ikaite crystal water and the pore water migrating into the ikaite void caused by diffusional Mg-Ca exchange. At first, a rim cement with a mean content of MgCO_3 (3 mol%) and higher MnCO_3 , FeCO_3 , and SrCO_3 concentrations is precipitated from this solution. The secondary rim cement results from the remaining, totally enriched fluid that is still present after the precipitation of the first

rim cement. Hence, the secondary rim cement bears the highest concentrations of MgCO_3 , MnCO_3 , FeCO_3 , and BaCO_3 found within the four different cement phases.

The fill cement (termed Fe-Mg-c) is the youngest cement generation and was formed from a fluid that had lower concentrations of Mg^{2+} , Mn^{2+} , Fe^{2+} , and Ba^{2+} than the fluid, which formed the secondary rim cement. The fill cement often leached away in the marginal part of the glendonite suggesting dissolution processes of fill cement during weathering, or that the voids of the glendonite were not completely filled. This cement stems from a later, pore space filling, compositionally different pore fluid. This assumption can be justified by (i) the chemical composition of the fill cement that is different from the rCc and rim cements, and by (ii) the absence of organic matter within this cement phase.

Open pore space was frequently found in tabular shapes in many glendonites surrounded by carbonate concretions (Fig. 7 A, C, and E). Teichert and Luppold (2013) proposed that the ikaite to glendonite transformation commences at the margin where a rim cement starts to grow around the rCc. Therefore, the shape of the ikaite could have been preserved in soft, marine sediments. Due to the fact that the inner part of the ikaite is preserved from collapsing, the rCc could take a longer time to grow and, thus, is larger in the centre than at the margins. In this study, the largest rCc was discovered in the middle of the glendonite and in pipes forming the granular structure between margin and centre. When pore water fluid was able to enter the glendonite after the formation of the rCc and the rim cements, the open pore space of the pipes was filled with the youngest fill cement.

The transformation of ikaite to glendonite was likely completed prior to the formation of the surrounding carbonate concretion. Otherwise, an inflow of pore waters from which the rim and the fill cements precipitated would have been impossible. Larsen (1994) suggested that the transformation of ikaite to glendonite occurred rather rapidly over a period of a day or more. However, considering the distinct differences in chemical and isotopic composition between the different cement generations, a longer time of transformation during diagenesis appears more likely. The assessment of the time span of an entire ikaite to glendonite transformation is difficult.

Intact diatom frustules were discovered within the replacive calcite and within the first rim cement (Fig. 12 E). Thus, diatoms must have been embedded in the ikaite during ikaite formation. Prior to this study, Geptner et al. (2014) reported diatoms within the glendonite of the White Sea. They denoted that the incorporation of diatom frustules results from the formation of carbonate material during the growth of glendonite.

5.1.2 The carbon source for ikaites and the newly built fill cements

Carbon isotopes allow constraining the carbon source due to distinctly different carbon isotopic compositions of carbon-bearing compounds such as organic matter, marine or freshwater carbonates, oceanic dissolved inorganic carbon (DIC), or methane (Clark and Fritz, 1997). Moreover, processes of carbon cycling can be revealed due to diagnostic magnitudes in carbon isotopic fractionation associated with respective processes (e.g. Hayes, 1993). These isotope effects will be superimposed on the carbon isotopic source signature.

Biosynthesis (e.g. via autotrophic carbon fixation) is generally associated with a preferential turnover of the light carbon isotope ^{12}C , resulting in ^{13}C depleted organic matter (Hoefs, 2015). Marine organic matter is characterised by $\delta^{13}\text{C}$ values between -22 and -17‰, while terrestrial organic matter is more depleted in ^{13}C showing $\delta^{13}\text{C}$ values between -27 and -20‰ (Rullkötter, 2006). In contrast, the oxidation of organic matter is not associated with a substantial shift in the carbon isotopic composition of the resulting CO_2 . Bacterial methanogenesis via acetoclastic fermentation, in turn, results in two isotopically distinct carbon-bearing products, notably strongly ^{13}C depleted methane and ^{13}C enriched CO_2 (e.g. Whiticar, 1999). Subsequent formation of DIC and, ultimately, mineral precipitation will result in ^{13}C enriched - methanogenic - carbonates and $\delta^{13}\text{C}$ values as high as +30‰ have been reported (Claypool and Kaplan, 1974). The formation of carbonates from DIC is accompanied by a shift in $\delta^{13}\text{C}$ of ca. 1‰, but a larger shift (6 – 9‰) is associated with the initial hydrolysis of carbon dioxide during the formation of bicarbonate (HCO_3^- ; Jimenez-Lopez et al., 2001).

Modern marine carbonates as well as ancient carbonate rocks and biogenic carbonates display a mean $\delta^{13}\text{C}$ value of 0 ± 5 ‰ (Veizer et al., 1999), although distinctly positive $\delta^{13}\text{C}_{\text{carb}}$ values characterise several time intervals in Earth history. The carbon isotopic composition of diagenetic carbonates that formed in the sediment is more complex. Their carbon isotopic composition includes ^{13}C depleted as well as ^{13}C enriched values. While the former indicates the turnover of organic matter (including methane consumption as suggested by strongly ^{13}C depleted values), the latter points to methanogenesis. Naturally, the mixing of different carbon sources will complicate an unequivocal identification of the carbon source and/or the process(es) that led to the formation of the carbonate under study.

The bulk carbonate carbon isotopic composition of glendonite as well as concretions from the Fur Formation (Fig. 14 and Fig. 15) vary between -26 and -17‰ V-PDB. The ^{13}C depletion observed suggests a strong contribution from the turnover of sedimentary organic matter. Terrestrial organic matter, notably wood from ash layer -25 of the Knudeklint Member, displays a $\delta^{13}\text{C}$ value of -29.8‰ V-PDB. Individual carbonate phases within glendonite sampled at high spatial resolution reveal that the replacive calcite (rCc) displays the most depleted carbon isotopic composition with $\delta^{13}\text{C}$ values as low as -24.7‰ V-PDB. The $\delta^{13}\text{C}$ value of the rCc is supposed to record the signature of the original carbon source for ikaite formation (e.g. Greinert and Derkachev, 2004; Lu et al., 2012). Frank et al. (2008) also reported that replacive calcite displayed the strongest ^{13}C depletion. In contrast, carbonate rim cements and bulk concretions bear

^{13}C enriched carbon isotope values. The strongest ^{13}C enrichment is found in the late diagenetically formed cement infills.

^{13}C depleted carbonates suggest that organic matter was the ultimate carbon source, likely derived via microbial decomposition. Previously, organotrophic sulphate reduction (OSR) was considered to be one of the most important processes for ikaite formation (e.g. Boggs, 1972; De Lurio and Frakes, 1999; Geptner et al., 2014). In addition, Greinert and Derkachev (2004) as well as Price and Nunn (2010) proposed that anaerobic oxidation of methane could be another formation process for ikaite. Less ^{13}C depleted carbonate precipitates suggest a decrease in the contribution of DIC resulting from the turnover of organic matter and the admixture of another, more ^{13}C enriched carbon source. This could point to a higher contribution of marine DIC, suggest the dissolution of marine carbonate in acidic pore water, or indicate an increasing importance of methanogenesis at greater burial depth (Huggett et al., 2005).

The carbonate carbon isotopic composition of glendonite has been investigated before, mostly via bulk carbonate analyses (Greinert and Derkachev, 2004; Huggett et al., 2005; Selleck et al., 2007; Spielhagen and Tripathi, 2009; Geptner et al., 2014; Morales et al., 2015), but few studies separated individual carbonate phases (Frank et al., 2008; Teichert and Luppold, 2013). Previous studies of glendonite from the Fur Formation yielded a range in $\delta^{13}\text{C}$ between -25.2 and -21.2‰ V-PDB (Pedersen and Buchardt, 1996; Huggett et al., 2005).

The results of carbonate carbon isotope reported in this study resemble previous observations. The analysis of individual carbonate phases, distinguished by detailed petrography and microdrilled, identify a transition from ^{13}C depleted replacive calcite, which formed early, to late(r) diagenetic cement infills, which exhibit less depleted $\delta^{13}\text{C}$ values. This transition indicates a change in the carbon source, notably a decrease in the contribution of carbon from organotrophic microbial sulphate reduction to the DIC pool and an increasing contribution of isotopically heavy DIC. Whether this reflects a higher contribution of marine DIC or whether this indicates bacterial methanogenesis remains unclear.

Ikaite formation occurred within the sediment as evident through the disruptions of lamination in the diatomite caused by the growth of ikaite crystals (Fig. 7 C and D). Considering an important contribution from microbial sulphate reduction, as revealed by the ^{13}C depleted nature of the early diagenetic replacive calcite (rCc), ikaite formation is likely constrained to the shallow subsurface, possibly within 10 m of the sediment-water interface (De Lurio and Frakes, 1999; Kodina et al., 2003; Zu et al., 2012; Teichert and Luppold, 2013; Grasby et al., 2017). Zhou et al. (2015) defined an ikaite-formation zone (IFZ) based on the distinct concentration depth profiles of Ca^{2+} and DIC. These authors concluded that the IFZ is located close to the sulphate-methane transition zone (SMTZ). Besides Ca^{2+} , DIC, sulphate and organic matter, the main factor constraining ikaite formation is a high concentration of orthophosphate, being the strongest inhibitor of calcite formation (Brooks et al., 1950; Berner and Morse, 1974; Burton and Walter, 1990; Bischoff et al., 1993; Hu et al., 2015).

5.1.3 Oxygen isotopes – temperature estimates vs. pore water composition

The $\delta^{18}\text{O}_{\text{carb}}$ values of this study range between -3.6 and -1.7‰ V-PDB and agree well with the previously measured data of -2.8‰ (Pedersen and Buchardt, 1996), -1.2 and -0.8‰ (Huggett et al., 2005) for the glendonite of the Fur Formation.

Stable oxygen isotopes of glendonite were used for the reconstructions of the paleotemperature or the isotopic composition of the surrounding water during the precipitation in previous studies (De Lurio and Frakes, 1999; Greinert and Derkachev, 2004; Frank et al., 2008). Due to the fact that calcite was formed directly after the transformation of ikaite to glendonite, the fractionation factors for calcite and ikaite were proposed to lie in the same range (De Lurio and Frakes, 1999; Buchardt et al., 2001; Kodina et al., 2003). Here, a fractionation factor of 1.01049 after Kim and O'Neil (1997) was used for the temperature reconstruction. Assuming a $\delta^{18}\text{O}$ value of -1‰ V-SMOW for Early Eocene seawater, because no sea ice has been found, temperatures of the ikaite decomposition ranging between +20.3 and +23.1 °C (calculation after Kim and O'Neil (1997)) are proposed. The rCc oxygen isotope value reflects the $\delta^{18}\text{O}_{\text{carb}}$ isotopic composition at the point of the ikaite to glendonite transformation. As a consequence, only this temperature can be reconstructed (Frank et al., 2008; Oehlerich et al., 2013). The Early Eocene was taken for the time of the ikaite transformation, because the ikaite to glendonite transformation is expected to have occurred during early diagenesis.

Suess et al. (1982) and Whiticar et al. (1998) proposed that the lighter $\delta^{18}\text{O}$ values reflect an increasing degree of dehydration and that the oxygen isotope signal is lost during dehydration at the breakdown of ikaite because of the reequilibration with aqueous phases at new temperatures. Rickaby et al. (2006) noted $\delta^{18}\text{O}$ values to be 1-2‰ lower than expected due to kinetic controls on oxygen isotope fractionation during ikaite decomposition. Considering this, newly calculated paleotemperatures for the decomposition of ikaite fall in a range between +10 and +15 °C.

Hu et al. (2014) proposed that the decomposition of ikaite occurs at a temperature above +4 °C. In contrast, De Lurio and Frakes (1999) estimated a temperature range of +5 to +8 °C for the transformation of ikaite into glendonite and, thus, calculated $\delta^{18}\text{O}$ values of -3.4 to -2.6‰ V-SMOW for the surrounding pore waters. Paleotemperature measurements based on the clumped isotopes (Δ_{47}) of two replacive calcite sample of the glendonite yield an average temperature value of +6 °C (further discussed in chapter 5.3). Based on this average temperature, the equation of Kim and O'Neil (1997) was solved for the $\delta^{18}\text{O}$ of the ambient pore water ($\delta^{18}\text{O}_{\text{H}_2\text{O}}$). Considering the $\delta^{18}\text{O}_{\text{carb}}$ values of this study, recalculating the $\delta^{18}\text{O}_{\text{H}_2\text{O}}$ value yields -4.5‰ V-SMOW, comparable to Geptner et al. (2014) who reported -4‰ for their pore water. Such negative values of pore water cannot be ruled out and are discussed in the following passages.

Teichert and Luppold (2013) proposed that during the transformation from ikaite to glendonite the oxygen equilibrates with the surrounding pore or seawater and that there are many uncertainties about the bottom water isotopic composition like changes due to diageneses, the influx of meteoric waters, etc.. The influence of meteoric groundwater mixing with the bottom

water in the Danish Basin was considered because of the vicinity of the glendonite bearing localities towards the coast and a possible input of groundwater. Van Geldern et al. (2013) reported fresh groundwater in flat-lying lenses with a mean $\delta^{18}\text{O}$ composition of -6.9‰ V-SMOW for the recent meteoric recharge of groundwater in 100 to 130 km offshore on the Atlantic continental shelf. Boggs (1972) and Selleck et al. (2007) denoted a modification of $\delta^{18}\text{O}_{\text{H}_2\text{O}}$ values towards ^{18}O depleted values of the formation of ikaite during interchange with meteoric and connate waters. The sediments of the Fur Formation were deposited not more than 100 km away off the Scandinavian coast during the Early Eocene (Larsson, 1975; Pedersen, 1981; Ansgore and Reich, 2004; Pedersen et al., 2011). Thus, groundwater influence during the formation of ikaite cannot be ruled out.

In addition to meteoric water, Permian salt brines could have influenced the oxygen isotopic composition of the pore water. Several salt domes consisting of Permian Zechstein salts were found in the underground of the Fur Formation (Madirazza, 1976; Larsen and Baumann, 1981; Jørgensen et al., 2005; Pedersen et al., 2011). Kloppmann et al. (2001) denoted $\delta^{18}\text{O}$ values lighter than -8‰ V-SMOW in the Permian salt brines of NW Germany. Dowgiallo and Tongiorgi (1993) reported $\delta^{18}\text{O}$ values between -9 and -3‰ in Mesozoic salt brines of NW Poland, while Fontes and Matray (1993) measured -2 and $+4\text{‰}$ in two brines of different origins within the Permian Paris Basin. Therefore, the $\delta^{18}\text{O}$ isotopic composition of Permian salt brines plots in a wide range of values, but most salt brines depict negative $\delta^{18}\text{O}$ values. De Lurio and Frakes (1999) assumed a low $\delta^{18}\text{O}$ isotopic composition of pore water to be an indicator for hypersaline water. Therefore, a direct influence of the Permian salt brines on the formation of ikaite within the Fur Formation might be possible (see chapter 5.1.5).

Microbial sulphate reduction was another factor of the ^{18}O depletion of ancient pore water within the sediments where the formation of ikaite occurred. During microbial sulphate reduction, the ^{18}O depleted oxygen from the sulphate ions succeeds in getting into the pore water bicarbonate reservoir, whose bicarbonate is used afterwards for the formation of ikaite (Sass et al., 1991).

An alternative factor influencing the $\delta^{18}\text{O}_{\text{H}_2\text{O}}$ towards lighter values are volcanic ash layers. Ca. 200 individual ash layers were identified in the Fur Formation. The glendonites with their surrounding carbonate concretions often occur below several of these ash layers. Water-rock interaction during the low temperature alteration of these ash layers is supposed to shift the $\delta^{18}\text{O}$ of the pore fluid towards more ^{18}O depleted values (ca. -3‰ V-SMOW) due to the formation of smectite of basalts, ashes, and continental detritus (Lawrence et al., 1979; Lawrence and Taviyani, 1988; Mozley and Burns, 1993; Dale et al., 2014). Due to the fact that the ikaite of the Fur Formation was formed within the sedimentary column, an influence of volcanic ash alteration on the oxygen isotopic composition of ikaite is expected.

5.1.4 Apatite as limiting factor for bulk $\delta^{18}\text{O}$ analyses of glendonite samples

Interestingly, the bulk $\delta^{18}\text{O}_{\text{carb}}$ analyses of the glendonite yield values outside the range of respective values for the three individual cements (rCc, ri, and c; Fig. 14). During microscopic and microprobe analyses, the mineral apatite was often found within the first rim cement. Apatite holds a certain concentration of carbonate within its structure. Consequently, apatite can change the $\delta^{18}\text{O}_{\text{carb}}$ values towards $\delta^{18}\text{O}$ depleted values. This is supported by the observation that the shift in the bulk $\delta^{18}\text{O}_{\text{carb}}$ values of glendonite correlates with the concentration of phosphate, which is the main anion of apatites (Tab. 28 and Fig. 30). The glendonites +9b of ash layer +9 and +15c of ash layer +15 show the highest phosphate contents. These samples are seen as offset samples due to another geochemistry (higher content of pyrite and apatite if compared to other glendonites) and, therefore, are not considered for the trend line of figure 30. However, the difference between bulk sample and the average value of the drilled cements correlate with the phosphate content for glendonites of a similar mineral composition.

Orthophosphate is required to stabilise ikaite (Burton, 1993; Bischoff et al., 1993; Larsen, 1994; De Lurio and Frakes, 1999; Buchardt et al., 2001; Hu et al., 2015) and is often incorporated into the glendonite as apatite (Huggett et al., 2005; McLachlan et al., 2006; Teichert and Luppold, 2013). Selleck et al. (2007) denoted glendonite within phosphate nodules. Carbonate can be incorporated in apatite (Chickerur et al., 1980). As a consequence, the $\delta^{13}\text{C}$ and $\delta^{18}\text{O}$ isotopic composition of these carbonates can be measured in mass spectrometers as CO_2 gas (Kolodny and Kaplan, 1970; Iacumin et al., 1996). The carbonate $\delta^{18}\text{O}$ isotopic compositions found within the apatites are difficult to measure if the apatites are situated in carbonates. In continuing studies, the separation of the oxygen isotope signal of the glendonite calcite and the carbonate of the apatites within glendonite should be attempted. Therefore, it will be necessary to gather enough and pure material from the apatites by microdrilling.

Tab. 28: Average values of the bulk samples compared to the average values of the micro twist drilled samples of the various cement phases against the XRF results for the apatite.

Ash layer	Sample ID	Profile height (m)	$\delta^{18}\text{O}_{\text{carb}}$ drilled bulk samples (‰V-PDB)	$\delta^{18}\text{O}_{\text{carb}}$ drilled cement samples (‰V-PDB)	Balance between average values (‰V-PDB)	P_2O_5 apatite content (wt.%)
+62	+62b	33.02	-2.34	-1.87	0.48	0.082
+62	+62c	33.02	-2.38	-2.34	0.04	0.046
+16	+16a	25.54	-2.55	-2.25	0.29	0.187
+15b,c	+15a	24.47	-2.54	-1.97	0.57	0.460
+15	+15c	24.47	-2.65	-1.91	0.74	7.636
+10	+10b	23.47	-2.47	-1.59	0.88	0.246
+9	+9b	22.92	-2.46	-1.99	0.47	1.008

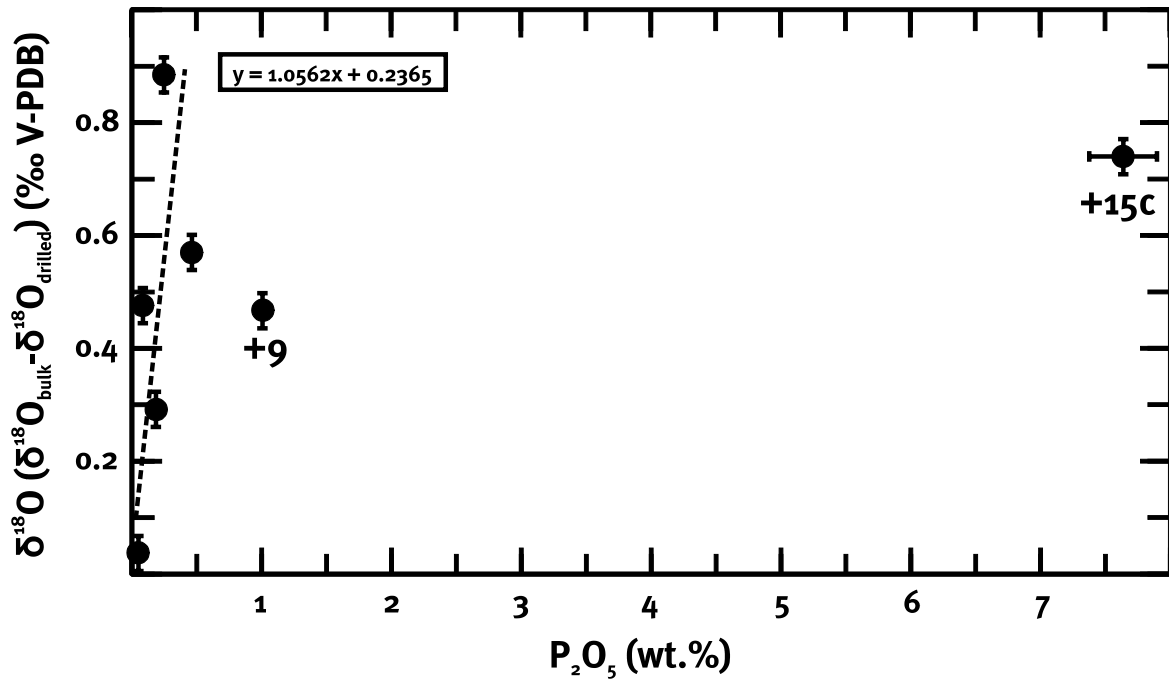


Fig. 30: Plot of the difference between the average of $\delta^{18}\text{O}$ of the bulk drilled values and the average of $\delta^{18}\text{O}$ of the drilled cement values against the concentration of apatite within the glendonite samples.

Consequently, all $\delta^{18}\text{O}_{\text{carb}}$ data that stem from powder samples drilled by a 2.3 mm thick microdrill and bulk samples in general should be used with care. The $\delta^{18}\text{O}$ lowering impact of carbonate inside the apatite cannot be excluded and should be taken into account if oxygen data are used for paleotemperature reconstructions.

5.1.5 Did the ash layers enhance the chance for ikaite formation?

One important fact for the formation of ikaite can be the vicinity of volcanic ash layers. Almost all glendonites have been found below certain ash layers (Fig. 7 and Fig. 8). All glendonites are located in the positive tholeiitic ash series and the ash layers holding glendonite are more than 7 cm thick. Thus, the thickness and the geochemistry of the ash layers might have contributed to the formation of ikaite. The thickness of an ash layer can point towards a cooler time after volcanic eruptions increasing the chance of ikaite formation during the warm Early Eocene. This is improbable, because, in the Danish Basin, there were ca. 500 m of water between ikaite formation depth and the atmosphere where the cooling took place. Therefore, a direct response in form of the formation of ikaite to a short term climatic cooling after an eruption seems unlikely.

After the deposition on the seawater surface, volcanic ash particles alternated in the water column and in the sedimentary column. Minerals were often etched, reworked to other minerals, and, thus, ions were released into the seawater and pore water. Due to the alteration of volcanic ash, clay minerals like smectite and palagonite were formed (Bonatti, 1965; Kawano

and Tomita, 2001; Teichert et al., 2009). Larsen et al. (2003) denoted heavily altered ash layers that were changed to clayey layers (also Madirazza and Fregerslev, 1969; Malm et al., 1984; Morton and Knox, 1990). Assuming the formation of clay minerals at the level of an ash layer, the formation of a layer with a lower permeability was established. This impermeable layer prevented pore waters, which bore a certain amount of captured pore water and Zechstein salt brines to migrate upwards causing supersaturation of Ca^{2+} and HCO_3^- . All glendonite crystals found within carbonate concretions stem from the Northern part of the island Mors (Tab. 3). Jørgensen et al. (2005) mapped the underground structures of Mors via large-scale transient electromagnetic method (TEM) surveys. They were able to prove the migration of salt diapirs below Mors and their associated faults. All glendonite sites of Mors are in the vicinity of a fault, which was identified during the study of Jørgensen et al. (2005). Glendonite moulds were observed on Fur at the Knudeklint site. Unfortunately, no TEM survey was conducted on the island of Fur, but a salt diapir is known ca. 10 km SE of the Knudeklint site (Pedersen and Surlyk, 1983).

In order to check this assumption, Sr and Ca isotopes were measured to gain insight into the origin of the Ca^{2+} ions that are needed to form ikaite. $^{87}\text{Sr}/^{86}\text{Sr}$ ratio vary depending on the source of Sr (Fig. 31). Zechstein salts, volcanic ash layers, sea water, and the riverine inflow of weathered continental rocks contribute to the Sr pool. Hence, the measured $^{87}\text{Sr}/^{86}\text{Sr}$ ratios point to the Sr source. All rCc and ri cements plot below the seawater $^{87}\text{Sr}/^{86}\text{Sr}$ values of Howarth and McArthur (1997), McArthur et al. (2001), and Hodell et al. (2007). Solely the fill cements have higher ^{87}Sr values. Therefore, they range within or above those of the reconstructed Early Eocene seawater (Fig. 31). Almost all $^{87}\text{Sr}/^{86}\text{Sr}$ values of the bulk analyses depict lower, less radiogenic ^{87}Sr depleted isotopic compositions than the various cements. Due to the fact that the volcanic ash layers depict Sr values between 0.704 and 0.706 (Larsen et al., 2003) or between 0.704 and 0.705 (Morton and Evans, 1987), the alteration of volcanic ash layers was identified as another Sr source (Fig. 32). An additional, but possible, Sr source could have been the brines of the Permian Zechstein salt diapirs. Just like Veizer and Compston (1974), Burke et al. (1982), and Martin and MacDougall (1995), Rahimpour-Bonab et al. (2009) analysed $^{87}\text{Sr}/^{86}\text{Sr}$ values of 0.7069 to 0.7075 within the anhydritic limestones of the Dalan Formation of the Persian Gulf. Due to the fact that the rCc and ri cements of the glendonite and all bulk analyses fall below the estimated seawater Sr values, it cannot be excluded that Permian salt brines migrated upwards into the Fur Formation.

Mixing calculation (see equation 4) using $^{87}\text{Sr}/^{86}\text{Sr}$ values of Early Eocene seawater (McArthur et al., 2001) and of the ash layers of the Fur Formation point to max. 2% Sr^{2+} from the volcanic ashes for the formation of ikaite.

$$^{87}\text{Sr}/^{86}\text{Sr}_{\text{meas}} = c[\text{ash}] * ^{87}\text{Sr}/^{86}\text{Sr}_{\text{ash}} + c[\text{seawater}] * ^{87}\text{Sr}/^{86}\text{Sr}_{\text{seawater}} \quad (4)$$

Using the Early Eocene seawater $^{87}\text{Sr}/^{86}\text{Sr}$ ratio of McArthur et al. (2001) and an average value of 0.7072 for the Zechstein salt brine, a proportion of 4 – 7% Zechstein salt brine was calculated for the ikaite formation. The biggest part of the Sr^{2+} ions stem from the seawater that was entrapped within the sedimentary column after the deposition of the diatoms and the ash

layers. The fill cements bear $^{87}\text{Sr}/^{86}\text{Sr}$ enriched values pointing either to seawater influence during the diagenesis or, more probable, to later diagenetic ^{87}Sr enriched pore waters.

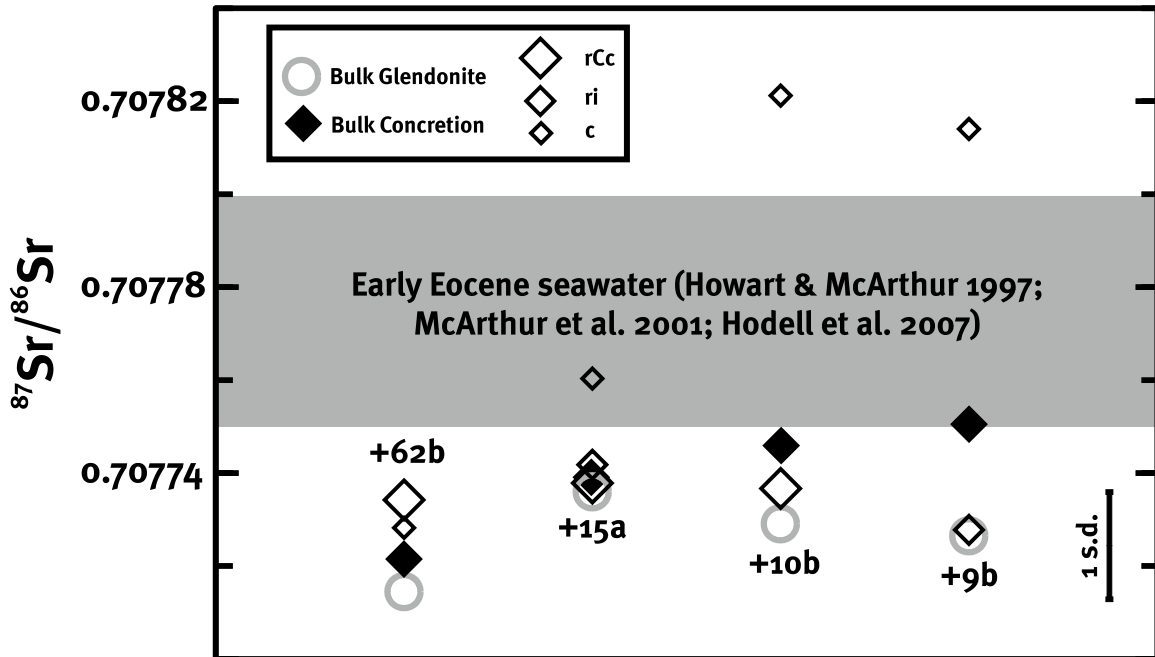


Fig. 31: $^{87}\text{Sr}/^{86}\text{Sr}$ of bulk samples and drilled cement phases of the glendonites and their surrounding carbonate concretions. The $^{87}\text{Sr}/^{86}\text{Sr}$ ratio of seawater at the time point of 55.5 m.a. for ash layer +19 as an average value is shown as shaded area.

In addition to Sr isotopes, the $^{44}\text{Ca}/^{40}\text{Ca}$ isotopic composition was determined to identify possible Ca^{2+} sources (Fig. 33). All $\delta^{44/40}\text{Ca}$ values lie in a range between 0.57 and 0.80‰ normalised to the standard SRM915a. An increase in ^{44}Ca enriched values is discernible from the lower glendonite bearing horizons to the highest glendonite horizon of ash layer +62. The average value of the glendonite of ash layer +9 was 0.62‰, followed by ash layer +10 and +15b,c with 0.71‰ to 0.76‰ at ash layer +62. The higher $^{44}\text{Ca}/^{40}\text{Ca}$ values of the +62 glendonite material can indicate that the depth of formation of the +62 glendonite occurred higher in the sedimentary column than at the older glendonite layers between +9 and +16. Due to the formation of calcite in the upper metres of the sedimentary column, the $^{44}\text{Ca}/^{40}\text{Ca}$ isotopic composition and the calcium concentration decrease with depth (Teichert et al., 2005).

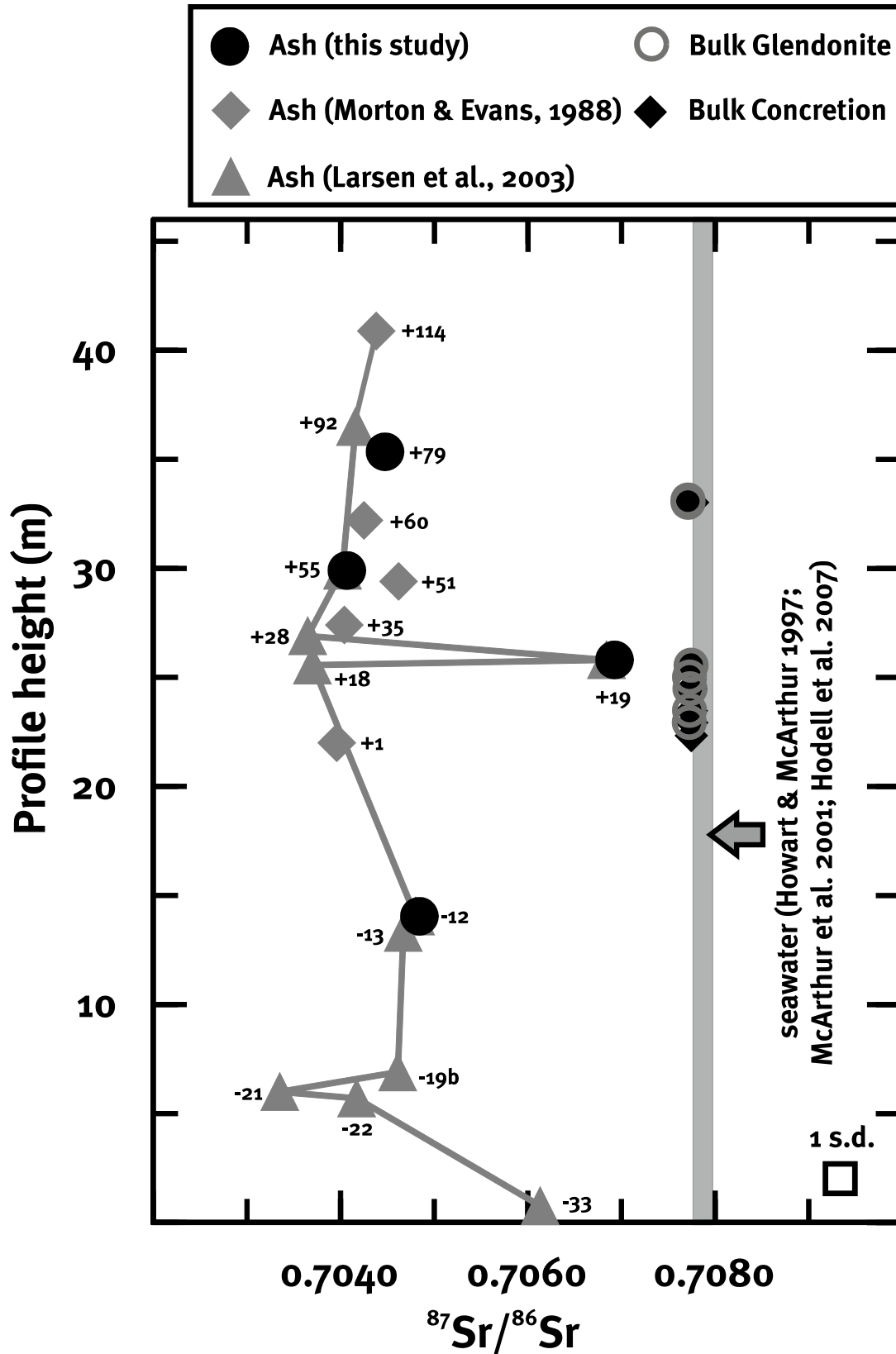


Fig. 32: $^{87}\text{Sr}/^{86}\text{Sr}$ ratios of bulk powders of glendonite crystals and their surrounding carbonate concretions together with the $^{87}\text{Sr}/^{86}\text{Sr}$ ratios of volcanic ash layers and Eocene seawater.

De La Rocha and DePaolo (2000) estimated a Ca isotopic composition to be -0.3‰ (normalised to a standard used by Skulan et al. (1997)) for Early Eocene marine carbonates. Recalculation this value into an SRM915a normalised value yields a value of $+0.7\text{‰}$ SRM915a (Nikolaus Gussone, pers. comm.). Assuming a similar isotope fractionation, the Ca^{2+} ions stem from the overlying seawater that was trapped in the sedimentary column after the accumulation of the sediments. Comparing Early Eocene seawater value of 0.7‰ SRM915a to other Cenozoic seawater values, the Early Eocene seawater was enriched in the heavy ^{44}Ca isotope due to a higher weathering input as the result of global warming (De La Rocha and DePaolo, 2000). Due to the fact that our data exclusively reflect the estimated value of Eocene seawater, the ikaite and subsequent glendonite were formed in a proximal layer that was located not very deep in the sedimentary column. The $\delta^{44/40}\text{Ca}$ isotope data of the fill cements are little enriched in ^{44}Ca which could be a sign of bigger depth of formation or later diagenetical processes, which was already seen within the carbonate oxygen isotopes as well.

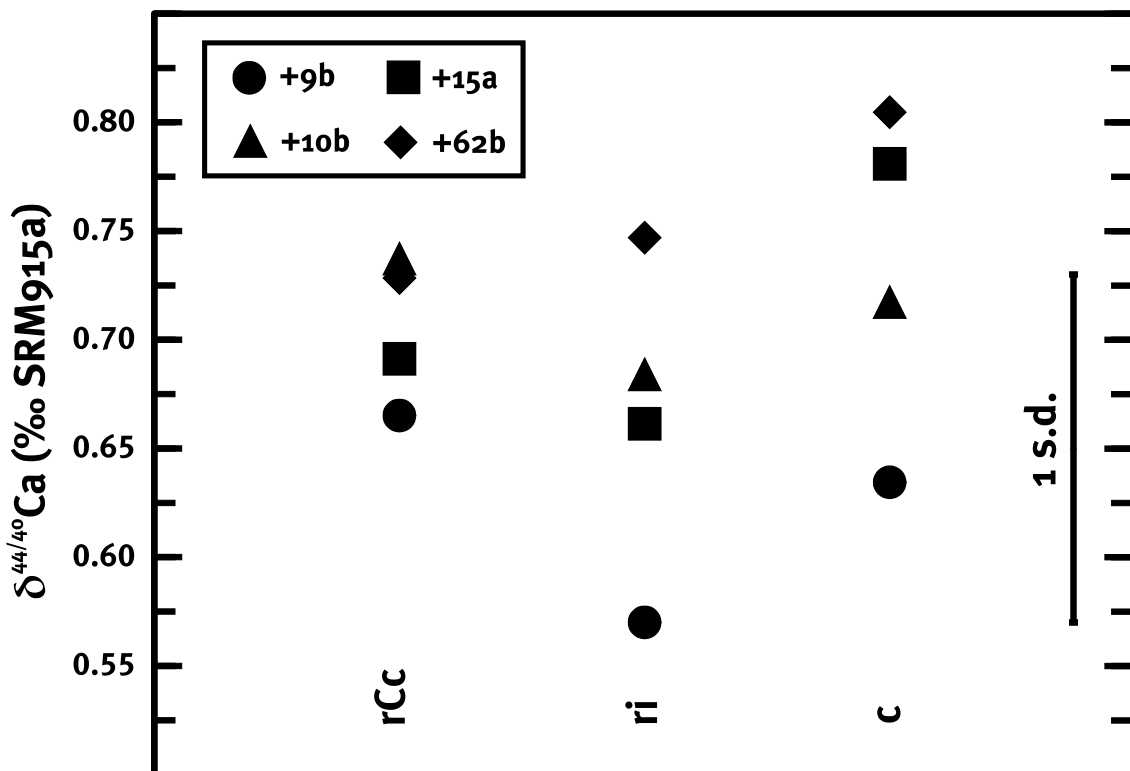


Fig. 33: $\delta^{44/40}\text{Ca}$ isotopes of various cement generations within the glendonite.

5.1.6 Paleoenvironmental conditions of ikaite formation and transformation

As already discussed in chapter 5.1.2, ikaite is believed to have formed at shallow depths in the sedimentary column. Few metres of the shallow subsurface were denoted to be the formation depth of ikaite by several authors (Boggs and Hull, 1975; De Lurio and Frakes, 1999; Frank et al., 2008; Pedersen et al., 2011; Teichert and Luppold, 2013). Ikaite is expected to form within the uppermost 10 metres below the sediment-water interface due to plastically deformed surrounding sediments.

The Fur Formation exhibits a high content of organic matter. Microbially induced remineralization of organic matter results in an enrichment of phosphorous levels in the pore water. This might have caused the formation of ikaite while the formation of calcite and aragonite was prevented (e.g. Bischoff et al., 1993; Hu et al., 2015). A high total sulphur content in the surrounding carbonate concretions and in two glendonite samples of ash layers +9 and +15 suggests anoxic conditions in the pore waters.

The $\delta^{34}\text{S}$ and $\delta^{18}\text{O}$ values of the CAS were measured in order to gain further insights into the process of ikaite formation. Clearly, the $\delta^{18}\text{O}_{\text{CAS}}$ and $\delta^{34}\text{S}_{\text{CAS}}$ values of the glendonite are more enriched in ^{18}O and ^{34}S than the respective carbonate concretions (Fig. 34). The lowest $\delta^{18}\text{O}_{\text{CAS}}$ and $\delta^{34}\text{S}_{\text{CAS}}$ values of glendonite were measured for those samples exhibiting the highest concentrations of pyrite. The $\delta^{34}\text{S}_{\text{CRS}}$ values of these pyrites range between -27 and -35‰ for glendonite +9b and +15c, respectively.

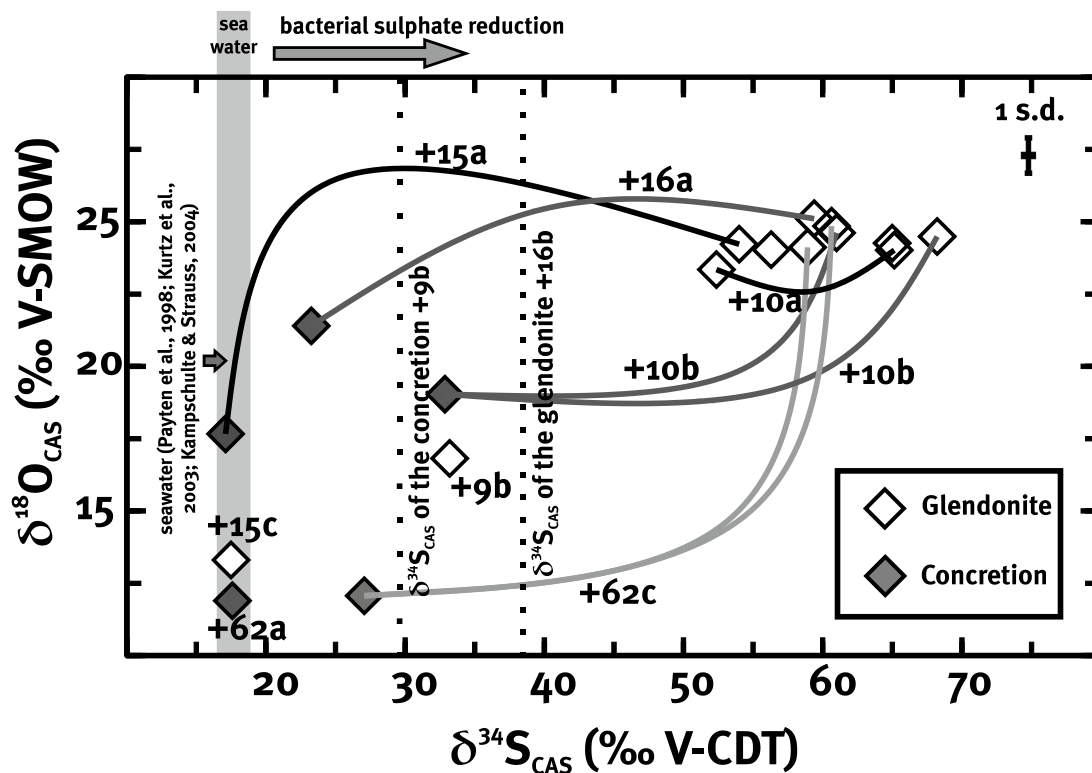


Fig. 34: $\delta^{18}\text{O}_{\text{CAS}}$ and $\delta^{34}\text{S}_{\text{CAS}}$ values are given in this diagram. Glendonites and their surrounding carbonate concretions are linked with a line.

Most glendonite samples display $\delta^{34}\text{S}_{\text{CAS}}$ values between +50 and +70‰ pointing to the zone of sulphate reduction via microbial organic matter degradation (Fig. 34). Loyd et al. (2012) studied the formation of concretions and its impact on the sulphur and oxygen isotopic composition of CAS. These authors delineated four different groups indicating differences in the depositional framework. The glendonite of the Fur Formation frequently falls within group 2 of Loyd et al. (2012), i.e. precipitation in the zone of sulphate reduction. The glendonite of ash layers +9b, +15c and +16b display $\delta^{34}\text{S}$ values between +15 and +40‰ suggesting that they were formed in shallower depths of the sedimentary column or during weaker OSR. Due to its high CAS concentration, which is close to the sulphate concentration of Eocene seawater of 7 mM (Wortmann and Paytan, 2012), the CAS values of the +62 glendonite fall into group 1 of Loyd et al. (2012) and, thus, suggest a formation at shallower depth possibly within the nitrate reduction zone. In general, the $\delta^{34}\text{S}$ values of the glendonite are much higher, i.e. ^{34}S enriched, compared to Early Eocene seawater with values between +17 and +19‰ (Paytan et al., 1998; Kurtz et al., 2003; Kampschulte and Strauss, 2004).

The carbonate concretions were formed after the ikaite to glendonite transformation which is in contrast to a proposed syngenetic formation of carbonate concretions (Boggs and Hull, 1975; Geptner et al., 2014). Instead, the carbonate concretions formed during early diagenesis and at low compaction as indicated by the high carbonate content of ca. 75 to 80 wt%. Boggs (1972) recorded no compaction at the time of the ikaite formation and proposed reducing conditions within a watery, organic-rich mud that was enriched in S, CO_2 , H and N due to the decay of organic matter. As displayed in figure 34, the concretions exhibit the lowest $\delta^{18}\text{O}_{\text{CAS}}$ and $\delta^{34}\text{S}_{\text{CAS}}$ values, but the concretions were still categorised in group 2, i.e. sulphate reduction, of Loyd et al. (2012) (Fig. 35). Because of the lower sulphur isotopic values of the concretions similar to the $\delta^{34}\text{S}$ of the seawater, the concretions are supposed to have formed in early diagenetic processes under use of the seawater sulphate as main sulphur source for the OSR. Since carbonate concretions formed after the transformation of ikaite to glendonite, the carbonate concretions formed in a phase of decreased sulphate reduction. This was triggered by the limitation of one parameter required for the organotrophic sulphate reduction via microbial decomposition of organic matter.

In summary, ikaite grew after the deposition of the diatomite and the ash layers, followed by the transformation from ikaite to glendonite. The ikaite formed within the zone of organotrophic sulphate reduction under use of entrapped seawater (Ca^{2+} and SO_4^{2-} ions) and organic matter below bigger ash layers that were alternated to impermeable clayey layers. The transition from ikaite to glendonite occurred due to shifts in the geochemical boundary conditions. Yet, the period for this transition remains elusive.

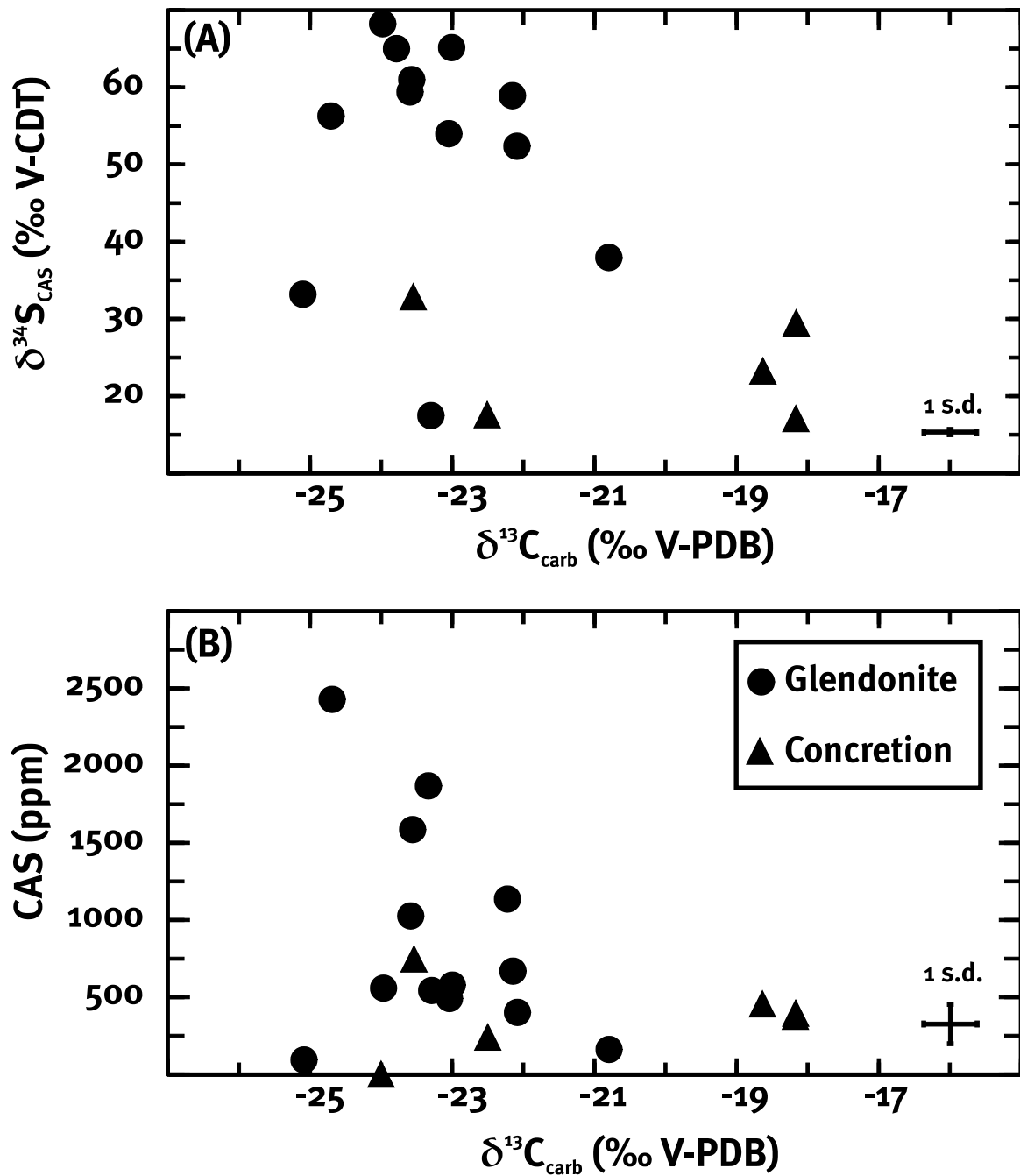


Fig. 35: Plot of CAS data of glendonite crystals and their surrounding carbonate concretions with (A) the $\delta^{34}\text{S}_{\text{CAS}}$ values and (B) the content of CAS are plotted against the $\delta^{13}\text{C}_{\text{carb}}$ values of the glendonite crystals and their surrounding carbonate concretions.

5.2 Carbonate concretions and volcanic ash layers of the Fur Formation

5.2.1 Volcanic ash layers – Their possible impact on the formation of carbonate concretions

Bøggild (1918) was the first to describe ash layers of the Fur Formation and to establish a numbering of 179 ash layers. He proposed a negative ash series with 39 ash layers and a positive ash series with 140 ash layers. Due to difficulties during his first field observations in the years 1913 to 1916, Bøggild solely noticed the positive ash series and numbered its ash layers. At some point, he realised that below these ash layers there are of them and he decided to give them negative numbers and to keep the numbering of the positive ash series, because ash layer +1 is well recognizable for correlation purposes (Bo Schultz, pers. comm.). Many other authors have described volcanic ash layers of the same origin deposited on the European continent and within the North Sea Basin (e.g. Knox and Harland, 1979; Huber et al., 2003; Larsen et al., 2014).

The volcanic ash layers consist of yellow, dark brown to black sharp-edged glass particles of a grain size ranging from fine sand to coarse silt (Pedersen et al., 1975; Pedersen and Surlyk, 1977; Larsen et al., 2003; Pedersen et al., 2011). Graded bedding was observed in most of the investigated ash layers (Bøggild, 1918; Pedersen, 1981; Pedersen et al., 1975, 2011). Dish and pillar structures within ash layers due to upward decreasing permeability have been found in ash layers +114 and +118. In these layers, water was released after the deposition of the specific ash layer forming these structures (Pedersen, 1981; Pedersen et al.; 2011).

In this study, two ash layers (+9 and +62; Tab. 12) were investigated using a microprobe. Geochemical compositions are comparable to data reported by Madirazza and Fregerslev (1969), Pedersen et al. (1975), and Larsen et al. (2003), except for lower Al concentrations in both samples. Larsen et al. (2003) defined both ash layers to be evolved, tholeiitic ferrobasalts, which stem from comagmatic eruptions of one single igneous suite, the East Greenland Gardiner complex. These tholeiites were formed within the rift during the widening of nascent Proto-Iceland, where a violent phreatomagmatic activity in shallow water depth occurred caused by the contact of magma with the seawater (Larsen et al., 2003).

The $^{87}\text{Sr}/^{86}\text{Sr}$ ratios were measured for four ash layers with values ranging between 0.704 and 0.707 (Fig. 36). The data are comparable to results published by Morton and Evans (1988) and Larsen et al. (2003) (Tab. 13) and even the high $^{87}\text{Sr}/^{86}\text{Sr}$ value of 0.707 of ash layer +19 was reproduced pointing to changes in the $^{87}\text{Sr}/^{86}\text{Sr}$ ratio due to another ash chemism. The ash layer +19 is a rhyolite of peralkaline composition ejected during a cataclysmic eruption in the rift zone (Larsen et al., 2003).

The ash layers usually resulted from a single eruption, but a few ash layers are double layers (ash layers +14, +16, +18, +30, and +90) containing two graded ash layers deposited on top of each other. These two eruptions are thought to have taken place within one year (Bøggild, 1918; Larsen et al., 2003). Following their eruption, the volcanic ash particles were transported by prevailing winds (Pedersen et al., 1975) in SE direction over a distance of 1,200 km (e.g. Knox and

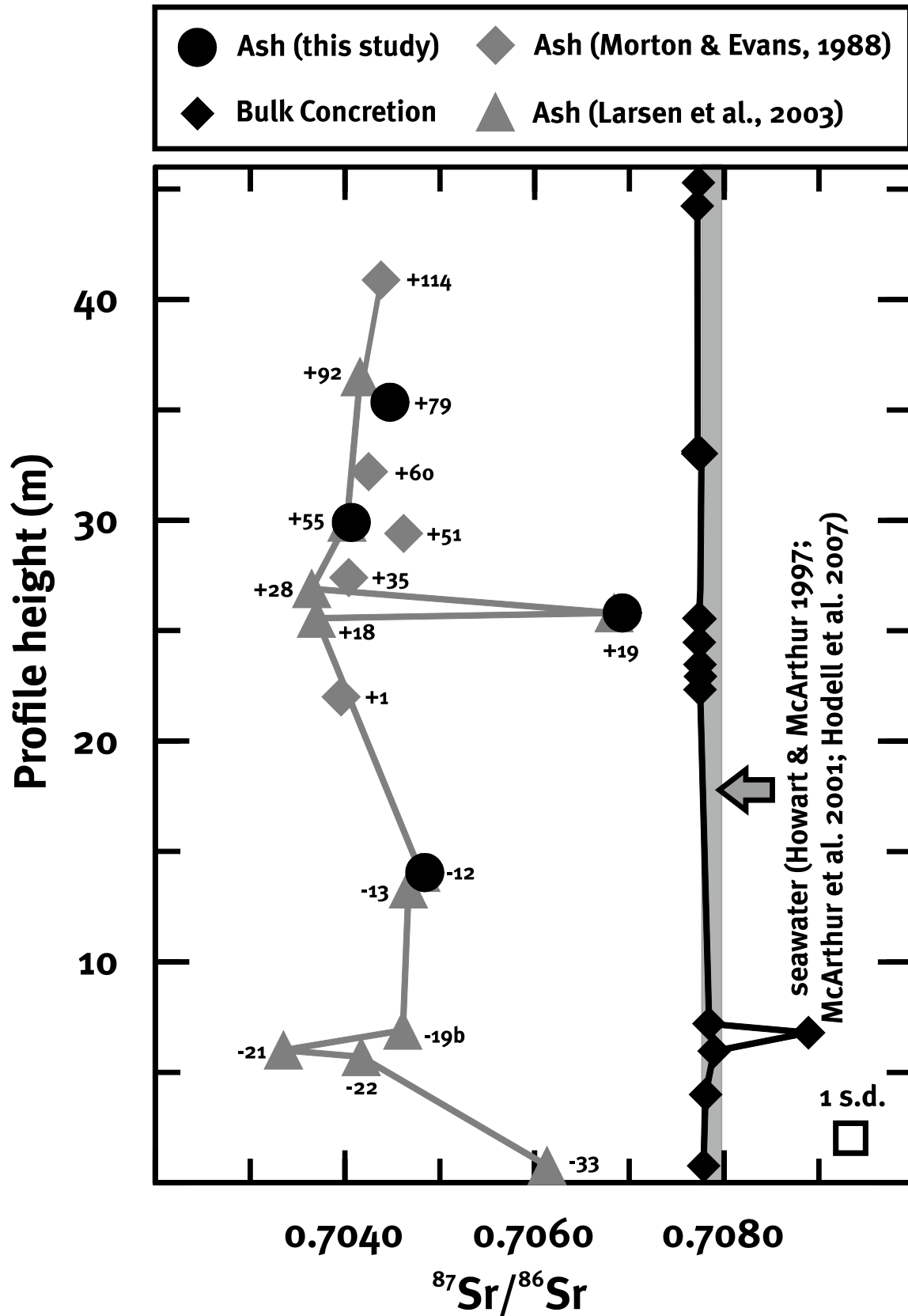


Fig. 36: Bulk $^{87}\text{Sr}/^{86}\text{Sr}$ ratios of carbonate concretions together with $^{87}\text{Sr}/^{86}\text{Sr}$ ratios of volcanic ash layers and Eocene seawater.

Harland, 1979; Pedersen et al., 2011). The settling rate of the volcanic ash layers within the marine water column was very high, as only few diatoms can be found within the ash layers. All volcanic ash particles settled down within a few days, as calculated by Pedersen (1981), who computed a duration of three days for the settlement of fine-grained sand particles at a speed of 15-60 cm/min and a water depth of maximum 500 m. Clay minerals found within diatomite above volcanic ash layers are thought to represent weathered ash material, which was transported into the Danish Basin by rivers (Madirazza and Fregerslev, 1969; Kender et al., 2012).

Volcanic glass particles were directly altered after the fall out. Thus, many mineral phases, which are usually found in fresh airborne ash deposits, could not be identified within the volcanic ash layers (Pedersen et al., 2011). Water-rock interactions in a cool environment were previously proposed in this work (chapters 5.1.3 and 5.1.5). Halmyrolytic processes led to the formation of montmorillonite at moderate pH and negative Eh (Madirazza and Fregerslev, 1969; Fairbridge, 1967). Smectite, a product of pyroclastic rock weathering, is often found within volcanic ash layers and in the diatomite (Heilmann-Clausen et al., 1985). Seafloor weathering and other alteration processes produce high volatile contents within volcanic ash particles (Larsen et al., 2003; Fig. 19 C and D). According to Larsen et al. (2003), the volcanic ashes gained SiO_2 and Al_2O_3 and lost Fe, CaO, and MgO in the Silstrup Member. Compared to the ash layers of the Knudeklint member, those of the Silstrup Member are less altered, but some are also partially converted to clay minerals (Pedersen et al., 2011).

The best preservation of ash particles is given in the carbonate concretions showing the least amount of clay minerals (Pedersen et al., 1975; Larsen et al., 2003). Carbonate concretions are often spatially connected to volcanic ash layers. While glendonite is frequently found below ash layers, the carbonate concretions grew around the volcanic ash layers. Hence, ash layers can often be traced into the centre of the carbonate concretions. It is proposed here that the volcanic ash layers might have acted as a nucleus for the growth of the carbonate concretions. Their formation could have been triggered by the leaching of ions from volcanic ash layers caused by water-rock interactions. Pedersen and Buchardt (1996) described that the horizontal permeability exceeded the vertical permeability within volcanic ash layers. This can indicate that the carbonate concretions formed as a result of a high ion concentration in pore waters around volcanic ash layers.

The $\delta^{18}\text{O}_{\text{carb}}$ data of the volcanic ash layers show slightly ^{18}O enriched values when compared to the values of the diatomite within the carbonate concretions. This could be a consequence of the low temperature alteration of volcanic glass particles lowering the oxygen isotopic composition of the pore water (Lawrence et al., 1979; Lawrence and Taviani, 1988; Mozley and Burns, 1993; Dale et al., 2014) and causing a ^{18}O enrichment within the carbonate cement of the ash particles.

5.2.2 Carbonate concretions – shape and composition

The carbonate concretions vary in size and distribution, they are 5 to 70 cm thick, and ellipsoidal in shape. Most concretions and cemented layers are found within the Silstrup Member. This was already delineated by various authors (Benda, 1972; Pedersen et al., 1975; Pedersen, 1981; Pedersen and Surlyk, 1983; Pedersen and Buchardt, 1996; Pedersen et al., 2011).

Forchhammer (1835) described cemented horizons between ash layers -13 and -10, between +25 to +30, at +101/+102, and at +130. Andersen (1948) proposed that pore waters cemented layers into cementstone and he described that most of the cementstone occur between ash layers +25 and +30. Pedersen and Buchardt (1996) added two horizons: one between ash layers -11 and +1 and the other below +19. Carbonate concretions locally occur above ash layer -17 and between ash layers +60 and +62 (Pedersen and Buchardt, 1996; Pedersen et al., 2011). They concluded that concretions are genetically more linked to distinct stratigraphic levels than to a certain sedimentary facies or to the distribution of fossils.

The highest carbonate concentration (CaCO_3) was detected in the centre of most of the concretions, but the highest CaCO_3 content was measured in the lower part of a few concretions, too. The higher CaCO_3 concentrations might indicate that the formation of the carbonate concretion started in the centre and at the lower part or that the rim material leached out during weathering processes. As the concretion started growing, the enclosing sediments got compacted resulting in a lower CaCO_3 concentration at the margin (Raiswell, 1971; Oertel and Curtis, 1972; Coleman, 1993; Pedersen and Buchardt, 1996). The lowest CaCO_3 concentration within carbonate concretions was measured within the ash layers. The initial porosity of the sand sized volcanic ash was lower than the porosity of the diatomite resulting in lower carbonate contents in the ash layers. According to Nielsen (1974), the concentrations of Ca and Mn are enriched within the concretions, while Fe and Mg are depleted. Furthermore, the porosity is greater inside the concretion than outside within the host sediment (Nielsen, 1974). Pedersen and Buchardt (1996) proposed that the present porosity of the incorporated diatomite ranges around 60%.

5.2.3 Carbon cycling within the Fur Formation – Signals from the PETM?

In several concretions, the lightest $\delta^{13}\text{C}_{\text{carb}}$ value was measured in the centre of the particular concretion. The distribution of the $\delta^{13}\text{C}_{\text{carb}}$ is not entirely the same: some concretions display variations across the whole concretion in their $\delta^{13}\text{C}_{\text{carb}}$ isotopic composition. Hence, no trend was visible in the distribution of the $\delta^{13}\text{C}_{\text{carb}}$ values within those concretions. In contrast to observations made in this study, Pedersen and Buchardt (1996) did not detect any systematic change in $\delta^{13}\text{C}$ within a concretion. The $\delta^{13}\text{C}_{\text{carb}}$ values of the calcitic bound volcanic ash layers fall within the same $\delta^{13}\text{C}_{\text{carb}}$ range of the diatomite bearing concretions (Fig. 22).

The $\delta^{13}\text{C}_{\text{carb}}$ values of the concretions range between -26 to -15‰ V-PDB suggesting that the formation of the carbonate concretions was mostly driven by organotrophic sulphate reduc-

tion (OSR), using C_3 plants mixed with carbonates from other sources like the anaerobic oxidation of methane. Minor contributions to the carbonate pool are dissolved marine limestones and marine DIC. Some carbonate concretions, like the ones in the interval between ash layers -20 and -13, exhibit ^{13}C enriched $\delta^{13}C_{carb}$ values suggesting the process of methanogenesis for their carbonate source.

The $\delta^{13}C_{carb}$ values across the Fur Formation display higher, ^{13}C enriched values between ash layers -20 and -13, but smaller shifts are detectable across the whole section (Fig. 37). In total, the $\delta^{13}C_{carb}$ values of the calcitic concretions range between -24 and -6‰, whereas the ankerite concretion of ash layer -20 and the dolomite concretion of ash layer -17 depict ^{13}C enriched values with +6 and +7‰, respectively. Pedersen and Buchardt (1996) measured similar $\delta^{13}C_{carb}$ values between -23 and -6 and concluded that these values indicate an intermediate mixture between DIC derived from the mineralization of organic matter and normal marine DIC, with bacterial DIC being the dominant carbon source. As the carbonate concretions are not bound to lamination and fossils, Pedersen and Buchardt (1996) explained the formation of these carbonate concretions via blooms of plankton that produce organic carbon and $CaCO_3$, which fall onto the seafloor. Both components, the organic carbon and the $CaCO_3$, are used in the process of OSR within the sedimentary column.

The highest C/N ratio was measured in the ankerite sample of ash layer -20 showing a low concentration of N, followed by the dolomite of ash layer -17. The C/N ratio of the dolomite concretion is slightly lower compared to those of the calcitic concretions. Nielsen (1974) reported that the organic-bound carbon concentration is higher in the lowest layers of the Fur Formation and in the cementstone layers. The C/N ratios oscillate across the profile, but the lowest value was measured for the concretion of ash layer -33 (Fig. 37). Diatomite samples taken a short distance above and below ash layer -33 depict C/N ratios between 20 and 30. Hence, the value (0.4) of the concretion -33 is considered as an offset value. In fact, the decarbonated sample of the concretion of ash layer -33 yielded a high volume of non-condensable gases during the preparation for $\delta^{13}C_{org}$ measurements pointing to a chemical behaviour different from all other concretions.

C/N ratios greater than 20 have been identified for terrigenous organic matter, while C/N ratios between 3 and 13 have been measured for marine organic matter (Schulz and Zabel, 2006). The varying C/N ratios across the profile reveal changes in the influx of terrestrial organic matter caused by climate changes (mainly precipitation) resulting in changes in river discharge. Based on their $\delta^{18}O_{carb}$ results, Schmitz et al. (1996) recognised an influence of fresh water input into the Danish Basin in the Early Eocene. According to Knox (1996), the benthic community, the relative dominance of terrestrial palynomorph assemblages, and the composition of clay mineral assemblages point to significant environmental changes at the Palaeocene-Eocene boundary in the North Sea Basin. During the PETM, the abundance and the diversity of benthic foraminiferal assemblages were dramatically reduced, while the sedimentation rate increased, resulting in an increased proportion of terrestrial palynomorphs. This points to a higher terrestrial runoff due to

sea-level fall or climate change resulting in an enhanced humidity in the source areas, which is a usual phenomenon of climatic warming (Knox 1996).

In the data analysed here, the beginning and the main phase of the PETM could not be analysed, because the layers containing PETM sediments were not accessible during the field trip in 2014. The lowermost $\delta^{13}\text{C}_{\text{org}}$ measurements of diatomite samples at ash layer -33 exhibit values for the beginning of the post-PETM phase (recovery phase), while the carbonate concretions between ash layers -28 and -24 shows an intermediate $\delta^{13}\text{C}_{\text{org}}$ isotopic composition between ash layer -33 and the other $\delta^{13}\text{C}_{\text{org}}$ values of the Fur Formation. In general, the $\delta^{13}\text{C}_{\text{org}}$ values of layers above the recovery phase fluctuate at a constant level between -28 and -26‰ (Fig. 37). A fossil wood sample discovered at ash layer -25 yielded a $\delta^{13}\text{C}_{\text{org}}$ value of -29.8‰ V-PDB. Most of the organic material of the decarbonated samples derived from a mixture of terrestrial and marine plants or algae all using the C_3 photosynthetic pathway.

Heilmann-Clausen and Schmitz (2000) studied the carbon isotopic excursion (CIE), which marks the beginning of the PETM, reporting a strong negative shift in the $\delta^{13}\text{C}_{\text{carb}}$ values in the sediments of the co-occurring Ølst Formation. Pedersen et al. (2004) pointed out that the strong negative shift in $\delta^{13}\text{C}_{\text{carb}}$ values corresponds to the global PETM. Moreover, Schmitz et al. (2004) proposed that the CIE might have been triggered by basaltic volcanism associated with the opening of the Greenland-Norwegian Sea. Schoon et al. (2015) investigated the CIE within glycerol dialkyl glycerol tetraethers (GDGTs) that stem from the marine algae *Thaumarchaeota* in samples of the Stolle Klint clay. In addition, they compared the results of the GDGTs with the $\delta^{13}\text{C}$ values of branched glycerol dialkyl glycerol tetraethers (br-GDGTs) derived from soils at Støre Belt (215 km; SE of the Fur Formation). They concluded that the detectable larger terrigenous CIE was caused by an increase in relative humidity or changes in vegetational types as a consequence of the PETM on land. Kender et al. (2012) denoted that an increased river runoff and a higher regional precipitation in NW Europe maintained elevated C/N ratios, increased formation of kaolinite and dinoflagellates, elevated nutrient levels, and reduced salinity conditions across the Palaeocene-Eocene boundary.

The PETM and the subsequent recovery phase had a duration of ~170 ka (Röhl et al., 2007). The recovery phase of the PETM as recorded in the sediments of the Fur Formation between ash layers -33 and -19b can be monitored using $\delta^{13}\text{C}_{\text{org}}$ values and C/N ratios (Fig. 23 and Fig. 37). According to Willumsen (2004), a pronounced change in marine microflora was determined at ash layer -19b where diatoms point to more shallow water conditions followed by a transgression in the upper part of the Knudeklint Member. While analysing the silicified (opal-CT) layers between ash layers -33 and -19b, Petersen (2016) was able to identify Milankovitch cycles forcing the deposition of unsilicified and silicified layers. The formation of silicified layers was driven by freshwater inputs where the salinity was lowered and the solubility of silica was increased. The deposition of opal-CT overlaps with times of increased solar insolation, while unsilicified layers occurred in times of less solar insolation. He observed 19.9 cycles of a duration

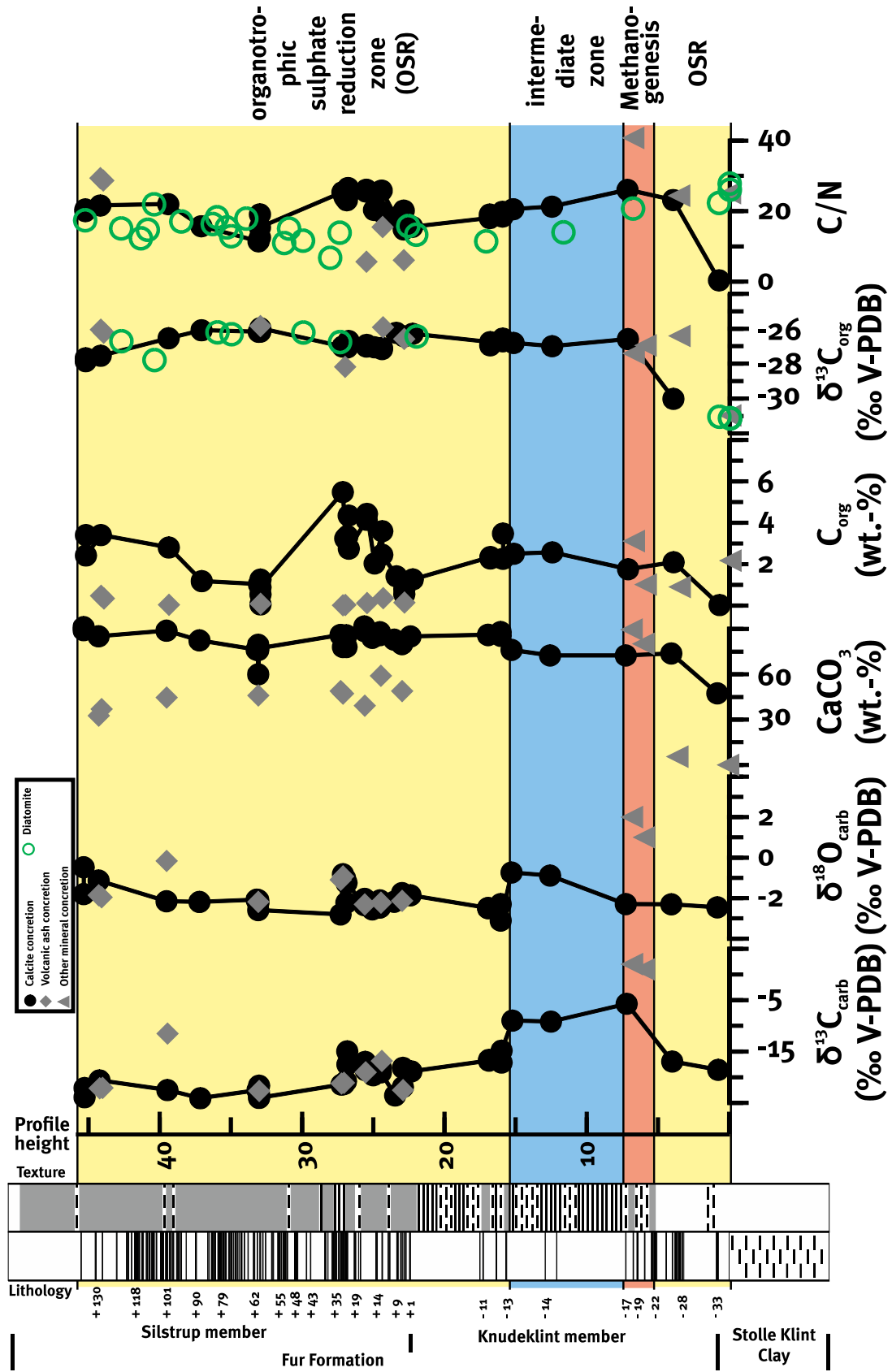


Fig. 37: Profiles of $\delta^{13}C_{carb}$ values, $\delta^{18}O_{carb}$ values, $CaCO_3$, $\delta^{13}C_{org}$ values, and C/N ratio against profile height. The C/N ratio for the ankerite concretion of ash layer -20 with a value of 108 was excluded.

of 11,000 years, 11.5 cycles of 19,000 years (precession), and 4.5 cycles of 48,400 years (obliquity) between ash layers -33 and -19b and he proposed a time span of 184,500 years for the recovery interval of the PETM.

Biomarker were analysed to advance our understanding of the various sources of organic compounds. The samples of ash layers -17 and -11 consist of an unresolved complex mixture that usually reflects biologically degraded material (details in chapter 4.2.4). The compounds of n-alkanes found within carbonate concretions derived from terrigenous material, especially plant waxes (Eglinton and Hamilton, 1967). Regarding the fatty acids, the long fatty acid chains of the concretions of ash layers -17 and +135 stemmed from terrestrial organic matter. These compounds were also determined within the surrounding diatomite. Due to the fact that even chains are larger than uneven chains within diatomite samples in their specific plots (Fig. 25), the material within the diatomite is more reduced than in the carbonate concretions. Fatty acids with 24 to 30 carbon atoms derived from eukaryotes and other higher organisms like zooplankton and land plants. Thus, these compounds stemmed from the water column. Biphytanic diacid was observed in the concretion of ash layer -17 and, for this, planktic archaea were degraded within the water column, which could be proven with an isotope value of -22‰ for this compound. The dialcohols found in some of the samples derived from algae. The n-alcohols determined within concretions originated from land plants (Daniel Birgel, pers. comm.). Summarizing, most organic compounds investigated in samples of the Fur Formation were transported by rivers from the land to the sea or were produced within the water column.

In summary, bulk carbon isotope values of carbonate concretions point to sulphate reducing conditions during carbonate formation for which marine algal material or detrital terrigenous plant material was reduced by bacteria. In the lower part of the Knudeklint Member, the recovery phase of the PETM is discernible by the distribution of $\delta^{13}\text{C}_{\text{org}}$ values and C/N ratios.

5.2.4 Pore water geochemistry

The diatomite can be found in three textures indicating different depositional environments reflecting the oxygen content at the sediment surface: laminated, weakly laminated, and structureless (bioturbated) diatomite (Pedersen, 1978; Bonde, 1979; Pedersen, 1981; Brooks, 2006; Pedersen et al., 2011; Pedersen and Pedersen; 2012; Fig. 16). The lamination within the Knudeklint Member indicates mostly anaerobic conditions during the deposition of these sediments. In contrast, the Silstrup Member holds more weakly laminated to structureless (bioturbated) diatomite pointing to dysoxic or oxic conditions.

Three kinds of laminae are observed in the laminated diatomite. The first type of the laminae are white to light yellowish in colour and 0.3 to 0.5 mm thick, reflecting large blooming events of a particular diatom species (Pedersen, 1981; Pedersen et al., 2011). The second kind of laminae are yellowish to pale-brown with diatoms of several blooming events and clay transported into the Danish Basin by rivers as background sedimentation. These laminae are 2 to

5 mm thick (Pedersen, 1981; Pedersen et al., 2011). In times of increased river runoff caused by heavy rainfall events, the third type of laminae with an increased concentration of clays was deposited. These laminae are light coloured to greyish and 0.25 mm or thinner (Pedersen, 1981; Pedersen et al., 2011). 38% of the sediments of the Knudeklint Member are laminated diatomite, whereas the percentage of laminated diatomite is only 4% in the Silstrup Member (Pedersen, 1981; Pedersen et al., 2011).

Another facies found within the diatomite is weakly laminated diatomite - a transitional facies between laminated and structureless diatomite (Pedersen, 1981). The Knudeklint Member displays ca. 16% and the Silstrup Member ca. 4% of weakly laminated diatomite. Regarding Pedersen et al. (2011), the weakly laminated diatomite was caused by a scarce benthic fauna in short periods.

The third facies is structureless diatomite with a homogenous mixture of ichnogenera and burrows extending down from ash layers (Pedersen, 1981). 44% of the Knudeklint Member and ca. 84% of the Silstrup Member are structureless (Pedersen, 1981). The ash layers are occasionally very disturbed (Fig. 17 D) and the burrows made in the unconsolidated sea floor by organisms extracting organic matter from the sediments are filled with ash particles (Brooks, 2006; Pedersen et al., 2011). The trace fossils were proposed to be produced by *Chondrites*, *Phycodes*, *Planolites*, *Taenidium*, and *Teichichnus* indicating a slightly more increased oxygen concentration within the bottom water during the deposition of the Silstrup Member (Pedersen and Surlyk, 1983; Pedersen et al., 2011).

A low oxygen concentration in the uppermost sedimentary column was tested by analysing of the water soluble sulphate of the CAS preparation. Most $\delta^{34}\text{S}_{\text{NaCl1}}$ values plot below the analysed $\delta^{34}\text{S}_{\text{CAS}}$ values of Early Eocene seawater with +17 to +19‰ (Paytan et al., 1998; Kurtz et al., 2003; Kampschulte and Strauss, 2004; Tab. 29 and Fig. 38). This indicates that the water-soluble sulphate derived from oxidised pyrites located within the carbonate concretions. These pyrites are thought to have been formed within the upper part of the sedimentary column. Hence, the bottom water and/or pore water was anoxic during the Early Eocene. Solely the values of concretion +9b, +10b and +15a, similar to the Early Eocene seawater $\delta^{34}\text{S}_{\text{CAS}}$ values, reveal oxygenated bottom waters, which was confirmed by investigating structureless sedimentary facies within these concretions.

Due to the fact that the bottom water was anoxic during the deposition of some parts of the Fur Formation (mainly the Knudeklint Member), there had to be a chemocline within the water column or directly at the water sediment interface. Additionally, Zabel and Schultz (2001) denoted that free oxygen can be determined few mm to cm of the sedimentary column, because oxygen is consumed during organic matter degradation processes. Previously, several authors reported a stagnant, poisonous bottom water that was toxic to higher organisms during the deposition of the Fur Formation (Bonde, 1966, 1973; Larsson, 1975; Pedersen, 1981; Beyer et al., 2001; Pedersen et al., 2011; Obst et al., 2015; Petersen, 2016). Thus, laminated sediments point to the lack of benthic animals (Pedersen, 1981; Pedersen and Surlyk, 1983; Schmitz et al.,

1997; Pedersen et al., 2011). For a rapid sedimentation of plankton, a large amount of oxygen was consumed at the sea surface forming of anoxic bottom waters (Pedersen et al., 2011). The age and slow renewal of the bottom water is another reason for its oxygen depletion causing the rise of the lysocline (Schmitz et al., 1996).

Tab.29: The values ($\delta^{34}\text{S}$ values, $\delta^{18}\text{O}$ values, concentration of SO_4^{2-}) of the water-soluble sulphates (NaCl_1) and CAS are given.

Ash layer	Sample ID	Profile height (m)	Type	Cement type	$\delta^{34}\text{S}_{\text{CAS}}$ (‰V-CDT)	$\delta^{18}\text{O}_{\text{CAS}}$ (‰V-SMOW)	$\text{SO}_{4\text{CAS}}$ (ppm)	$\delta^{34}\text{S}_{\text{NaCl}_1}$ (‰V-CDT)	$\text{SO}_{4\text{NaCl}_1}$ (ppm)
+130	+130a	44.24	diatomite	calcite	26.80	22.43	1159	-26.55	696
+62	+62a	33.12	diatomite	calcite	17.60	11.89	244	-0.10	228
+62	+62c_3	33.02	diatomite	calcite	27.00	12.06	3	n.a.	1274
+18	+15-19	25.56	diatomite	calcite	26.30	17.28	250	-5.40	486
+16	+16a_1	25.54	diatomite	calcite	23.26	21.39	460	3.84	389
+15	+15a	24.47	diatomite	calcite	17.10	17.66	379	17.00	280
+10	+10b	23.47	diatomite	calcite	32.86	19.04	752	18.45	590
+9	+9b_1	22.92	diatomite	calcite	29.50	n.a.	400	20.30	415
+3	+3/4	22.33	diatomite	calcite	23.83	12.95	238	6.90	1090
-17	-17a	7.20	diatomite	calcite	12.50	8.08	434	0.40	2421
-17	-17b	6.80	diatomite	dolomite	n.a.	n.a.	23	-23.50	1310
-24	-24-28	4.00	diatomite / ash layer	calcite	-5.60	2.88	297	-22.50	3644
-33	-33	0.77	diatomite	calcite	n.a.	n.a.	239	0.50	592

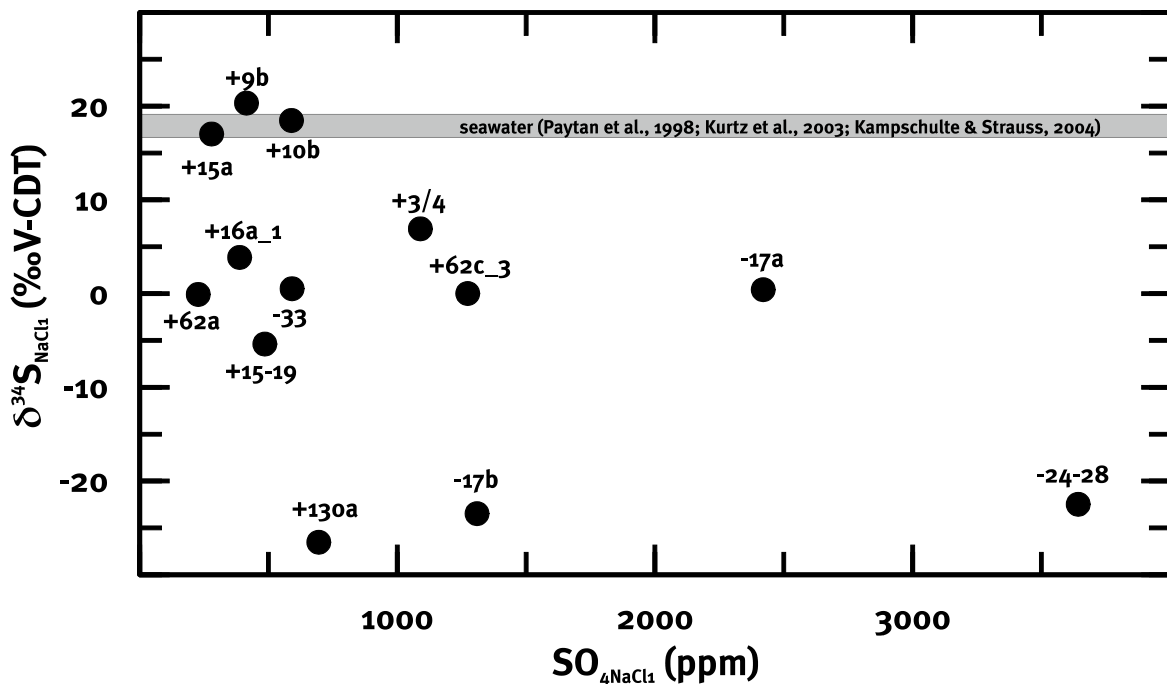


Fig. 38: Concentration and $\delta^{34}\text{S}$ values of the first water-soluble sulphates (NaCl_1) processed during the CAS extraction.

In contemporary upwelling zones, a chemocline is found in a counterflow parallel to the coast at a depth of a few hundred meters where nutrients are recycled causing a rich pelagic wildlife in the surface waters. A stable three-layer system with maintained oxygen deficiency in a stagnant bottom water body was established in the Early Eocene (Bonde, 1979; Petersen, 2016), where the upper water body was oxygen rich and separated from the lower body mass by the chemocline. Other reasons for the stratification of seawater within the Danish Basin were the

warmer climate (Pedersen et al., 2011) and an enhanced fresh water input from rivers around the basin (Petersen, 2016).

The change from anoxic to dysoxic conditions found within the sediments of the Fur Formation could be an indicator of the filling of an initial depression in the Danish Basin as recognised by Hallam and Bradshaw (1979) and by Pedersen and Surlyk (1983). Pedersen (1981) denoted that the shift from anoxic to oxic bottom waters was fast and that it was triggered by an external mechanism like climate.

In conclusion, during the deposition of the Knudeklint Member, the bottom water conditions were anoxic. In contrast, during the formation of the Silstrup Member the bottom water exhibited more oxygen, probably caused by an external mechanism.

5.2.5 Diagenetic zones within the sedimentary column

The formation of the carbonate concretions occurred within the sedimentary column where different processes enabled the release of necessary calcium and carbonate ions.

Sr^{2+} ions were incorporated into the calcite crystal lattice. The $^{87}\text{Sr}/^{86}\text{Sr}$ ratios of most of the carbonate concretions plot at the lower boundary of the data reported for Early Eocene seawater (Howarth and McArthur, 1997; McArthur et al., 2001; Hodell et al., 2007; Fig. 36). Applying equation 4 (see chapter 5.1.5) and using $^{87}\text{Sr}/^{86}\text{Sr}$ ratios of Early Eocene seawater and of volcanic ashes as endmembers, the analysed $^{87}\text{Sr}/^{86}\text{Sr}$ values led to the conclusion that less than 5% of the Sr^{2+} ions stem from volcanic ash layers. Only the $^{87}\text{Sr}/^{86}\text{Sr}$ ratio of dolomite concretion -17b of ash layer -17 lies above the Early Eocene seawater $^{87}\text{Sr}/^{86}\text{Sr}$ ratio. This suggests a larger influx of radiogenic Sr from continental weathering or a shift to ^{87}Sr enriched values due to diagenesis.

$\delta^{44}/^{40}\text{Ca}$ values measured for glendonite reveal a seawater origin of the Ca^{2+} ion (see chapter 5.1.5). A similar origin is assumed for the Ca^{2+} ions in the carbonate concretions. This was already proposed by Pedersen and Buchardt (1996) who added pore water dissolution of skeletal material from fish and invertebrates and volcanic dust as two other possible Ca^{2+} sources. According to Pedersen et al. (1975), the tholeiitic ash layers of the Silstrup Member comprise ca. 10% CaO and the partial solution of these ashes could have increased the Ca^{2+} ion pool used for the formation of the carbonate concretions. However, there are no signs of an intensified dissolution of volcanic glass particles. Thus, most of the Ca^{2+} ions stem from the seawater similar to the Sr ions that mainly stem from the same source.

CAS was investigated to identify different diagenetic zones within the sedimentary column via $\delta^{34}\text{S}$ values, $\delta^{18}\text{O}$ values, and CAS concentration. Two carbonate concretions (+15a, +62a) display $\delta^{34}\text{S}_{\text{CAS}}$ values of Early Eocene seawater and their CAS stems from ambient seawater (Fig. 24). For most of the concretions, the $\delta^{34}\text{S}_{\text{CAS}}$ values are ^{34}S enriched compared to the seawater value, which means that the CAS was affected by bacterial sulphate reduction. In contrast, $\delta^{34}\text{S}_{\text{CAS}}$ values for concretions below seawater value indicate a sulphate contribution from the

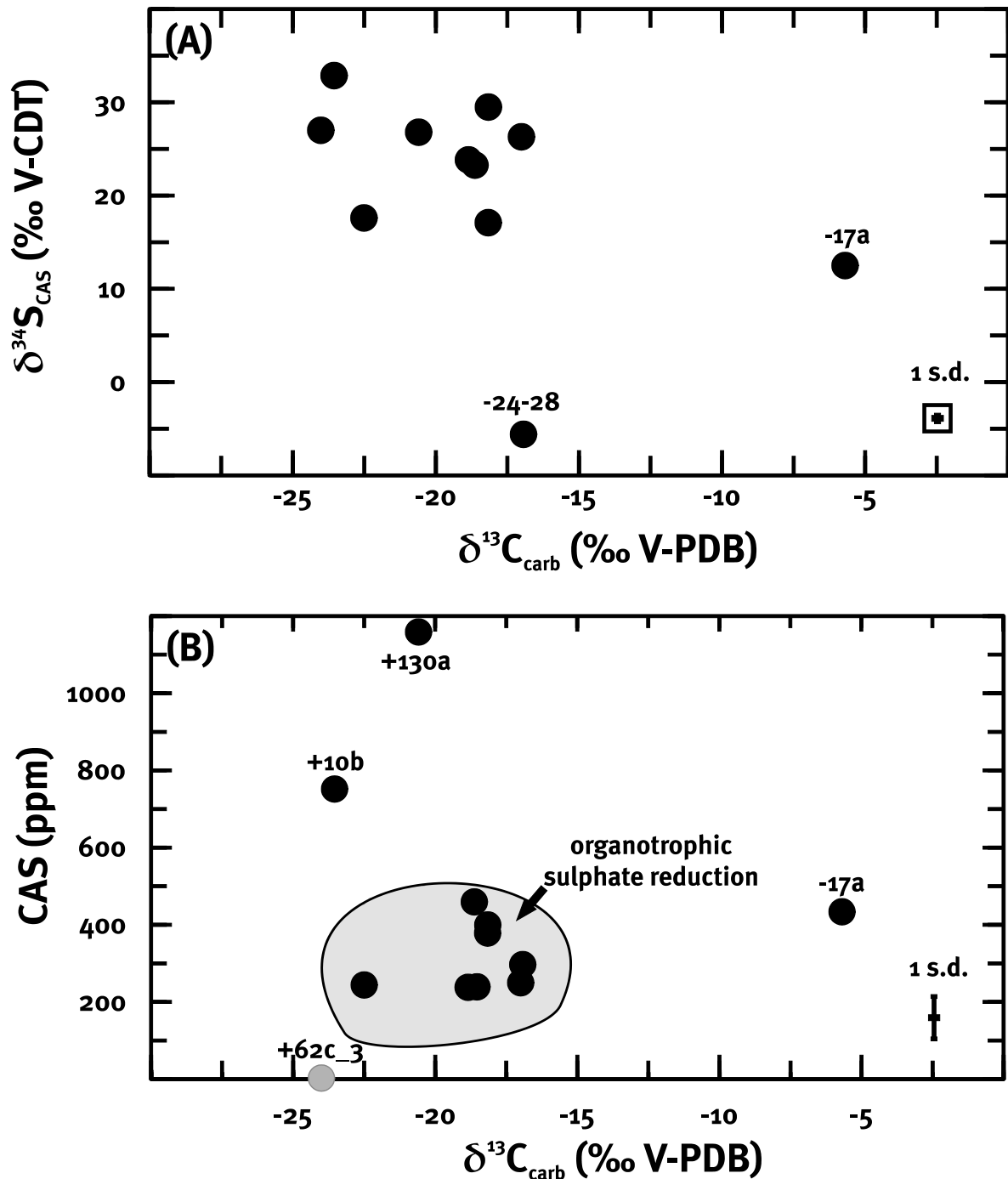


Fig. 39: Plot of CAS data of the carbonate concretions with (A) the $\delta^{34}\text{S}_{\text{CAS}}$ values and (B) the content of CAS plotted against the $\delta^{13}\text{C}_{\text{carb}}$ values of the carbonate concretions.

oxidation of pyrite. Two concretions from the profile (concretion of ash layers +10b and of +130) exhibit very high CAS concentrations (Fig. 39). The CAS concentration of the concretion of ash layer +130 coincides well with higher TS values compared to other carbonate concretions and, therefore, more sulphur was buried within the sediments of the uppermost Fur Formation.

The $\delta^{13}\text{C}_{\text{carb}}$ value of -5‰ for concretion -17a of ash layer -17 led to the conclusion that this concretion was formed by carbonate derived from an admixture of methanogenesis and OSR.

In the same profile height, a dolomite concretion (-17b) was investigated. The dolomite concretion -17b is not illustrated in figure 39, because no $\delta^{34}\text{S}_{\text{CAS}}$ value was measured for this sample. The high $\delta^{13}\text{C}_{\text{carb}}$ value (+7‰), the low CAS concentration (23 ppm), and the biomarker analyses of this concretion (-17b) collectively provide evidence for methanogenesis.

Using all available data to test various formation depths within the sedimentary column, three major zones of the carbonate formation caused by different chemical processes can be discussed: methanogenesis, intermediate zone between methanogenesis and OSR, and OSR (Fig. 37 and Fig. 40).

The diagenetic zone of methanogenesis was recognised in the profile between ash layers -21 and -17, where an ankerite and a dolomite concretion were investigated. The dolomite concretion -17b of ash layer -17 was formed by methanogenesis, because the sample depicts ^{13}C enriched $\delta^{13}\text{C}_{\text{carb}}$ values, and a low CAS concentration. In addition to CAS, biomarker compounds also permit conclusions about this formation process. Hopanoic acids derived from bacteria, whereas archaeol and phytanyl monoetherlipid, both found in dolomite concretion -17b with an isotopic composition of -33‰, could be formed by methanogenic archaea and other methanogenic bacteria within the sedimentary column. Hence, the carbonate formation could have been driven by these bacteria and archaea.

In the profiles (Fig. 37 and Fig. 40), there is an intermediate zone discernible between ash layers -17 and -13. There, the $\delta^{13}\text{C}_{\text{carb}}$ values range between the values of the diagnostic methanogenesis zone and the OSR zone.

The third diagenetic zone is the zone of organotrophic sulphate reduction (OSR). Due to the fact that in some of the concretions, which were formed in the zone of OSR, glendonite is found, the precursor mineral ikaite is supposed to have been formed very early after the deposition of the sediments. After the transformation to glendonite, the carbonate concretions precipitated. Most of the carbonate concretions fall into the area above the Early Eocene seawater $\delta^{34}\text{S}$ value (Fig. 24) and indicate the formation of a higher proportion of bacterial sulphate reduction via degradation of organic matter. The majority of the carbonate concretions plot in the field of the sulphate reduction (Fig. 39). Within this field, lower CAS concentrations, elevated $\delta^{34}\text{S}_{\text{CAS}}$, and negative $\delta^{13}\text{C}_{\text{carb}}$ values were measured. According to Loyd et al. (2012), sulphate reduction produces alkalinity favouring carbonate precipitation if around 40% of the generated sulphide is removed as pyrite. Pyrites investigated within the carbonate concretion point to sulphate reduction prior to the precipitation of the concretion (Raiswell 1976; Raiswell et al., 2002). According to Zabel and Schultz (2001), high $\delta^{34}\text{S}_{\text{CAS}}$ values are found in non-bioturbated sediments, where the diffusion of oxygen was limited. In the biomarker analyses of one of the concretions of the OSR zone (+135), hopanoids and dialkyl glycerol diether (DAGE) were found. Hopanoids were obtained from non specified bacteria, whereas dialkyl glycerol diethers are supposed to be formed by sulphate reducing bacteria (Langworthy et al., 1983; Pancost et al., 2001).

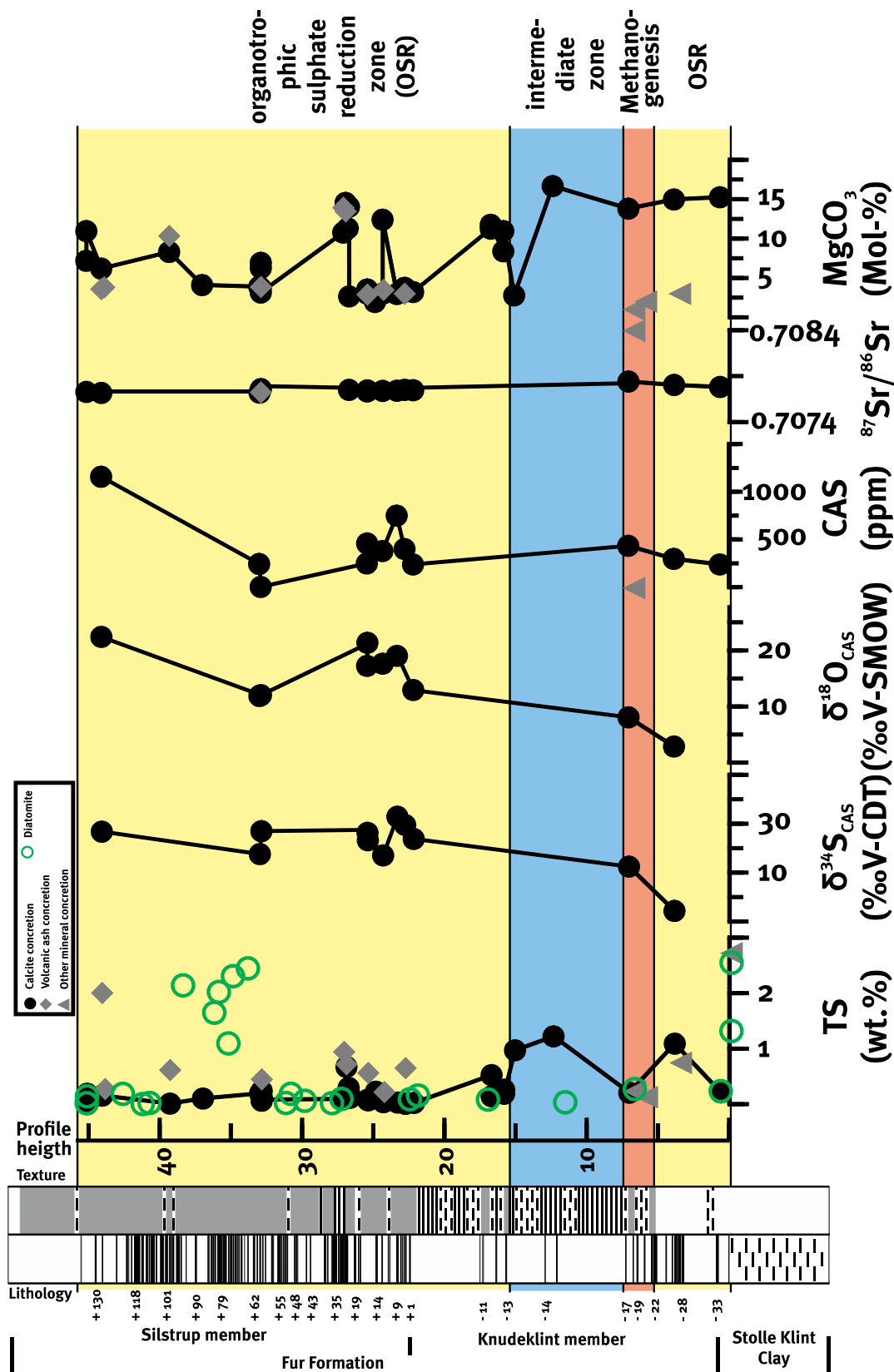


Fig. 40: Profiles of TS, $\delta^{34}\text{S}_{\text{CAS}}$ values, $\delta^{18}\text{O}_{\text{CAS}}$ values, CAS, $^{87}\text{Sr}/^{86}\text{Sr}$ ratios, and MgCO_3 against profile height.

Nielsen (1974) described that anaerobic decomposition of organic carbon during organotrophic sulphate reduction produces ammonia raising the pH values and finally causing the precipitation of carbonates. Pedersen and Buchardt (1996) were the first to link the formation of the carbonates of the Fur Formation with the microbial decomposition of organic matter by sulphate reducing bacteria. Suess et al. (1982) and Buchardt and Holmes (1995) denoted an increased pore water alkalinity due to sulphate reduction in organic rich deposits. Pedersen and Buchardt (1996) proposed that the concretion grew in equilibrium with the pore water in different stages of evolution. Agreeing with Pedersen et al. (2011), the carbonate carbon isotopic composition points to bacterial degradation of organic matter in the sediments as the main carbon source. The $\delta^{13}\text{C}_{\text{carb}}$ values between -30 and -20‰ indicate a less pronounced, secondary carbon source: the anaerobic oxidation of methane.

Most authors state the formation of the carbonate concretion to be of an early diagenetic origin and named different indicators for the early diagenetic age. The most prominent indicator is the porosity that is larger within the concretion than in the surrounding sediments showing that the carbonate concretions were formed prior to the compaction (Pedersen and Surlyk, 1983; Pedersen and Buchardt, 1996; Brooks, 2006; Pedersen et al., 2011). Nielsen (1974) proposed that the compaction was enhanced by the fast settlement of ash layers. Pedersen and Buchardt (1996) added that no obvious displacement structures caused by the formation of the carbonate concretion were found and, thus, the sediment was not compacted during the formation of the concretions.

Petersen (2016) introduced the term eogenesis for the sediments of the Fur Formation. Eogenesis is the earliest diagenetical stage in shallow sedimentary depths with the same conditions found in the bottom water. According to Petersen (2016), the following diagenetical stage, mesogenesis, was not reached. Therefore, the temperatures within the sedimentary column were not higher than 75 °C based on the absence of high temperature clay minerals. Boggs (2009) described high salinity, alkalinity, and alkaline pH conditions within the eogenesis with high concentrations of bicarbonate formed by degradation of organic matter. In this zone, unstable, fine-grained components are dissolved and new mineral phases including pyrite, glauconite, illite, smectite, zeolite, Fe-rich chlorite minerals, feldspar, silica, and carbonates are often formed (Riech and von Rad, 1979; Bjørlykke, 1983; Malm et al., 1984; Morton and Knox, 1990). This could be another fact indicating an early diagenetic formation of these carbonate concretions during the process of the OSR.

Fenchel and Riedl (1970) denoted a discontinuity of the redox potential, i.e. the boundary between dissolved oxygen and hydrogen sulphide (H_2S) in pore fluids, close to the water sediment interface in fine-grained sediments in low-energy depositional environments. Laminated sediments and the water-soluble sulphates analysed during the CAS extraction point out that the redox potential discontinuity must have been within the water column or close to the water sediment interface (see chapter 5.2.4).

The Ca^{2+} and Sr^{2+} ions used for the formation of the carbonate concretions stem from ambient seawater, while the carbonate ions were produced by OSR and subordinate anaerobic oxidation of methane, which was proven by several geochemical proxies. Additionally, two other processes were identified: (i) In the lower part of the Knudeklint Member, organotrophic sulphate reduction and methanogenesis initiated carbonate formation. Hence, the redox potential discontinuity was above the water sediment interface somewhere in the water column. (ii) In the Silstrup Member, this boundary layer is supposed to have been straight few cm below the sea floor. Consequently, all carbonate concretions of the Fur Formation were formed throughout early diagenetic processes within the uppermost 10 m of the sedimentary column.

5.3 Paleotemperatures

5.3.1 Previous paleotemperature estimates for the Fur Formation

Paleoclimatic indications from macrofossil assemblages

Several authors (e.g. Bonde, 1966; Rust, 1998; Pedersen et al., 2011; Bourdon et al., 2016) studied macrofossils in sediments of the Fur Formation. Summarizing the faunal biodiversity, Pedersen et al. (2011) described a percentage share of 31% insects, of 29% fish, and of 12% birds in the macrofossil record. Besides, some other animal remains like reptiles were reported in the last century.

Fossil insects were investigated by several scientists (e.g. Andersen and Andersen, 1996; Rust, 1998; Rust and Andersen, 1999; Archibald and Makarkin, 2006; Pedersen et al., 2011; Rasmussen et al., 2016). 172 fossil bird specimens were identified (e.g. Dyke and Lindow, 2009; Bertelli et al., 2010; Mayr and Bertelli, 2011; Sakala and Gryc, 2011; Pedersen et al., 2011; Bourdon et al., 2016) and also ca. 60 species of marine fish (Bonde, 1966, 1997; Pedersen et al., 2011; Rasmussen et al., 2016). Turtles, marine snakes, and lizards were found, too (Nielsen, 1959, 1963; Bonde, 1966; Pedersen et al., 2011; Rasmussen et al., 2016). Marine invertebrates are represented by snails, crabs, clams, echinoderms, bivalves, gastropods, marine sponges, and decapods (Collins et al., 2005; Pedersen et al., 2011).

Besides a rich fossil fauna, abundant terrestrial plant material, like branches, leaves, fruits, seeds, etc. were found (Hartz, 1909; Koch, 1960; Larsson, 1975; Pedersen et al., 2011). Leaves of *Salvinia*, *Ginkgo* and a cone of *Pinus* were investigated pointing to meadows and slowly moving streams in the continental area characterised by a vegetation with bushes and shrubs.

Based on the fossil record, Bonde (1966) was the first to propose a tropical to subtropical climate. Andersen and Andersen (1996), Lindow and Dyke (2006), and Pedersen et al. (2011) added that the climate was warm and moist with mean annual air temperatures between +15 and +21 °C for the Early Eocene. In addition, Pedersen et al. (2011) concluded that the insect fauna of the Fur Formation provided evidence for a tropical climate with average temperatures some 10 °C higher than today.

Previous paleotemperature estimates for the Fur Formation

Pedersen and Buchardt (1996) reported the first $\delta^{18}\text{O}_{\text{carb}}$ measurements on the carbonate concretions of the Fur Formation. They proposed that respective temperatures represent the temperatures at a shallow sedimentary depth and, hence, also represent ambient seafloor temperatures. Buchardt (1978) measured an average $\delta^{18}\text{O}_{\text{carb}}$ value of -2.5‰ V-PDB for Early Eocene mollusc shells from the North Sea area, but did not calculate a paleotemperature. Following Kim and O'Neil (1997), when taking this $\delta^{18}\text{O}_{\text{carb}}$ value with a $\delta^{18}\text{O}$ value of -4.5‰ V-SMOW for Early Eocene bottom water, a temperature of +4.8 °C results. This temperature value falls into the same temperature range as all the values of this study.

According to Pedersen et al. (2011), the surface temperatures were affected by a short term, hot period in the Early Eocene as a direct consequence of the PETM, whereas less extreme temperatures occurred during the deposition of the Knudeklint Member. Schoon et al. (2015) investigated the glycerol dialkyl glycerol tetraethers (GDGT) (TEX_{86}), the branched and isoprenoid tetraether (BIT) index, and the methylation of branched tetraether/cyclisation of branched tetraether (MBT/CBT) ratio in the sediments of the Fur Formation and of the co-occurring Støre Belt. For the onset of the PETM, a maximum sea surface temperature (SST) of +31 °C was determined, followed by a decrease from +24 to +17 °C (analysed for sediments at ash layers -26 and -17).

5.3.2 Concept of the multiproxy paleotemperature reconstruction

Fossils described from the Fur Formation provide a semiquantitative estimate for paleotemperatures in their habitat. In contrast, geochemical proxies (Δ_{47} , $\delta^{18}\text{O}_{\text{carb}}$, and $\delta^{18}\text{O}_{\text{diatom}}$) allow to determine ambient temperatures during which the sediments formed (ikaite, carbonate concretions, and diatomite). A new multiproxy approach to reconstructing the paleotemperatures was successful. Therefore, three paleotemperature proxies were applied in order to gain insights into the formation temperature of ikaite and carbonate concretions. Clumped isotopes (Δ_{47}) of replacive calcite, the cement phase directly formed at the ikaite breakdown, were analysed to unravel the temperature of the ikaite-glendonite transformation. The replacive calcite was measured twice – Δ_{47} and the oxygen isotopic composition of carbonate ($\delta^{18}\text{O}_{\text{carb}}$). Considering the paleotemperature based on clumped isotopes, the $\delta^{18}\text{O}_{\text{H}_2\text{O}}$ value was reconstructed for the early diagenetic formation of ikaite and the subsequent transformation to glendonite. This $\delta^{18}\text{O}_{\text{H}_2\text{O}}$ value was also applied for calculating the temperature of the successive formation of carbonate concretions.

Besides early diagenetic carbonates, diatomite was analysed for the oxygen isotopic composition of its diatom frustules ($\delta^{18}\text{O}_{\text{diatom}}$). Although diatoms were formed in the upper water column, the $\delta^{18}\text{O}$ signal of the diatom frustules is thought to be overprinted due to post-mortem maturation of the frustule (e.g. Schmidt et al., 2001; Moschen et al., 2006; Swann and Leng, 2009).

There are only a few localities where $\delta^{18}\text{O}_{\text{carb}}$ and $\delta^{18}\text{O}_{\text{diatom}}$ values can be determined for diatoms and early diagenetic, authigenic carbonates. The pH value found within the sedimentary column had to be between 7 and 8 in order to preserve diatom frustules and carbonates. This makes the Fur Formation a unique location to decipher the thermal history of early diagenesis within the upper sedimentary column.

5.3.3 Paleotemperatures derived from clumped isotopes (Δ_{47})

The clumped isotopes (Δ_{47}) determined for replacive calcite from the glendonite of ash layer +16 revealed an average paleotemperature of +6 °C and for the glendonite of ash layer +62 a value of +5 °C (Fig. 43). These temperatures are thought to reflect the temperature when ikaite was transformed to glendonite (Hu et al., 2014). Hence, the formation of ikaite could have occurred at low temperatures within the first metres of the sedimentary column. These cold bottom water/pore water temperatures reflect good growing conditions for ikaite (e.g. Pauly, 1963; Marland, 1975; Kennedy et al., 1987; Hu et al., 2015).

Previously, clumped isotopes were used to calibrate the $\delta^{18}\text{O}$ of the ambient water (Ghosh et al., 2006; Came et al., 2007; Affek et al., 2008; Huntington et al., 2009, 2011; Quade et al., 2011; Kluge et al., 2013; Cummins et al., 2014). Therefore, paleotemperature values determined for the Fur Formation via clumped isotopes serves as the input oxygen isotopic composition for ambient pore water/bottom water ($\delta^{18}\text{O}_{\text{H}_2\text{O}}$) in order to calculate a paleotemperature following the equation of Kim and O'Neil (1997) (see equation 6 in table 20). The resulting oxygen isotopic composition of the pore water was calculated to have a $\delta^{18}\text{O}$ value of -4.5‰ V-SMOW. This $\delta^{18}\text{O}_{\text{H}_2\text{O}}$ was subsequently used for all other temperature reconstructions ($\delta^{18}\text{O}_{\text{carb}}$, $\delta^{18}\text{O}_{\text{diatom}}$).

In contrast to the Fur Formation, the glendonite from the Simeulue Seep off Sumatra yielded an average temperature of +13 °C. This obvious temperature difference can result from different processes. Based on ^{13}C depleted $\delta^{13}\text{C}_{\text{carb}}$ values of -49‰ V-PDB and ^{18}O enriched $\delta^{18}\text{O}_{\text{carb}}$ values of +2.7‰ V-PDB for the Sumatra glendonite, the formation of ikaite via anaerobic oxidation of thermogenic methane is proposed and its subsequent transformation to glendonite at the Simeulue methane seep like in Teichert (2007). Thus, the conditions under which the ikaites were formed at the Sumatra site differed significantly when compared to the Danish Fur Formation. Loyd et al. (2016) proposed that the kinetic isotope signal of clumped isotopes at cold methane seeps was overprinted due to CO_2 hydration and hydroxylation reactions shifting the results towards warmer temperatures. The anaerobic oxidation of methane causes a decrease in Δ_{47} yielding higher temperatures (Loyd et al., 2016). According to DePaolo (2011), rapid mineralization, which takes place at methane seeps, results in geochemical signatures that are frequently out of equilibrium with the ambient environment. This might have been the case at the Simeulue Seep off Sumatra. Other disequilibrium processes affecting the Δ_{47} value are known about speleothems (Daëron et al., 2011). In addition to or alternatively, the temperature difference could reflect the incorporation of a rim cement within the whitish replacive calcite during analysis causing a shift towards lower Δ_{47} values and, consequently, resulting in higher temperatures.

Ghosh et al. (2006) proposed that the carbonate growth temperature determined via Δ_{47} measurements is independent of the $\delta^{18}\text{O}$ of the ambient water. Subsequently, Guo et al. (2009) developed a kinetic model allowing to reconstruct the (paleo)temperatures at the time of formation. Calculations for this study are based on at least four replicate measurements yielding an uncertainty better than 4 °C for the temperature or ± 0.026 for the Δ_{47} value. Comparing these

error values with other publications dealing with clumped isotope thermometry, the errors of the analyses in this study fall into the same range as in other publications (e.g. Ghosh et al., 2006; Eagle et al., 2010; Huntington et al., 2011; Loyd et al., 2012; Peters et al., 2013; Stolper and Eiler, 2015).

5.3.4 Paleotemperatures derived from carbonate oxygen isotopes ($\delta^{18}\text{O}_{\text{carb}}$)

Calculated paleotemperatures based on $\delta^{18}\text{O}_{\text{carb}}$ values yielded average values of +2.4 and +5.4 °C for bulk carbonate concretions and bulk glendonite, respectively (Fig. 28 and Fig. 41). The replacive calcite exhibits an average temperature of +3.9 °C, the rim cement one of +3.3 °C, and the fill cement one of +1 °C. All of these temperatures fall entirely into the stability field of ikaite (e.g. Pauly, 1963; Jansen et al., 1987; Oehlerich et al., 2013; Field et al., 2016).

The lowest temperature value of the glendonite was observed for the latest cement phase (fill cement) that precipitated later than the replacive calcite and the rim cements, as suggested by heavier $\delta^{18}\text{O}_{\text{carb}}$ values and higher $^{87}\text{Sr}/^{86}\text{Sr}$ ratios. The ikaite formed during early diagenesis and the transformation of ikaite to glendonite occurred in a certain sedimentary depth as the upper temperature boundary for ikaite with a value of ca. +5.5 °C (average value of the clumped isotope temperature of both glendonite samples) was reached. This temperature necessary for the transformation was reached during the burial of the ikaite crystal within the upper sedimentary column. A specific depth remains unclear, but the transformation is thought to have occurred ca. 5 m below the sediment-water interface (Kaplan, 1979; Larsen, 1994; De Lurio and Frakes, 1999; Kodina et al., 2003; Zu et al., 2012). As the fill cement precipitated later in a greater depth, another $\delta^{18}\text{O}_{\text{H}_2\text{O}}$ must be considered for the calculation of a paleotemperature. This $\delta^{18}\text{O}_{\text{H}_2\text{O}}$ value of the pore water would have been ^{18}O enriched due to different diagenetical processes like clay dewatering, silica diagenesis, carbonate dissolution, or the influx of brine fluids (Gross, 1964; Clayton et al., 1966; Hitchon and Friedman, 1969; Allan and Mathews, 1982; Morton and Land, 1987; Lohmann, 1988; Behl and Garrison, 1994), but the exact value for it cannot be given. For the Fur Formation, the diagenesis of silica (e.g. Aoyagi and Kazama, 1980) is the most probable cause for the ^{18}O enrichment of the pore water due to the maturation of diatom silica.

The spatial distribution of $\delta^{18}\text{O}_{\text{carb}}$ within a carbonate concretion is supposed to provide further insights into the formation process of the calcitic cement and into the prevailing paleotemperatures during the formation of the carbonate concretion. In most of the carbonate concretions, a trend was identified with the lightest $\delta^{18}\text{O}_{\text{carb}}$ / highest temperature values found in the centre of each carbonate concretion. In contrast to this study, Pedersen and Buchardt (1996) were not able to identify any trend in their $\delta^{18}\text{O}_{\text{carb}}$ values within carbonate concretions. Pedersen and Buchardt (1996) determined a maximal temperature range of ± 6 °C within one concretion. More carbonate concretions were investigated during this study with a more detailed look at the pattern of the $\delta^{18}\text{O}_{\text{carb}}$ values. In contrast, four carbonate concretions were identified bearing a temperature range larger than ± 7 °C (+25/+29, +31, +135b, and +135a). The heaviest $\delta^{18}\text{O}_{\text{carb}}$ values resulting in lower temperatures were either found at the marginal rim in the horizontal

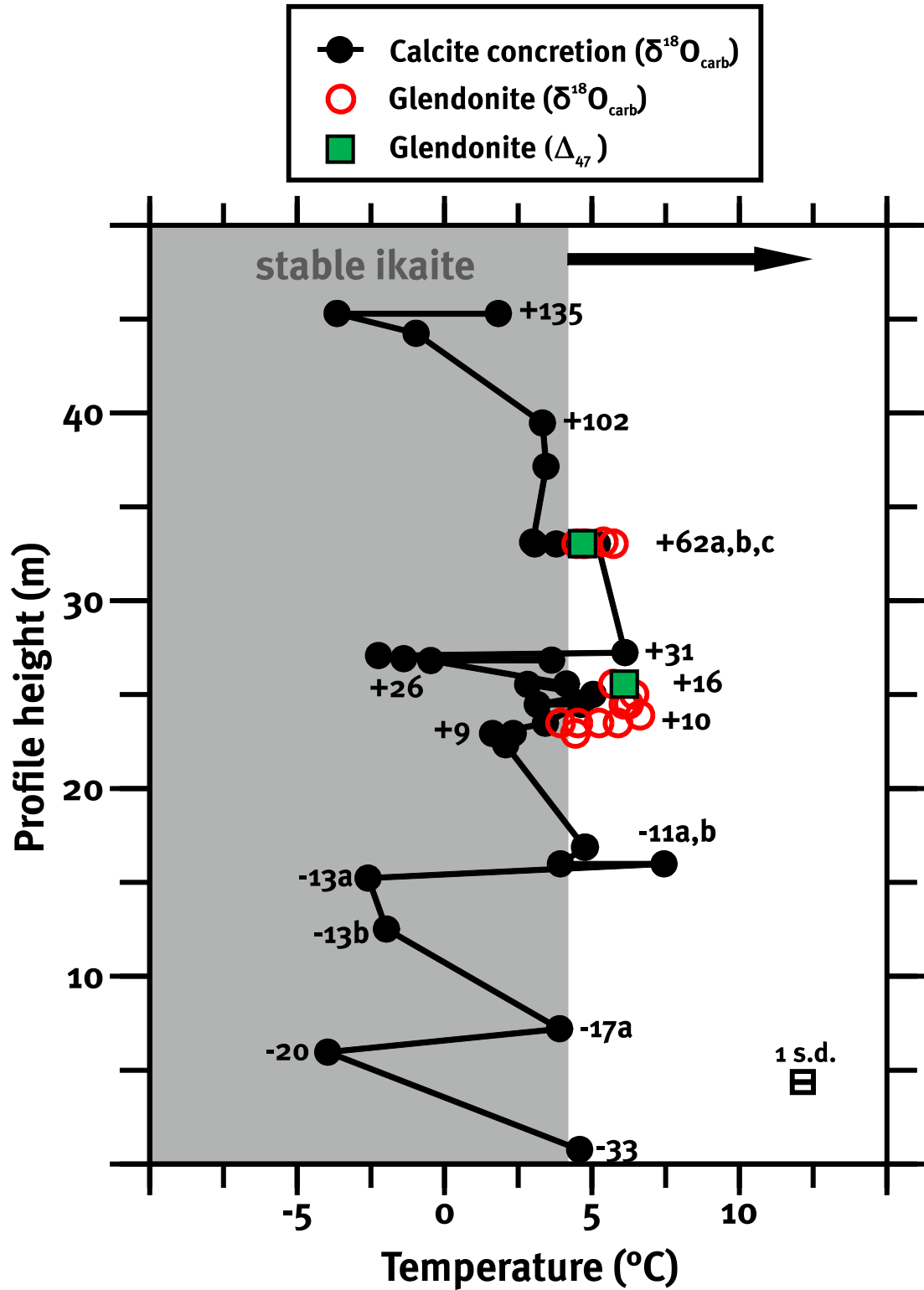


Fig. 41: Paleotemperatures calculated from the $\delta^{18}\text{O}_{\text{carb}}$ values of glendonite and carbonate concretions after Kim and O'Neil with a $\delta^{18}\text{O}_{\text{H}_2\text{O}}$ of -4.5‰ V-SMOW plotted against profile height. The clumped isotope values of glendonites +16a and +62b are plotted in green for comparison. The grey area marks the temperature range of ikaite stability (Hu et al., 2014). The black arrow points to temperatures of ikaite transformation.

profile or at the bottom of a concretion. Some of the concretions depict a lighter colour at their rim pointing to leaching due to weathering processes. An influence of weathering on the $\delta^{18}\text{O}_{\text{carb}}$ value could not be entirely excluded, but the $\delta^{18}\text{O}_{\text{carb}}$ values for drilled samples taken between the centre and the margin of a carbonate concretion are in between the values of centre and margin. Thus, the enrichment in ^{18}O towards the margin of a concretion appears to be a gradual one. Certain horizons are completely cemented resulting in thick carbonate banks mostly associated with ash layers: ash layers +62, +101/+102, +129/+130, and +135. Solely the samples of ash layer +135 depict a wide range of $\delta^{18}\text{O}_{\text{carb}}$ values, whereas other cemented horizons appear more homogenous. Thus, the $\delta^{18}\text{O}_{\text{carb}}$ values plotting in a wide range suggest a longer time for the formation of these carbonate concretions or cemented horizons and, possibly, a greater depth.

Within the Fur Formation, $\delta^{18}\text{O}_{\text{carb}}$ values enriched in ^{18}O (ca. 1.5‰) were measured in concretions from three levels between ash layers -20 and -13, between ash layers +26 and +30, and around ash layer +135 resulting in lower temperature values for these concretions. The carbonate concretions yielded paleotemperature values between -5 and +7 °C for all bulk samples of the carbonate concretions (Fig. 41). The carbonate concretions depict temperature values lower than the values of glendonites and their replacive cements (Fig. 41). These lower temperatures remain questionable, because the estimated pore water $\delta^{18}\text{O}$ of -4.5‰ V-SMOW cannot be used for the calculation of paleotemperatures due to the later diagenetic origin in a greater depth. A greater burial depth for the formation of carbonate concretion causes a higher, ^{18}O enriched pore fluid. Thus, the temperature values for the formation of carbonate concretions must lie above the temperatures for the ikaite transformation (>6 °C).

Listing the temperature values for their environmental indications implies the formation of ikaite at temperatures below +5.5 °C as determined via clumped isotope analyses of replacive calcite. The subsequently calculated $\delta^{18}\text{O}$ value of -4.5‰ V-SMOW for the pore water points to low temperatures for all glendonite subsamples. Considering the chronological sequence of formation of authigenic carbonates, the $\delta^{18}\text{O}_{\text{H}_2\text{O}}$ value of the pore water increased during diagenesis towards ^{18}O enriched $\delta^{18}\text{O}$ values. Unfortunately, the $\delta^{18}\text{O}_{\text{H}_2\text{O}}$ could not be identified and, thus, the temperature and the depth of the formation of carbonate concretions remain elusive.

5.3.5 Paleotemperatures derived from oxygen isotopes of diatom frustules ($\delta^{18}\text{O}_{\text{diatom}}$)

At first, the oxygen isotopic composition of diatom frustules was analysed to determine prevailing paleotemperatures of the upper water column. These values were compared to both paleotemperature proxies described above (Δ_{47} and $\delta^{18}\text{O}_{\text{carb}}$). However, several authors proposed that the $\delta^{18}\text{O}$ values of diatoms changed after death (Schmidt et al., 1997; Brandriss et al., 1998; Schmidt et al., 2001; Moschen et al., 2006; Swann and Leng, 2009; Dodd and Sharp, 2010; Dodd, 2011). Consequently, the recorded paleotemperatures reflect the temperature during deposition. A $\delta^{18}\text{O}$ value of -4.5‰ V-SMOW was applied for the ambient water when calculating the paleotemperatures. Most calculated paleotemperatures range between -3.6 and +8 °C with an average value of +0.9 °C. A few offset values determined for the coastal outcrops of Knudeklint

and Stolleklint were excluded when calculating this average value (abbreviations “Kn” and “St” in figure 43). Paleotemperatures based on $\delta^{18}\text{O}_{\text{diatom}}$ values agree with temperatures based on $\delta^{18}\text{O}_{\text{carb}}$ values indicating cold bottom waters (Fig. 43).

Some samples were measured in duplicate or triplicate. Sample Ej+14_2 was the one with the largest standard deviation of $\pm 1.3\text{‰}$, which results in a maximum temperature difference of $\pm 7.1\text{ °C}$ (equation of Dodd and Sharp (2010) and a $\delta^{18}\text{O}_{\text{H}_2\text{O}}$ of -4.5‰ V-SMOW). The samples St o. -33, Kn -10_7, Kn +1_1, Kn +14_2, and Kn +42_1 yielded temperature values higher than $+10\text{ °C}$. Other SiO_2 bearing minerals and microfossils are thought to have influenced the $\delta^{18}\text{O}$ isotopic composition of the diatom samples. Although diatom samples with $> 95\%$ SiO_2 fossils had been chosen, residual clay and silt particles in samples were determined via SEM and light microscopy. $\delta^{18}\text{O}$ results were corrected for a potential influence of clay and silt particles using a mixing equation (see equation 3 in chapter 4.3.3; Morley et al., 2004; Leng and Barker, 2006). Usually, the effect of these particles on the $\delta^{18}\text{O}_{\text{diatom}}$ value should be minimal, as indicated by the absence of a clear correlation between the abundance of mineral contaminants and shifts in the paleotemperature curve towards higher temperatures (Fig. 42 and Fig. 43).

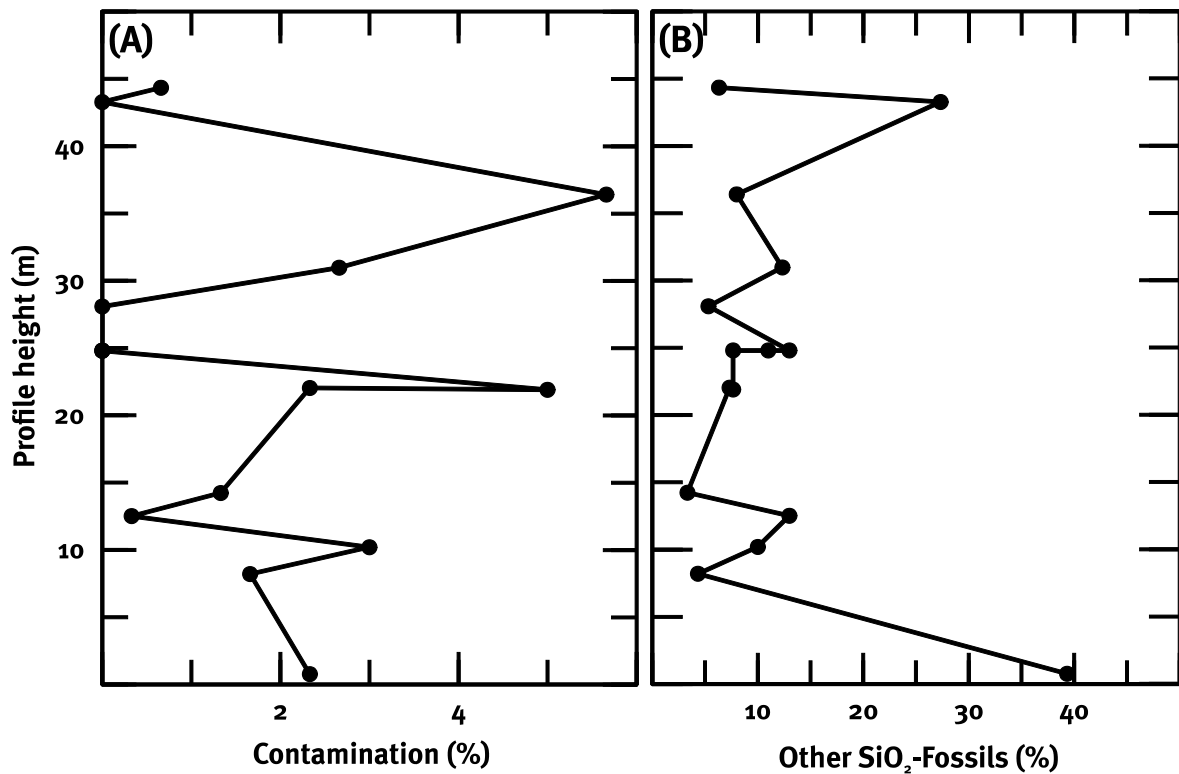


Fig. 42: Quantification of (A) mineral contaminants and (B) proportional abundance of other SiO_2 fossils (silicoflagellates, sponge spiculae, ebridians, etc.) within the diatom samples against profile height.

Thus, the shift towards lower $\delta^{18}\text{O}_{\text{diatom}}$ values must have been caused by another factor. Three diatom samples between ash layers +14 and +16 yielded different $\delta^{18}\text{O}_{\text{diatom}}$ values, which might have been caused by different diatom assemblages or related to their location. The samples of the moler pits Ejerslev and Råkilde display $\delta^{18}\text{O}_{\text{diatom}}$ values of $+33.2\text{‰}$ (-3.6 °C) and

+32.8‰ (-2.3 °C), respectively. In contrast, the sample of the Knudeklint coastal outcrop on the island of Fur shows a $\delta^{18}\text{O}$ value of +29.1‰ (+14 °C). Several other samples of the Knudeklint also exhibit lower $\delta^{18}\text{O}$ values, which might point to ongoing coastal weathering processes changing the $\delta^{18}\text{O}$ signal.

Although there are some factors influencing the oxygen isotopic composition of recent diatom frustules like light, nutrient availability, seasonality, and temperature (e.g. Kowalczyk, 2006; Swann et al., 2008; Swann and Leng, 2009), these factors could be ignored, because the diatom frustules are thought to be overprinted due to post-mortem maturation processes. Even the fact that all diatom samples comprise more than one single species, which was firstly proposed by Juillet-Leclerc and Labeyrie (1987), can be neglected due to post-mortem overprinting. Schmidt et al. (1997) were the first to note that the $\delta^{18}\text{O}$ signal of diatoms is affected by isotope exchange processes during sedimentation and that the determined $\delta^{18}\text{O}$ values don't reflect ambient water temperatures. This was confirmed by Brandriss et al. (1998) who measured 6 to 8‰ lower values for diatoms grown in lab studies compared to values for fossil samples of the same species. Schmidt et al. (2001) denoted that silica maturation occurring in surface sediments resulted in increasing Si-O-Si/Si-OH ratios and higher $\delta^{18}\text{O}$ values. These authors concluded that the $\delta^{18}\text{O}$ value of marine diatoms does not reflect the sea surface temperature, but rather the bottom water temperature. Further works on silica maturation within diatom frustules were done by Moschen et al. (2006), Swann and Leng (2009), Dodd and Sharp (2010), and Dodd (2011).

Despite analytical difficulties, the $\delta^{18}\text{O}_{\text{diatom}}$ proxy was successfully used in several studies dealing with paleoenvironmental reconstructions for terrestrial and marine settings (e.g. Mikkelsen et al., 1978; Jiang et al., 2001; Morley et al., 2005; Moschen et al., 2005; Mackay et al., 2008; Dodd and Sharp, 2010), but questions remain and are discussed in the literature (Leng et al., 2001; Lamb et al., 2005).

A benefit of the Fur Formation are co-occurring carbonates and diatomite allowing the paired measurements of $\delta^{18}\text{O}_{\text{carb}}$ and $\delta^{18}\text{O}_{\text{diatom}}$ values. Results obtained for the Fur Formation clearly point to cool bottom and pore water paleotemperatures during the formation of ikaite. Yet based on the discussion above, the paleotemperatures obtained via $\delta^{18}\text{O}_{\text{carb}}$ measurements on glendonite and carbonate concretions are considered more reliable than the paleotemperatures calculated based on $\delta^{18}\text{O}_{\text{diatom}}$ values.

Determining the paleotemperature of ambient seawater and/or bottom/pore water has been challenging in this study. The $\delta^{18}\text{O}$ of the ambient water was determined by analysing clumped isotopes (Δ_{47}). Applying this value to the specific temperature equation resulted in a $\delta^{18}\text{O}$ for the water. Respective calculated temperature values fall into a range between -5 and +10 °C pointing to cold bottom water within the Danish Basin during the Early Eocene. In contrast, a subtropical to tropical climate is indicated by the fossil content. Consequently, a thermocline within the Danish Basin is proposed, but the depth of this thermocline remains elusive.

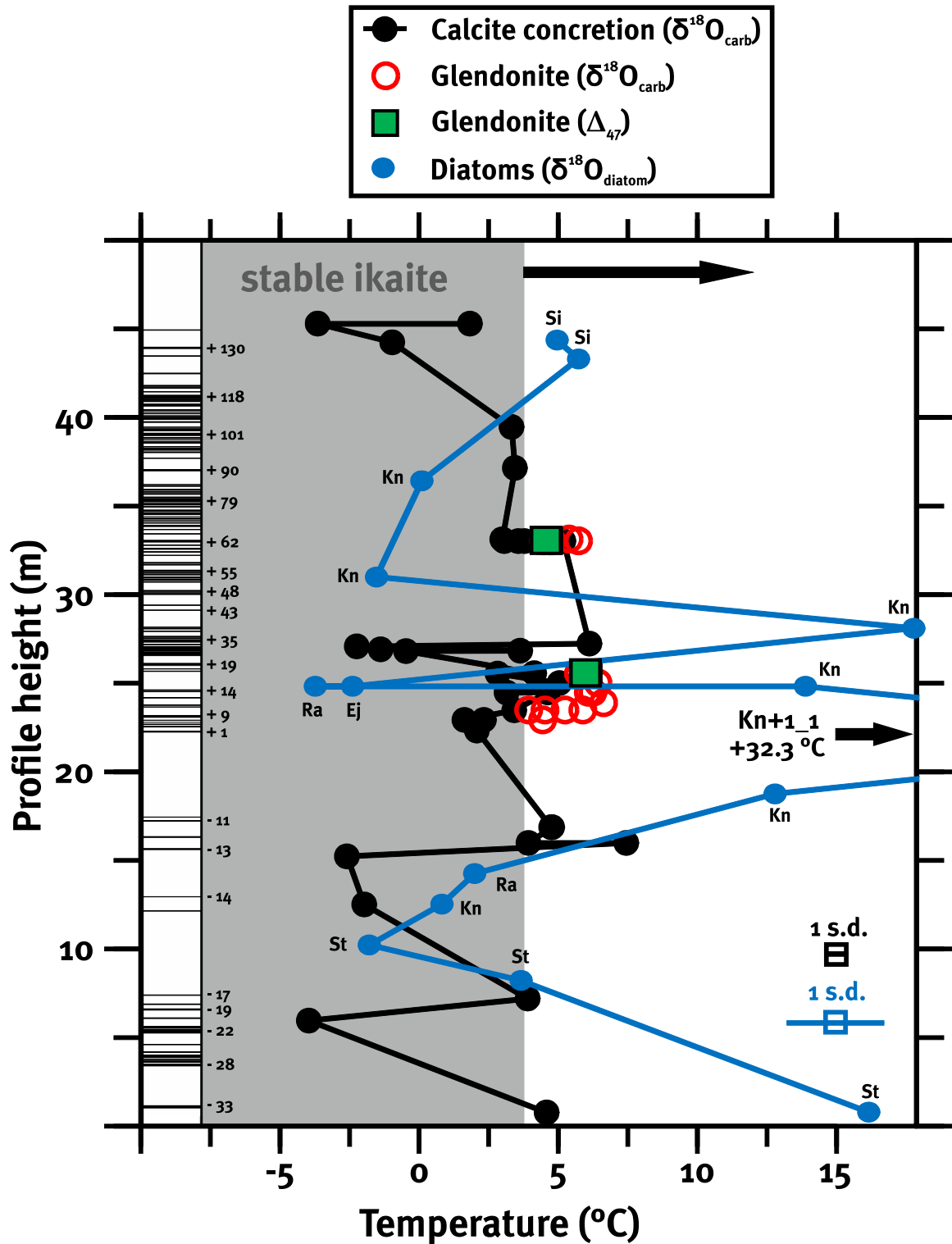


Fig. 43: Paleotemperatures calculated from $\delta^{18}\text{O}_{\text{carb}}$, Δ_{47} , and $\delta^{18}\text{O}_{\text{diatom}}$ with profile height. The localities of the diatom samples are noted as: Si: Silstrup, Kn: Knudeklint, Ra: Råkilde, Ej: Ejerslev, and St: Stolleklint. The grey area marks the temperature range of ikaite stability (Hu et al., 2014). The black arrow points to temperatures of ikaite transformation.

6 Model of the Fur Formation deposition

The processes of ikaite formation and its subsequent transformation to glendonite in sediments of the Early Eocene Fur Formation were investigated in this study. Considering results from previous works and adding the results of this work, a depositional model for the Fur Formation was developed (Fig. 44 and Fig. 45).

The sediments were deposited in the semi-enclosed, ca. 500 m deep Danish Basin, which was characterised by an upwelling zone located in the NW. Diatom blooms occurred in the upper water column, diatoms settled down through the water column, and they subsequently formed the diatomite. Episodic volcanic eruptions took place within the Gardiner complex, East Greenland, and the Faroe islands during the Early Eocene resulting in numerous ash layers interbedding the diatomite (Fig. 44). The deposition of the Fur Formation is estimated to have lasted for ca. 1.1 m.a..

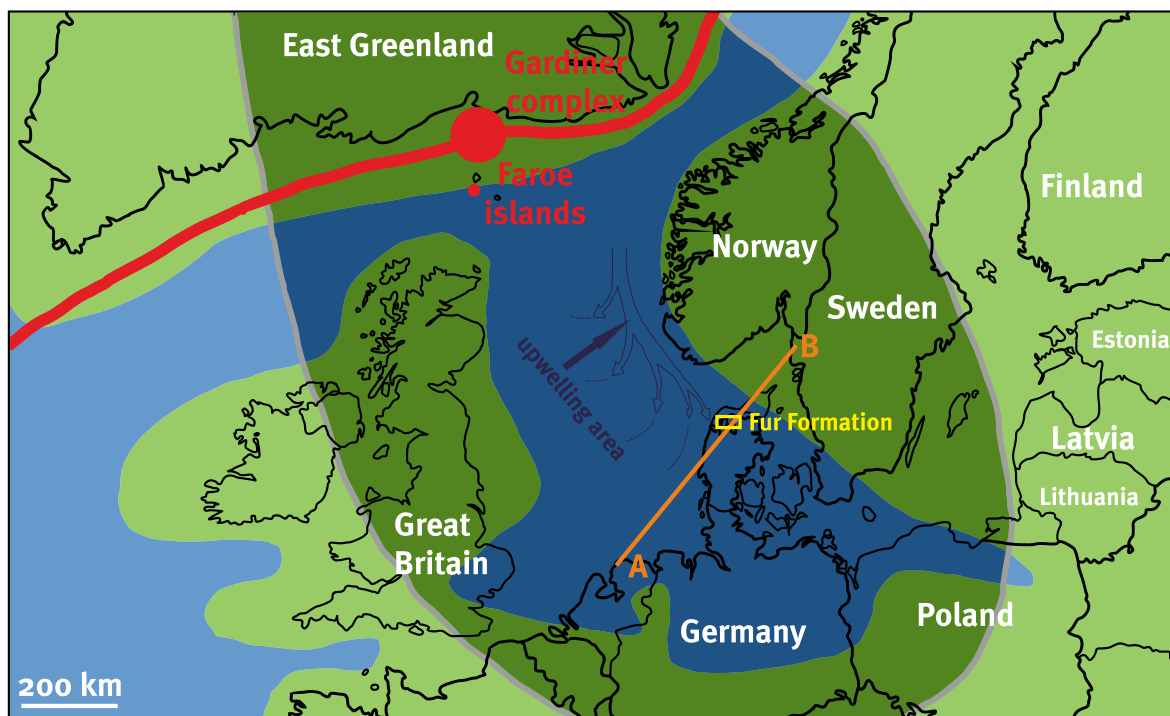


Fig. 44: Map of the Early Eocene North Sea Basin and adjacent North Atlantic Ocean. The red colour indicates the rifting zone of the NAIP, the greyish coloured area the disposal zone of volcanic ash layers of the NAIP. A cross section through the Danish Basin is marked with amber colour, whereas the deposition zone of the Fur Formation is marked yellow (modified after Schultz et al. (2011)).

Different early diagenetic calcites were formed in the sediments: (i) glendonite, a calcite pseudomorph after ikaite, and (ii) carbonate concretions. Ikaite precipitated in organic-rich sediments in the uppermost sedimentary column via organotrophic sulphate reduction at temperatures lower than +5.5 °C (Fig. 45; box 1). The transformation of ikaite to glendonite occurred at

an average temperature of +5.5 °C as indicated by clumped isotope data. Based on petrographical and isotopic analyses, replacive calcite was identified as the first mineral phase after the breakdown of the ikaite crystal (Fig. 45; box 2). Several rim cements precipitated from the water released during ikaite ($\text{CaCO}_3 \cdot 6\text{H}_2\text{O}$) breakdown. Open pore space was subsequently filled with another calcitic cement during ongoing early diagenetic processes. This later cement displayed different $\delta^{18}\text{O}_{\text{carb}}$ values and $^{87}\text{Sr}/^{86}\text{Sr}$ ratios compared to previous cement phases.

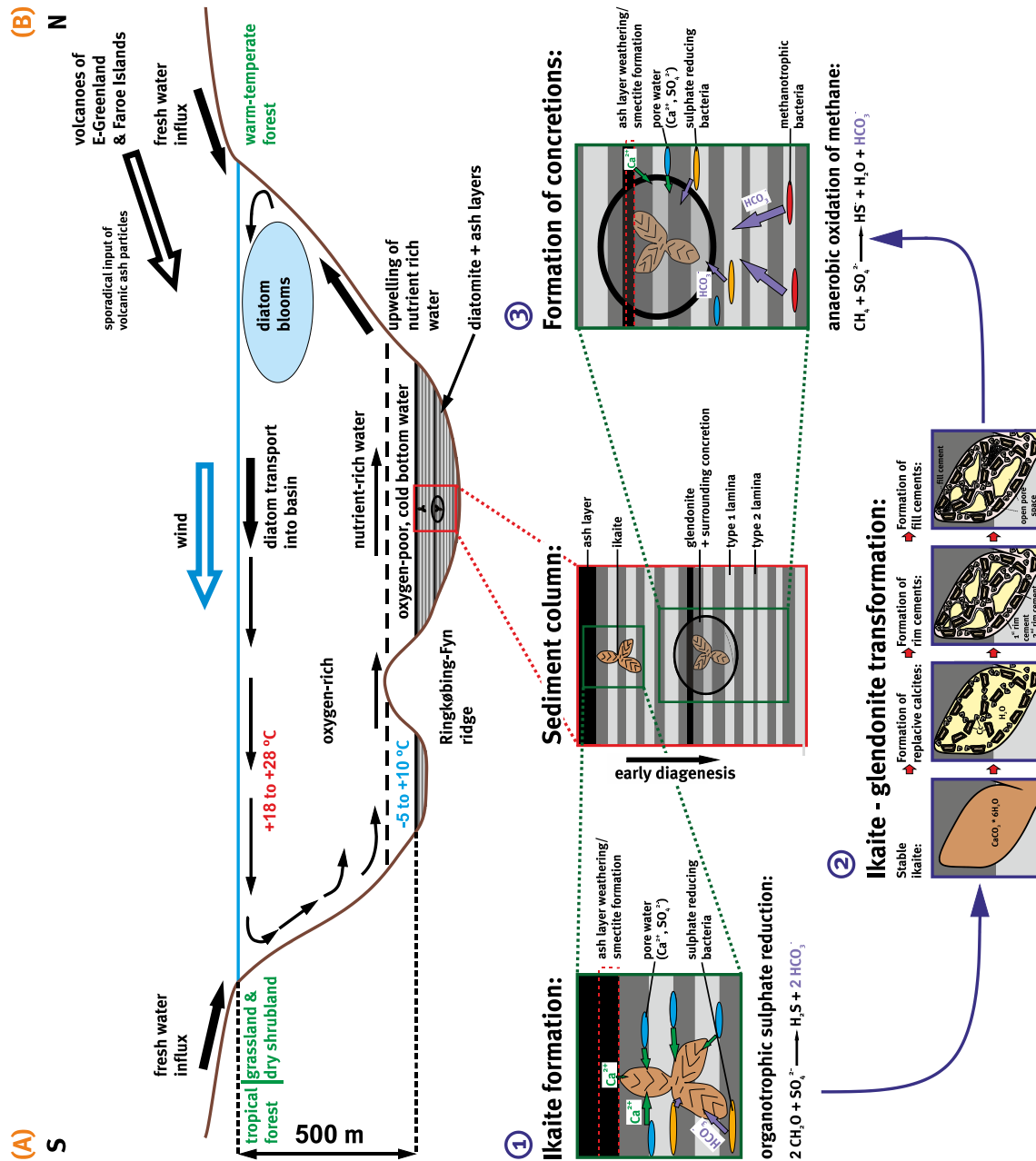


Fig. 45: Paleoenvironmental model for ikaite formation within the Danish Basin (modified after Bonde (1979) and Pedersen et al. (2011)).

Following the transformation of ikaite to glendonite, carbonate concretions precipitated in the uppermost 10 m of the sedimentary column, but not until some time after the transformation had been completed (Fig. 45; box 3). The carbonate concretions precipitated during early diagenetic processes proven by a high concentration of carbonate (ca. 81 wt%), negative $\delta^{13}\text{C}_{\text{carb}}$ values indicating a lower formation depth (but above methanogenesis zone), and a higher porosity than the surrounding diatomite. Additionally, the formation of carbonate concretions was mostly coupled to organotrophic sulphate reduction. In contrast, a single dolomite and a single ankerite concretion in the lower Knudeklint Member suggest carbonate formation driven by methanotrophic bacteria and archaea.

A paleotemperature range between -5 and +10 °C is proposed for the sediments of the uppermost sedimentary column. This temperature range was determined using several paleotemperature proxies (Δ_{47} , $\delta^{18}\text{O}_{\text{carb}}$, and $\delta^{18}\text{O}_{\text{diatom}}$). Thus, in combination with the microfossil record indicating a subtropical to tropical climate and additional geochemical proxies for the surface waters (TEX_{86} , MBT/CBT, and BIT index; Schoon et al., (2015), a thermocline within the water column in the Danish Basin is required, and herewith proposed, separating warm, oxygen rich surface waters from cold, oxygen depleted bottom waters.

7 Summary and outlook

7.1 Summary

Glendonite of the Fur Formation

Petrographic, geochemical, and isotope data for Early Eocene glendonite from the Fur Formation yielded information about the internal structure of the glendonite and the transformation processes from ikaite to glendonite. Moreover, environmental conditions during ikaite formation could be reconstructed:

1. Glendonite from the Early Eocene Fur Formation consists of four calcitic cements. Initially, a replacive calcite formed during the breakdown of the ikaite, representing the original CaCO_3 of the ikaite. Thereafter, these replacive calcites were covered by two rim cements (Mg-ri, yellow-brown; Fe-Mn-Mg-ri, translucent) that precipitated from the ikaite crystal water and an admixture of surrounding pore water. Finally, the open pore space was filled by a diagenetic (fill) cement with a chemically distinctly different composition.
2. Organotrophic sulphate reduction was the main process for ikaite precipitation as well as for the carbonate concretions that subsequently formed around the glendonites. A minor contribution of anaerobic oxidation of methane as secondary carbon source cannot be ruled out. Ikaite formed in the shallow subsurface of the marine sedimentary column.
3. Paleotemperature calculations yielded a range of +2 to +8 °C for the ikaite to glendonite transformation, which is at the upper boundary of the ikaite stability field. The oxygen isotopic composition of Early Eocene bottom water was low (-4.5‰ V-SMOW) caused by organotrophic sulphate reduction and the weathering of volcanic glass particles.
4. Apatite occurring within the glendonite is supposed to shift the $\delta^{18}\text{O}_{\text{carb}}$ values towards ^{18}O depleted ones. Carbonate is incorporated into the apatite mineral and this carbonate is likely liberated during $\delta^{18}\text{O}_{\text{carb}}$ analyses due to sample leaching via addition of phosphoric acid.
5. A contribution of Sr from the Zechstein salt brines cannot be ruled out, but most of the Ca^{2+} and Sr^{2+} ions of the ikaite derived from ambient seawater.
6. Volcanic ash layers are thought to contribute to ikaite formation. The geochemistry and thickness of the ash layers are suggested as controlling factors for the precipitation of the ikaite. Ions dissolved from the volcanic glass particles were incorporated into the ikaite crystals.

Ikaite was formed by bacterially induced organotrophic sulphate reduction within phosphate- and organic-rich sediments below ash layers of more than 7 cm thickness. It can be concluded that the geochemical environment below an ash layer was most suitable for the formation of the ikaite for the Fur Formation.

Carbonate concretions and volcanic ashes of the Fur Formation

Carbonate concretions occur at certain horizons within the Fur Formation. Studying several geochemical proxies revealed the following aspects:

1. Volcanic ash layers contribute to the formation of carbonate concretions, because many ash layers were incorporated into concretions. Thus, the ash layer leaching is thought to provide ions necessary for the formation of these concretions.
2. The key process related to the formation of carbonate concretions was organotrophic sulphate reduction. Yet, as indicated by the negative $\delta^{13}\text{C}_{\text{carb}}$ values, a contribution from anaerobic methane oxidation cannot be ruled out. Additionally, $\delta^{13}\text{C}_{\text{carb}}$ values of +7‰ for the dolomite concretion -17b around ash layer -17 and of +6‰ V-PDB for the ankerite concretion of ash layer -20 suggest that methanogenesis delivered the bicarbonate for the formation of these concretions.
3. Rain events during the Early Eocene sporadically caused a riverine influx of terrestrial organic matter. This was seen via C/N ratios oscillating over the entire formation. Between ash layers -33 and -19b, sediments of the recovery phase after the PETM were investigated. Low $\delta^{13}\text{C}_{\text{org}}$ values of -31‰ V-PDB and high C/N ratios of ca. 26 supported this conclusion.
4. Negative $\delta^{34}\text{S}$ values of the water soluble sulphate extracted from carbonate concretions suggest the oxidation of the pyrite, which formed in the sediment.
5. $^{87}\text{Sr}/^{86}\text{Sr}$ ratios indicate that most of the Sr^{2+} ions stem from Early Eocene seawater trapped in the sediment. Only a minor contribution of Sr results from the leaching of volcanic ash particles.
6. The majority of $\delta^{34}\text{S}$ and $\delta^{18}\text{O}$ values of carbonate-associated sulphate (CAS) indicate that organotrophic sulphate reduction was the main process for the formation of carbonate concretions. Only between ash layers -20 and -17 of the Fur Formation, $\delta^{13}\text{C}_{\text{carb}}$ and $\delta^{18}\text{O}_{\text{carb}}$ values, C/N ratio, and biomarker information point to methanogenesis as the main bicarbonate source. A transitional zone between methanogenesis and organotrophic sulphate reduction was observed between ash layers -17 and -13 within the Knudeklint Member.
7. The carbonate concretions formed after the ikaite to glendonite transformation was completed. Yet, all parameters imply their early diagenetic formation close to the seafloor.

Paleotemperatures

Paleotemperature values reconstructed from different geochemical parameters revealed:

1. The clumped isotopes of replacive calcite of glendonite yielded a temperature range between +2 and +10 °C. From these, a seawater $\delta^{18}\text{O}$ composition of -4.5‰ V-SMOW was calculated. This $\delta^{18}\text{O}$ value was subsequently used as characteristic of the ambient water in the respective paleotemperature equations for carbonates and diatom silica.
2. Temperatures calculated based on $\delta^{18}\text{O}_{\text{carb}}$ values display a range between -5 and +10 °C. Taking the burial history into account, the temperatures derived for the fill cement of the glendonite and those for the carbonate concretions appear too low and the usage of another ^{18}O enriched $\delta^{18}\text{O}$ value for the pore water is suggested.
3. Temperature values based on the oxygen isotopic composition of diatom silica range between -4 and +10 °C, but several samples yielded temperatures higher than +10 °C.
4. In summary, all three isotopic proxies (Δ_{47} , $\delta^{18}\text{O}_{\text{carb}}$, and $\delta^{18}\text{O}_{\text{diatom}}$) point to low bottom water temperatures between -5 and +10 °C during the formation of ikaite in the Early Eocene.
5. Finally, the subtropical to tropical temperatures indicated by the fossil record and the cold temperatures of the bottom water require the presence of a thermocline within the water column. As bottom water temperatures were cold enough, ikaite precipitated in the sediments of the Early Eocene Fur Formation.

Several factors increased the chance of ikaite forming within the sediments of the Fur Formation. Besides the migration of Zechstein salt brines into the vicinity of glendonite sites, the volcanic ash layers essentially contributed to the formation of ikaite: due to ash leaching, the formation of impermeable clay layers, and, even more important, an increase in the pH value because of their alteration. The migration of Zechstein salt brines and seawater entrapped in the sediments was prevented causing the saturated pore water from which ikaite precipitated. The carbonate-free diatomite and the volcanic ash layers were the basis for the formation of ikaite, because no carbonate minerals leached out and ikaite could precipitate as a consequence of organotrophic sulphate reduction in a cold environment. Due to cold temperatures, a high pH value, and a high phosphate concentration, which can be seen in some underlying sediments as phosphate nodules or coprolites and as apatite within the glendonite, the formation of calcite and aragonite was prevented and large ikaite formed that nowadays has been identified as “mega-glendonite”.

The most important conclusion drawn from this study of glendonites from the Fur Formation is that ikaite formed in cool bottom/pore waters and shallow sediments even during the warm Early Eocene. Thus, while glendonite formation is related to cool ambient water temperatures, it does not necessarily identify an ice age. Instead, ikaite formation and its subsequent

transformation to glendonite proceed under cool environmental conditions as they can also occur nowadays (e.g. winter season, shelf sediments in a certain water depth with cold water temperatures at the water sediment interface, polar regions, etc.).

7.2 Outlook

Several questions about the formation of ikaite during the warm Early Eocene and the subsequent transformation to glendonite could not entirely be answered in this study. One of these questions is whether or not the Zechstein salt brines influenced the formation of ikaite and subsequent carbonate concretions within the Fur formation. Jørgensen et al. (2005) explored the migration of Zechstein salt diapirs in the underground of Mors and their associated faults. Pathways for salt brines in order to reach the sedimentary layers, where the formation of ikaite took place, were only assumed, but could not be completely proven via analyses on glendonite. XRF measurements of glendonite revealed no direct influence of a salt brine due to low Na₂O and K₂O concentrations (see appendix 7). Nevertheless, analyses of the ⁸⁷Sr/⁸⁶Sr ratios of carbonate concretions point to a higher proportion of Zechstein salt brines for the formation of the concretions of the Silstrup Member. Therefore, carbonate concretions formed in greater burial depth showing a higher proportion of salt brine might point towards a higher impact of salt brines on their formation. Therefore, additional XRF analyses are suggested to unravel the influence of salt brines.

A second very promising approach to further investigations on the formation of ikaite are upcoming research cruises to modern upwelling systems where cold, dense bottom waters are raised onto the continental shelf (e.g. Benguela upwelling system and Humboldt upwelling system). Within those upwelling systems, a high production of silica-dominated phytoplankton results in high burial rates of organic-rich sediments. According to Jones et al. (2006), ikaite formation in Eastern Australia was driven by upwelling processes causing cool climate conditions in this region during the Permian age. If similar environmental conditions occur in shelf sediments nowadays, why is ikaite only rarely found in the sediments of recent upwelling systems? In the Fur Formation, proto-glendonites without protecting carbonate concretions were investigated in several depths. These proto-glendonites comprising loosely packed replacive calcites are supposed to be a consequence of a fast transformation caused by a higher sedimentation rate, but this has yet to be proven. As the upper temperature boundary for ikaite stability is reached faster in modern upwelling systems, ikaite crystals are smaller in these regions and the transformation to glendonite cannot entirely take place. Thus, small-grained conglomerate of loosely packed calcite crystals found within drill cores of modern marine sediments might indicate the presence of former ikaite. Due to the fact that these calcite crystals appear as mush in a drill core, this ikaite might be missed. Consequently, further investigations of sediments in these upwelling regions might yield former ikaite crystals, which have become loosely packed calcite crystals. Further analyses of the thermal gradient found within the sedimentary column in these modern systems might be able to clarify the thermal history of proto-glendonite and answer the question.

8 References

- Affek, H. P., Bar-Matthews, M., Ayalon, A., Matthews, A., and Eiler, J. M., 2008. Glacial/interglacial temperature variations in Soreq cave speleothems as recorded by 'clumped isotope' thermometry. *Geochimica et Cosmochimica Acta* **72**, 5351-5360.
- Affek, H. P., 2012. Clumped isotope paleothermometry: principles, applications, and challenges. *The Paleontological Society Papers* **18**, 101-114.
- Allan, J. R. and Matthews, R. K., 1982. Isotope signatures associated with early meteoric diagenesis. *Sedimentology* **29**, 797-817.
- Andersen, I., 1948. Den sribede cementsten i de danske eocæne molerlag. *Meddelelser fra Dansk Geologisk Forening* **11**, 189-196.
- Andersen, N. and Andersen, S., 1996. Kæmpemyrer og andre danekræ fra det danske Moler. Studiet af en uddød insektfauna fra Danmarks Palæogen. *Naturens Verden* **11**, 417-432.
- Anderson, T., 1983. Stable isotopes of oxygen and carbon and their application to sedimentologic and environmental problems. In: *Stable Isotopes in Sedimentary Geology*, Society of Economic Paleontologists and Mineralogists, Tulsa.
- Ansorge, J. and Reich, M., 2004. Die Eozän-Tonschollen von Wobbanz (SE-Rügen). *Archiv für Geschichte der Geologie* **3**, 651-678.
- Aoyagi, K. and Kazama, T., 1980. Transformational changes of clay minerals, zeolites and silica minerals during diagenesis. *Sedimentology* **27**, 179-188.
- Archibald, S. B. and Makarkin, V. N., 2006. Tertiary giant lacewings (Neuroptera: Polystoechotidae): Revision and description of new taxa from western north America and Denmark. *Journal of Systematic Palaeontology* **4**, 119-155.
- Bannikov, A. and Tyler, J., 2008. A new species of the pufferfish Eotetraodon (Tetraodontiformes, Tetraodontidae) from the Eocene of the Northern Caucasus. *Paleontological Journal* **42**, 526-530.
- Barker, S., Greaves, M., and Elderfield, H., 2003. A study of cleaning procedures used for foraminiferal Mg/Ca paleothermometry. *Geochemistry, Geophysics, Geosystems* **4**, n/a-n/a.
- Baudrand, M., Grossi, V., Pancost, R., and Aloisi, G., 2010. Non-isoprenoid macrocyclic glycerol diethers associated with authigenic carbonates. *Organic Geochemistry* **41**, 1341-1344.
- Behl, R. and Garrison, R., 1994. The origin of chert in the Monterey Formation of California (USA). Siliceous, phosphatic and glauconitic sediments of the Tertiary and Mesozoic: *Proceedings of the 29th International Geological Congress, Part C*.
- Bell, J. B., Aquilina, A., Woulds, C., Glover, A. G., Little, C. T. S., Reid, William D. K., Hepburn, L. E., Newton, J., and Mills, R. A., 2016. Geochemistry, faunal composition and trophic structure in reducing sediments on the southwest South Georgia margin. *Royal Society Open Science* **3**, 160284.
- Benda, L., 1972. Diatoms of the Moler Formation of Denmark (Lower Eocene). A preliminary report. *Beihefte Nova hedwigia* **39**, 251-266.
- Berggren, W. A., Kent, D. V., Swisher, C. C., and Aubry, M.-P., 1995. A revised Cenozoic geochronology and chronostratigraphy. *SEPM Special Publication* **54**, 129-212.
- Berner, R. A. and Morse, J. W., 1974. Dissolution kinetics of calcium carbonate in sea water; IV, Theory of calcite dissolution. *American Journal of Science* **274**, 108-134.
- Bertelli, S., Lindow, B. E. K., Dyke, G. J., and Chiappe, L. M., 2010. A well-preserved 'charadriiform-like' fossil bird from the Early Eocene Fur Formation of Denmark. *Palaeontology* **53**, 507-531.
- Beyer, C., Heilmann-Clausen, C., and Abrahamson, N., 2001. Magnetostratigraphy of the Upper Paleocene-Lower Eocene deposits in Denmark. *Newsletters on Stratigraphy* **39**, 1-19.
- Birgel, D., Thiel, V., Hinrichs, K.-U., Elvert, M., Campbell, K. A., Reitner, J., Farmer, J. D., and

- Peckmann, J., 2006. Lipid biomarker patterns of methane-seep microbialites from the Mesozoic convergent margin of California. *Organic Geochemistry* **37**, 1289-1302.
- Birgel, D., Elvert, M., Han, X., and Peckmann, J., 2008. ^{13}C -depleted biphytanic diacids as tracers of past anaerobic oxidation of methane. *Organic Geochemistry* **39**, 152-156.
- Birgel, D., Guido, A., Liu, X., Hinrichs, K.-U., Gier, S., and Peckmann, J., 2014. Hypersaline conditions during deposition of the Calcare di Base revealed from archaeal di- and tetraether inventories. *Organic Geochemistry* **77**, 11-21.
- Bischoff, J. L., Herbst, D. B., and Rosenbauer, R. J., 1991. Gaylussite formation at Mono Lake, California. *Geochimica et Cosmochimica Acta* **55**, 1743-1747.
- Bischoff, J. L., Fitzpatrick, J. A., and Rosenbauer, R. J., 1993. The solubility and stabilization of ikaite ($\text{CaCO}_3 \cdot 6\text{H}_2\text{O}$) from 0° to 25°C : environmental and paleoclimatic implications for thino-lite tufa. *The Journal of Geology* **101**, 21-33.
- Bjørlykke, K., 1983. Diagenetic Reactions in Sandstones. In: *Sediment Diagenesis*, Springer Netherlands, Dordrecht.
- Blumenberg, M., Seifert, R., Petersen, S., and Michaelis, W., 2007. Biosignatures present in a hydrothermal massive sulfide from the Mid-Atlantic Ridge. *Geobiology* **5**, 435-450.
- Boch, R., Dietzel, M., Reichl, P., Leis, A., Baldermann, A., Mittermayr, F., and Pölt, P., 2015. Rapid ikaite ($\text{CaCO}_3 \cdot 6\text{H}_2\text{O}$) crystallization in a man-made river bed: Hydrogeochemical monitoring of a rarely documented mineral formation. *Applied Geochemistry* **63**, 366-379.
- Bøggild, O. B., 1903. Vulkansk Aske i Moleret. *Meddelelser fra Dansk geologisk Forening* **2**, 1-12.
- Bøggild, O. B., 1918. Den vulkanske Aske i Moleret samt en Oversigt over Danmarks ældre Tertiæbjergarter. *Danmarks Geologiske Undersøgelse, II Række* **33**, 1-159.
- Boggs, S. A. M., 1972. Petrography and geochemistry of rhombic, calcite pseudomorphs from mid-Tertiary mudstones of the Pacific Northwest, U.S.A. *Sedimentology* **19**, 219-235.
- Boggs, S. and Hull, D. A., 1975. "Glendonites" from Oregon and Washington. *The Ore Bin* **37**, 89-103.
- Boggs, S., 2009. *Petrology of sedimentary rocks*. Cambridge University Press.
- Bonatti, E., 1965. Palagonite, hyaloclastites and alteration of volcanic glass in the ocean. *Bulletin Volcanologique* **28**, 257-269.
- Bonde, N., 1966. The fishes of the Mo-clay formation: (Lower Eocene). *Meddelelser fra Dansk Geologisk Forening* **16**, 198-201.
- Bonde, N., 1973. Palaeoenvironment as indicated by the 'Mo-clay Formation' (Lowermost Eocene of Denmark). *Tertiary Times* **2**, 29-36.
- Bonde, N., 1979. Palaeoenvironment in the 'North Sea' as indicated by the fish bearing Mo-clay deposit (Paleocene/Eocene), Denmark. *Mededelingen van de Werkgroep voor Tertiaire en Kwartaire Geologie* **16**, 3-16.
- Bonde, N. C., 1997. A distinctive fish fauna in the basal ash-series of the Fur/Ølst Formation (U. Paleocene, Denmark). *Aarhus Geoscience* **6**, 33-48.
- Bonde, N., Andersen, S., Hald, N., & Jakobsen, S. L., 2008. *Danekræ - Danmarks bedste fossiler*, Gyldendal.
- Bonde, N., 2008. Osteoglossomorphs of the marine Lower Eocene of Denmark – with remarks on other Eocene taxa and their importance for palaeobiogeography. *Geological Society, London, Special Publications* **295**, 253-310.
- Bourdon, E., Kristoffersen, A. V., and Bonde, N., 2016. A roller-like bird (Coraci) from the Early Eocene of Denmark. *Scientific Reports* **6**, 34050.
- Bornhold, B. D. and Firth, J. V., 1998. Sites 1033 and 1034. *Proceedings of the Ocean Drilling Program, Initial Reports* **169S**, 51.
- Bowen, G. J., Maibauer, B. J., Kraus, M. J., Rohl, U., Westerhold, T., Steimke, A., Gingerich, P. D., Wing, S. L., and Clyde, W. C., 2015. Two massive, rapid releases of carbon during the onset of the Palaeocene-Eocene thermal maximum. *Nature Geoscience* **8**, 44-47.
- Bralower, T. J., Zachos, J. C., Thomas, E., Parrow, M., Paull, C. K., Kelly, D. C., Silva, I. P., Sliter, W.

- V., and Lohmann, K. C., 1995. Late Paleocene to Eocene paleoceanography of the equatorial Pacific Ocean: Stable isotopes recorded at Ocean Drilling Program Site 865, Allison Guyot. *Paleoceanography* **10**, 841-865.
- Brandriss, M. E., O'Neil, J. R., Edlund, M. B., and Stoermer, E. F., 1998. Oxygen isotope fractionation between diatomaceous silica and water. *Geochimica et Cosmochimica Acta* **62**, 1119-1125.
- Brechevic, L. and Nielsen, A. E., 1993. Solubility of calcium carbonate hexahydrate. *Acta chemica scandinavica* **47**, 668-673.
- Brewer, T. S., Leng, M. J., Mackay, A. W., Lamb, A. L., Tyler, J. J., and Marsh, N. G., 2008. Unravelling contamination signals in biogenic silica oxygen isotope composition: the role of major and trace element geochemistry. *Journal of Quaternary Science* **23**, 321-330.
- Brookes, I. A., McAndrews, J. H., and von Bitter, P. H., 1982. Quaternary interglacial and associated deposits in southwest Newfoundland. *Canadian Journal of Earth Sciences* **19**, 410-423.
- Brooks, R., Clark, L. M., and Thurston, E. F., 1950. Calcium carbonate and its hydrates. *Philosophical Transactions of the Royal Society of London. Series A, Mathematical and Physical Sciences* **243**, 145-167.
- Brooks, K., 2006. When the sun died over northern Europe: the unique geology of Denmark's inland islands. *Geology Today* **22**, 180-186.
- Buchardt, B., 1978. Oxygen isotope palaeotemperatures from the Tertiary period in the North Sea area. *Nature* **275**, 121-123.
- Buchardt, B. and Holmes, M. A., 1995. Initial transgressive phase of Leg 144 guyots: evidence of extreme sulfate reduction, *Papers in the Earth and Atmospheric Sciences*, Paper 62.
- Buchardt, B., Seaman, P., Stockmann, G., Vous, M., Wilken, U., Düwel, L., Kristiansen, A., Jenner, C., Whiticar, M. J., Kristensen, R. M., Petersen, G. H., and Thorbjörn, L., 1997. Submarine columns of ikaite tufa. *Nature* **390**, 129 - 130.
- Buchardt, B., Israelson, C., Seaman, P., and Stockmann, G., 2001. Ikaite tufa towers in Ikka Fjord, southwest Greenland: their formation by mixing of seawater and alkaline spring water. *Journal of Sedimentary Research* **71**, 176-189.
- Burke, W. H., Denison, R. E., Hetherington, E. A., Koepnick, R. B., Nelson, H. F., and Otto, J. B., 1982. Variation of seawater $^{87}\text{Sr}/^{86}\text{Sr}$ throughout Phanerozoic time. *Geology* **10**, 516-519.
- Burton, E. A. and Walter, L. M., 1990. The role of pH in phosphate inhibition of calcite and aragonite precipitation rates in seawater. *Geochimica et Cosmochimica Acta* **54**, 797-808.
- Burton, E. A., 1993. Controls on marine carbonate cement mineralogy: review and reassessment. *Chemical Geology* **105**, 163-179.
- Came, R. E., Eiler, J. M., Veizer, J., Azmy, K., Brand, U., and Weidman, C. R., 2007. Coupling of surface temperatures and atmospheric CO₂ concentrations during the Palaeozoic era. *Nature* **449**, 198-201.
- Chambers, L., Pringle, M., Fitton, G., Larsen, L. M., Pederson, A. K., and Parrish, R., 2003. Recalibration of the Palaeocene-Eocene boundary (P-E) using high precision U-Pb and Ar-Ar isotopic dating. *Geophysical Research Abstracts* **5**, 09681.
- Chickerur, N. S., Tung, M. S., and Brown, W. E., 1980. A mechanism for incorporation of carbonate into apatite. *Calcified Tissue International* **32**, 55-62.
- Clark, I. and Fritz, P., 1997. *Environmental isotopes in hydrology*, CRC Press/Lewis Publishers.
- Claypool, G. E. and Kaplan, I. R., 1974. The Origin and Distribution of Methane in Marine Sediments. In: *Natural Gases in Marine Sediments*, Springer US, Boston, MA.
- Clayton, R. N., Friedman, I., Graf, D. L., Mayeda, T. K., Meents, W. F., and Shimp, N. F., 1966. The origin of saline formation waters: 1. Isotopic composition. *Journal of Geophysical Research* **71**, 3869-3882.
- Clayton, R. N., O'Neil, J. R., and Mayeda, T. K., 1972. Oxygen isotope exchange between quartz and water. *Journal of Geophysical Research* **77**, 3057-3067.
- Coleman, M. L., Raiswell, R., Brown, A., Curtis, C. D., Aplin, A. C., Ortoleva, P. J., Gruszczynski, M., Lyons, T., Lovley, D. R., and Eglinton, G., 1993. Microbial Mineralization of Organic Matter: Mechanisms of Self-Organization and Inferred Rates of Precipitation of Diagenetic Minerals

[and Discussion]. *Philosophical Transactions of the Royal Society of London. Series A: Physical and Engineering Sciences* **344**, 69-87.

Coleyshaw, E. E., Crump, G., and Griffith, W. P., 2003. Vibrational spectra of the hydrated carbonate minerals ikaite, monohydrocalcite, lansfordite and nesquehonite. *Spectrochimica Acta Part A: Molecular and Biomolecular Spectroscopy* **59**, 2231-2239.

Collins, J. S., Schulz, B. P., and Jakobsen, S. L., 2005. First record of brachyuran decapods (Crustacea, Decapoda) from Fur Formation (early Eocene) of Mors and Fur Island, Denmark. *Bulletin of the Mizunami Fossil Museum* **32**, 17-22.

Compston, W. and Oversby, V., 1969. Lead isotopic analysis using a double spike. *Journal of Geophysical Research* **74**, 4338-4348.

Council, T. C. and Bennett, P. C., 1993. Geochemistry of ikaite formation at Mono Lake, California: Implications for the origin of tufa mounds. *Geology* **21**, 971-974.

Craig, H., 1965. The measurement of oxygen isotope paleotemperatures. *Stable isotopes in oceanographic studies and paleotemperatures* **23**.

Cummins, R. C., Finnegan, S., Fike, D. A., Eiler, J. M., and Fischer, W. W., 2014. Carbonate clumped isotope constraints on Silurian ocean temperature and seawater $\delta^{18}\text{O}$. *Geochimica et Cosmochimica Acta* **140**, 241-258.

Daëron, M., Guo, W., Eiler, J., Genty, D., Blamart, D., Boch, R., Drysdale, R., Maire, R., Wainer, K., and Zanchetta, G., 2011. $^{13}\text{C}^{18}\text{O}$ clumping in speleothems: Observations from natural caves and precipitation experiments. *Geochimica et Cosmochimica Acta* **75**, 3303-3317.

Dale, A., John, C. M., Mozley, P. S., Smalley, P. C., and Muggeridge, A. H., 2014. Time-capsule concretions: Unlocking burial diagenetic processes in the Mancos Shale using carbonate clumped isotopes. *Earth and Planetary Science Letters* **394**, 30-37.

Dana, J., 1849. Geology: United States Exploring Expedition. *George P. Putnam, New York* **10**, 127.

David, T. W. E., Taylor, T. G., Woolnough, W.G., Foxall, H.G., 1905. Occurrence of the pseudomorph glendonites in New South Wales. *Records*

of the Geological Survey of New South Wales **8**, 163-179.

De La Rocha, C. L. and DePaolo, D. J., 2000. Isotopic evidence for variations in the marine calcium cycle over the Cenozoic. *Science* **289**, 1176-1178.

De Lurio, J. L. and Frakes, L. A., 1999. Glendonites as a paleoenvironmental tool: implications for early Cretaceous high latitude climates in Australia. *Geochimica et Cosmochimica Acta* **63**, 1039-1048.

Demichelis, R., Raiteri, P., and Gale, J. D., 2014. Structure of hydrated calcium carbonates: A first-principles study. *Journal of Crystal Growth* **401**, 33-37.

Dempster, T. and Jess, S. A., 2015. Ikaite pseudomorphs in Neoproterozoic Dalradian slates record Earth's coldest metamorphism. *Journal of the Geological Society* **172**, 459-464.

DePaolo, D. J., 2011. Surface kinetic model for isotopic and trace element fractionation during precipitation of calcite from aqueous solutions. *Geochimica et Cosmochimica Acta* **75**, 1039-1056.

Dickens, G. R., O'Neil, J. R., Rea, D. K., and Owen, R. M., 1995. Dissociation of oceanic methane hydrate as a cause of the carbon isotope excursion at the end of the Paleocene. *Paleoceanography* **10**, 965-971.

Dieckmann, G. S., Nehrke, G., Papadimitriou, S., Göttlicher, J., Steininger, R., Kennedy, H., Wolf-Gladrow, D., and Thomas, D. N., 2008. Calcium carbonate as ikaite crystals in Antarctic sea ice. *Geophysical Research Letters* **35**, L08501.

Dieckmann, G. S., Nehrke, G., Uhlig, C., Göttlicher, J., Gerland, S., Granskog, M. A., and Thomas, D. N., 2010. Brief Communication: Ikaite ($\text{CaCO}_3 \cdot 6\text{H}_2\text{O}$) discovered in Arctic sea ice. *The Cryosphere* **4**, 227-230.

Dodd, J. P. and Sharp, Z. D., 2010. A laser fluorination method for oxygen isotope analysis of biogenic silica and a new oxygen isotope calibration of modern diatoms in freshwater environments. *Geochimica et Cosmochimica Acta* **74**, 1381-1390.

- Dodd, J., 2011. *Oxygen isotopes in diatom silica: a new understanding of silica-water oxygen isotope fractionation in diatom frustules and an application of diatom d_{18O} values as a record of paleohydrologic variability in a middle-Pleistocene lacustrine core from the Valles Caldera, New Mexico*. University of New Mexico, Albuquerque, New Mexico.
- Domack, E. W., Halverson, G., Willmott, V., Leventer, A., Brachfeld, S., and Ishman, S., 2007. Spatial and temporal distribution of ikaite crystals in Antarctic glacial marine sediments. *USGS Open-File Report* **1047**.
- Dowgiallo, I. and Tongiorgi, E., 1972. The isotopic composition of oxygen and hydrogen in some brines from the Mesozoic in North-west Poland. *Geothermics* **1**, 67-69.
- Dyke, G. and Lindow, B., 2009. Taphonomy and abundance of birds from the Lower Eocene Fur Formation of Denmark. *Geological Journal* **44**, 365-373.
- Eagle, R. A., Schauble, E. A., Tripathi, A. K., Tütken, T., Hulbert, R. C., and Eiler, J. M., 2010. Body temperatures of modern and extinct vertebrates from ^{13}C - ^{18}O bond abundances in bioapatite. *Proceedings of the National Academy of Sciences* **107**, 10377-10382.
- Eglinton, G. and Hamilton, R. J., 1967. Leaf Epicuticular Waxes. *Science* **156**, 1322-1335.
- Eiler, J. M., 2007. "Clumped-isotope" geochemistry—The study of naturally-occurring, multiply-substituted isotopologues. *Earth and Planetary Science Letters* **262**, 309-327.
- Epstein, S., Buchsbaum, R., Lowenstam, H. A., and Urey, H. C., 1953. Revised carbonate-water isotopic temperature scale. *Geological Society of America Bulletin* **64**, 1315-1326.
- Fairbridge, R. W., 1967. Chapter 2 Phases of Diagenesis and Authigenesis. In: *Developments in Sedimentology*, Elsevier.
- Fenner, J., 1994. Diatoms of the Fur Formation, their taxonomy and biostratigraphic interpretation. – Results from the Harre borehole, Denmark. *Aarhus Geoscience* **1**, 99-163.
- Fiebig, J., Hofmann, S., Löffler, N., Lüdecke, T., Methner, K., and Wacker, U., 2016. Slight pressure imbalances can affect accuracy and precision of dual inlet-based clumped isotope analysis. *Isotopes in Environmental and Health Studies* **52**, 12-28.
- Field, L., Milodowski, A., Shaw, R., Stevens, L., Hall, M., Kilpatrick, A., Gunn, J., Kemp, S., and Ellis, M., 2016. PREPUBLICATION: Unusual morphologies and the occurrence of pseudomorphs after ikaite ($CaCO_3 \cdot 6H_2O$) in fast growing, hyperalkaline speleothem. *Mineralogical Magazine*.
- Fischer, M., 2009. *Carbonate chemistry and $CaCO_3$ precipitation as ikaite in Antarctic sea ice - Analysis in the Southern Ocean and off Adélie Land, Antarctica*. Universität Leipzig, Leipzig, Germany.
- Fischer, M., Thomas, D. N., Krell, A., Nehrke, G., Göttlicher, J., Norman, L., Meiners, K. M., Riaux-Gobin, C., and Dieckmann, G. S., 2013. Quantification of ikaite in Antarctic sea ice. *Antarctic Science* **25**, 421-432.
- Föllmi, K. B., 2012. Early Cretaceous life, climate and anoxia. *Cretaceous Research* **35**, 230-257.
- Fontes, J. C. and Matray, J. M., 1993. Geochemistry and origin of formation brines from the Paris Basin, France. *Chemical Geology* **109**, 149-175.
- Forchhammer, J. G., 1835. *Danmarks geognostiske Forhold, forsaavidt som de ere afhaengige af Dannelser, der ere sluttede*, Schulz.
- Frank, T. D., Thomas, S. G., and Fielding, C. R., 2008. On using carbon and oxygen isotope data from glendonites as paleoenvironmental proxies: a case study from the Permian system of Eastern Australia. *Journal of Sedimentary Research* **78**, 713-723.
- Freiesleben, J. C., 1827. Ueber einige Vorkommnisse im Schlottenleimen (Alluvialthon) bey Obersdorf, ohnweit Sangerhausen. *Isis* **20**, 334-337.
- Frieling, J., Svensen, H. H., Planke, S., Cramwinckel, M. J., Selnes, H., and Sluijs, A., 2016. Thermogenic methane release as a cause for the long duration of the PETM. *Proceedings of the National Academy of Sciences* **113**, 12059-12064.
- Gal, J.-Y., Bollinger, J.-C., Tolosa, H., and Gache, N., 1996. Calcium carbonate solubility: a reappraisal of scale formation and inhibition. *Talanta* **43**, 1497-1509.

- Geptner, A. R., Vetoshkina, O. S., and Petrova, V. V., 2014. New data on the composition of stable isotopes in glendonites of the White Sea and their genesis. *Lithology and Mineral Resources* **49**, 473-490.
- Ghosh, P., Adkins, J., Affek, H., Balta, B., Guo, W., Schauble, E. A., Schrag, D., and Eiler, J. M., 2006. ^{13}C - ^{18}O bonds in carbonate minerals: A new kind of paleothermometer. *Geochimica et Cosmochimica Acta* **70**, 1439-1456.
- Grasby, S. E., McCune, G. E., Beauchamp, B., and Galloway, J. M., 2017. Lower Cretaceous cold snaps led to widespread glendonite occurrences in the Sverdrup Basin, Canadian High Arctic. *Geological Society of America Bulletin*, doi: 10.1130/B31600.1.
- Greinert, J. and Derkachev, A., 2004. Glendonites and methane-derived Mg-calcites in the Sea of Okhotsk, Eastern Siberia: implications of a venting-related ikaite/glendonite formation. *Marine Geology* **204**, 129-144.
- Gripp, K. and Tufar, W., 1974. Pseudogaylussit führende Konkretionen aus dem Wattenmeer. *Meyniana* **25**, 21-30.
- Gross, M. G., 1964. Variations in the $^{18}\text{O}/^{16}\text{O}$ and $^{13}\text{C}/^{12}\text{C}$ ratios of diagenetically altered limestones in the Bermuda Islands. *The Journal of Geology* **72**, 170-194.
- Gry, H., 1940. De istektoniske Forhold i Moleret. Med bemærkninger om vore dislocerede klinters dannelse og om den negative askeserie. *Meddelelser fra Dansk Geologisk Forening* **9**, 586-627.
- Gry, H., 1965. Furs geologi. *Dansk natur - dansk skole, Årsskrift* **1964**, 45-55.
- Guo, W., Mosenfelder, J. L., Goddard lii, W. A., and Eiler, J. M., 2009. Isotopic fractionations associated with phosphoric acid digestion of carbonate minerals: Insights from first-principles theoretical modeling and clumped isotope measurements. *Geochimica et Cosmochimica Acta* **73**, 7203-7225.
- Gussone, N., Nehrke, G., and Teichert, B. M. A., 2011. Calcium isotope fractionation in ikaite and vaterite. *Chemical Geology* **285**, 194-202.
- Haase, V., 1998. Untersuchungen zur Genese von Ikait aus der Laptevsee – Laborteil. Bergakademie Freiberg, Freiberg, Germany.
- Hallam, A. and Bradshaw, M. J., 1979. Bituminous shales and oolitic ironstones as indicators of transgressions and regressions. *Journal of the Geological Society* **136**, 157-164.
- Hansen, M. O., Buchardt, B., Kühl, M., and Elberling, B., 2011. The fate of the submarine ikaite tufa columns in southwest Greenland under changing climate conditions. *Journal of Sedimentary Research* **81**, 553-561.
- Hatté, C., Hodgins, G., Jull, A. J. T., Bishop, B., and Tesson, B., 2008. Marine chronology based on ^{14}C dating on diatoms proteins. *Marine Chemistry* **109**, 143-151.
- Hayes, J. M., 1993. Factors controlling ^{13}C contents of sedimentary organic compounds: Principles and evidence. *Marine Geology* **113**, 111-125.
- Heilmann-Clausen, C., 1982. The Paleocene - Eocene boundary in Denmark. *Newsletters on Stratigraphy* **11**, 55-63.
- Heilmann-Clausen, C., Nielsen, O., and Gersner, F., 1985. Lithostratigraphy and depositional environments in the Upper Paleocene and Eocene of Denmark. *Bulletin of the Geological Society of Denmark* **33**, 287-323.
- Heilmann-Clausen, C. and Schmitz, B., 2000. The late Paleocene thermal maximum $\delta^{13}\text{C}$ excursion in Denmark? *GFF* **122**, 70-70.
- Heilmann-Clausen, C. and Rasmussen, E. S., 2010. Danmarks geologiske udvikling fra 65 til 2,6 mio. år før nu. *Geviden - Geologi og Geografi* **3**, 20.
- Hensen, C., Zabel, M., Pfeifer, K., Schwenk, T., Kasten, S., Riedinger, N., Schulz, H. D., and Boetius, A., 2003. Control of sulfate pore-water profiles by sedimentary events and the significance of anaerobic oxidation of methane for the burial of sulfur in marine sediments. *Geochimica et Cosmochimica Acta* **67**, 2631-2647.
- Herold, N., Buzan, J., Seton, M., Goldner, A., Green, J. A. M., Müller, R. D., Markwick, P., and Huber, M., 2014. A suite of early Eocene (~ 55 Ma) climate model boundary conditions. *Geoscientific Model Development* **7**, 2077-2090.
- Herrle, J. O., Schröder-Adams, C. J., Davis, W., Pugh, A. T., Galloway, J. M., and Fath, J., 2015. Mid-Cretaceous High Arctic stratigraphy, climate,

- and Oceanic Anoxic Events. *Geology* **43**, 403-406.
- Heuser, A., Eisenhauer, A., Gussone, N., Bock, B., Hansen, B., and Nägler, T. F., 2002. Measurement of calcium isotopes ($\delta^{44}\text{Ca}$) using a multi-collector TIMS technique. *International Journal of Mass Spectrometry* **220**, 385-397.
- Hitchon, B. and Friedman, I., 1969. Geochemistry and origin of formation waters in the western Canada sedimentary basin—I. Stable isotopes of hydrogen and oxygen. *Geochimica et Cosmochimica Acta* **33**, 1321-1349.
- Hodell, D. A., Kamenov, G. D., Hathorne, E. C., Zachos, J. C., Röhl, U., and Westerhold, T., 2007. Variations in the strontium isotope composition of seawater during the Paleocene and early Eocene from ODP Leg 208 (Walvis Ridge). *Geochemistry, Geophysics, Geosystems* **8**, Q09001.
- Hoefs, J., 2015. *Isotope Fractionation Processes of Selected Elements, Stable Isotope Geochemistry*. Springer International Publishing, Cham.
- Hoffmann-Sell, L., Birgel, D., Arning, E. T., Föllmi, K. B., and Peckmann, J., 2011. Archaeal lipids in Neogene dolomites (Monterey and Sisquoc Formations, California) – Planktic versus benthic archaeal sources. *Organic Geochemistry* **42**, 593-604.
- House, W. A., 1987. Inhibition of calcite crystal growth by inorganic phosphate. *Journal of Colloid and Interface Science* **119**, 505-511.
- Howarth, R. J. and McArthur, J. M., 1997. Statistics for strontium isotope stratigraphy: a robust LOWESS fit to the marine Sr-isotope curve for 0 to 206 Ma, with look-up table for derivation of numeric age. *The Journal of Geology* **105**, 441-456.
- Hu, Y.-B., Wolf-Gladrow, D. A., Dieckmann, G. S., Völker, C., and Nehrke, G., 2014. A laboratory study of ikaite ($\text{CaCO}_3 \cdot 6\text{H}_2\text{O}$) precipitation as a function of pH, salinity, temperature and phosphate concentration. *Marine Chemistry* **162**, 10-18.
- Hu, Y.-B., Wolthers, M., Wolf-Gladrow, D. A., and Nehrke, G., 2015. Effect of pH and phosphate on calcium carbonate polymorphs precipitated at near-freezing temperature. *Crystal Growth & Design* **15**, 1596-1601.
- Huber, H., Koeberl, C., and Egger, H., 2003. Geochemical study of lower Eocene volcanic ash layers from the Alpine Anthering Formation, Austria. *Geochemical Journal* **37**, 123-134.
- Huggett, J. M., Schultz, B. P., Shearman, D. J., and Smith, A. J., 2005. The petrology of ikaite pseudomorphs and their diagenesis. *Proceedings of the Geologists' Association* **116**, 207-220.
- Huntington, K., Eiler, J., Affek, H., Guo, W., Bonifacie, M., Yeung, L., Thiagarajan, N., Passey, B., Tripathi, A., and Daëron, M., 2009. Methods and limitations of 'clumped' CO_2 isotope (Δ_{47}) analysis by gas-source isotope ratio mass spectrometry. *Journal of Mass Spectrometry* **44**, 1318-1329.
- Huntington, K. W., Budd, D. A., Wernicke, B. P., and Eiler, J. M., 2011. Use of clumped-isotope thermometry to constrain the crystallization temperature of diagenetic calcite. *Journal of Sedimentary Research* **81**, 656-669.
- Iacumin, P., Bocherens, H., Mariotti, A., and Longinelli, A., 1996. Oxygen isotope analyses of co-existing carbonate and phosphate in biogenic apatite: a way to monitor diagenetic alteration of bone phosphate? *Earth and Planetary Science Letters* **142**, 1-6.
- Ito, T., 1996. Ikaite from cold spring water at Shiowakka, Hokkaido, Japan. *Journal of mineralogy, petrology and economic geology* **91**, 209-219.
- Ito, T., 1998. Factors controlling the transformation of natural ikaite from Shiowakka, Japan. *Geochemical Journal-Japan*, **32**, 267-274.
- James, N. P., Narbonne, G. M., Dalrymple, R. W., and Kyser, T. K., 2005. Glendonites in Neoproterozoic low-latitude, interglacial, sedimentary rocks, northwest Canada: Insights into the Cryogenian ocean and Precambrian cold-water carbonates. *Geology* **33**, 9-12.
- Jansen, J. H. F., Woensdregt, C. F., Kooistra, M. J., and van der Gaast, S. J., 1987. Ikaite pseudomorphs in the Zaire deep-sea fan: An intermediate between calcite and porous calcite. *Geology* **15**, 245-248.
- Jiang, H., Seidenkrantz, M.-S., Knudsen, K. L., and Eriksson, J., 2002. Late-Holocene summer

sea-surface temperatures based on a diatom record from the north Icelandic shelf. *The Holocene* **12**, 137-147.

Jiménez-López, C., Caballero, E., Huertas, F. J., and Romanek, C. S., 2001. Chemical, mineralogical and isotope behavior, and phase transformation during the precipitation of calcium carbonate minerals from intermediate ionic solution at 25°C. *Geochimica et Cosmochimica Acta* **65**, 3219-3231.

Johnston, J. D., 1995. Pseudomorphs after ikaite in a glaciomarine sequence in the Dalradian of Donegal, Ireland. *Scottish Journal of Geology* **31**, 3-9.

Jones, A. T., Frank, T. D., and Fielding, C. R., 2006. Cold climate in the eastern Australian mid to late Permian may reflect cold upwelling waters. *Palaeogeography, Palaeoclimatology, Palaeoecology* **237**, 370-377.

Jones, M. T. and Gislason, S. R., 2008. Rapid releases of metal salts and nutrients following the deposition of volcanic ash into aqueous environments. *Geochimica et Cosmochimica Acta* **72**, 3661-3680.

Jørgensen, F., Sandersen, P. B., Auken, E., Lykke-Andersen, H., and Sørensen, K., 2005. Contributions to the geological mapping of Mors, Denmark—a study based on a large-scale TEM survey. *Bulletin of the Geological Society of Denmark* **52**, 53-75.

Juillet-Leclerc, A. J. and Labeyrie, L., 1987. Temperature dependence of the oxygen isotopic fractionation between diatom silica and water. *Earth and Planetary Science Letters* **84**, 69-74.

Kampschulte, A. and Strauss, H., 2004. The sulfur isotopic evolution of Phanerozoic seawater based on the analysis of structurally substituted sulfate in carbonates. *Chemical Geology* **204**, 255-286.

Kaplan, M., 1979. Calcite pseudomorphs (pseudogaylussite, jarrowite, thinolite, glendonite, gennoishi, White Sea hornlets) in sedimentary rocks: origins of the pseudomorphs. *Lithology and Mineral Resources* **14**, 623-636.

Kawano, M. and Tomita, K., 2001. Microbial biomineralization in weathered volcanic ash de-

posit and formation of biogenic minerals by experimental incubation. *American Mineralogist* **86**, 400-410.

Kemper, E. and Schmitz, H., 1975. Stellate nodules from the upper Deer Bay Formation (Valanginian) of Arctic Canada. *Geological Survey of Canada, Paper* **75**, 109-119.

Kemper, E. and Schmitz, H., 1981. Glendonite — Indikatoren des polarmarinen Ablagerungsmilieus. *Geologische Rundschau* **70**, 759-773.

Kemper, E., 1987. Das Klima der Kreide-Zeit. *Geologisches Jahrbuch Reihe A* **96**, 184.

Kender, S., Stephenson, M. H., Riding, J. B., Leng, M. J., Knox, R. W. O. B., Peck, V. L., Kendrick, C. P., Ellis, M. A., Vane, C. H., and Jamieson, R., 2012. Marine and terrestrial environmental changes in NW Europe preceding carbon release at the Paleocene–Eocene transition. *Earth and Planetary Science Letters* **353–354**, 108-120.

Kennedy, G., Hopkins, D., and Pickthorn, W., 1987. Ikaite, the glendonite precursor, in estuarine sediments at Barrow, Arctic Alaska. *Geological Society of America, Abstracts with Programs* 143712.

Kennett, J. and Stott, L., 1991. Abrupt deep-sea warming, palaeoceanographic changes and benthic extinctions at the end. *Nature* **353**, 19.

Kiel, S., Birgel, D., Campbell, K. A., Crampton, J. S., Schiøler, P., and Peckmann, J., 2013. Cretaceous methane-seep deposits from New Zealand and their fauna. *Palaeogeography, Palaeoclimatology, Palaeoecology* **390**, 17-34.

Kim, S.-T. and O'Neil, J. R., 1997. Equilibrium and nonequilibrium oxygen isotope effects in synthetic carbonates. *Geochimica et Cosmochimica Acta* **61**, 3461-3475.

Kita, I., Taguchi, S., and Matsubaya, O., 1985. Oxygen isotope fractionation between amorphous silica and water at 34-93°C. *Nature* **314**, 83-84.

Klint, K. E. S. and Pedersen, S. A. S., 1995. The Hanklit glaciotectionic thrust fault complex, Mors, Denmark. *Danmarks Geologiske Undersøgelse Række A* **35**.

Kloppmann, W., Négrel, P., Casanova, J., Klinge, H., Schelkes, K., and Guerrot, C., 2001. Halite

- dissolution derived brines in the vicinity of a Permian salt dome (N German Basin). Evidence from boron, strontium, oxygen, and hydrogen isotopes. *Geochimica et Cosmochimica Acta* **65**, 4087-4101.
- Kluge, T., Affek, H. P., Marx, T., Aeschbach-Hertig, W., Riechelmann, D. F. C., Scholz, D., Riechelmann, S., Immenhauser, A., Richter, D. K., Fohlmeister, J., Wackerbarth, A., Mangini, A., and Spötl, C., 2013. Reconstruction of drip-water $\delta^{18}\text{O}$ based on calcite oxygen and clumped isotopes of speleothems from Bunker Cave (Germany). *Climate of the Past* **9**, 377-391.
- Knauth, L. P., 1973. *Oxygen and hydrogen isotope ratios in cherts and related rocks*, California Institute of Technology.
- Knox, R. W. O. B. and Ellison, R. A., 1979. A Lower Eocene ash sequence in SE England. *Journal of the Geological Society* **136**, 251-253.
- Knox, R. W. O. B. and Harland, R., 1979. Stratigraphical relationships of the early Palaeogene ash-series of NW Europe. *Journal of the Geological Society* **136**, 463-470.
- Knox, R. O. B., 1996. Correlation of the early Paleogene in northwest Europe: an overview. *Geological Society, London, Special Publications* **101**, 1-11.
- Knox, R., 1997. The Late Paleocene to Early Eocene ash layers of the Danish Mo-Clay (Fur Formation): stratigraphic and tectonic significance. *Aarhus Geoscience* **6**, 7-11.
- Knox, R.W.O'B, Bosch, J.H.A., Rasmussen, E.S., Heilmann-Clausen, C., Hiss, M., De Lugt, I.R., Kasinski, J., King, C., Köthe, A., Slodkowska, B., Standke, G., Vandenberghe, N., 2010: Cenozoic. In: *Petroleum Geological Atlas of the Southern Permian Basin Area*, EAGE Publications b.v., Houten.
- Kockum, P. C. F., Herbert, R. B., and Gislason, S. R., 2006. A diverse ecosystem response to volcanic aerosols. *Chemical Geology* **231**, 57-66.
- Kodina, L. A., Tokarev, L. N., Vlasova, L. N., Bychkov, A. M., and Mardanjan, I. Y., 2002. New findings of ikaite in the Kara Sea during R/V "Akademik Boris Petrov" Cruise 36, September 2001.
- Kodina, L., Tokarev, V., Vlasova, L., and Korobeinik, G., 2003. Contribution of biogenic methane to ikaite formation in the Kara Sea; evidence from the stable carbon isotope geochemistry. *Proceedings in Marine Science* **6**, 349-374.
- Kolodny, Y. and Kaplan, I., 1970. Carbon and oxygen isotopes in apatite CO_2 and co-existing calcite from sedimentary phosphorite. *Journal of Sedimentary Research* **40**, 954-959.
- Kowalczyk, K., 2006. *The isotopic composition of valves and organic tissue of diatoms grown in steady state cultures under varying conditions of temperature, light and nutrients. Implications for the interpretation of oxygen isotopes from sedimentary biogenic opal as proxies of environmental variations*, Universität Köln, Köln.
- Kurtz, A., Kump, L., Arthur, M., Zachos, J., and Paytan, A., 2003. Early Cenozoic decoupling of the global carbon and sulfur cycles. *Paleoceanography* **18**, 1090.
- Lamb, A., Leng, M., Sloane, H., and Telford, R., 2005. A comparison of $\delta^{18}\text{O}$ data from calcite and diatom silica from early Holocene in a small crater lake in the tropics. *Palaeogeography Palaeoclimatology Palaeoecology* **223**, 290-300.
- Langworthy, T. A., Mayberry, W. R., and Smith, P. F., 1974. Long-Chain Glycerol Diether and Polyol Dialkyl Glycerol Triether Lipids of *Sulfolobus acidocaldarius*. *Journal of Bacteriology* **119**, 106-116.
- Larsen, G. and Baumann, J., 1981. Træk af Mors salthorstens udvikling. *DGF Årsskrift for 1981*, 151-155.
- Larsen, D., 1994. Origin and paleoenvironmental significance of calcite pseudomorphs after ikaite in the Oligocene Creede Formation, Colorado. *Journal of Sedimentary Research* **64**, 593-603.
- Larsen, L. M., Fitton, J. G., and Pedersen, A. K., 2003. Paleogene volcanic ash layers in the Danish Basin: compositions and source areas in the North Atlantic Igneous Province. *Lithos* **71**, 47-80.
- Larsen, L. M., Pedersen, A. K., Tegner, C., and Duncan, R. A., 2014. Eocene to Miocene igneous activity in NE Greenland: northward younging of magmatism along the East Greenland margin. *Journal of the Geological Society* **171**, 539-553.

- Larsson, S. G., 1975. Palaeobiology and mode of burial of the insects of the Lower Eocene Mo-clay of Denmark. *Bulletin of the Geological Society of Denmark* **24**, 193-209.
- Last, F. M., Last, W. M., and Halden, N. M., 2010. Carbonate microbialites and hardgrounds from Manito Lake, an alkaline, hypersaline lake in the northern Great Plains of Canada. *Sedimentary Geology* **225**, 34-49.
- Lawrence, J. R., Drever, J. I., Anderson, T. F., and Brueckner, H. K., 1979. Importance of alteration of volcanic material in the sediments of deep sea drilling site 323: chemistry, $^{18}\text{O}/^{16}\text{O}$ and $^{87}\text{Sr}/^{86}\text{Sr}$. *Geochimica et Cosmochimica Acta* **43**, 573-588.
- Lawrence, J. R. and Taviani, M., 1988. Extreme hydrogen, oxygen and carbon isotope anomalies in the pore waters and carbonates of the sediments and basalts from the Norwegian Sea: methane and hydrogen from the mantle? *Geochimica et Cosmochimica Acta* **52**, 2077-2083.
- Leng, M., Barnker, P., Greenwood, P., Roberts, N., and Reed, J., 2001. Oxygen isotope analysis of diatom silica and authigenic calcite from Lake Pinarbasi, Turkey. *Journal of Paleolimnology* **25**, 343-349.
- Leng, M. J. and Marshall, J. D., 2004. Palaeoclimate interpretation of stable isotope data from lake sediment archives. *Quaternary Science Reviews* **23**, 811-831.
- Leng, M. J. and Barker, P. A., 2006. A review of the oxygen isotope composition of lacustrine diatom silica for palaeoclimate reconstruction. *Earth-Science Reviews* **75**, 5-27.
- Lennie, A. R., Tang, C. C., and Thompson, S. P., 2004. The structure and thermal expansion behaviour of ikaite, $\text{CaCO}_3 \cdot 6\text{H}_2\text{O}$, from $T = 114$ to $T = 293$ K. *Mineralogical Magazine* **68**, 135-146.
- Lin, Y.-P. and Singer, P. C., 2006. Inhibition of calcite precipitation by orthophosphate: Speciation and thermodynamic considerations. *Geochimica et Cosmochimica Acta* **70**, 2530-2539.
- Lindgren, J., Uvdal, P., Sjövall, P., Nilsson, D. E., Engdahl, A., Schultz, B. P., and Thiel, V., 2012. Molecular preservation of the pigment melanin in fossil melanosomes. *Nature Communications* **3**, 824.
- Lindow, B. E. K. and Dyke, G. J., 2006. Bird evolution in the Eocene: climate change in Europe and a Danish fossil fauna. *Biological Reviews* **81**, 483-499.
- Lindow, B. E. K. and Dyke, G. J., 2007. A small galiform bird from the Lower Eocene Fur Formation, northwestern Denmark. *Bulletin of the Geological Society of Denmark* **55**, 59-63.
- Lohmann, K. C., 1988. *Geochemical patterns of meteoric diagenetic systems and their application to studies of paleokarst*. Springer.
- Loyd, S. J., Berelson, W. M., Lyons, T. W., Hammond, D. E., and Corsetti, F. A., 2012. Constraining pathways of microbial mediation for carbonate concretions of the Miocene Monterey Formation using carbonate-associated sulfate. *Geochimica et Cosmochimica Acta* **78**, 77-98.
- Loyd, S. J., Sample, J., Tripathi, R. E., Defliese, W. F., Brooks, K., Hovland, M., Torres, M., Marlow, J., Hancock, L. G., Martin, R., Lyons, T., and Tripathi, A. E., 2016. Methane seep carbonates yield clumped isotope signatures out of equilibrium with formation temperatures. *Nature Communications* **7**, 12274.
- Lu, Z., Rickaby, R. E. M., Kennedy, H., Kennedy, P., Pancost, R. D., Shaw, S., Lennie, A., Wellner, J., and Anderson, J. B., 2012. An ikaite record of late Holocene climate at the Antarctic Peninsula. *Earth and Planetary Science Letters* **325**, 108-115.
- Lumsden, D. N., 1979. Discrepancy between thin-section and X-ray estimates of dolomite in limestone. *Journal of Sedimentary Research* **49**, 429-435.
- Mackay, A. W., Karabanov, E., Leng, M. J., Sloane, H. J., Morley, D. W., Panizzo, V. N., Khursevich, G., and Williams, D., 2008. Reconstructing hydrological variability in Lake Baikal during MIS 11: an application of oxygen isotope analysis of diatom silica. *Journal of Quaternary Science* **23**, 365-374.
- Madirazza, I. and Fregerslev, S., 1969. Lower Eocene tuffs at Mønsted, North Jutland. *Bulletin of the Geological Society of Denmark* **19**, 283-318.
- Madirazza, I., 1976. Zechstein bassinet og saltstrukturer i Nordjylland med særligt henblik på Nøvling og Paarup. *Dansk Geologisk Forening, Årsskrift for 1976*, 57-68.

- Malm, O. A., Christensen, O. B., Furnes, H., Løvlie, R., Ruselåtten, H., and Østby, K. L., 1984. The Lower Tertiary Balder Formation: An organogenic and tuffaceous deposit in the North Sea region. In: *Petroleum Geology of the North European Margin: Proceedings of the North European Margin Symposium (NEMS '83), organized by the Norwegian Petroleum Society and held at the Norwegian Institute of Technology (NTH) in Trondheim 9–11 May, 1983*. Springer Netherlands, Dordrecht.
- Marland, G., 1975. The stability of $\text{CaCO}_3 \cdot 6\text{H}_2\text{O}$ (ikaite). *Geochimica et Cosmochimica Acta* **39**, 83-91.
- Martin, E. E. and MacDougall, J. D., 1995. Sr and Nd isotopes at the permian/triassic boundary: a record of climate change. *Chemical Geology* **125**, 73-99.
- Mayr, G. and Bertelli, S., 2011. A record of Rhynchaeites (Aves, Threskiornithidae) from the early Eocene Fur Formation of Denmark, and the affinities of the alleged parrot Mopsitta. *Palaeobiodiversity and Palaeoenvironments* **91**, 229-236.
- McArthur, J. M., Howarth, R. J., and Bailey, T. R., 2001. Strontium isotope stratigraphy: LOWESS version 3: best fit to the marine Sr-isotope curve for 0-509 Ma and accompanying look-up table for deriving numerical age. *The Journal of Geology* **109**, 155-170.
- McCune, G. E., Grasby, S. E., and Beauchamp, B., 2011. Geochemical Conditions Related to Glendonite Formation: a Case Study from Ellef Ringnes Island, Nunavut/Recovery, CSPG CSEG CWLS Convention.
- McInerney, F. A. and Wing, S. L., 2011. The Paleocene-Eocene Thermal Maximum: a perturbation of carbon cycle, climate, and biosphere with implications for the future. *Annual Review of Earth and Planetary Sciences* **39**, 489-516.
- McLachlan, I. R., Tsikos, H., and Cairncross, B., 2001. Glendonites (pseudomorphs after ikaite) in late carboniferous marine Dwyka beds in Southern Africa. *South African Journal of Geology* **104**, 265-272.
- Mikkelsen, N., Labeyrie, L., and Berger, W. H., 1978. Silica oxygen isotopes in diatoms: a 20,000 yr record in deep-sea sediments. *Nature* **271**, 536-538.
- Milodowski, A., Rushton, J., Purser, G., Rochelle, C., Kemp, S., Shaw, R., and Ellis, M., 2014. The formation of ikaite ($\text{CaCO}_3 \cdot 6\text{H}_2\text{O}$) in hyperalkaline springs associated with the leaching of lime kiln waste. *Goldschmidt 2014 Abstracts* **2014**, 1697.
- Mizutani, Y. and Rafter, T. A., 1973. Isotopic behaviour of sulphate oxygen in the bacterial reduction of sulphate. *Geochemical Journal* **6**, 183-191.
- Morales, C., Suan, G., Wierzbowski, H., Rogov, M., Teichert, B., Kienhuis, M. V., Polerecky, L., Middelburg, J., Reichart, G.-J., and van de Schootbrugge, B., 2015. Mesozoic authigenic carbonate deposition in the Arctic: do glendonites record gas hydrate destabilization during the Jurassic? *EGU General Assembly Conference Abstracts* **17**, 14517.
- Morley, D., Leng, M., Mackay, A., Sloane, H., Rioual, P., and Battarbee, R., 2004. Cleaning of lake sediment samples for diatom oxygen isotope analysis. *Journal of Paleolimnology* **31**, 391-401.
- Morley, D. W., Leng, M. J., Mackay, A. W., and Sloane, H. J., 2005. Late glacial and Holocene environmental change in the Lake Baikal region documented by oxygen isotopes from diatom silica. *Global and Planetary Change* **46**, 221-233.
- Morton, R. A. and Land, L. S., 1987. Regional variations in formation water chemistry, Frio formation (Oligocene), Texas Gulf Coast. *AAPG Bulletin* **71**, 191-206.
- Morton, A. C. and Evans, J. A., 1988. Geochemistry of basaltic ash beds from the Fur Formation, Island of Fur, Denmark. *Bulletin of the Geological Society of Denmark* **37**, 1-9.
- Moschen, R., Lücke, A., and Schleser, G. H., 2005. Sensitivity of biogenic silica oxygen isotopes to changes in surface water temperature and palaeoclimatology. *Geophysical Research Letters* **32**, L07708.
- Mozley, P. S. and Burns, S. J., 1993. Oxygen and carbon isotopic composition of marine carbonate concretions: an overview. *Journal of Sedimentary Research* **63**.
- Nielsen, E., 1959. *Eocene turtles from Denmark*. Fr. Bagges Kgl. Hofbogtrykkeri.

- Nielsen, E., 1963. *On the post-cranial skeleton of Eosphargis breineri Nielsen*. Bagge.
- Nielsen, O. B., 1974. Sedimentation and diagenesis of Lower Eocene sediments at Ölst, Denmark. *Sedimentary Geology* **12**, 25-44.
- Nielsen, O., Baumann, J., Deyu, Z., Heilmann-Clausen, C., and Larsen, G., 1986. Tertiary deposits in Store Bælt. *The Tertiary section of borehole DGI 83101*, 235-253.
- Nomura, D., Assmy, P., Nehrke, G., Granskog, M. A., Fischer, M., Dieckmann, G. S., Fransson, A., Hu, Y., and Schnetger, B., 2013. Characterization of ikaite ($\text{CaCO}_3 \cdot 6\text{H}_2\text{O}$) crystals in first-year Arctic sea ice north of Svalbard. *Annals of Glaciology* **54**, 125-131.
- Obst, K., Ansorge, J., Matting, S., and Hüneke, H., 2015. Early Eocene volcanic ashes on Greifswalder Oie and their depositional environment, with an overview of coeval ash-bearing deposits in northern Germany and Denmark. *International Journal of Earth Sciences* **104**, 2179-2212.
- Oehlerich, M., Mayr, C., Griesshaber, E., Lücke, A., Oeckler, O. M., Ohlendorf, C., Schmahl, W. W., and Zolitschka, B., 2013. Ikaite precipitation in a lacustrine environment – implications for palaeoclimatic studies using carbonates from Laguna Potrok Aike (Patagonia, Argentina). *Quaternary Science Reviews* **71**, 46-53.
- Oertel, G. and Curtis, C. D., 1972. Clay-ironstone concretion preserving fabrics due to progressive compaction. *Geological Society of America Bulletin* **83**, 2597-2606.
- Omelson, C. R., Pollard, W. H., and Marion, G. M., 2000. Seasonal formation of ikaite ($\text{CaCO}_3 \cdot 6\text{H}_2\text{O}$) in saline spring discharge at Expedition Fiord, Canadian High Arctic: Assessing conditional constraints for natural crystal growth. *Geochimica et Cosmochimica Acta* **65**, 1429-1437.
- O'Neil, J. R., Clayton, R. N., and Mayeda, T. K., 1969. *Oxygen isotope fractionation in divalent metal carbonate*, University of Chicago.
- Papadimitriou, S., Kennedy, H., Kennedy, P., and Thomas, D. N., 2014. Kinetics of ikaite precipitation and dissolution in seawater-derived brines at sub-zero temperatures to 265 K. *Geochimica et Cosmochimica Acta* **140**, 199-211.
- Pauly, H., 1963. "Ikaite", a new mineral from Greenland. *Arctic* **16**, 263-264.
- Paytan, A., Kastner, M., Campbell, D., and Thiemens, M. H., 1998. Sulfur isotopic composition of Cenozoic seawater sulfate. *Science* **282**, 1459-1462.
- Pearson, P. N., van Dongen, B. E., Nicholas, C. J., Pancost, R. D., Schouten, S., Singano, J. M., and Wade, B. S., 2007. Stable warm tropical climate through the Eocene Epoch. *Geology* **35**, 211-214.
- Pedersen, A. K., Engell, J., and Rønsbo, J. G., 1975. Early tertiary volcanism in the Skagerrak: new chemical evidence from ash-layers in the mo-clay of northern Denmark. *Lithos* **8**, 255-268.
- Pedersen, G. K. and Surlyk, F., 1977. Dish structures in Eocene volcanic ash layers, Denmark. *Sedimentology* **24**, 581-590.
- Pedersen, G., 1978. *Molerets sedimentology*, Unpublished thesis, University of Copenhagen.
- Pedersen, G. K., 1981. Anoxic events during sedimentation of a Palaeogene diatomite in Denmark. *Sedimentology* **28**, 487-504.
- Pedersen, G. K. and Surlyk, F., 1983. The Fur Formation, a late Palaeocene ash-bearing diatomite from northern Denmark. *Bulletin of the Geological Society of Denmark* **32**, 43-65.
- Pedersen, G. K. and Buchardt, B., 1996. The calcareous concretions (cementsten) in the Fur Formation (Paleogene, Denmark): isotopic evidence of early diagenetic growth. *Bulletin of the Geological Society of Denmark* **43**, 78-86.
- Pedersen, G. K., Pedersen, S. A. S., Steffensen, J., and Pedersen, C., 2004. Clay content of a clayey diatomite, the Early Eocene Fur Formation, Denmark. *Bulletin of the Geological Society of Denmark* **51**, 159-177.
- Pedersen, S. A. S., 2008. Palaeogene diatomite deposits in Denmark: geological investigations and applied aspects. *Geological Survey of Denmark and Greenland Bulletin* **15**, 21-24.
- Pedersen, G. K., Pedersen, S. A. S., Bonde, N., Heilmann-Clausen, C., Larsen, L. M., Lindow, B., Madsen, H., Pedersen, A. K., Rust, J., Schultz, B. P., Storey, M., and Willumsen, P. S., 2011. Moleromradets geologi - sedimenter, fossiler,

- askelag og glacialtektonik. *Geologisk Tidsskrift* **2011**, 41 - 135.
- Pedersen, S. A. S. and Pedersen, G. K., 2012. Molerets historie. *Geoviden - Geologi og Geografi* **3**, 1-20.
- Pelouze, J., 1831. Sur la production artificielle du carbonate de chaux cristallise, et sur deux combinaisons de ce sel avec l'eau. *Annales de Chimie et de Physique Series* **2** (48), 301–307.
- Peters, N. A., Huntington, K. W., and Hoke, G. D., 2013. Hot or not? Impact of seasonally variable soil carbonate formation on paleotemperature and O-isotope records from clumped isotope thermometry. *Earth and Planetary Science Letters* **361**, 208-218.
- Petersen, J., 2016. *Silikadiagenese, mineralogi og geokemi i den nedre del af Fur og Olst Formationerne: mulige cykliske variationer i "Skiferserien"*, Aarhus University.
- Price, G. D. and Nunn, E. V., 2010. Valanginian isotope variation in glendonites and belemnites from Arctic Svalbard: transient glacial temperatures during the Cretaceous greenhouse. *Geology* **38**, 251-254.
- Pueyo, J. J., Sáez, A., Giral, S., Valero-Garcés, B. L., Moreno, A., Bao, R., Schwalb, A., Herrera, C., Klosowska, B., and Taberner, C., 2011. Carbonate and organic matter sedimentation and isotopic signatures in Lake Chungará, Chilean Altiplano, during the last 12.3 kyr. *Palaeogeography, Palaeoclimatology, Palaeoecology* **307**, 339-355.
- Quade, J., Breecker, D. O., Daëron, M., and Eiler, J., 2011. The paleoaltimetry of Tibet: An isotopic perspective. *American Journal of Science* **311**, 77-115.
- Rahimpour-Bonab, H., Asadi-Eskandar, A., and Sonei, R., 2009. Effects of the Permian–Triassic boundary on reservoir characteristics of the South Pars gas field, Persian Gulf. *Geological Journal* **44**, 341-364.
- Raiswell, R., 1971. The growth of Cambrian and Liassic concretions. *Sedimentology* **17**, 147-171.
- Raiswell, R., 1976. The microbiological formation of carbonate concretions in the Upper Lias of NE England. *Chemical Geology* **18**, 227-244.
- Raiswell, R., Bottrell, S., Dean, S., Marshall, J., Carr, A., and Hatfield, D., 2002. Isotopic constraints on growth conditions of multiphase calcite–pyrite–barite concretions in Carboniferous mudstones. *Sedimentology* **49**, 237-254.
- Rasmussen, J. A., Madsen, H., Schultz, B. P., Sylvestersen, R. L., and Bonde, N., 2016. *The lowermost Eocene deposits and biota of the western Limfjord region, Denmark*, 2nd International Moler Meeting, 2-4 Nov. 2016.
- Raven, M. J. and Dickson, J. A. D., 1989. Fir-tree zoning: an indicator of pulsed crystallization in calcite cement crystals. *Sedimentary Geology* **65**, 249-259.
- Rickaby, R. E. M., Shaw, S., Bennitt, G., Kennedy, H., Zabel, M., and Lennie, A., 2006. Potential of ikaite to record the evolution of oceanic $\delta^{18}\text{O}$. *Geology* **34**, 497-500.
- Riech, V. and von Rad, U., 1979. Silica diagenesis in the Atlantic Ocean: diagenetic potential and transformations. *Deep drilling results in the Atlantic Ocean: continental margins and paleoenvironment*, 315-340.
- Röhl, U., Westerhold, T., Bralower, T. J., and Zachos, J. C., 2007. On the duration of the Paleocene-Eocene thermal maximum (PETM). *Geochemistry, Geophysics, Geosystems* **8**, Q12002.
- Rogala, B., James, N. P., and Reid, C. M., 2007. Deposition of polar carbonates during interglacial highstands on an Early Permian Shelf, Tasmania. *Journal of Sedimentary Research* **77**, 587-606.
- Rogov, M. and Zakharov, V., 2010. Jurassic and Lower Cretaceous glendonite occurrences and their implication for Arctic paleoclimate reconstructions and stratigraphy. *Earth Science Front* **17**, 345-347.
- Rullkötter, J., 2006. *Organic matter: the driving force for early diagenesis*. In: *Marine Geochemistry*, Springer-Verlag, Berlin Heidelberg, 125–168.
- Rust, J., 1998. Biostratonomie von Insekten aus der Fur-Formation von Dänemark (Moler, oberes Paleozän/unteres Eozän). *Paläontologische Zeitschrift* **72**, 41-58.

- Rust, J. E. S. and Andersen, N. M., 1999. Giant ants from the Paleogene of Denmark with a discussion of the fossil history and early evolution of ants (Hymenoptera: Formicidae). *Zoological Journal of the Linnean Society* **125**, 331-348.
- Rysgaard, S., Glud, R. N., Lennert, K., Cooper, M., Halden, N., Leakey, R. J. G., Hawthorne, F. C., and Barber, D., 2012. Ikaite crystals in melting sea ice – implications for pCO₂ and pH levels in Arctic surface waters. *The Cryosphere* **6**, 901-908.
- Shahar, A., Bassett, W. A., Mao, H.-k., Chou, I.-M., and Mao, W., 2005. The stability and Raman spectra of ikaite, CaCO₃·6H₂O, at high pressure and temperature. *American Mineralogist* **90**, 1835-1839.
- Sakala, J. and Gryc, V., 2011. A new species of Rhysocaryoxylon (Juglandaceae) from the Lower Eocene Fur Formation of Mors island (northwest Jutland, Denmark). *Bulletin of the Geological Society of Denmark* **59**, 45-49.
- Sass, E., Bein, A., and Almogi-Labin, A., 1991. Oxygen-isotope composition of diagenetic calcite in organic-rich rocks: evidence for δ¹⁸O depletion in marine anaerobic pore water. *Geology* **19**, 839-842.
- Saunders, A., Fitton, J., Kerr, A. C., Norry, M., and Kent, R., 1997. The north Atlantic igneous province. *Large igneous provinces: Continental, oceanic, and planetary flood volcanism*, 45-93.
- Schiøler, P., Andsbjerg, J., Clausen, O. R., Dam, G., Dybkjær, K., Hamberg, L., Heilmann-Clausen, C., Johannessen, E. P., Kristensen, L. E., and Prince, I., 2007. Lithostratigraphy of the Palaeogene-lower Neogene succession of the Danish North Sea. *Geological Survey of Denmark and Greenland Bulletin* **12**.
- Schmidt, M., Botz, R., Stoffers, P., Anders, T., and Bohrmann, G., 1997. Oxygen isotopes in marine diatoms: A comparative study of analytical techniques and new results on the isotope composition of recent marine diatoms. *Geochimica et Cosmochimica Acta* **61**, 2275-2280.
- Schmidt, M., Botz, R., Rickert, D., Bohrmann, G., Hall, S. R., and Mann, S., 2001. Oxygen isotopes of marine diatoms and relations to opal-A maturation. *Geochimica et Cosmochimica Acta* **65**, 201-211.
- Schmidt, M., Priemé, A., and Stougaard, P., 2006. Bacterial diversity in permanently cold and alkaline ikaite columns from Greenland. *Extremophiles* **10**, 551-562.
- Schmitz, B., Heilmann-Clausen, C., King, C., Steurbaut, E., Andreasson, F. P., Corfield, R. M., and Cartlidge, J. E., 1996. Stable isotope and biotic evolution in the North Sea during the early Eocene: the Albæk Hoved section, Denmark. *Geological Society, London, Special Publications* **101**, 275-306.
- Schmitz, B., Peucker-Ehrenbrink, B., Heilmann-Clausen, C., Åberg, G., Asaro, F., and Lee, C.-T. A., 2004. Basaltic explosive volcanism, but no comet impact, at the Paleocene–Eocene boundary: high-resolution chemical and isotopic records from Egypt, Spain and Denmark. *Earth and Planetary Science Letters* **225**, 1-17.
- Schoon, P. L., 2013. Impact of CO₂ and pH on the distribution and stable carbon isotopic composition of microbial biomarker lipids. *Dissertation at University of Utrecht*, ISBN 978-94-6203-299-6, Wöhrmann Print Service, Zutphen.
- Schoon, P. L., Heilmann-Clausen, C., Schultz, B. P., Sinninghe Damsté, J. S., and Schouten, S., 2015. Warming and environmental changes in the eastern North Sea Basin during the Palaeocene–Eocene Thermal Maximum as revealed by biomarker lipids. *Organic Geochemistry* **78**, 79-88.
- Schubert, C. J., Nürnberg, D., Scheele, N., Pauer, F., and Kriews, M., 1997. ¹³C isotope depletion in ikaite crystals: evidence for methane release from the Siberian shelves? *Geo-Marine Letters* **17**, 169-174.
- Schultz, B.P. 2009: Pseudomorph after ikaite – called glendonite, is it a geological thermometer in cold sediments or geological oddity as it occurs close to PETM in the Fur formation. *IOP Conference Series: Earth and Environmental Science* **6**, doi:10.1088/1755-1307/6/7/072059.
- Schultz, B. P., Madsen, H., Sylvestersen, R., and Bonde, N. C., 2011. Moler. *Geologiske Naturperler*, 68-86.
- Schulz, H. D. and Zabel, M., 2006. *Marine geochemistry*. Springer.

- Selleck, B. W., Carr, P. F., and Jones, B. G., 2007. A review and synthesis of glendonites (pseudomorphs after ikaite) with new data: assessing applicability as recorders of ancient coldwater conditions. *Journal of Sedimentary Research* **77**, 980-991.
- Shackleton, N. J. and Kennett, J. P., 1975. Paleotemperature history of the Cenozoic and the initiation of Antarctic glaciation: oxygen and carbon isotope analyses in DSDP Sites 277, 279, and 281. *Initial reports of the deep sea drilling project* **29**, 743-755.
- Shahar, A., Bassett, W. A., Mao, H.-k., Chou, I.-M., and Mao, W., 2005. The stability and Raman spectra of ikaite, $\text{CaCO}_3 \cdot 6\text{H}_2\text{O}$, at high pressure and temperature. *American Mineralogist* **90**, 1835-1839.
- Sharma, P. V., 1969. Early Tertiary field reversals recorded in volcanic ash layers of northern Denmark. *Meddelelser dansk geologisk Forening* **19**, 218-223.
- Shearman, D. J. and Smith, A. J., 1985. Ikaite, the parent mineral of jarroviite-type pseudomorphs. *Proceedings of the Geologists' Association* **96**, 305-314.
- Shearman, D. J., McGugan, A., Stein, C., and Smith, A. J., 1989. Ikaite, $\text{CaCO}_3 \cdot 6\text{H}_2\text{O}$, precursor of the thinolites in the Quaternary tufas and tufa mounds of the Lahontan and Mono Lake Basins, western United States. *Geological Society of America Bulletin* **101**, 913-917.
- Shemesh, A., Charles, C., and Fairbanks, R., 1992. Oxygen isotopes in biogenic silica: global changes in ocean temperature and isotopic composition. *Science* **256**, 1434-1436.
- Shemesh, A., Burckle, L. H., and Hays, J. D., 1995. Late Pleistocene oxygen isotope records of biogenic silica from the Atlantic sector of the Southern Ocean. *Paleoceanography* **10**, 179-196.
- Shiro, Y. and Sakai, H., 1972. Calculation of the Reduced Partition Function Ratios of alpha, beta-quartz and calcite. *Bulletin of the Chemical Society of Japan* **45**, 2355-2359.
- Skulan, J., DePaolo, D. J., and Owens, T. L., 1997. Biological control of calcium isotopic abundances in the global calcium cycle. *Geochimica et Cosmochimica Acta* **61**, 2505-2510.
- Sluijs, A., Schouten, S., Pagani, M., Woltering, M., Brinkhuis, H., Damsté, J. S. S., Dickens, G. R., Huber, M., Reichert, G.-J., and Stein, R., 2006. Subtropical Arctic Ocean temperatures during the Palaeocene/Eocene thermal maximum. *Nature* **441**, 610-613.
- Smith, M. and White, M., 1985. Observations on lakes near Mount St Helens: phytoplankton. *Archiv für Hydrobiologie* **104**, 345-362.
- Spielhagen, R. F. and Tripathi, A., 2009. Evidence from Svalbard for near-freezing temperatures and climate oscillations in the Arctic during the Paleocene and Eocene. *Palaeogeography, Palaeoclimatology, Palaeoecology* **278**, 48-56.
- Stein, C. L. and Smith, A. J., 1985. Authigenic carbonate nodules in the Nankai Trough, Site 583. *Initial reports of the deep sea drilling project* **87**, 659-668.
- Stolley, E., 1909. Pseudo-Gaylussit, Pseudo-Pirssonit und Protospongia im cambrischen Alaunschiefer Bornholms. *Meddelelser fra Dansk geologisk Forening* **15**, 351 - 368.
- Stolper, D. A. and Eiler, J. M., 2015. The kinetics of solid-state isotope-exchange reactions for clumped isotopes: A study of inorganic calcites and apatites from natural and experimental samples. *American Journal of Science* **315**, 363-411.
- Storey, M., Duncan, R. A., and Swisher, C. C., 2007. Paleocene-Eocene thermal maximum and the opening of the Northeast Atlantic. *Science* **316**, 587-589.
- Stougaard, P., Jørgensen, F., Johnsen, M. G., and Hansen, O. C., 2002. Microbial diversity in ikaite tufa columns: an alkaline, cold ecological niche in Greenland. *Environmental Microbiology* **4**, 487-493.
- Strauss, H., Marais, D., Hayes, J. M., and Summons, R., 1992. Proterozoic organic carbon — Its preservation and isotopic record. In: *Early Organic Evolution*, Springer Berlin Heidelberg.
- Suess, E., Balzer, W., Hesse, K.-F., Müller, P. J., Ungerer, C. A., and Wefer, G., 1982. Calcium carbonate hexahydrate from organic-rich sediments of the Antarctic Shelf: Precursors of glendonites. *Science* **216**, 1128-1131.
- Svensen, H., Planke, S., Malthes-Sorensen, A., Jamtveit, B., Myklebust, R., Rasmussen Eidem,

- T., and Rey, S. S., 2004. Release of methane from a volcanic basin as a mechanism for initial Eocene global warming. *Nature* **429**, 542-545.
- Swann, G. E. A., Leng, M. J., Sloane, H. J., and Maslin, M. A., 2008. Isotope offsets in marine diatom $\delta^{18}\text{O}$ over the last 200 ka. *Journal of Quaternary Science* **23**, 389-400.
- Swann, G. E. A. and Leng, M. J., 2009. A review of diatom $\delta^{18}\text{O}$ in palaeoceanography. *Quaternary Science Reviews* **28**, 384-398.
- Swisher, C., and Knox, R., 1991, The age of the Paleocene/Eocene boundary: $^{40}\text{Ar}/^{39}\text{Ar}$ dating of the lower part of NP10, North Sea Basin and Denmark. *International Annual Meeting and Field Conference, 2-6 December 1991, Brussels, Abstracts With Program*, p. 16.
- Tang, C. C., Thompson, S. P., Parker, J. E., Lennie, A. R., Azough, F., and Kato, K., 2009. The ikaite-to-vaterite transformation: new evidence from diffraction and imaging. *Journal of Applied Crystallography* **42**, 225-233.
- Teichert, B. M. A., Torres, M. E., Bohrmann, G., and Eisenhauer, A., 2005. Fluid sources, fluid pathways and diagenetic reactions across an accretionary prism revealed by Sr and B geochemistry. *Earth and Planetary Science Letters* **239**, 106-121.
- Teichert, B., 2007. The Simeulue Seep—observations on a methane seep in the forearc of Sumatra. *Geophysical Research Abstracts* **9**, 02376.
- Teichert, B. M. A., Gussone, N., and Torres, M. E., 2009. Controls on calcium isotope fractionation in sedimentary porewaters. *Earth and Planetary Science Letters* **279**, 373-382.
- Teichert, B. and Luppold, F. W., 2009. Glendonite Formation in Early Jurassic dark shales—Evidence for methane seepage in northern Germany. *Goldschmidt Conference Abstracts* **2009**, A1319.
- Teichert, B. M. A. and Luppold, F. W., 2013. Glendonites from an Early Jurassic methane seep — Climate or methane indicators? *Palaeogeography, Palaeoclimatology, Palaeoecology* **390**, 81-93.
- Thomas, S. G., Fielding, C. R., and Frank, T. D., 2007. Lithostratigraphy of the late Early Permian (Kungurian) Wandrawandian Siltstone, New South Wales: record of glaciation? *Australian Journal of Earth Sciences* **54**, 1057-1071.
- Tripathi, A. and Elderfield, H., 2005. Deep-sea temperature and circulation changes at the Paleocene-Eocene Thermal Maximum. *Science* **308**, 1894-1898.
- van Geldern, R., Hayashi, T., Böttcher, M. E., Mottl, M. J., Barth, J. A. C., and Stadler, S., 2013. Stable isotope geochemistry of pore waters and marine sediments from the New Jersey shelf: Methane formation and fluid origin. *Geosphere* **9**, 96-112.
- Vasconcelos, C., McKenzie, J. A., Warthmann, R., and Bernasconi, S. M., 2005. Calibration of the $\delta^{18}\text{O}$ paleothermometer for dolomite precipitated in microbial cultures and natural environments. *Geology* **33**, 317-320.
- Vedding Kristoffersen, A., 1999. Lithornithid birds (Aves, Palaeognathae) from the Lower Palaeogene of Denmark. *Geologie en Mijnbouw* **78**, 375-381.
- Veizer, J. and Compston, W., 1974. $^{87}\text{Sr}/^{86}\text{Sr}$ composition of seawater during the Phanerozoic. *Geochimica et Cosmochimica Acta* **38**, 1461-1484.
- Veizer, J., Ala, D., Azmy, K., Bruckschen, P., Buhl, D., Bruhn, F., Carden, G. A. F., Diener, A., Ebner, S., Godderis, Y., Jasper, T., Korte, C., Pawellek, F., Podlaha, O. G., and Strauss, H., 1999. $^{87}\text{Sr}/^{86}\text{Sr}$, $\delta^{13}\text{C}$ and $\delta^{18}\text{O}$ evolution of Phanerozoic seawater. *Chemical Geology* **161**, 59-88.
- Vennemann, T. W., Morlok, A., von Engelhardt, W., and Kyser, K., 2001. Stable isotope composition of impact glasses from the Nördlinger Ries impact crater, Germany. *Geochimica et Cosmochimica Acta* **65**, 1325-1336.
- Wachter, E. A. and Hayes, J. M., 1985. Exchange of oxygen isotopes in carbon dioxide-phosphoric acid systems. *Chemical Geology: Isotope Geoscience section* **52**, 365-374.
- Wacker, U., Fiebig, J., and Schoene, B. R., 2013. Clumped isotope analysis of carbonates: comparison of two different acid digestion techniques. *Rapid Communications in Mass Spectrometry* **27**, 1631-1642.
- Wacker, U., Fiebig, J., Tödter, J., Schöne, B. R., Bahr, A., Friedrich, O., Tütken, T., Gischler, E.,

- and Joachimski, M. M., 2014. Empirical calibration of the clumped isotope paleothermometer using calcites of various origins. *Geochimica et Cosmochimica Acta* **141**, 127-144.
- Wang, D. T., Gruen, D. S., Lollar, B. S., Hinrichs, K.-U., Stewart, L. C., Holden, J. F., Hristov, A. N., Pohlman, J. W., Morrill, P. L., Könneke, M., Delwiche, K. B., Reeves, E. P., Sutcliffe, C. N., Ritter, D. J., Seewald, J. S., McIntosh, J. C., Hemond, H. F., Kubo, M. D., Cardace, D., Hoehler, T. M., and Ono, S., 2015. Nonequilibrium clumped isotope signals in microbial methane. *Science* **348**, 428-431.
- Wang, Z., Wang, J., Suess, E., Wang, G., Chen, C., and Xiao, S., 2016. Silicified glendonites in the Ediacaran Doushantuo Formation (South China) and their potential paleoclimatic implications. *Geology*.
- Westerhold, T., Röhl, U., Laskar, J., Raffi, I., Bowles, J., Lourens, L.J. & Zachos, J.C. 2007: On the duration of magnetochrons C24r and C25n and the timing of early Eocene global warming events: implications from the Ocean Drilling Program Leg 208 Walvis Ridge depth transect. *Paleoceanography* **22**, doi: 10.1029.2006PA001322.
- Westerhold, T., Röhl, U., McCarren, H. K., and Zachos, J. C., 2009. Latest on the absolute age of the Paleocene–Eocene Thermal Maximum (PETM): New insights from exact stratigraphic position of key ash layers +19 and –17. *Earth and Planetary Science Letters* **287**, 412-419.
- Westerhold, T., Röhl, U., and Laskar, J., 2012. Time scale controversy: Accurate orbital calibration of the early Paleogene. *Geochemistry, Geophysics, Geosystems* **13**, Q06015.
- Whiticar, M. and Suess, E., 1998. The cold carbonate connection between Mono Lake, California and the Bransfield Strait, Antarctica. *Aquatic Geochemistry* **4**, 429-454.
- Whiticar, M. J., 1999. Carbon and hydrogen isotope systematics of bacterial formation and oxidation of methane. *Chemical Geology* **161**, 291-314.
- Wiedicke-Hombach, M., Ardhayastuti, S., Bruns, A., Delisle, G., Goergens, R., Hermawan, T., Kanamatsu, T., Lückge, A., Mohtadi, M., and Mühr, P., 2006. *SUMATRA–The Hydrocarbon System of the Sumatra Forearc–SO189-2 Cruise Report*, Hannover: Bundesanstalt für Geowissenschaften und Rohstoffe.
- Willumsen, P., 2004. Palynology of the Lower Eocene deposits of northwest Jutland, Denmark. *Bulletin of the Geological Society of Denmark* **51**, 141-157.
- Wing, S. L., Bown, T. M., and Obradovich, J. D., 1991. Early Eocene biotic and climatic change in interior western North America. *Geology* **19**, 1189-1192.
- Wortmann, U. G. and Paytan, A., 2012. Rapid Variability of Seawater Chemistry Over the Past 130 Million Years. *Science* **337**, 334-336.
- Wotte, T., Shields-Zhou, G. A., and Strauss, H., 2012. Carbonate-associated sulfate: experimental comparisons of common extraction methods and recommendations toward a standard analytical protocol. *Chemical Geology* **326**, 132-144.
- Yao, X., Zhou, Y., and Hinnov, L. A., 2015. Astronomical forcing of a Middle Permian chert sequence in Chaohu, South China. *Earth and Planetary Science Letters* **422**, 206-221.
- Zabel, M. and Schulz, H. D., 2001. Importance of submarine landslides for non-steady state conditions in pore water systems — lower Zaire (Congo) deep-sea fan. *Marine Geology* **176**, 87-99.
- Zachos, J. C., Stott, L. D., and Lohmann, K. C., 1994. Evolution of Early Cenozoic marine temperatures. *Paleoceanography* **9**, 353-387.
- Zachos, J. C., Wara, M. W., Bohaty, S., Delaney, M. L., Petrizzo, M. R., Brill, A., Bralower, T. J., and Premoli-Silva, I., 2003. A transient rise in tropical sea surface temperature during the Paleocene-Eocene Thermal Maximum. *Science* **302**, 1551-1554.
- Zachos, J. C., Dickens, G. R., and Zeebe, R. E., 2008. An early Cenozoic perspective on greenhouse warming and carbon-cycle dynamics. *Nature* **451**, 279-283.
- Zaoui, A. and Sekkal, W., 2014. Mechanisms behind the ikaite-to-calcite phase transformation from molecular dynamics calculations. *Geoderma* **235–236**, 329-333.

Zeelmaekers, E., Vandenberghe, N., and ŚRODOŃ, J., 2012. Presence of bentonite beds in the earliest Eocene Tienen Formation in Belgium as evidenced by clay mineralogical analyses. *Austrian Journal of Earth Sciences* **105**, 110-116.

Zhou, X., Lu, Z., Rickaby, R. E. M., Domack, E. W., Wellner, J. S., and Kennedy, H. A., 2015. Ikaite abundance controlled by porewater phosphorus level: potential links to dust and productivity. *The Journal of Geology* **123**, 269-281.

Ziegler, W. H., 1975. *Outline of the geological history of the North Sea*. Esso Europe, Incorporated.

9 Appendices

App. 1: Thickness of the individual ash layers and clay and diatomite inbetween. Note that not all ash layers were seen. Thus, the distance between two visible ash layers was measured and is given in the third column. The lower part of the Fur Formation and the Stolle Klint Clay were no accessible. Therefore, two other studies were taken for the thicknesses this part of the profile.

Ash layer	Thickness ash layer (cm)	Thickness clay + diatomite (cm)	Locality	Reference
+140		504	Silstrup	This study
+135	2	98	Silstrup	This study
+130	7	43	Silstrup	This study
+129	3	97	Silstrup	This study
+123	4	67	Silstrup	This study
+122	2	3	E-Knudeklint	This study
+121	2	7	E-Knudeklint	This study
+120	3	20	E-Knudeklint	This study
+119	2	19	E-Knudeklint	This study
+118	14	4	E-Knudeklint	This study
+117	2	5	E-Knudeklint	This study
+116	5	5	E-Knudeklint	This study
+115	2	14	E-Knudeklint	This study
+114	12	20	E-Knudeklint	This study
+112	1.5	6	E-Knudeklint	This study
+111	3	10	E-Knudeklint	This study
+110	4	11	E-Knudeklint	This study
+109	2.5	6	E-Knudeklint	This study
+108	4	3.5	E-Knudeklint	This study
+107	0.5	2	E-Knudeklint	This study
+106	3	13	E-Knudeklint	This study
+105	4	28	E-Knudeklint	This study
+104	0.5	6	E-Knudeklint	This study
+103	1	5	E-Knudeklint	This study
+102	8	14	W-Knudeklint	This study
+101	14	12	W-Knudeklint	This study
+99	5	8	W-Knudeklint	This study
+98	0.5	9	W-Knudeklint	This study
+97	3	3	W-Knudeklint	This study
+96	3	20	W-Knudeklint	This study
+95	1	7	W-Knudeklint	This study
+94	5	6	W-Knudeklint	This study
+93	2	10	W-Knudeklint	This study
+92	4	33	W-Knudeklint	This study
+91	0.5	64	W-Knudeklint	This study
+90	8	80	W-Knudeklint	This study
+87	0.5	8	W-Knudeklint	This study
+85	1	16	W-Knudeklint	This study
+84	1	2	W-Knudeklint	This study
+83	4	8	W-Knudeklint	This study
+82	3	3	W-Knudeklint	This study
+81	4	16	W-Knudeklint	This study
+80	7	5	W-Knudeklint	This study
+79	16	9	W-Knudeklint	This study
+78	1.5	5	W-Knudeklint	This study
+77	2	8	W-Knudeklint	This study
+76		2	W-Knudeklint	This study
+75		16	W-Knudeklint	This study
+74		15	W-Knudeklint	This study
+73		2	W-Knudeklint	This study
+72		4	W-Knudeklint	This study
+71		4	W-Knudeklint	This study
+70		1	W-Knudeklint	This study
+69		6	W-Knudeklint	This study
+68		3	W-Knudeklint	This study
+67		2	W-Knudeklint	This study
+66		2	W-Knudeklint	This study
+65		0.5	W-Knudeklint	This study
+64		2	W-Knudeklint	This study
+63		2	W-Knudeklint	This study
+62		10	W-Knudeklint	This study
+61		6	W-Knudeklint	This study
+60		3	W-Knudeklint	This study
+59		18	W-Knudeklint	This study
+58		1	W-Knudeklint	This study
+57		4	W-Knudeklint	This study
+56		3	W-Knudeklint	This study
+55		9	W-Knudeklint	This study
+54		3	W-Knudeklint	This study
+53		1.5	W-Knudeklint	This study
+52		4	W-Knudeklint	This study
+51		2	W-Knudeklint	This study
+50		0.5	W-Knudeklint	This study
+49		3	W-Knudeklint	This study
+48		5.5	W-Knudeklint	This study
+47		2	W-Knudeklint	This study
+46		2	W-Knudeklint	This study
+44		2	W-Knudeklint	This study
+43		2	W-Knudeklint	This study
+42		2	W-Knudeklint	This study
+41		2	W-Knudeklint	This study
+40		2	W-Knudeklint	This study
+36		4	W-Knudeklint	This study
+35		6	W-Knudeklint	This study
+34		0.5	W-Knudeklint	This study
+33		1	W-Knudeklint	This study
+32		1	W-Knudeklint	This study
+31		13	W-Knudeklint	This study
+30		3	W-Knudeklint	This study
+29		3	W-Knudeklint	This study
+28		1	W-Knudeklint	This study
+27		0.5	W-Knudeklint	This study
+26		8	W-Knudeklint	This study
+25		15	W-Knudeklint	This study
+24		4	W-Knudeklint	This study
+23		3	W-Knudeklint	This study
+22		22	W-Knudeklint	This study
+21		9	W-Knudeklint	This study
+20		4	W-Knudeklint	This study
+19		7	W-Knudeklint	This study
+18		4	W-Knudeklint	This study
+17		3	W-Knudeklint	This study
+16		8	W-Knudeklint	This study
+15		8	W-Knudeklint	This study
+14		15	W-Knudeklint	This study
+13		6	W-Knudeklint	This study
+12		5	W-Knudeklint	This study
+11		8	W-Knudeklint	This study
+10		5	W-Knudeklint	This study
+9		7	W-Knudeklint	This study
+8		14	W-Knudeklint	This study
+7		16	W-Knudeklint	This study
+6		18	W-Knudeklint	This study
+5		41	W-Knudeklint	This study
+4		7	W-Knudeklint	This study
+3		30	W-Knudeklint	This study
+2		6	W-Knudeklint	This study
+1		6	W-Knudeklint	This study
-10		0.5	W-Knudeklint	This study
-11		4	W-Knudeklint	This study
-12		5	W-Knudeklint	This study
-13		6	W-Knudeklint	This study
-14		15	W-Knudeklint	This study
-17		3	W-Knudeklint	This study
-18		3	W-Knudeklint	This study
-19		7	W-Knudeklint	This study
-20		4	W-Knudeklint	This study
-21		9	W-Knudeklint	This study
-22		22	W-Knudeklint	This study
-23		3	W-Knudeklint	This study
-24		4	W-Knudeklint	This study
-25		15	W-Knudeklint	This study
-26		3	W-Knudeklint	This study
-27		8	W-Knudeklint	This study
-28		10	W-Knudeklint	This study
-33		15	W-Knudeklint	This study
-34		1.5	W-Knudeklint	This study
-35		2	W-Knudeklint	This study
-36		0.3	W-Knudeklint	This study
-37		0.3	W-Knudeklint	This study
-38		100	W-Knudeklint	This study
-39		2	W-Knudeklint	This study
+26		0.5	W-Knudeklint	This study
+25		5.5	W-Knudeklint	This study
+24		0.5	W-Knudeklint	This study
+23		3	W-Knudeklint	This study
+22		2	W-Knudeklint	This study
+21		6	W-Knudeklint	This study
+20		1	W-Knudeklint	This study
+19		12	W-Knudeklint	This study
+18		1	W-Knudeklint	This study
+16		2	W-Knudeklint	This study
+14		4	W-Knudeklint	This study
+13		0.5	W-Knudeklint	This study
+12		4	W-Knudeklint	This study
+11		2	W-Knudeklint	This study
+10		0.5	W-Knudeklint	This study
+9		7	W-Knudeklint	This study
+8		5	W-Knudeklint	This study
+6		0.5	W-Knudeklint	This study
+5		1	W-Knudeklint	This study
+4		2	W-Knudeklint	This study
+3		5	W-Knudeklint	This study
+1		6	W-Knudeklint	This study
-10		0.5	W-Knudeklint	This study
-11		4	W-Knudeklint	This study
-12		5	W-Knudeklint	This study
-13		6	W-Knudeklint	This study
-14		15	W-Knudeklint	This study
-17		3	W-Knudeklint	This study
-18		3	W-Knudeklint	This study
-19		7	W-Knudeklint	This study
-20		4	W-Knudeklint	This study
-21		9	W-Knudeklint	This study
-22		22	W-Knudeklint	This study
-23		3	W-Knudeklint	This study
-24		4	W-Knudeklint	This study
-25		15	W-Knudeklint	This study
-26		3	W-Knudeklint	This study
-27		8	W-Knudeklint	This study
-28		10	W-Knudeklint	This study
-33		15	W-Knudeklint	This study
-34		1.5	W-Knudeklint	This study
-35		2	W-Knudeklint	This study
-36		0.3	W-Knudeklint	This study
-37		0.3	W-Knudeklint	This study
-38		100	W-Knudeklint	This study
-39		2	W-Knudeklint	This study

App. 2: $\delta^{13}\text{C}_{\text{carb}}$ and $\delta^{18}\text{O}_{\text{carb}}$ values of drilled glendonite samples.

Ash layer	Sample ID	Profile height (m)	$\delta^{13}\text{C}_{\text{carb}}$ (‰V-PDB)	$\delta^{18}\text{O}_{\text{carb}}$ (‰V-PDB)	Ash layer	Sample ID	Profile height (m)	$\delta^{13}\text{C}_{\text{carb}}$ (‰V-PDB)	$\delta^{18}\text{O}_{\text{carb}}$ (‰V-PDB)	Ash layer	Sample ID	Profile height (m)	$\delta^{13}\text{C}_{\text{carb}}$ (‰V-PDB)	$\delta^{18}\text{O}_{\text{carb}}$ (‰V-PDB)
+62	+62aG_b1	33.12	-23.42	-2.54	+62	+62cG_b18	33.02	-24.86	-2.49	+15	+15bG_b13	24.47	-21.30	-2.19
+62	+62aG_b2	33.12	-23.94	-2.57	+62	+62cG_b19	33.02	-24.73	-2.39	+15	+15cG_b1	24.47	-23.94	-2.98
+62	+62aG_b3	33.12	-24.00	-2.75	+62	+62cG_b20	33.02	-24.73	-2.56	+15	+15cG_b2	24.47	-23.41	-2.53
+62	+62aG_b4	33.12	-22.62	-2.33	+62	+62cG_b21	33.02	-24.72	-2.55	+15	+15cG_b3	24.47	-23.88	-2.97
+62	+62aG_b5	33.12	-24.24	-2.85	+62	+62cG_b22	33.02	-24.50	-2.32	+15	+15cG_b4	24.47	-23.21	-2.52
+62	+62aG_b6	33.12	-24.18	-2.57	+16	+16aG_b1	25.54	-22.87	-2.54	+15	+15cG_b5	24.47	-23.39	-2.44
+62	+62aG_b7	33.12	-22.91	-2.63	+16	+16aG_b2	25.54	-24.31	-2.69	+15	+15cG_b6	24.47	-23.65	-2.60
+62	+62aG_b8	33.12	-24.29	-2.36	+16	+16aG_b3	25.54	-20.25	-2.38	+15	+15cG_b7	24.47	-23.71	-3.00
+62	+62aG_b9	33.12	-24.06	-2.38	+16	+16aG_b4	25.54	-23.07	-2.55	+15	+15cG_b8	24.47	-23.49	-2.45
+62	+62aG_b10	33.12	-23.71	-2.61	+16	+16aG_b5	25.54	-24.26	-2.95	+15	+15cG_b9	24.47	-23.80	-2.63
+62	+62aG_b11	33.12	-24.04	-2.54	+16	+16aG_b6	25.54	-24.26	-2.82	+14	+14bG_b1	23.88	-21.41	-2.54
+62	+62aG_b12	33.12	-24.19	-2.92	+16	+16aG_b7	25.54	-24.24	-2.67	+14	+14bG_b2	23.88	-21.18	-2.85
+62	+62aG_b13	33.12	-23.89	-2.80	+16	+16aG_b8	25.54	-24.33	-2.70	+14	+14bG_b3	23.88	-22.00	-3.21
+62	+62aG_b14	33.12	-22.87	-2.81	+16	+16aG_b9	25.54	-24.45	-2.67	+14	+14bG_b4	23.88	-22.56	-3.24
+62	+62aG_b15	33.12	-23.43	-2.93	+16	+16aG_b10	25.54	-24.65	-2.80	+14	+14bG_b5	23.88	-23.47	-3.41
+62	+62aG_b16	33.12	-23.47	-2.61	+16	+16aG_b11	25.54	-24.19	-2.69	+14	+14bG_b6	23.88	-18.47	-2.28
+62	+62aG_b17	33.12	-24.23	-2.67	+16	+16aG_b12	25.54	-23.30	-2.54	+14	+14bG_b7	23.88	-18.63	-2.36
+62	+62aG_b18	33.12	-23.75	-2.46	+16	+16aG_b13	25.54	-19.10	-2.21	+10	+10aG_b1	23.48	-23.96	-2.55
+62	+62aG_b19	33.12	-24.15	-2.63	+16	+16aG_b14	25.54	-19.68	-2.37	+10	+10aG_b2	23.48	-21.46	-2.26
+62	+62aG_b20	33.12	-24.14	-2.61	+16	+16aG_b15	25.54	-23.79	-2.11	+10	+10aG_b3	23.48	-21.51	-2.29
+62	+62aG_b21	33.12	-23.95	-2.84	+16	+16aG_b16	25.54	-21.80	-2.32	+10	+10aG_b4	23.48	-21.18	-2.25
+62	+62bG_b1	33.02	-22.59	-2.25	+16	+16aG_b17	25.54	-24.35	-2.97	+10	+10aG_b5	23.48	-21.77	-2.25
+62	+62bG_b2	33.02	-22.39	-2.18	+16	+16aG_b18	25.54	-19.96	-2.22	+10	+10aG_b6	23.48	-23.98	-2.86
+62	+62bG_b3	33.02	-23.75	-2.77	+16	+16aG_b19	25.54	-23.28	-2.68	+10	+10aG_b7	23.48	-23.76	-2.85
+62	+62bG_b4	33.02	-21.47	-2.10	+16	+16bG_b1	25.00	-23.84	-3.65	+10	+10aG_b8	23.48	-24.05	-2.93
+62	+62bG_b5	33.02	-21.52	-2.13	+16	+16bG_b2	25.00	-23.68	-3.59	+10	+10aG_b9	23.48	-23.76	-2.64
+62	+62bG_b6	33.02	-22.11	-2.08	+16	+16bG_b3	25.00	-18.88	-2.70	+10	+10aG_b10	23.48	-22.05	-2.55
+62	+62bG_b7	33.02	-22.08	-2.13	+16	+16bG_b4	25.00	-23.71	-3.18	+10	+10aG_b11	23.48	-21.36	-2.23
+62	+62bG_b8	33.02	-22.71	-2.29	+15	+15aG_b1	24.47	-22.06	-2.61	+10	+10aG_b12	23.48	-23.17	-2.34
+62	+62bG_b9	33.02	-22.98	-2.57	+15	+15aG_b2	24.47	-21.36	-2.50	+10	+10aG_b13	23.48	-22.79	-2.20
+62	+62bG_b10	33.02	-20.86	-1.83	+15	+15aG_b3	24.47	-23.19	-2.53	+10	+10aG_b14	23.48	-23.54	-2.24
+62	+62bG_b11	33.02	-21.43	-1.77	+15	+15aG_b4	24.47	-21.89	-2.36	+10	+10aG_b15	23.48	-23.77	-2.71
+62	+62bG_b12	33.02	-20.89	-1.93	+15	+15aG_b5	24.47	-22.98	-2.65	+10	+10aG_b16	23.48	-24.53	-3.20
+62	+62bG_b13	33.02	-23.03	-2.45	+15	+15aG_b6	24.47	-24.10	-2.81	+10	+10aG_b17	23.48	-23.55	-2.82
+62	+62bG_b14	33.02	-23.44	-2.64	+15	+15aG_b7	24.47	-19.12	-2.36	+10	+10aG_b18	23.48	-23.85	-2.89
+62	+62bG_b15	33.02	-23.77	-2.68	+15	+15aG_b8	24.47	-21.56	-2.23	+10	+10aG_b19	23.48	-22.75	-2.60
+62	+62bG_b16	33.02	-22.73	-2.27	+15	+15aG_b9	24.47	-22.66	-2.54	+10	+10aG_b20	23.48	-22.59	-2.63
+62	+62bG_b17	33.02	-23.01	-2.53	+15	+15aG_b10	24.47	-21.86	-2.60	+10	+10aG_b21	23.48	-22.26	-2.60
+62	+62bG_b18	33.02	-23.48	-2.86	+15	+15aG_b11	24.47	-21.19	-2.33	+10	+10bG_b1	23.47	-23.19	-2.70
+62	+62bG_b19	33.02	-22.79	-2.79	+15	+15aG_b12	24.47	-23.01	-2.35	+10	+10bG_b2	23.47	-23.89	-2.79
+62	+62bG_b20	33.02	-23.57	-2.83	+15	+15aG_b13	24.47	-23.67	-2.29	+10	+10bG_b3	23.47	-21.90	-2.31
+62	+62bG_b21	33.02	-24.00	-2.86	+15	+15aG_b14	24.47	-22.80	-2.20	+10	+10bG_b4	23.47	-23.35	-2.74
+62	+62bG_b22	33.02	-23.06	-2.46	+15	+15aG_b15	24.47	-24.18	-3.02	+10	+10bG_b5	23.47	-22.73	-2.23
+62	+62bG_b23	33.02	-23.21	-2.22	+15	+15aG_b16	24.47	-22.73	-2.66	+10	+10bG_b6	23.47	-21.95	-2.18
+62	+62bG_b24	33.02	-23.70	-2.36	+15	+15aG_b17	24.47	-21.47	-2.25	+10	+10bG_b7	23.47	-21.00	-1.77
+62	+62bG_b25	33.02	-23.75	-2.63	+15	+15aG_b18	24.47	-23.60	-2.71	+10	+10bG_b8	23.47	-23.65	-2.63
+62	+62cG_b1	33.02	-24.47	-2.41	+15	+15aG_b19	24.47	-23.54	-2.77	+10	+10bG_b9	23.47	-23.81	-2.73
+62	+62cG_b2	33.02	-24.32	-2.47	+15	+15aG_b20	24.47	-21.78	-2.30	+10	+10bG_b10	23.47	-23.54	-2.57
+62	+62cG_b3	33.02	-23.29	-2.66	+15	+15aG_b21	24.47	-23.76	-3.04	+10	+10bG_b11	23.47	-23.26	-2.44
+62	+62cG_b4	33.02	-24.69	-2.58	+15	+15aG_b22	24.47	-23.47	-3.19	+10	+10bG_b12	23.47	-23.33	-2.60
+62	+62cG_b5	33.02	-24.57	-2.54	+15	+15aG_b23	24.47	-23.45	-2.68	+10	+10bG_b13	23.47	-23.74	-2.82
+62	+62cG_b6	33.02	-24.38	-2.35	+15	+15bG_b1	24.47	-24.87	-2.98	+10	+10bG_b14	23.47	-23.23	-2.44
+62	+62cG_b7	33.02	-24.60	-2.08	+15	+15bG_b2	24.47	-24.01	-2.54	+10	+10bG_b15	23.47	-23.64	-2.56
+62	+62cG_b8	33.02	-24.65	-2.02	+15	+15bG_b3	24.47	-21.99	-2.27	+10	+10bG_b16	23.47	-22.44	-2.46
+62	+62cG_b9	33.02	-24.69	-2.33	+15	+15bG_b4	24.47	-23.95	-2.61	+10	+10bG_b17	23.47	-23.58	-2.59
+62	+62cG_b10	33.02	-24.76	-2.40	+15	+15bG_b5	24.47	-24.51	-2.99	+9	+9bG_b1	22.92	-25.67	-2.40
+62	+62cG_b11	33.02	-24.89	-2.27	+15	+15bG_b6	24.47	-24.39	-3.12	+9	+9bG_b2	22.92	-25.11	-2.34
+62	+62cG_b12	33.02	-24.87	-2.57	+15	+15bG_b7	24.47	-23.66	-2.55	+9	+9bG_b3	22.92	-25.83	-2.74
+62	+62cG_b13	33.02	-24.32	-2.35	+15	+15bG_b8	24.47	-23.82	-2.55	+9	+9bG_b4	22.92	-25.77	-2.84
+62	+62cG_b14	33.02	-24.88	-2.32	+15	+15bG_b9	24.47	-23.93	-2.57	+9	+9bG_b5	22.92	-25.31	-2.48
+62	+62cG_b15	33.02	-24.76	-2.20	+15	+15bG_b10	24.47	-23.87	-2.65	+9	+9bG_b6	22.92	-25.68	-2.35
+62	+62cG_b16	33.02	-24.49	-2.40	+15	+15bG_b11	24.47	-23.57	-2.36	+9	+9bG_b7	22.92	-24.78	-2.31
+62	+62cG_b17	33.02	-24.80	-2.82	+15	+15bG_b12	24.47	-21.54	-2.10					

App. 3: $\delta^{13}\text{C}_{\text{carb}}$ and $\delta^{18}\text{O}_{\text{carb}}$ values of drilled carbonate concretions.

Ash layer	Sample ID	Profile height (m)	$\delta^{13}\text{C}_{\text{carb}}$ (‰V-PDB)	$\delta^{18}\text{O}_{\text{carb}}$ (‰V-PDB)	Ash layer	Sample ID	Profile height (m)	$\delta^{13}\text{C}_{\text{carb}}$ (‰V-PDB)	$\delta^{18}\text{O}_{\text{carb}}$ (‰V-PDB)
+135	+135a_b1	45.29	-22.53	-0.29	+31	+31_b5	27.23	-21.62	-2.26
+135	+135a_b2	45.29	-24.49	-0.34	+31	+31_b6	27.23	-21.48	-3.13
+135	+135a_b3	45.29	-23.87	-0.58	+31	+31_b7	27.23	-21.56	-3.25
+135	+135a_b4	45.29	-18.48	-1.40	+31	+31_b8	27.23	-21.15	-1.39
+135	+135a_b5	45.29	-22.03	-1.82	+31	+31_b9	27.23	-21.52	-1.46
+135	+135a_b6	45.29	-15.85	-0.83	+31	+31_b10	27.23	-21.74	-0.76
+135	+135a_b7	45.29	-22.69	-0.85	+31	+31_b11	27.23	-20.97	-0.88
+135	+135b_b1	45.29	-18.13	-1.34	+30	+30a_b1	27.07	-21.90	-0.84
+135	+135b_b2	45.29	-21.19	-1.88	+30	+30a_b2	27.07	-21.72	-0.67
+135	+135b_b3	45.29	-22.01	-1.75	+30	+30a_b3	27.07	-21.83	-0.94
+135	+135b_b4	45.29	-24.19	-0.62	+30	+30a_b4	27.07	-21.27	-0.82
+135	+135b_b5	45.29	-16.99	1.48	+30	+30a_b5	27.07	-21.89	-0.80
+130	+130a_b1	44.24	-20.02	-0.93	+30	+30a_b6	27.07	-21.60	-0.73
+130	+130a_b2	44.24	-23.57	-1.34	+30	+30b_b1	27.07	-21.04	-1.02
+130	+130a_b3	44.24	-23.01	-1.29	+30	+30b_b2	27.07	-21.09	-0.98
+130	+130a_b4	44.24	-21.15	-1.18	+28	+28_b1	26.91	-20.39	-1.27
+130	+130a_b5	44.24	-21.41	-1.23	+28	+28_b2	26.91	-20.77	-1.27
+130	+130a_b6	44.24	-21.89	-1.07	+28	+28_b3	26.91	-20.77	-1.11
+130	+130a_b7	44.24	-22.60	-1.25	+26	+26_b1	26.83	-14.47	-2.27
+129	+129/130_b1	44.03	-23.93	-2.07	+26	+26_b2	26.83	-14.29	-2.13
+129	+129/130_b2	44.03	-24.04	-2.27	+26	+26_b3	26.83	-14.41	-2.48
+129	+129/130_b3	44.03	-21.45	-2.33	+26	+26_b4	26.83	-14.11	-2.62
+129	+129/130_b4	44.03	-23.22	-2.62	+25	+25-29_b1	26.81	-21.32	-1.57
+129	+129/130_b5	44.03	-18.99	-2.22	+25	+25-29_b2	26.81	-21.26	-1.74
+129	+129/130_b6	44.03	-18.73	-2.35	+25	+25-29_b3	26.81	-19.40	-1.29
+102	+102b_b1	39.46	-11.65	-0.46	+25	+25-29_b4	26.81	-19.46	-1.86
+102	+102b_b2	39.46	-21.83	-2.31	+25	+25-29_b5	26.81	-11.89	-0.01
+102	+102b_b3	39.46	-21.85	-2.32	+25	+25-29_b6	26.81	-10.93	0.02
+102	+102b_b4	39.46	-21.95	-2.33	+18	+15-19_b1	25.56	-18.75	-2.81
+102	+102b_b5	39.46	-22.66	-2.62	+18	+15-19_b2	25.56	-15.96	-2.39
+90	+90_b1	37.14	-23.82	-2.45	+18	+15-19_b3	25.56	-15.75	-2.42
+90	+90_b2	37.14	-24.02	-2.50	+18	+15-19_b4	25.56	-15.43	-2.47
+90	+90_b3	37.14	-24.35	-2.30	+18	+15-19_b5	25.56	-15.35	-2.50
+90	+90_b4	37.14	-24.12	-2.57	+18	+15-19_b6	25.56	-15.15	-2.59
+90	+90_b5	37.14	-24.61	-2.32	+18	+15-19_b7	25.56	-17.32	-2.01
+62	+62a_b1	33.12	-21.95	-2.05	+16	+16a_b1	25.54	-22.37	-2.43
+62	+62a_b2	33.12	-23.38	-2.18	+16	+16a_b2	25.54	-19.39	-2.45
+62	+62a_b3	33.12	-22.60	-2.37	+16	+16a_b3	25.54	-18.40	-2.22
+62	+62a_b4	33.12	-23.60	-2.05	+16	+16a_b4	25.54	-18.59	-2.27
+62	+62a_b5	33.12	-22.18	-2.43	+16	+16a_b5	25.54	-18.26	-2.37
+62	+62a_b6	33.12	-23.80	-1.96	+16	+16a_b6	25.54	-21.65	-1.99
+62	+62a_b7	33.12	-20.88	-2.63	+16	+16a_b7	25.54	-19.17	-2.10
+62	+62a_b8	33.12	-23.68	-2.38	+16	+16a_b8	25.54	-20.96	-2.07
+62	+62a_b9	33.12	-22.13	-2.34	+16	+16a_b9	25.54	-18.40	-2.16
+62	+62b_b1	33.02	-24.12	-2.56	+16	+16a_b10	25.54	-21.50	-1.80
+62	+62b_b2	33.02	-21.61	-2.38	+16	+16a_b11	25.54	-18.27	-2.03
+62	+62b_b3	33.02	-23.07	-2.72	+16	+16a_b12	25.54	-21.63	-2.05
+62	+62b_b4	33.02	-23.54	-2.40	+16	+16a_b13	25.54	-18.45	-2.14
+62	+62b_b5	33.02	-24.37	-2.25	+16	+16a_b14	25.54	-21.09	-2.03
+62	+62b_b6	33.02	-22.86	-2.14	+16	+15/16_b1	25.00	-18.23	-2.60
+62	+62c_b1	33.02	-23.78	-2.14	+16	+15/16_b2	25.00	-19.14	-2.62
+62	+62c_b2	33.02	-23.22	-2.07	+15	+15a_b1	24.47	-18.97	-2.17
+62	+62c_b3	33.02	-22.77	-2.24	+15	+15a_b2	24.47	-18.11	-2.23
+62	+62c_b4	33.02	-23.36	-2.17	+15	+15a_b3	24.47	-18.32	-2.34
+62	+62c_b5	33.02	-23.57	-2.14	+15	+15a_b4	24.47	-21.74	-2.31
+62	+62c_b6	33.02	-24.25	-2.11	+15	+15a_b5	24.47	-17.76	-2.19
+62	+62c_b7	33.02	-24.68	-2.03	+15	+15a_b6	24.47	-17.17	-2.18
+62	+62c_b8	33.02	-24.59	-2.23	+15	+15d_b1	24.47	-20.43	-2.30
+31	+31_b1	27.23	-21.14	-0.70	+15	+15d_b2	24.47	-20.37	-2.29
+31	+31_b2	27.23	-21.37	-2.34	+15	+15d_b3	24.47	-20.22	-2.54
+31	+31_b3	27.23	-21.42	-2.90	+15	+15d_b4	24.47	-20.77	-2.60
+31	+31_b4	27.23	-21.36	-1.43	+15	+15d_b5	24.47	-21.92	-2.34

App. 3: (continued).

Ash layer	Sample ID	Profile height (m)	$\delta^{13}\text{C}_{\text{carb}}$ (‰V-PDB)	$\delta^{18}\text{O}_{\text{carb}}$ (‰V-PDB)	Ash layer	Sample ID	Profile height (m)	$\delta^{13}\text{C}_{\text{carb}}$ (‰V-PDB)	$\delta^{18}\text{O}_{\text{carb}}$ (‰V-PDB)
+15	+15d_b6	24.47	-21.67	-2.34	-11	-11a_2b1	16.87	-20.29	-2.49
+15	+15d_b7	24.47	-22.33	-2.32	-11	-11a_2b2	16.87	-19.86	-2.69
+15	+15d_b8	24.47	-21.88	-2.42	-11	-11a_2b3	16.87	-13.33	-2.83
+15	+15d_b9	24.47	-22.46	-2.46	-11	-11a_2b4	16.87	-18.60	-3.44
+14	+14a_b1	24.41	-24.32	-2.08	-11	-11a_2b5	16.87	-20.60	-2.75
+14	+14a_b2	24.41	-17.47	-2.14	-11	-11b_1b1	15.98	-17.82	-2.01
+14	+14a_b3	24.41	-18.93	-2.16	-11	-11b_1b2	15.98	-17.85	-2.17
+14	+14a_b4	24.41	-16.68	-2.35	-11	-11b_1b3	15.98	-18.03	-2.45
+10	+10b_b1	23.47	-23.51	-2.17	-11	-11b_1b4	15.98	-18.00	-2.67
+10	+10b_b2	23.47	-23.12	-2.37	-11	-11b_1b5	15.98	-18.18	-2.30
+10	+10b_b3	23.47	-23.67	-2.37	-11	-11b_2b1	15.98	-14.25	-3.24
+10	+10b_b4	23.47	-23.40	-2.32	-11	-11b_2b2	15.98	-14.13	-3.20
+10	+10b_b5	23.47	-23.06	-2.71	-11	-11b_2b3	15.98	-13.54	-3.09
+10	+10b_b6	23.47	-23.75	-2.49	-13	-13a_b1	15.23	-8.69	-0.57
+10	+10b_b7	23.47	-23.12	-2.81	-13	-13a_b2	15.23	-8.11	-0.92
+10	+10b_b8	23.47	-23.72	-2.76	-13	-13a_b3	15.23	-7.81	-0.75
+10	+10b_b9	23.47	-23.62	-2.73	-13	-13a_b4	15.23	-7.85	-0.78
+10	+10b_b10	23.47	-23.53	-2.76	-13	-13a_b5	15.23	-7.84	-0.82
+9	+9a_b1	22.92	-23.88	-2.01	-13	-13b_b1	12.51	-9.26	-0.99
+9	+9a_b2	22.92	-16.33	-2.30	-13	-13b_b2	12.51	-8.99	-0.65
+9	+9a_b3	22.92	-20.45	-2.07	-13	-13b_b3	12.51	-9.00	-0.95
+9	+9a_b4	22.92	-15.79	-2.37	-13	-13b_b4	12.51	-9.05	-0.78
+9	+9a_b5	22.92	-23.62	-2.09	-17	-17a_b1	7.20	-6.32	-1.54
+9	+9a_b6	22.92	-24.05	-2.42	-17	-17a_b2	7.20	-6.00	-1.69
+9	+9a_b7	22.92	-16.59	-2.45	-17	-17a_b3	7.20	-4.87	-2.10
+9	+9a_b8	22.92	-19.68	-2.38	-17	-17a_b4	7.20	-5.67	-2.22
+9	+9a_b9	22.92	-19.90	-2.30	-17	-17a_b5	7.20	-4.46	-2.57
+9	+9a_b10	22.92	-18.62	-2.43	-17	-17b_b1	6.80	6.94	1.17
+9	+9a_b11	22.92	-16.89	-2.39	-17	-17b_b2	6.80	6.62	1.22
+9	+9a_b12	22.92	-23.98	-2.42	-17	-17b_b3	6.80	6.78	1.37
+9	+9a_b13	22.92	-20.06	-2.16	-17	-17b_b4	6.80	6.76	1.19
+9	+9b_b1	22.92	-24.06	-2.39	-17	-17b_b5	6.80	7.01	1.15
+9	+9b_b2	22.92	-22.21	-2.05	-20	-20_b1	5.96	5.85	-0.54
+9	+9b_b3	22.92	-23.04	-2.14	-20	-20_b2	5.96	5.56	-0.63
+9	+9b_b4	22.92	-19.62	-2.27	-20	-20_b3	5.96	5.47	-0.52
+9	+9b_b5	22.92	-23.66	-2.32	-20	-20_b4	5.96	5.41	-0.68
+9	+9b_b6	22.92	-22.76	-1.87	-20	-20_b5	5.96	5.71	-0.61
+9	+9b_b7	22.92	-24.26	-2.11	-20	-20_b6	5.96	5.62	-0.52
+9	+9b_b8	22.92	-21.97	-2.11	-24	-24-28_b1	4.00	-17.16	-2.23
+3	+3/4_b1	22.33	-16.16	-2.14	-24	-24-28_b2	4.00	-20.32	-2.23
+3	+3/4_b2	22.33	-20.99	-1.51	-24	-24-28_b3	4.00	-21.69	-2.19
+3	+3/4_b3	22.33	-22.32	-1.78	-24	-24-28_b4	4.00	-20.24	-2.30
+3	+3/4_b4	22.33	-23.20	-2.10	-24	-24-28_b5	4.00	-15.73	-2.26
+3	+3/4_b5	22.33	-21.35	-1.82	-24	-24-28_b6	4.00	-23.35	-2.13
+3	+3/4_b6	22.33	-15.45	-2.20	-24	-24-28_b7	4.00	-23.42	-2.09
+3	+3/4_b7	22.33	-13.60	-2.20	-24	-24-28_b8	4.00	-20.89	-2.08
+3	+3/4_b8	22.33	-21.58	-2.02	-24	-24-28_b9	4.00	-24.82	-2.04
+3	+3/4_b9	22.33	-22.50	-2.11	-24	-24-28_b10	4.00	-24.70	-2.18
+3	+3/4_b10	22.33	-22.39	-2.01	-24	-24-28_b11	4.00	-22.18	-1.98
+3	+3/4_b11	22.33	-22.17	-2.00	-24	-24-28_b12	4.00	-19.05	-2.01
+3	+3/4_b12	22.33	-21.68	-1.98	-24	-24-28_b13	4.00	-15.18	-2.43
+3	+3/4_b13	22.33	-16.97	-2.07	-24	-24-28_b14	4.00	-23.22	-2.06
-11	-11a_1b1	16.87	-16.59	-2.49	-24	-24-28_b15	4.00	-24.67	-1.95
-11	-11a_1b2	16.87	-16.68	-2.45	-24	-24-28_b16	4.00	-21.70	-2.28
-11	-11a_1b3	16.87	-16.83	-2.39	-24	-24-28_b17	4.00	-25.18	-1.84
-11	-11a_1b4	16.87	-16.86	-2.51	-24	-24-28_b18	4.00	-24.92	-1.97
-11	-11a_1b5	16.87	-17.01	-2.44	-24	-24-28_b19	4.00	-24.46	-2.12
-11	-11a_1b6	16.87	-16.91	-2.41	-24	-24-28_b20	4.00	-19.86	-2.06
-11	-11a_1b7	16.87	-16.79	-2.39	-24	-24-28_b21	4.00	-23.43	-2.26
-11	-11a_1b8	16.87	-16.67	-2.30	-24	-24-28_b22	4.00	-21.14	-2.55
-11	-11a_1b9	16.87	-16.20	-2.45	-24	-24-28_b23	4.00	-21.15	-2.06
-11	-11a_1b10	16.87	-16.34	-2.46	-24	-24-28_b24	4.00	-16.19	-2.35

**App. 4: MgCO₃ concentration calculated based on the 2θ peak measurement after Lumsden (1979).
Above black line: glendonite; below black line: carbonate concretions.**

Ash layer	Sample ID	Profile height (m)	Qz-Peak [2θ] (° Theta)	calc. d Qz [101] (Å)	meas. d Qz [101] (Å)	Cc-Peak [2θ; 104] (° Theta)	calc. d Cc [104] (Å)	meas. d Cc [104] (Å)	Cc-Peak [2θ; 113] (° Theta)	calc. d Cc [113] (Å)	calc. MgCO ₃ (mol%)	meas. MgCO ₃ (mol%)	Deviation (%)
+62	+62a	33.02	n.a.	n.a.	n.a.	n.a.	n.a.	n.a.	n.a.	n.a.	n.a.	n.a.	n.a.
+62	+62b	33.02	26.58	3.35	3.35	29.40	3.04	3.04	39.41	2.29	2.7	2.6	3.2
+62	+62c	33.02	26.63	3.35	3.34	29.44	3.03	3.03	39.46	2.28	2.0	1.9	4.5
+62	+62c dup1	33.02	26.62	3.35	3.35	29.42	3.04	3.03	39.44	2.28	1.9	1.8	4.6
+16	+16a	25.54	26.60	3.35	3.35	29.39	3.04	3.04	39.39	2.29	1.7	1.6	5.2
+16	+16b	25.00	26.59	3.35	3.35	29.39	3.04	3.04	39.41	2.29	2.2	2.1	4.0
+15b,c	+15a	24.47	26.60	3.35	3.35	29.39	3.04	3.04	39.40	2.29	1.9	1.8	4.6
+15	+15c	24.47	26.62	3.35	3.35	29.42	3.04	3.03	39.44	2.28	1.7	1.6	5.1
+14	+14b	23.88	n.a.	n.a.	n.a.	n.a.	n.a.	n.a.	n.a.	n.a.	n.a.	n.a.	n.a.
+10	+10a_1	23.475	26.57	3.35	3.35	29.39	3.04	3.04	39.41	2.29	2.9	2.8	3.0
+10	+10a_2	23.475	26.61	3.35	3.35	29.41	3.04	3.03	39.42	2.29	2.0	1.9	4.4
+10	+10b_1	23.47	26.64	3.35	3.34	29.44	3.03	3.03	39.45	2.28	1.9	1.8	4.7
+10	+10b_2	23.47	26.59	3.35	3.35	29.39	3.04	3.04	39.41	2.29	2.2	2.1	4.2
+9	+9b	22.92	26.61	3.35	3.35	29.42	3.04	3.03	39.43	2.29	2.4	2.3	3.7
+135	+135a	45.29	26.65	3.35	3.34	29.61	3.02	3.01	39.66	2.27	7.2	7.1	1.2
+135	+135b	45.29	26.64	3.35	3.34	29.72	3.01	3.00	39.79	2.27	11.0	10.9	0.8
+130	+130a	44.24	26.60	3.35	3.35	29.52	3.03	3.02	39.56	2.28	6.2	6.1	1.4
+130	+130b	44.24	26.65	3.35	3.34	29.51	3.03	3.02	39.50	2.28	3.6	3.5	2.5
+129	+129/130	44.03	26.66	3.34	3.34	29.53	3.02	3.02	39.51	2.28	3.8	3.7	2.3
+102	+102a	39.46	26.59	3.35	3.35	29.58	3.02	3.02	39.63	2.27	8.3	8.2	1.1
+102	+102b	39.46	26.58	3.35	3.35	29.62	3.02	3.01	39.70	2.27	10.3	10.2	0.9
+90	+90	37.14	26.63	3.35	3.34	29.50	3.03	3.03	39.52	2.28	4.1	4.0	2.1
+62	+62a	33.12	26.58	3.35	3.35	29.43	3.03	3.03	39.45	2.28	3.9	3.8	2.3
+62	+62b_1	33.02	26.61	3.35	3.35	29.46	3.03	3.03	39.45	2.28	3.7	3.6	2.3
+62	+62b_2	33.02	26.59	3.35	3.35	29.44	3.03	3.03	39.43	2.29	3.9	3.8	2.3
+62	+62c_1	33.02	26.63	3.35	3.34	29.59	3.02	3.02	39.65	2.27	6.9	6.8	1.3
+62	+62c_2	33.02	26.61	3.35	3.35	29.54	3.02	3.02	39.50	2.28	6.3	6.2	1.4
+62	+62c_3	33.02	26.63	3.35	3.34	29.47	3.03	3.03	39.48	2.28	3.2	3.1	2.9
+31	+31a	27.23	26.59	3.35	3.35	29.64	3.01	3.01	39.73	2.27	10.8	10.7	0.8
+31	+31b	27.23	26.60	3.35	3.35	29.76	3.00	3.00	39.40	2.29	13.9	13.8	0.7
+30	+30a	27.07	26.62	3.35	3.35	29.81	3.00	3.00	39.44	2.28	14.6	14.5	0.6
+30	+30b	27.07	26.66	3.34	3.34	29.81	3.00	2.99	39.91	2.26	13.4	13.3	0.7
+28	+28	26.91	26.65	3.34	3.34	29.56	3.02	3.02	40.06	2.25	5.3	5.2	1.7
+26	+26	26.83	26.59	3.35	3.35	29.75	3.00	3.00	39.41	2.29	14.1	14.0	0.7
+25	+25-29	26.81	26.60	3.35	3.35	29.42	3.04	3.03	39.43	2.29	2.7	2.6	3.2
+18	+15-19	25.56	26.59	3.35	3.35	29.42	3.04	3.03	39.43	2.29	3.0	3.0	2.8
+16	+16a_1	25.54	26.61	3.35	3.35	29.46	3.03	3.03	39.47	2.28	3.6	3.5	2.5
+16	+16a_2	25.54	26.65	3.35	3.34	29.48	3.03	3.03	39.47	2.28	2.9	2.8	2.9
+16	+15/16	25.00	26.67	3.34	3.34	29.48	3.03	3.03	39.82	2.26	2.0	1.9	4.6
+15	+15a	24.47	26.60	3.35	3.35	29.43	3.04	3.03	39.44	2.28	3.0	2.9	2.8
+15	+15d	24.47	26.62	3.35	3.35	29.73	3.00	3.00	39.44	2.28	12.4	12.3	0.7
+14	+14a	24.41	26.61	3.35	3.35	29.46	3.03	3.03	39.46	2.28	3.5	3.4	2.5
+10	+10b	23.47	26.63	3.35	3.35	29.46	3.03	3.03	39.48	2.28	3.0	2.9	2.8
+9	+9a	22.92	26.59	3.35	3.35	29.44	3.03	3.03	39.47	2.28	3.8	3.7	2.3
+9	+9b_1	22.92	26.66	3.34	3.34	29.51	3.03	3.02	39.52	2.28	3.3	3.2	2.6
+9	+9b_2	22.92	26.63	3.35	3.34	29.46	3.03	3.03	39.46	2.28	3.0	2.9	2.8
+3	+3/4	22.33	26.59	3.35	3.35	29.43	3.04	3.03	39.44	2.28	3.2	3.2	2.7
-11	-11a_1	16.87	26.62	3.35	3.35	29.70	3.01	3.01	39.79	2.27	11.3	11.2	0.8
-11	-11a_2	16.87	26.66	3.34	3.34	29.67	3.01	3.01	39.74	2.27	8.4	8.3	1.1
-11	-11b_1	15.98	26.64	3.35	3.34	29.71	3.01	3.00	39.80	2.26	11.0	10.9	0.8
-11	-11b_2	15.98	26.60	3.35	3.35	29.69	3.01	3.01	39.77	2.27	11.8	11.7	0.8
-13	-13a	15.23	26.63	3.35	3.34	29.46	3.03	3.03	39.45	2.28	2.8	2.7	3.1
-13	-13b	12.51	26.60	3.35	3.35	29.85	2.99	2.99	39.45	2.28	16.7	16.6	0.6
-17	-17a	7.20	26.60	3.35	3.35	29.75	3.00	3.00	39.44	2.28	13.8	13.7	0.7
-17	-17b	6.80	26.63	3.35	3.34	30.86	2.90	2.89	39.45	2.28	47.7	47.6	0.3
-20	-20	5.96	26.59	3.35	3.35	30.76	2.91	2.90	39.41	2.29	46.3	46.1	0.3
-24	-24-28	4.00	26.59	3.35	3.35	29.77	3.00	3.00	39.86	2.26	15.0	14.9	0.6
-26	-20-30	3.58	n.a.	n.a.	n.a.	n.a.	n.a.	n.a.	n.a.	n.a.	n.a.	n.a.	n.a.
-33	-33	0.77	26.59	3.35	3.35	29.78	3.00	3.00	39.43	2.29	15.3	15.2	0.6
-34	-34	0.00	n.a.	n.a.	n.a.	n.a.	n.a.	n.a.	n.a.	n.a.	n.a.	n.a.	n.a.

App. 5: Summary of microprobe results of the Fur Formation glendonite.

Sample ID	Cement phase	Calculation	MgCO ₃ (mol%)	SrCO ₃ (mol%)	FeCO ₃ (mol%)	BaCO ₃ (mol%)	MnCO ₃ (mol%)
+9b; +62b	rcc inside	Average	1.59	0.12	0.04	0.01	0.02
+9b; +62b	rcc inside	Min	0.00	0.00	0.00	0.00	0.00
+9b; +62b	rcc inside	Max	3.57	0.31	0.21	0.12	0.34
+14b; +16b	rcc inside	Average	0.89	0.12	0.07	0.02	0.04
+14b; +16b	rcc inside	Min	0.00	0.00	0.00	0.00	0.00
+14b; +16b	rcc inside	Max	2.82	0.35	1.02	0.16	0.38
+9b; +14b; +16b	rcc zonation	Average	1.71	0.16	0.06	0.03	0.03
+9b; +14b; +16b	rcc zonation	Min	0.05	0.00	0.00	0.00	0.00
+9b; +14b; +16b	rcc zonation	Max	2.78	0.73	2.24	0.19	0.14
+9b; +62b	rcc edge	Average	1.95	0.13	0.10	0.02	0.08
+9b; +62b	rcc edge	Min	0.38	0.00	0.00	0.00	0.00
+9b; +62b	rcc edge	Max	3.47	0.28	2.43	0.09	1.28
+14b; +16b	rcc edge	Average	2.07	0.21	1.56	0.05	0.54
+14b; +16b	rcc edge	Min	0.39	0.00	0.00	0.00	0.00
+14b; +16b	rcc edge	Max	3.53	6.19	35.43	3.90	2.77
+9b; +62b	1. rim	Average	3.17	0.16	0.12	0.03	0.20
+9b; +62b	1. rim	Min	1.12	0.00	0.00	0.00	0.00
+9b; +62b	1. rim	Max	4.68	0.48	1.77	0.16	1.66
+14b; +16b	1. rim	Average	3.10	0.15	0.70	0.05	0.61
+14b; +16b	1. rim	Min	1.75	0.00	0.00	0.00	0.00
+14b; +16b	1. rim	Max	4.72	0.60	39.69	0.30	3.93
+9b	2. rim	Average	7.53	0.14	1.10	0.08	1.49
+9b	2. rim	Min	1.88	0.00	0.13	0.00	0.08
+9b	2. rim	Max	10.10	0.32	5.72	0.23	2.67
+9b	fill cem	Average	2.48	0.13	0.60	0.06	0.14
+9b	fill cem	Min	1.30	0.00	0.19	0.00	0.04
+9b	fill cem	Max	2.88	0.28	3.45	0.10	0.62
+62b	fill cem	Average	2.17	0.12	1.77	0.01	2.82
+62b	fill cem	Min	0.48	0.00	0.11	0.00	0.96
+62b	fill cem	Max	3.40	0.26	5.60	0.04	7.59
+16b	fill cem	Average	3.51	0.16	0.31	0.05	0.93
+16b	fill cem	Min	2.74	0.06	0.00	0.00	0.64
+16b	fill cem	Max	3.81	0.22	1.45	0.21	1.37

App. 6: Summary of microprobe results of the Sumatra glendonite.

Sample ID	Cement phase	Comment	Calculation	Mg/Ca (-)	MgCO ₃ (mol%)	CaCO ₃ (mol%)	SrCO ₃ (mol%)	FeCO ₃ (mol%)	BaCO ₃ (mol%)	MnCO ₃ (mol%)
SO189 13156 342	rCc gelb	inside	Average	0.82	0.81	99.05	0.08	0.04	0.00	0.02
SO189 13156 342	rCc gelb	inside	Min	0.06	0.06	97.56	0.00	0.00	0.00	0.00
SO189 13156 342	rCc gelb	inside	Max	2.50	2.44	99.85	0.21	0.13	0.02	0.10
SO189 13156 342	rCc gelb	mix	Average	1.35	1.33	98.56	0.09	0.01	0.00	0.00
SO189 13156 342	rCc gelb	mix	Min	1.15	1.14	98.26	0.00	0.00	0.00	0.00
SO189 13156 342	rCc gelb	mix	Max	1.55	1.52	98.86	0.19	0.03	0.00	0.00
SO189 13156 342	rCc gelb	edge	Average	3.28	3.17	96.73	0.06	0.02	0.01	0.01
SO189 13156 342	rCc gelb	edge	Min	1.98	1.94	95.51	0.00	0.00	0.00	0.00
SO189 13156 342	rCc gelb	edge	Max	4.59	4.38	98.04	0.20	0.09	0.04	0.06
SO189 13156 342	rCc weiß	inside	Average	0.46	0.46	99.38	0.11	0.02	0.01	0.03
SO189 13156 342	rCc weiß	inside	Min	0.00	0.00	98.00	0.00	0.00	0.00	0.00
SO189 13156 342	rCc weiß	inside	Max	1.80	1.77	99.92	0.42	0.07	0.06	0.12
SO189 13156 342	rCc weiß	edge	Average	1.78	1.74	98.13	0.09	0.01	0.01	0.03
SO189 13156 342	rCc weiß	edge	Min	0.61	0.61	96.78	0.00	0.00	0.00	0.00
SO189 13156 342	rCc weiß	edge	Max	3.14	3.04	99.39	0.19	0.07	0.03	0.06
SO189 13156 342	Aggregate	inside	Average	1.36	1.32	98.53	0.09	0.02	0.01	0.02
SO189 13156 342	Aggregate	inside	Min	0.00	0.00	95.95	0.00	0.00	0.00	0.00
SO189 13156 342	Aggregate	inside	Max	4.04	3.88	99.88	0.28	0.09	0.05	0.12
SO189 13156 342	Aggregate	edge	Average	2.89	2.79	97.08	0.10	0.01	0.01	0.02
SO189 13156 342	Aggregate	edge	Min	0.36	0.36	94.84	0.00	0.00	0.00	0.00
SO189 13156 342	Aggregate	edge	Max	5.28	5.01	99.51	0.33	0.09	0.12	0.10
SO189 13156 322	Aggregate	inside	Average	0.81	0.79	99.05	0.11	0.02	0.01	0.02
SO189 13156 322	Aggregate	inside	Min	0.16	0.16	96.04	0.00	0.00	0.00	0.00
SO189 13156 322	Aggregate	inside	Max	3.90	3.74	99.74	0.28	0.21	0.07	0.11
SO189 13156 322	Aggregate	edge	Average	1.77	1.72	98.09	0.13	0.02	0.01	0.03
SO189 13156 322	Aggregate	edge	Min	0.38	0.38	95.83	0.00	0.00	0.00	0.00
SO189 13156 322	Aggregate	edge	Max	4.08	3.91	99.52	0.30	0.08	0.08	0.09

App. 7: XRF results of bulk glendonite samples. “bdl” stands for “below detection limit”.

Ash layer	Sample ID	Profile height (m)	Na ₂ O (%)	MgO (%)	Al ₂ O ₃ (%)	SiO ₂ (%)	P ₂ O ₅ (%)	K ₂ O (%)	CaO (%)	TiO ₂ (%)	Cr (ppm)	MnO (%)	Fe ₂ O ₃ (%)
+62	+62b	33.02	0.00	1.17	0.00	0.02	0.08	0.03	53.87	0.02	0.37	0.24	0.36
+62	+62c	33.02	0.00	1.11	0.00	0.00	0.05	0.02	54.92	0.02	1.44	0.05	0.07
+16	+16a	25.54	0.00	1.11	0.00	0.17	0.19	0.00	53.64	0.03	2.20	0.37	0.16
+16	+16b	25.00	0.00	0.98	0.00	0.33	0.50	0.01	53.04	0.03	2.00	0.34	0.13
+15	+15a	24.27	0.00	1.20	0.00	1.32	0.46	0.00	52.37	0.03	2.09	0.41	0.22
+15	+15c	24.27	0.00	0.00	1.07	1.79	7.64	0.00	48.94	0.02	0.48	0.35	3.40
+10	+10b	23.47	0.00	1.51	0.00	0.08	0.25	0.00	52.64	0.03	2.20	0.33	0.60
+10	+10b repeat	23.47	0.00	1.55	0.00	0.08	0.25	0.00	52.48	0.03	2.05	0.33	0.59
+9	+9b	22.92	0.08	1.20	0.06	1.91	1.01	0.02	53.19	0.03	2.06	0.15	0.33

Ash layer	Sample ID	Profile height (m)	Co (ppm)	Ni (ppm)	Zn (ppm)	Ga (ppm)	Rb (ppm)	Sr (ppm)	Y (ppm)	Zr (ppm)	Nb (ppm)	LOI (%)	Sum (%)
+62	+62b	33.02	4.04	17.30	7.89	bdl	4.30	1008.27	bdl	6.11	2.89	43.40	99.19
+62	+62c	33.02	3.46	3.70	6.17	bdl	3.28	896.86	4.11	5.54	2.38	43.30	99.54
+16	+16a	25.54	5.64	3.23	4.97	bdl	1.76	1054.39	bdl	5.66	2.75	43.00	98.66
+16	+16b	25.00	8.76	8.08	19.21	bdl	2.95	1102.19	13.62	5.11	2.32	42.90	98.24
+15	+15a	24.27	6.04	6.53	8.67	0.00	1.23	965.23	bdl	6.05	2.73	42.40	98.40
+15	+15c	24.27	0.00	7.67	118.32	6.33	1.16	1122.90	0.72	6.05	2.17	39.10	102.30
+10	+10b	23.47	7.84	6.49	8.90	0.00	4.78	1140.54	2.34	5.24	2.27	43.20	98.62
+10	+10b repeat	23.47	6.36	6.01	7.96	0.00	3.93	1137.06	2.68	5.57	2.42	43.20	98.50
+9	+9b	22.92	8.99	14.17	12.74	0.00	3.47	1472.83	3.00	6.47	2.89	42.20	100.19

App. 8: ⁸⁷Sr/⁸⁶Sr ratios of bulk glendonite samples.

Ash layer	Sample ID	Profile height (m)	⁸⁷ Sr/ ⁸⁶ Sr
+62	+62a	33.02	0.70771
+16	+16a	25.54	0.70775
+16	+16b	25.00	0.70773
+15	+15a	24.27	0.70774
+10	+10b	23.47	0.70773
+9	+9b	22.92	0.70773

App. 9: Weight of samples for decarbonatization, C/N ratio and δ¹³C_{org} analyses, N and C content within bulk carbonate concretion samples.

Ash layer	Sample ID	Profile height (m)	Net weight for preparation (g)	Decarbonated sample (g)	TIC calc. (%)	Net weight for C/N analyses (mg)	N (%)	C (%)	Net weight for δ ¹³ C _{org} analyses (mg)	C in CO ₂ (μmol)
+135	+135a	45.29	1.29	0.06	95.35	17.39	0.19	3.41	20.39	60.91
+135	+135b	45.29	1.12	0.09	92.25	19.81	0.14	2.42	41.07	86.65
+130	+130a	44.24	1.22	0.07	94.31	22.48	0.18	3.41	28.61	81.42
+130	+130b	44.24	1.10	0.43	61.15	24.14	0.02	0.48	144.87	58.70
+129	+129/130	44.03	1.34	0.60	55.09	24.13	0.01	0.34	185.58	56.47
+102	+102a	39.46	1.01	0.05	94.76	21.09	0.15	2.81	20.72	47.93
+102	+102b	39.46	1.05	0.45	57.28	34.20	0.00	0.04	n.a.	n.a.
+90	+90	37.14	1.08	0.14	87.41	23.11	0.09	1.19	48.21	48.05
+62	+62a	33.12	1.24	0.18	85.21	21.50	0.11	1.04	70.31	64.49
+62	+62b_1	33.02	1.16	0.49	58.00	25.04	0.00	0.06	n.a.	n.a.
+62	+62b_2	33.02	1.11	0.48	56.94	21.22	0.00	0.09	401.66	29.05
+62	+62c_1	33.02	1.11	0.17	84.82	20.28	0.08	1.26	71.04	75.88
+62	+62c_2	33.02	1.25	0.20	84.12	22.41	0.07	0.92	93.63	73.06
+62	+62c_3	33.02	1.25	0.20	84.12	22.60	0.07	0.87	n.a.	n.a.
+31	+31a	27.23	1.10	0.11	90.29	21.90	0.25	5.48	17.06	82.10
+31	+31b	27.23	1.08	0.47	56.40	25.02	0.00	0.02	n.a.	n.a.
+30	+30a	27.07	1.10	0.18	83.64	20.58	0.16	3.24	38.67	103.42
+30	+30b	27.07	1.18	0.56	52.79	25.12	0.00	0.04	400.68	13.73
+28	+28	26.91	1.13	0.14	87.66	18.33	0.17	3.36	28.59	84.25
+26	+26	26.83	1.06	0.09	91.16	21.20	0.24	4.65	17.48	64.45
+25	+25-29	26.81	1.01	0.10	89.68	21.07	0.13	2.76	35.94	70.18
+18	+15-19	25.56	1.11	-0.05	104.66	22.73	0.19	4.15	18.01	63.40
+16	+16a_1	25.54	1.06	0.05	95.05	22.00	0.20	4.43	17.39	75.35
+16	+16a_2	25.54	1.29	0.65	49.94	37.57	0.00	0.08	18.63	71.33
+16	+15/16	25.00	1.20	0.15	87.56	23.12	0.12	2.05	54.63	95.84
+15	+15a	24.47	1.66	0.08	95.01	19.24	0.21	3.56	25.43	79.97
+15	+15d	24.47	1.13	0.10	91.41	21.24	0.11	2.46	25.21	61.05
+14	+14a	24.41	1.03	0.29	72.34	37.49	0.03	0.36	171.48	57.06
+10	+10b	23.47	1.02	0.09	91.36	22.82	0.09	1.42	51.32	62.75
+9	+9a	22.92	1.09	0.12	89.34	24.04	0.04	0.56	91.59	45.05
+9	+9b_1	22.92	1.10	0.14	87.52	30.12	0.05	0.80	n.a.	n.a.
+9	+9b_2	22.92	1.25	0.53	57.84	29.91	0.03	0.15	421.52	56.44
+3	+3/4	22.33	1.07	0.08	92.18	30.59	0.10	1.27	49.77	56.16
-11	-11a_1	16.87	1.48	0.10	93.16	20.16	0.15	2.36	26.85	50.99
-11	-11a_2	16.87	1.20	0.13	89.58	18.68	0.13	2.26	17.24	49.43
-11	-11b_1	15.98	1.13	0.09	92.43	20.39	0.14	2.28	37.13	69.59
-11	-11b_2	15.98	1.08	0.05	95.04	17.05	0.22	3.49	29.37	38.33
-13	-13a	15.23	1.03	0.15	85.14	29.12	0.14	2.51	27.71	47.52
-13	-13b	12.51	1.01	0.16	84.45	21.27	0.14	2.57	37.22	57.27
-17	-17a	7.20	1.06	0.16	85.01	20.08	0.02	1.96	41.79	56.50
-17	-17b	6.80	1.07	0.11	89.62	24.34	0.09	3.12	28.31	99.95
-20	-20	5.96	1.13	0.19	83.15	20.78	0.01	1.02	71.13	46.07
-24	-24-28	4.00	1.13	0.24	78.65	25.58	0.08	2.15	66.66	116.48
-26	-20-30	3.58	1.05	0.62	41.35	25.00	0.00	1.32	37.82	20.07
-33	-33	0.77	1.02	0.47	53.91	37.49	0.10	0.04	294.44	1.90
-34	-34	0.00	1.06	0.83	22.30	26.87	0.10	2.18	41.28	59.04

App. 10: CAS preparation data of glendonite and carbonate concretion.

Ash layer	Sample ID	Profile height (m)	NaCl ₁ (mg)	NaCl steps (-)	SO _{4NaCl} (ppm)	CAS residue (g)	CAS (ppm)	$\delta^{34}\text{S}_{\text{CAS}}$ (‰V-CDT)	$\delta^{18}\text{O}_{\text{CAS}}$ (‰V-SMOW)
+62	+62a	33.02	n.a.	n.a.	n.a.	n.a.	n.a.	n.a.	n.a.
+62	+62b	33.02	6.98	4	82	1.21	1141	65.00	24.25
+62	+62c	33.02	7.93	4	165	0.97	2437	56.30	24.03
+62	+62c dup1	33.02	30.47	15	1535	n.a.	1592	60.60	24.75
+16	+16a	25.54	20.94	4	383	0.79	1031	59.40	25.10
+16	+16b	25.00	0.97	4	217	0.25	164	37.96	n.a.
+15b,c	+15a	24.47	18.18	10	593	1.00	495	54.00	24.22
+15	+15c	24.47	237.02	19	5245	2.02	547	17.49	13.30
+14	+14b	23.88	n.a.	n.a.	n.a.	n.a.	n.a.	n.a.	n.a.
+10	+10a_1	23.48	6.06	3	102	0.94	583	65.16	24.02
+10	+10a_2	23.48	9.86	5	431	0.61	404	52.36	23.34
+10	+10b_1	23.47	5.30	4	321	0.70	563	68.23	24.49
+10	+10b_2	23.47	13.90	4	213	1.11	673	58.91	24.11
+9	+9b	22.92	0.78	4	15	1.42	96	33.20	16.82
+130	+130a	44.24	50.69	9	931	3.13	1159	26.80	22.43
+62	+62a	33.12	16.66	8	1368	6.47	244	17.60	11.89
+62	+62c_3	33.02	31.57	15	1074	n.a.	3	27.00	12.06
+18	+15-19	25.56	35.94	15	1466	2.59	250	26.30	17.28
+16	+16a_1	25.54	28.36	6	857	3.44	460	23.26	21.39
+15	+15a	24.47	20.55	6	671	3.54	379	17.10	17.66
+10	+10b	23.47	46.49	6	974	10.80	752	32.86	19.04
+9	+9b_1	22.92	30.22	6	861	5.98	400	29.50	n.a.
+3	+3/4	22.33	79.48	13	2646	3.61	238	23.83	12.95
-17	-17a	7.20	169.48	5	2866	6.82	434	12.50	8.08
-17	-17b	6.80	96.82	12	2821	6.10	23	n.a.	n.a.
-24	-24-28	4.00	264.30	12	5754	12.97	297	-5.60	2.88
-33	-33	0.77	28.92	7	1246	10.88	239	n.a.	n.a.

App. 11: $\delta^{34}\text{S}$ values of water soluble sulphate (NaCl-step) recovered during CAS preparation.

Ash layer	Sample ID	Profile height (m)	NaCl step	$\delta^{34}\text{S}$ (‰V-CDT)
+62	+62b	33.02	NaCl1	42.21
+62	+62c	33.02	NaCl1	44.13
+62	+62c dup1	33.02	NaCl1	37.87
+16	+16a	25.54	NaCl1	42.73
+15b,c	+15a	24.47	NaCl1	19.05
+15	+15c	24.47	NaCl1	-19.09
+15	+15c	24.47	NaCl5	-42.40
+15	+15c	24.47	NaCl9	-37.34
+15	+15c	24.47	NaCl14	-28.02
+15	+15c	24.47	NaCl18	-35.35
+10	+10a_1	23.475	NaCl1	39.02
+10	+10a_2	23.475	NaCl1	32.30
+10	+10b_1	23.47	NaCl1	40.89
+10	+10b_2	23.47	NaCl1	42.04
+130	+130a	44.24	NaCl1	-26.55
+62	+62a	33.12	NaCl1	-0.07
+18	+15-19	25.56	NaCl1	-5.41
+18	+15-19	25.56	NaCl5	-22.66
+18	+15-19	25.56	NaCl9	-15.87
+18	+15-19	25.56	NaCl14	-14.16
+16	+16a_1	25.54	NaCl1	3.84
+15	+15a	24.47	NaCl1	17.05
+10	+10b	23.47	NaCl1	18.45
+9	+9b_1	22.92	NaCl1	20.30
+3	+3/4	22.33	NaCl1	6.94
+3	+3/4	22.33	NaCl5	1.34
+3	+3/4	22.33	NaCl10	7.23
-17	-17a	7.20	NaCl1	0.37
-17	-17b	6.80	NaCl1	-23.46
-17	-17b	6.80	NaCl7	-26.56
-24	-24-28	4.00	NaCl1	-22.52
-24	-24-28	4.00	NaCl7	-25.46
-24	-24-28	4.00	NaCl12	-19.70
-33	-33	0.77	NaCl1	0.48

App. 12: Diatomite samples taken during the field investigation in 2014.

Ash layer	Sample ID	Position	Locality	Ash layer	Sample ID	Position	Locality
+135	Si +135_7	3.2 m above +135	Silstrup	+19	Ej +19_1	between +19 and +20	Ejerslev
+135	Si +135_6	2.7 m above +135	Silstrup	+19	Kn +19_1	between +19 and +20	W Knudeklint
+135	Si +135_5	2.2 m above +136	Silstrup	+16	Ej +16_1	between +16 and +19	Ejerslev
+135	Si +135_4	1.7 m above +136	Silstrup	+16	Kn +16_1	between +16 and +19	W Knudeklint
+135	Si +135_3	1.2 m above +135	Silstrup	+14	Ej +14_2	directly below +16	Ejerslev
+130	Si +130_2	0.7 m above +130	Silstrup	+14	Ra u. +16	directly below +16	Råkilde
+130	Si +130_1	0.2 m above +130	Silstrup	+14	Kn +14_2	directly below +16	W Knudeklint
+123	Si +123_2	0.7 m above +123	Silstrup	+14	Kn +14_1	directly above +14	W Knudeklint
+123	Si +123_1	0.2 m above +123	Silstrup	+14	Ra o.+14	directly above +14	Råkilde
+122	Si +122_2	0.6 m above +122	Silstrup	+12	Kn+12_1	between +12 and +13	W Knudeklint
+122	Si +122_1	0.1 m above +122	Silstrup	+11	Kn +11_1	between +11 and +12	W Knudeklint
+120	Si +120_1	between +120 and +121	Silstrup	+9	Kn +9_1	between +9 and +10	W Knudeklint
+118	Kn2 +118_1	between +118 and +119	E Knudeklint	+9	Ra o.+9	between +9 and +10	Råkilde
+114	Kn2 +114_1	between +114 and +115	E Knudeklint	+5	Kn +5_1	between +5 and +6	W Knudeklint
+110	Kn2 +110_1	between +109 and +110	E Knudeklint	+1	Kn +1_1	between +1 and +3	W Knudeklint
+105	Kn2 +105_1	between +105 and +106	E Knudeklint	-10	Kn -10_9	0.3 m below +1	W Knudeklint
+104	Kn2 +104_1	between +104 and +105	E Knudeklint	-10	Kn -10_8	0.8 m below +1	W Knudeklint
+102	Kn2 +102_1	between +102 and +103	E Knudeklint	-10	Kn -10_7	1.3 m below +1	W Knudeklint
+99	Kn2 +99_1	between +99 and +101	E Knudeklint	-10	Kn -10_6	1.8 m below +2	W Knudeklint
+99	Kn +99_1	between +99 and +101	W Knudeklint	-10	Kn -10_5	2.3 m below +2	W Knudeklint
+95	Kn +95_1	between +95 and +96	W Knudeklint	-10	Kn -10_4	2.8 m below +3	W Knudeklint
+91	Kn +91_1	between +91 and +92	W Knudeklint	-10	Kn -10_3	3.3 m below +3	W Knudeklint
+90	Kn +90_1	between +90 and +91	W Knudeklint	-10	Kn -10_2	3.8 m below +4	W Knudeklint
+87	Kn +87_2	directly below +90	W Knudeklint	-10	Kn -10_1	4.3 m below +4	W Knudeklint
+87	Kn +87_1	directly above +87	W Knudeklint	-11	Ra 1m o.-11	1 m above -11	Råkilde
+83	Kn +83_1	between +82 and +83	W Knudeklint	-11	Ra o.6m o.-11	0.6 m above -11	Råkilde
+79	Ej +79_1	between +80 and +81	Ejerslev	-11	Kn -11_1	between -11 and -10	W Knudeklint
+79	Kn +79_1	between +80 and +81	W Knudeklint	-12	Kn -12_1	directly above -12	W Knudeklint
+75	Ej +75_1	between +74 and +75	Ejerslev	-12	Ra -12_1	directly above -12	Råkilde
+75	Kn +75_1	between +74 and +75	W Knudeklint	-14	Kn -13_1	between -13 and -12	W Knudeklint
+70	Ej +70_1	between +70 and +71	Ejerslev	-14	Kn -14_6	2.8 m above -14	W Knudeklint
+70	Kn +70_1	between +70 and +71	W Knudeklint	-14	St 0.5m u. -13	0.5 m below -13	Stolleklint
+66	Ej +66_1	between +66 and +67	Ejerslev	-14	Kn -14_5	2.3 m above -14	W Knudeklint
+66	Kn +66_1	between +66 and +67	W Knudeklint	-14	Kn -14_4	1.8 m above -14	W Knudeklint
+63	Kn +63_1	between +63 and +64	W Knudeklint	-14	Kn -14_3	1.3 m above -14	W Knudeklint
+61	Kn +61_1	between +61 and +62	W Knudeklint	-14	Kn -14_2	0.8 m above -14	W Knudeklint
+59	Kn +59_1	between +59 and +60	W Knudeklint	-14	Kn -14_1	0.3 m above -14	W Knudeklint
+57	Kn +57_1	between +57 and +58	W Knudeklint	-14	St o.-14	directly above -14	Stolleklint
+55	Kn +55_1	between +55 and +56	W Knudeklint	-15	St -15_1	between -15 and -14	Stolleklint
+52	Kn +52_1	between +52 and +53	W Knudeklint	-17	St -17_8	directly below -15	Stolleklint
+48	Kn +48_1	between +48 and +49	W Knudeklint	-17	St -17_7	0.6 m below -15	Stolleklint
+46	Kn +46_1	between +46 and +47	W Knudeklint	-17	St -17_6	1.1 m below -15	Stolleklint
+44	Kn +44_1	0.2 m above +44	W Knudeklint	-17	St -17_5	1.6 m below -15	Stolleklint
+42	Kn +42_2	0.9 m above +42	W Knudeklint	-17	St -17_4	2.1 m below -15	Stolleklint
+42	Kn +42_1	0.4 m above +42	W Knudeklint	-17	St -17_3	2.6 m below -15	Stolleklint
+41	Kn +41_1	between +41 and +42	W Knudeklint	-17	St -17_2	3.1 m below -15	Stolleklint
+40	St u.+40	directly below +44	Stolleklint	-18	St -17_1	3.6 m below -15	Stolleklint
+36	St o.+36	directly above +36	Stolleklint	-18	St 0.5m u. -17	0.5 m below -17	Stolleklint
+35	Ej +35_1	between +35 and +36	Ejerslev	-18	St 1m u. -17	1 m below -17	Stolleklint
+35	Kn +35_1	between +35 and +36	W Knudeklint	-18	St 1.5m u. -17	1.5 m below -17	Stolleklint
+29	Ej +29_1	between +29 and +30	Ejerslev	-18	St 2m u. -17	2 m below -17	Stolleklint
+29	Kn +29_1	between +29 and +30	W Knudeklint	-33	St o. -33	0.5 m above -33	Stolleklint
+21	Ej +21_1	between +21 and +22	Ejerslev	-34	St zw. -33 & -34	between -34 and -33	Stolleklint
+21	Kn +21_1	between +21 and +22	W Knudeklint	-35	St 0.2 m u.-34	0.2 m below -34	Stolleklint

App.13: Overview of diatomite sample prepared for $\delta^{18}\text{O}_{\text{diatom}}$ isotopic analyses.

Ash layer	Sample ID	Colour (-)	Comment	Net weight (g)	Sieve >80 μm	Sieve >40 μm	Diatom weight (mg)
+135	Si +135_6	n.a.	n.a.	11.18	yes	yes	13.81
+135	Si +135_3	brown	loose	5.19	yes	yes	95.03
+130	Si +130_2	bright grey	loose	43.06	yes	yes	125.25
+123	Si +123_2	white	loose	10.05	yes	yes	223.27
+118	Kn2 +118_1	dark brown	loose	16.95	yes	yes	8.77
+114	Kn2 +114_1	dark grey	sticky	11.45	yes	yes	48.42
+104	Kn2 +104_1	white	loose	23.65	no	yes	15.42
+90	Kn +90_1	bright grey	loose	12.29	yes	yes	21.76
+87	Kn +87_2	n.a.	n.a.	17.66	no	yes	127.09
+83	Kn +83_1	n.a.	n.a.	14.55	yes	yes	117.17
+79	Ej +79_1	white	loose	10.87	yes	yes	85.53
+79	Kn +79_1	dark grey	sticky	12.15	yes	yes	7.05
+66	Ej +66_1	dark grey	loose	10.79	yes	yes	22.87
+61	Kn +61_1	dark grey	sticky	57.78	no	no	15.98
+59	Kn +59_1	bright grey	loose	11.47	yes	yes	39.37
+52	Kn +52_1	white	loose	9.68	no	yes	269.03
+44	Kn +44_1	bright grey	loose	13.24	yes	yes	178.31
+42	Kn +42_1	bright grey	loose	14.94	no	yes	193.21
+21	Ej +21_1	bright grey	loose	11.86	yes	yes	130.84
+21	Kn +21_1	bright grey	loose	5.7	yes	yes	163.44
+14	Ej +14_2	white	loose	9.41	yes	yes	340.18
+14	Ra u. +16	white	loose	10.52	yes	yes	247.51
+14	Kn +14_2	white	loose	11.48	yes	yes	502.52
+11	Kn +11_1	white	loose	31.75	yes	yes	121.06
+1	Kn +1_1	white	loose	11.96	yes	yes	296.78
-10	Kn -10_7	brown	loose	10.42	no	yes	97.60
-10	Kn -10_4	n.a.	n.a.	11.55	no	no	6.12
-11	Kn -11_1	brown	loose	11.29	no	no	14.88
-12	Kn -12_1	brown	loose	10.56	yes	yes	324.41
-12	Ra -12_1	brown	loose	10.2	no	yes	180.97
-14	St 0.5m u. -13	dark grey	sticky	56.03	yes	yes	33.45
-14	Kn -14_2	white	loose	11.23	yes	yes	367.98
-17	St -17_8	brown	loose	11.29	no	no	36.70
-17	St -17_6	white	loose	10.16	yes	yes	118.19
-17	St -17_5	brown	loose	5.21	yes	yes	31.48
-17	St -17_2	white	loose	12.2	yes	yes	507.08
-18	St 0.5m u. -17	dark grey	sticky	15.88	no	yes	15.54
-18	St 1m u. -17	dark grey	sticky	11.15	no	no	13.15
-33	St o. -33	n.a.	n.a.	10.12	no	yes	37.66
-34	St zw. -33 & -34	n.a.	n.a.	11.23	no	yes	371.84
-35	St 0.2 m u. -34	white	loose	10.28	no	yes	300.84

App. 14: Results of the point count analyses of the diatom samples.

Ash layer	Sample ID	Diatoms (%)	Other SiO ₂ fossils (%)	Minerals (%)
+135	Si +135_6	5.32	3.99	90.66
+135	Si +135_3	1.99	4.66	93.33
+130	Si +130_2	92.65	6.66	0.66
+123	Si +123_2	72.65	27.33	0.00
+118	Kn2 +118_1	9.66	2.00	83.99
+114	Kn2 +114_1	0.00	0.33	97.32
+104	Kn2 +104_1	10.65	3.33	84.33
+90	Kn +90_1	1.00	1.00	93.32
+87	Kn +87_2	85.65	8.66	5.66
+83	Kn +83_1	80.65	12.33	7.00
+79	Ej +79_1	66.99	8.66	24.33
+79	Kn +79_1	0.66	1.33	93.00
+66	Ej +66_1	2.33	0.66	90.66
+61	Kn +61_1	73.31	5.66	21.00
+59	Kn +59_1	6.99	5.66	80.66
+52	Kn +52_1	85.00	12.33	2.66
+44	Kn +44_1	5.98	1.00	93.00
+42	Kn +42_1	94.65	5.33	0.00
+21	Ej +21_1	6.33	0.33	93.33
+21	Kn +21_1	1.66	0.00	98.33
+14	Ej +14_2	86.98	13.00	0.00
+14	Ra u. +16	88.98	11.00	0.00
+14	Kn +14_2	92.31	7.66	0.00
+11	Kn +11_1	61.98	9.66	28.33
+1	Kn +1_1	87.31	7.66	5.00
-10	Kn -10_7	90.32	7.33	2.33
-10	Kn -10_4	13.99	18.66	67.33
-11	Kn -11_1	3.99	3.32	92.66
-12	Kn -12_1	95.31	3.33	1.33
-12	Ra -12_1	45.65	51.33	3.00
-14	St 0.5m u. -13	88.66	5.33	6.00
-14	Kn -14_2	86.64	13.00	0.33
-17	St -17_8	64.98	15.99	18.99
-17	St -17_6	86.99	10.00	3.00
-17	St -17_5	56.32	12.32	31.33
-17	St -17_2	93.98	4.33	1.66
-18	St 0.5m u. -17	16.00	25.99	51.99
-18	St 1m u. -17	35.98	8.33	48.66
-33	St 0. -33	58.32	39.33	2.33
-34	St zw. -33 & -34	2.99	0.00	97.00
-35	St 0.2 m u. -34	0.99	0.00	98.99

10 Acknowledgements and Curriculum Vitae

10.1. Acknowledgements

First of all, I extend gratitude to my dissertation supervisor Prof. Dr. Harald Strauß for his support and help with this study.

I would like to thank PD Dr. Matthias Zabel for his willingness to review my thesis.

I thank the German Research Foundation (DFG, Project TE 642/3) for the funding of this thesis.

My many thanks to my advisor Dr. Barbara Teichert, who gave me the chance to do this research.

This thesis was supported by material supply from the Moler Museet Mors and the Fur Museum. I appreciate Hendrik Madsen and Bo Pagh Schultz for collecting all glendonites and carbonate concretions. Bo is thanked for giving nice inputs on the newest research on the Fur Formation and all his help during the field work in 2014.

I am grateful to Julius Petersen, Prof. Dr. Gunver Pedersen, Joost Frieling, Dr. Pi Willumsen, Dr. Petra Schoon, Dr. Morgan Jones, and Dr. Jan Rasmussen for their discussions and advice during the UNESCO World Heritage Symposium.

For the technical help and support, my thanks to Artur Fugmann who analysed most of my samples. I also would like to thank Andreas Lutter, Dr. Peter Schmid-Beurmann, Heide-Marie Baier, Ulrike Berning-Mader, and Anne Niehus for their laboratory support. Beate Schmitte, Dr. Jasper Berndt-Gerdes, Thorsten Grundt, and Manuel Tiedeken are thanked for the instruction and execution of microprobe and SEM analyses. Additionally, PD Dr. Nikolaus Gussone is acknowledged for the Sr and Ca isotope measurements and the subsequent data analyses. Dr. Daniel Birgel is acknowledged for the biomarker analyses, Prof. Dr. Torsten Vennemann for the $\delta^{18}\text{O}_{\text{diatom}}$ investigations, and Prof. Dr. Jens Fiebig for the measurement of the clumped isotopes. Traudel Fahrenkemper is thanked for her assistance for problems with graphic programs.

A big “thank you” goes to my mensa colleagues Dr. Sven Hartenfels, Stefan Helling, and Sören Stichling for all the nice conversations during meals. Many thanks to Dr. Flora Boekhout, Katharina Siedenber, Simon Schurr, Caroline Heineke, Dr. Reinhard Wolff, Martin Hoferichter, and Jaqueline Bertlich for their friendly and loyal support. I owe a great depth of gratitude to Vanessa Fichtner for the friendship during all these years. Without these people I wouldn't have had this wonderful time at the institute.

Rosel Horsters-Bromkamp is acknowledged for her help with the English language.

Finally, I want to thank my parents, my brother, and my sister for the encouragement received. I thank my boyfriend Uli for his care and support.

10.2. Curriculum vitae